processes

Photocatalytic Processes for Environmental Applications

Edited by
Olivier Monfort and Yanlin Wu

Printed Edition of the Special Issue Published in *Processes*

www.mdpi.com/journal/processes

MDPI

Photocatalytic Processes for Environmental Applications

Photocatalytic Processes for Environmental Applications

Editors

Olivier Monfort
Yanlin Wu

MDPI • Basel • Beijing • Wuhan • Barcelona • Belgrade • Manchester • Tokyo • Cluj • Tianjin

Editors
Olivier Monfort
Comenius University in Bratislava
Slovakia

Yanlin Wu
Fudan University
China

Editorial Office
MDPI
St. Alban-Anlage 66
4052 Basel, Switzerland

This is a reprint of articles from the Special Issue published online in the open access journal *Processes* (ISSN 2227-9717) (available at: https://www.mdpi.com/journal/processes/special_issues/photocatalytic_processes).

For citation purposes, cite each article independently as indicated on the article page online and as indicated below:

LastName, A.A.; LastName, B.B.; LastName, C.C. Article Title. *Journal Name* **Year**, *Volume Number*, Page Range.

ISBN 978-3-0365-3435-0 (Hbk)
ISBN 978-3-0365-3436-7 (PDF)

Contents

About the Editors

Olivier Monfort is an expert in photochemical processes for the treatment of water from organic contamination using nanomaterials. He received his PhD in Inorganic Chemistry in 2017 at the Faculty of Natural Sciences, Comenius University in Bratislava (FNS CU), Slovakia. He was a postdoctoral fellow in France at the Ecole National Supérieure de Chimie de Rennes (from 2017 to 2018) and at the Université Clermont Auvergne (from 2018 to 2019). At the end of 2019, he returned to his alma mater at Comenius University as a senior scientist, where he is now the co-leader of the Laboratory of Photoactive Materials at the Department of Inorganic Chemistry, FNS CU. In 2021, he was the finalist of the prestigious "Falling Walls Lab Slovakia". To date, Dr. Olivier Monfort has an h-index of 10, published 2 book chapters, and received several financial supports for mobility and scientific projects.

Yanlin Wu is an expert in iron chemistry and radicals-based oxidation systems for the degradation of contaminants of emerging concern in water and soil. She received her PhD degree in 2014 from a "co-tutelle" between Fudan University, China and Université Clermont Auvergne, France. She started her scientific career as postdoctoral fellow at the Université Clermont Auvergne (from 2014 to 2015) and then at the Tongji University (from 2015 to 2017). Since 2017, Dr. Yanlin Wu has been employed as associate researcher at Fudan University, China. In her short career, she has received the financial support from the China Postdoctoral Science Foundation (2016), National Natural Science Foundation of China (2017) and Foundation of Key Laboratory of Yangtze River Water Environment, Ministry of Education (2021). She has published more than 30 research papers.

Preface to "Photocatalytic Processes for Environmental Applications"

Photocatalysis, especially heterogeneous photocatalysis, is one of the most widely investigated processes for environmental applications. Indeed, the activation of photocatalytic materials by solar light, which is an infinite source of energy, is considered as a sustainable technology. The conversion of solar light into chemical energy via heterogeneous photocatalysts is a powerful tool to decontaminate different environment compartments (water, air, and soil). In addition to photocatalysis, other photochemical processes can be used for environmental purposes, including the photo-Fenton process and photolysis. This Special Issue on "Photocatalytic Processes for Environmental Applications" summarizes these crucial challenges faced by current and future generations.

Olivier Monfort and Yanlin Wu
Editors

processes

MDPI

Editorial

Photocatalytic Processes for Environmental Applications

Olivier Monfort [1,*] and Yanlin Wu [2]

[1] Department of Inorganic Chemistry, Faculty of Natural Sciences, Comenius University in Bratislava, Ilkovicova 6, Mlynska Dolina, 84215 Bratislava, Slovakia
[2] Department of Environmental Science and Engineering, Fudan University, 2005 Songhu Road, Shanghai 200438, China; wuyanlin@fudan.edu.cn
* Correspondence: monfort1@uniba.sk; Tel.: +421-(0)290142141

Photocatalysis, especially heterogeneous photocatalysis, is one of the most investigated processes for environmental remediation. Indeed, the use of solar light, which is an infinite source of energy, to activate photocatalysts is a sustainable technology [1]. The conversion of solar light into chemical energy via a heterogeneous photocatalyst is a powerful tool to decontaminate the natural environment (water, air, and soil), but also to produce green energy such as hydrogen, which is considered as the most promising alternative to fossil energy [1]. Beside photocatalysis, other photochemical processes can be used for environmental applications, including the photo-Fenton process and photolysis. The Special Issue on "Photocatalytic Processes For Environmental Applications" summarizes all these crucial challenges that the future generation will have to solve. The Special Issue is available online at https://www.mdpi.com/journal/processes/special_issues/photocatalytic_processes (access date: 19 November 2021).

A well-known family of heterogeneous photocatalysts are transition metal chalcogenides. Among them, the most popular one is titanium dioxide (TiO_2), which is still the most investigated owing to its non-toxicity, low cost, and relatively high efficiency under UVA light. While several methods including the design of composite and doping are often found to successfully increase the photocatalytic activity of TiO_2 under visible light, innovative methods could also be used, such as photocatalytic activation through electron beam [2]. In this special issue, Gallegos et al. have demonstrated that microparticulate TiO_2 activated with e-beam exhibited a higher degradation rate constant for Direct Blue 1 removal [2].

It is worth reminding the photocatalytic mechanism during the degradation of organic pollutants in water. After the generation of electron/hole (e^-/h^+) pairs under suitable irradiation ($h\nu > E_g$), highly reactive inorganic radicals, especially reactive oxygen species (ROS), are produced:

$$h^+ + OH^- \rightarrow HO^\bullet \quad (1)$$

$$e^- + O_2 \rightarrow O_2^{\bullet -} \quad (2)$$

These "primary" radicals are responsible of the efficient degradation of water contaminants.

On the other hand, as UVA light represents only 5% of the solar spectrum, intense research is also focused on visible light-driven photocatalysts like, for example, vanadium- and iron-based oxides (V_2O_5, $BiVO_4$, Fe_2O_3, $CoFe_2O_4$, and so on), as well as metal sulfides (CdS, ZnS, CuS, and so on) [1,3,4]. Some of these materials are ternary oxides. Indeed, it helps to tune the energy bandgap, which is an essential feature in heterogeneous photocatalysis [1]. In addition, another important physical factor that should be considered in heterogeneous photocatalysis is the morphology of materials. Morphology can influence the specific surface area as well as the transport properties of charge carriers. In this way, Ullah et al. have published in this Special Issue work related to the preparation of CdS nanorods, which have excellent photocatalytic properties in the degradation of Rhodamine

Citation: Monfort, O.; Wu, Y. Photocatalytic Processes for Environmental Applications. *Processes* **2021**, *9*, 2080. https://doi.org/10.3390/pr9112080

Received: 11 November 2021
Accepted: 12 November 2021
Published: 20 November 2021

B [3]. Moreover, photocatalysts can be composed of chemical elements that are active in Fenton-based reactions (Equations (3)–(5)). It is the case of $CoFe_2O_4$ that has been investigated by To Loan et al. [4]. Indeed, this visible light-driven photocatalyst in combination with Fenton-based processes can almost completely degrade Rhodamine B [4].

$$Fe^{2+} + H_2O_2 \rightarrow Fe^{3+} + OH^- + HO^\bullet \quad (3)$$

$$Fe^{3+} + H_2O_2 \rightarrow Fe^{2+} + H^+ + HO_2^\bullet \quad (4)$$

$$Fe^{3+} + H_2O + h\nu \rightarrow Fe^{2+} + H^+ + HO^\bullet \quad (5)$$

Concerning these Fenton-based processes, they are usually performed in homogeneous systems using dissolved iron species, thus exhibiting higher kinetic rates compared with heterogeneous systems. By looking at these reactions (Equations (3) and (4)), it appears as a catalytic process owing to the iron cycle ($Fe^{2+} \leftrightarrow Fe^{3+}$). However, in an aqueous solution, Fenton-based reactions face two main drawbacks, including (i) the stability of iron species and (ii) the reduction of Fe^{3+} into Fe^{2+} (which is the limiting step). Therefore, using non-toxic and biodegradable ligands, stable iron complexes can be used under visible light, thus allowing their use at environmental pH and favoring the reduction process via iron photolysis (Equation (5)). That has been investigated in the work of Huang et al., where 2,4-dichlorophenol has been successfully degraded using the Fe(III)–EDDS complex in both synthetic and real water bodies [5].

Another interesting photochemical process is the photolysis of radical precursors. In such a configuration, no material is needed as the action of light of suitable energy can generate ROS like $HO^\bullet$. Usually, hydroxyl radicals can be generated by photolysis of H_2O_2 under UVB light, while strong UVC is required to photolyze water molecules. For the latter, a VUV/UV photoreactor is necessary. In this Special Issue, Luo et al. have investigated the fluid dynamics in a VUV/UV photoreactor by correlating simulations with experiments for the degradation of organic pollutants [6]. Therefore, their work brings interesting knowledge for the development of such a technology for water treatments.

The improvement of photochemical processes can also be reached using physical methods. An example is the application of a voltage to a photocatalyst in the form of a photoelectrode. Such a photoelectrocatalytic process can be employed for various applications including the production of hydrogen by water splitting, the enhanced degradation of water contaminants, and the production of hydrogen peroxide. In this Special Issue, Papagiannis et al. have studied the latter system using a photoanode [7]. Indeed, the production of H_2O_2 by WO_3 photoanode is made sustainable by using organic fuels from biomass derivatives such as glycerol and ethanol. H_2O_2 is a well-known oxidant that is used in both conventional oxidation and advanced oxidation processes. It is a radical precursor used in the production of hydroxyl radicals.

This Special Issue on "Photocatalytic Processes For Environmental Applications" offers an overview (through original full-length and review articles) of the different photochemical processes (photocatalysis, photo-Fenton, and photolysis) triggered by different inorganic compounds that can be used for environmental applications, not for only water treatment, but also for hydrogen production. As guest editors, we thank all the contributors and the editorial team of *Processes* for their work and the successful publication of this Special Issue.

Funding: There is no external funding.

Conflicts of Interest: The authors declare no conflict of interest.

References

1. Monfort, O.; Petriskova, P. Binary and ternary vanadium oxides: General overview, physical properties, and photochemical processes for environmental applications. *Processes* **2021**, *9*, 214. [CrossRef]
2. Gallegos, E.; Bisesti, F.M.; Vaca-Escobar, K.; Santacruz, C.; Fernandez, L.; Debut, A.; Espinoza-Montero, P.J. Degradation of direct blue 1 through heterogeneous photocatalysis with TiO_2 irradiated with e-beam. *Processes* **2020**, *8*, 1181. [CrossRef]

3. Ullah, H.; Viglasova, E.; Galambos, M. Visible light-driven photocatalytic rhodamine B degradation using CdS nanorods. *Processes* **2021**, *9*, 263. [CrossRef]
4. Loan, N.T.T.; Lan, N.T.H.; Hang, N.T.T.; Hai, N.Q.; Anh, D.T.T.; Hau, V.T.; Van Tan, L.; Van Tran, T. $CoFe_2O_4$ nanomaterials: Effect of annealing temperature on characterization, magnetic, photocatalytic, and photo-Fenton properties. *Processes* **2019**, *7*, 885. [CrossRef]
5. Huang, W.; Huang, Y.; Wang, S.; Lin, H.; Mailhot, G. Degradation of 2,4-dichlorophenol by ethylenediamine-N,N′-disuccinic acid-modified photo-Fenton system: Effects of chemical compounds present in natural waters. *Processes* **2021**, *9*, 29. [CrossRef]
6. Luo, M.; Xu, W.; Kang, X.; Ding, K.; Jeong, T. Computational fluid dynamics modeling of rotating annular VUV/UV photoreactor for water treatment. *Processes* **2021**, *9*, 79. [CrossRef]
7. Papagiannis, I.; Balis, N.; Dracopoulos, V.; Lianos, P. Photoelectrocatalytic hydrogen peroxide production using nanoparticulate WO3 as photocatalyst and glycerol or ethanol as sacrificial agents. *Processes* **2020**, *8*, 37. [CrossRef]

processes

MDPI

Review

Binary and Ternary Vanadium Oxides: General Overview, Physical Properties, and Photochemical Processes for Environmental Applications

Olivier Monfort [1,*] and Patrícia Petrisková [2]

[1] Department of Inorganic Chemistry, Faculty of Natural Sciences, Comenius University in Bratislava, Ilkovicova 6, Mlynska Dolina, 842 15 Bratislava, Slovakia
[2] Institute of Inorganic Chemistry, Slovak Academy of Sciences, Dubravska Cesta 9, 845 36 Bratislava, Slovakia; patricia.petriskova@savba.sk
* Correspondence: monfort1@uniba.sk; Tel.: +421-290142141

Abstract: This review article is a comprehensive report on vanadium oxides which are interesting materials for environmental applications. Therefore, a general overview of vanadium and its related oxides are presented in the first two parts. Afterwards, the physical properties of binary and ternary vanadium oxides in single and mixed valence states are described such as their structural, optical, and electronic properties. Finally, the use of these vanadium oxides in photochemical processes for environmental applications is detailed, especially for the production of hydrogen by water splitting and the degradation of organic pollutants in water using photocatalytic and photo-Fenton processes. The scientific aim of such a review is to bring a comprehensive tool to understand the photochemical processes triggered by vanadium oxide based materials where the photo-induced properties are thoroughly discussed based on the detailed description of their intrinsic properties.

Keywords: vanadium oxide; photochemistry; environment; materials; pollutant; hydrogen

Citation: Monfort, O.; Petrisková, P. Binary and Ternary Vanadium Oxides: General Overview, Physical Properties, and Photochemical Processes for Environmental Applications. *Processes* **2021**, *9*, 214. https://doi.org/10.3390/pr9020214

Academic Editor: Monika Wawrzkiewicz
Received: 30 December 2020
Accepted: 21 January 2021
Published: 24 January 2021

1. Introduction

Vanadium (V) is a chemical element discovered by Andres Manuel Del Rio in 1801 in the form of an ore, called today vanadinite ($Pb_5(VO_4)_3Cl$) [1,2]. At that time, vanadium was named "panchromium" since its different salts exhibit a wide variety of colors. In 1831, Nils Gabriel Sefstrom (re)discovered this chemical element in the form of oxide [3]. He called this chemical element "vanadium" after Vanadis, a goddess in the Norse mythology. Vanadium is an early first-row transition metal (Group 5; Z = 23), with the electronic configuration of $[Ar]3d^34s^2$ [4]. In the earth's crust, vanadium is 5th (0.019%) among all transitional metals and 22nd among all discovered elements [5,6], that corresponds to an average amount of 159 g per ton [7]. In the soil, the average abundance of vanadium is > 100 $mg{\cdot}kg^{-1}$, but this value depends strongly on the geology and the human activity [2,7]. Vanadium can be found in various minerals in the form of either vanadate, silicate, sulfide, sulfate, phosphate, or oxide, such as vanadinite, carnotite, roscoelite, patronite, bravoite and davidite [2,8]. Concerning the physico-chemical properties of this transition metal, vanadium has a melting point at 1910 °C and forms oxide with different oxidation states (from +II to +V) and with various crystalline structures [9].

Vanadium is a transition metal of high environmental and biological importance. Indeed, vanadium is ubiquitously distributed in soil, water, air and living organisms. For instance, in sea water, vanadium (mainly in the form of $H_2VO_4^-$) is the second most abundant transition metal element with a mean concentration of 2 $\mu g{\cdot}L^{-1}$ [2,10] while in rivers, lakes and groundwater, the maximum concentration of vanadium is up to 30 $\mu g{\cdot}L^{-1}$ [2,11]. The presence of vanadium in the environment is due to both natural and human activities. The main natural sources for vanadium are marine aerosols, dust

from soils and rocks weathering, and volcanic emissions [12–15]. From anthropogenic activity, vanadium loads are mainly from mining and burning of crude oil, thus resulting in atmospheric pollution. Vanadium from human contamination is also observed in water resources (rivers, lakes and seas). The quantity of vanadium released into the atmosphere is estimated at more than 60,000 tons each year, and mostly from combustion of fossil fuels [16]. In addition, V has the ability to stay in the air, water and soil for long period of time [17].

In biochemistry, vanadium is an essential trace element for several mammals. Indeed, V has a key role in some enzymes such as nitrogenase and haloperoxidase [2]. Vanadium enters in the blood through gastro-intestinal and respiratory systems and then is transported into the other parts of the body in the form of citrates, lactates, or phosphates [18]. Most of V accumulates in vital organs such as kidneys, spleen and liver [19]. In the human body, about 100 μg of vanadium is present. It is important to notice that vanadium in the form of vanadate (VO_4^{3-}) is isostructural to phosphate. It is therefore a competitive element with PO_4^{3-} and can inhibit and/or motivate several phosphate-metabolizing enzymes [20]. Therefore, at high levels, vanadates can be fatal for human [2]. For plants, it is known that V can affect the metabolism including mineral uptake, enzymatic activities, photosynthetic activity, and the biological yield of plants.

This review article starts with an overview of the applications of various vanadium compounds (Section 2). Afterwards binary and ternary vanadium oxides are introduced (Section 3) with an emphasis on their structure and physical properties before a discussion on their use in photochemical processes for environmental applications (Section 4). Usually, transition metal oxides (TMOs) and especially vanadium oxides have unique physical, chemical, optical, electronic, thermal, and magnetic properties. Therefore, vanadium oxides can find promising applications in various fields such as energy conversion and storage [21]. The particularity of vanadium oxide based materials is that most of them exhibit an insulator-to-metal transition (IMT). Indeed, below a critical temperature (T_c), the properties of the material are insulating or semiconducting while at temperature above they have a metallic behavior. There are different vanadium oxides, therefore the IMT are observed over a wide range of temperatures depending on the oxide, i.e., O/V ratio [22,23]. Due tof this IMT, vanadium oxides are known to be chromogenic materials: they can change their optical properties by applying some external stimuli in the form of photon radiation, temperature change and voltage pulse, thus defining vanadium oxides as photochromic, thermochromic, and electrochromic materials, respectively [22].

In addition to the potential use of vanadium oxides in new technologies, the challenge of environmental remediation is one of the most crucial issues for the present and future generations. The deterioration and contamination of the environment combined to the threat of energy shortage have led the society to explore alternatives to fossil fuels and to pay more attention to our actual way of life. One of the main goals of national governments is to reduce their energy consumption and greenhouse gas emission and to save the natural environment [24]. Indeed, international agreements, such as Kyoto protocol (1995), Stockholm convention (2001), and Paris agreements (2015) have been signed, thus limiting our impact on the planet. Although these attempts are unprecedented, the development of green and efficient remediation treatments is necessary. Our natural environment has been considerably damaged, especially from the last industrial revolution, and is still being deteriorated due to the human activity, in particular factories in the field of textile, chemistry, agriculture, and pharmacy [25–27]. For instance, the quality of water which is a rare and precious resource (around 0.5% of water on the Earth is drinkable and accessible) is alarming because the different types of industry release many organic and inorganic pollutants such as pesticides and fertilizers, sulfur derivatives, active pharmaceutical ingredients, etc. [25–28]. Among them, many pollutants are persistent and of emerging concern, i.e., they are known compounds which are detected by accumulation effect and whose chemistry and interaction with the environment are unknown. Such pollutants may have harmful effects because they include endocrine disruptor compounds, pharmaceutical

and personal care products, etc. [29–32]. These contaminants are potentially toxic for humans, animals and plants, thus pushing the national environmental agencies to impose strict measures to limit the pollution [26]. However, limiting the pollution does not remediate the damages already caused to the planet [33]. In addition, the water resources are subjected to an imbalance between availability and demand in water which is caused by its overuse for domestic, industrial, and agricultural purposes, but also by the climate disorder (longer, more intense and more frequent droughts).

Regarding these issues, vanadium oxides are promising materials. As semiconductors, vanadium oxides can be employed in photocatalysis which is a viable alternative to conventional biological, chemical, and physical technologies for the removal of pollutants, especially in water [25,26]. In addition, these photocatalytic (and other photo-induced processes) can be triggered by solar energy for environmental applications. In addition to decontamination treatments (Section 4.2), another task is the supply of sustainable and clean energy (Section 4.1). Indeed, vanadium oxide based materials are also able to convert solar energy for the production of hydrogen. To resume, binary and ternary vanadium oxides are attractive for a wide range of environmental applications [9]. Despite the numerous scientific contributions on vanadium oxides, the novelty of this review article is to (i) introduce this versatile element in a global overview, followed by (ii) a strong emphasis on the physical properties of vanadium oxides based materials and their use in (iii) photochemical processes for environmental applications which are one of the biggest issues in the modern time.

2. Vanadium: A Versatile Element for Various Applications

2.1. Vanadium Compounds in Homogeneous Systems

The common oxidation states of vanadium are from +II to +V. The chemistry of this transition element in aqueous solution is a key point to understand its versatile properties. In water, vanadium with oxidation states from +II to +V form either aqua-complexes or oxo-cations with typical colors. The hexa-aqua-complexes $[V^{II}(H_2O)_6]^{2+}$ and $[V^{III}(H_2O)_6]^{3+}$ are violet and green, while vanadyl ($V^{IV}O^{2+}$) and pervanadyl ($V^{V}O_2{}^{+}$) cations are blue and yellow, respectively. Regarding the aqueous redox reactions (Equations (1)–(3)), vanadium (II) is a reducing agent while vanadium (V) is an oxidant [34,35]. In the environment, V (IV) and V (V) are in the form of vanadyl and vanadate, respectively, while V (II) is thermodynamically unstable and V (III) is stable only under strongly anoxic conditions [2].

$$VO_2{}^{+} + 2H^{+} + e^{-} = VO^{2+} + H_2O;\ E^0 = 1.0\ V \quad (1)$$

$$VO^{2+} + 5H_2O + 2H^{+} + e^{-} = [V(H_2O)_6]^{3+};\ E^0 = 0.24\ V \quad (2)$$

$$[V(H_2O)_6]^{3+} + e^{-} = [V(H_2O)_6]^{2+};\ E^0 = -0.26\ V \quad (3)$$

In this section, the chemistry of vanadium (V) in aqueous solution is briefly discussed since many molecular species have been discovered [36]. The speciation of these V (V) compounds depends mainly on vanadium concentration, temperature, and solution pH. There are basically two main types of reaction which control the formation of vanadium (V) species: hydrolysis and condensation [37]. At room temperature, dissolved V (V) salts are solvated in aqueous solution by water molecules, thus giving rise to hydrated species $[V(H_2O)_n]^{5+}$ [37]. However, the water molecule ligands are partially deprotonated (Equation (4)) due to the strong polarizing power of highly charged vanadium (V). This hydrolysis process results in a decrease in pH.

$$[V(H_2O)_6]^{5+} + hH_2O \rightarrow [V(H_2O)_{6-h}(OH)_h]^{(5-h)+} + hH_3O^{+} \quad (4)$$

The term "*h*" is the hydrolysis ratio and it increases with increasing pH, thus leading to the formation of aqua, hydroxo, and oxo species. Therefore, at low pH (pH < 2), the hydrolysis ration $h = 4$ and $[V(OH)_4(H_2O)_2]^{+}$ is formed. Since V (V) is highly charged, internal proton transfer occurs to decrease this high positive charge and it leads to the

formation of pervanadyl species $[VO_2(H_2O)_4]^+$ or $[VO_2]^+$ with V=O double bonds (vanadyl groups) in *cis* position [38]. At pH ≈ 6, the coordination number of V (V) decreases from 6 to 4 since V-O bonds are more covalent, thus leading to the formation of four-fold coordinated vanadate $[H_nVO_4]^{(3-n)-}$. Above pH = 12, vanadate species are fully deprotonated. It is worth noting that monomeric species are observed only in dilute solutions. At higher vanadium concentration, condensation process dominates and occurs through olation and oxolation (Equations (5) and (6)) [37]:

$$\text{Olation: } >V-OH+ > V-OH_2 \rightarrow >V-O(H)-V < +H_2O \quad (5)$$

$$\text{Oxolation: } >V-OH+ >V-OH \rightarrow >V-O-V < +H_2O \quad (6)$$

The temperature has also strong effect on the molecular structure of vanadium species [37]. Once vanadium precursors have been condensed to decavanadate species, they can transform upon heating into cyclic metavanadates (Equation (7)) [39]. This dissociation process is a reversible reaction:

$$2[H_2V_{10}O_{28}]^{6-} + 4H_2O = 5[V_4O_{12}]^{4-} + 12H^+ \quad (7)$$

In addition to the chemistry of aqueous vanadium species, their biological relevance (Figure 1) is also a point which needs to be briefly developed. Only higher oxidation states of vanadium are considered in the physiological pH (2 < pH < 8), i.e., V (IV) and V (V) in cationic and anionic forms. On the other hand, V (III) is mainly present in primitive organisms such as ascidians and worms and it is not present in complex organisms [40,41]. Vanadium at higher oxidation states is present in most of mammal tissues (around 20 nM). In the human body, the average vanadium concentration is approximately 0.3 μM [42–48]. Vanadium in the form of vanadate ($H_2VO_4^-$), which can be present in drinking water, is partially reduced in the stomach before being precipitated in the intestines in the form of $VO(OH)_2$ [10]. Vanadium can also enter directly in the blood stream by intravenously injection [49]. Once in the blood, vanadium undergoes redox conversion between V (V) and V (IV) according to the level of oxygen and the presence of reductants/oxidants. Thus, vanadium could form either anionic VO_4^{3-}, cationic VO^{2+} or neutral/charged vanadium complex. Concerning the toxicity of vanadium, the limit values to observe harmful effect on human health during one-time exposure is around 7 mg by intravenous application and 35 mg by inhalation [10,50]. Vanadium contents (in the blood) can decrease to about 30% within 24 h [49,50] since it is eliminated via urine or distributed in tissues. In bones, the residence time is of about one month since vanadium can replace phosphorus in hydroxyapatite [51]. The vanadium path in the body is summarized in Figure 1.

On the other hand, vanadium has high potential as metallodrugs, especially for the treatment of diabetes which was the first use of vanadium in pharmacology. Indeed, in the form of salts including sodium metavanadate, sodium orthovanadate, and vanadyl sulphate, the effect on patient whom needed insulin is positive. This is due to the ability of these vanadium species to activate insulin receptor [42]. Vanadium derivatives can also inhibit/activate several ATPases and phosphatases enzymes since vanadate is a phosphate mimic anion [34,42]. Vanadium is also used for the treatment of several pathologies such as hyper-lipidemia, obesity, and hyper-tension [42]. It is worth mentioning that V has anti-cancer properties. Indeed, vanadium compounds can be used to prevent wear and tear of essential biomolecules such as DNA, thus protecting the genomic stability [52,53]. Vanadium derivatives can be also used in anti-bacterial and anti-viral applications [34,42].

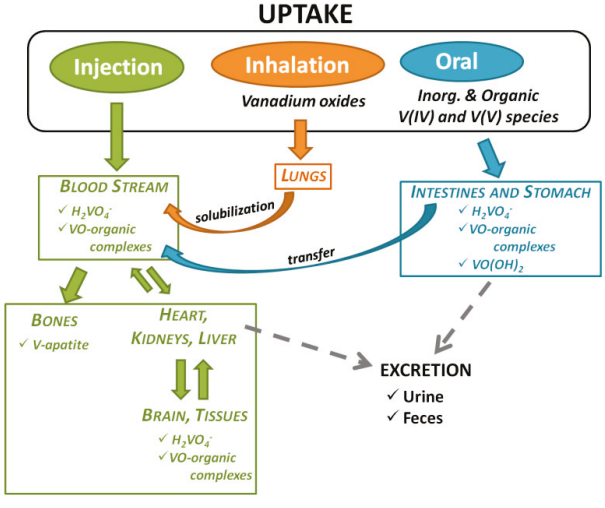

Figure 1. The pathway of vanadium in the human metabolism.

In addition to medicinal applications, vanadium can be used in the field of energy production as, for instance, the redox flow battery. A redox flow battery is similar to an electrochemical cell composed of two compartments and two electrolyte reservoirs (Figure 2). The electrolytes circulate through the cell by a pump while the compartments are separated by an ion exchange membrane to allow the diffusion of ions (Figure 2) [54]. The main disadvantage in typical redox flow batteries such as iron/chromium or iron/titanium is the cross contamination of the electrolytes due to different redox couple species in each half-cell compartment [55,56]. In vanadium redox flow batteries, this problem is overcome by employing the same electrolyte in both compartments, thus eliminating the cross-contamination as well as the problems from the maintenance of electrolyte solution. Indeed, a vanadium electrolyte is used in both half-cells where the V^{2+}/V^{3+} redox couple operates in the negative one while the VO^{2+}/VO_2^+ redox couple operates in the positive half-cell [54]. Therefore, such pioneered vanadium-based batteries are considered as the 1st generation of such a type of battery.

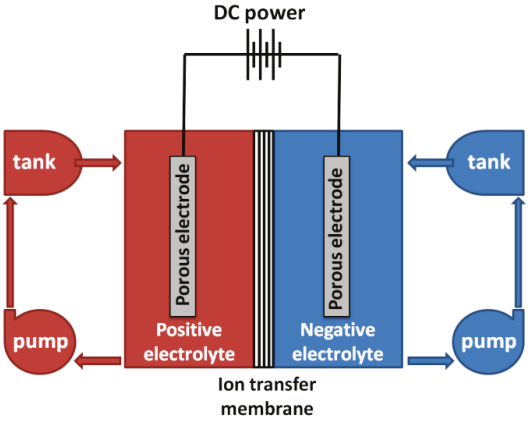

Figure 2. Scheme of a redox flow battery.

All the above applications of vanadium in homogeneous systems are very different from each other due to the chemical versatility of vanadium. Depending on its oxidation states, this element promotes a wide variety of chemistries, especially in catalysis (Figure 3). Concerning the chemistry of coordination compounds, vanadium is very flexible, especially V (V). Vanadium (V) has not rigid stereochemical requirements and, thus, can form a variety of complexes, including tetrahedral and octahedral geometries, as well as trigonal and pentagonal bipyramids [57]. On the other hand, vanadium (IV) is less flexible and forms mainly square pyramidal complexes or distorted octahedral geometries [57]. Vanadium complexes like peroxido-vanadium complexes can be involved in biological and catalytic applications [34,58]. Indeed, catalytic properties of peroxido-vanadium complexes are focused on the oxidation of organic compounds. In these oxidative reactions, the complex is formed in-situ from either ammonium vanadate or V_2O_5 by reaction with hydrogen peroxide and the resulting complex can oxidize aliphatic and aromatic hydrocarbon structures [58]. Other catalytic applications involving vanadium complexes exist, such as polymerization, C-C bond cleavage and activation, hydrogenation, etc. (Figure 3) [59–61].

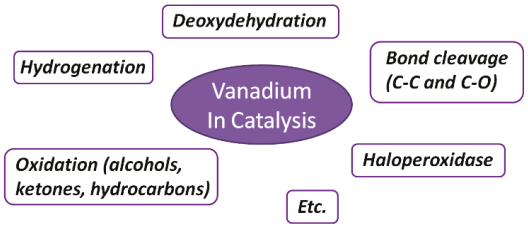

Figure 3. Some of the possible uses of vanadium in catalytic processes.

2.2. Vanadium Materials in Heterogeneous Systems

In this section, other applications than environmental ones (Section 4) are discussed. In the form of solid materials, vanadium is mainly used in metallurgy for the formation of ferrovanadium alloy (FeV) or as steel additive [34]. Mixed with aluminum in titanium alloys, vanadium is also used in jet engines, high-speed airframes, and dental implants [34]. The metallurgy accounts for 85% of the vanadium use. Moreover, vanadium is also used for the storage of hydrogen [62]. Hydrogen is considered as the alternative source of energy to fossil fuels. Even if it is an eco-friendly energy which is relatively easy to produce, its storage and transportation are crucial for the development of hydrogen-based energy system since hydrogen is an explosive compound [62,63]. Usually, the storage and transportation of hydrogen is based on high-pressure gaseous H_2 and cryogenically-cooled liquid hydrogen. In such conditions, the storage and transportation is associated with safety issues and unpractical heavy tanks [64]. Therefore, to avoid these problems, hydrogen can be stored in the form of metal hydrides like those of vanadium which are considered as a viable method [63]. In addition to the high hydrogen storage capacity of vanadium hydrides including vanadium based alloys also exhibit good hydrogenation-dehydrogenation kinetics at room temperature [62].

On the other hand, vanadium can be used in the form of chalcogenides (oxides, sulfides, etc.), nitrides, carbides, and a number of halides which are stable materials [35]. Vanadium sulfide (VS_2) which belongs to the group of transition metal dichalcogenide (TMD) has a structure composed of V layers sandwiched between two layers of S [65]. These layers are stacked together by Van der Walls interactions. Vanadium sulfide has interesting electrical properties, especially high 2D metallic behavior. This 2D conducting material is of high interest for the design of planar supercapacitors [66,67]. Indeed, VS_2 in the form of nanosheets can be used in next-generation energy storage devices [68]. However, the most important vanadium chalcogenide are the oxides which are the most commercially available. Among vanadium oxides, V_2O_5 is the most used. This yellow-

brown oxide can be obtained easily either by calcination of vanadium metal powder in an excess of oxygen or by thermal decomposition of ammonium metavanadate (Equation (8)):

$$2NH_4VO_3 \rightarrow V_2O_5 + 2NH_3 + H_2O \quad (8)$$

Nowadays, vanadium pentoxide is a key component in the production of sulfuric acid since it catalyzes the oxidation of sulfur dioxide to sulfur trioxide. In addition, V_2O_5 and materials containing vanadium pentoxide are used in many other catalytic reactions [34,69]. Due to its catalytic activity and selectivity, V_2O_5 is a known catalyst for the selective oxidation of various organic compounds, mainly hydrocarbons and alcohols, e.g., butane to maleic anhydride, propene to acrolein and methanol to formaldehyde [34,70]. These latter cases are examples of commercial products synthesized using vanadium pentoxide. V_2O_5 is also used in other oxidative processes such as the oxidative dehydrogenation of alkanes [34,71]. However, V_2O_5 and generally vanadium oxide based materials are also important catalysts for environmental applications which are developed in Section 4. Besides the catalytic properties, the layered structure of vanadium pentoxide is promising for the design of electrodes in lithium ion batteries (LIB) [72]. Indeed, V_2O_5 has high ionic storage capacity and as a cathode material, vanadium pentoxide has a theoretical energy density of about 1.1 $kW{\cdot}h{\cdot}Kg^{-1}$ which corresponds to 440 $mA{\cdot}h{\cdot}g^{-1}$ for fully-lithiated V_2O_5 ($Li_3V_2O_5$) [73]. It is far more than classical cathode material like coarse-grained $LiCoO_2$ which has a practical energy density < 0.5 $kW{\cdot}h{\cdot}Kg^{-1}$ (274 $mA{\cdot}h{\cdot}g^{-1}$). However, charging more than one Li ion per V_2O_5 unit cell leads to irreversible structural changes [74]. When one lithium is stored (LiV_2O_5), the lattice structure is extremely reversible with over 1000 cycles without capacity loss and the energy density is still higher than classical CoO_2 cathode (294 $mA{\cdot}h{\cdot}g^{-1}$) [75]. It is worth noting that Panasonic has commercialized vanadium pentoxide as cathode material in rechargeable Li-ion batteries. Such a cathode can be used for low-energy application only because of kinetic problems, thus other layered vanadium oxides should be designed to improve the LIB performance [76]. That is the case of V_6O_{13} which is obtained from V_2O_5 (Equation (9)). Indeed, the theoretical specific capacity of V_6O_{13} reaches up to 420 $mA{\cdot}h{\cdot}g^{-1}$. In addition, 8 mol Li^+ can be inserted in the layered structure of 1 mol V_6O_{13}. However, the poor cycling performance of this vanadium oxide is one of the most serious drawbacks for a use as cathode materials in LIBs [77]. Therefore, another strategy is to substitute V cations or vanadium vacancies with other cations such as Ag^+, Mn^{2+}, and Ti^{4+}, thus improving the electrochemical properties of V_6O_{13} cathode.

$$9V_2O_5 + 4NH_3 \rightarrow 3V_6O_{13} + 2N_2 + 6H_2O \quad (9)$$

Vanadium dioxide is also an intensively studied vanadium oxide phase, especially for its thermochromic properties. Indeed, in the form of coating, VO_2 can change its appearance from transmissive to opaque due to a reversible insulator-to-metal transition (IMT) [78]. At a critical temperature (T_C = 68 °C) and without any additional external stimuli, phase transition between IR-transparent VO_2(M) and IR-translucent VO_2(R) occurs (Figure 4). The insulator-to-metal transition is not only accompanied by optical changes, but also by changes in electrical properties. For instance, the electrical resistivity of VO_2 varies at the critical temperature from 20 Ω·cm in the insulating phase to about 0.1 Ω·cm in the metallic phase, which is accounts to a factor 200 [79]. This reversible change in electrical properties occurs within 100 fs [80]. Regarding the ultrafast switching time and the sharp change in resistivity, VO_2 is an excellent temperature sensor. Regarding all these properties, the VO_2 IMT is an excellent feature for the design of smart windows since energy consumption can be saved and greenhouse gas emission reduced [9]. This is an actual issue since, according to a survey, buildings are one of the main problems in this field with an energy consumption of 40% along with 30% of anthropogenic greenhouse gas emission [81]. These negative statistics are due to the excessive use of lighting, air-conditioning and heating [81]. In addition, the heat exchange between building indoor and

the outdoor environment are occurring through the windows and, thus, amplifying the energy consumption.

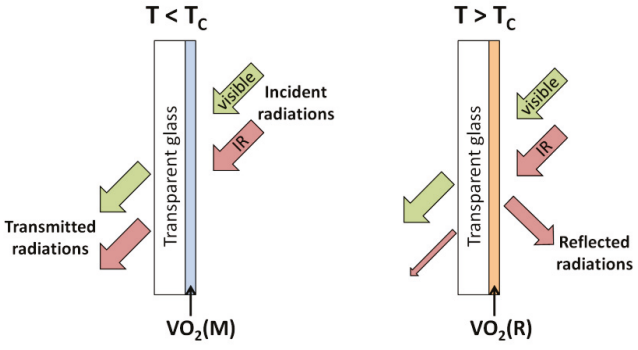

Figure 4. Principle of VO_2 thermochromic coating deposited on transparent support.

The vanadium oxides are also widely used in recent technologies such as memory devices and sensors [82]. Vanadium oxide based materials are attractive due to their easy way of fabrication which is inexpensive, non-toxic, and using scalable wet chemical techniques [83]. It is important to remind that vanadium can form a large number of oxides but only few of them provide stability needed in microelectronic devices. That is the case of VO_2, V_2O_3, and V_2O_5 which are oxides containing vanadium in a single oxidation state. Because of their reversible changes of physical properties, these thermo- and electro-chromic vanadium oxides exhibit hysteresis loop. The width of this loop is a crucial parameter for applications in microelectronics. Indeed, the memory aspect of vanadium oxides materials lies in the hysteresis of the insulator-to-metal transition. One of the most known applications involving vanadium oxides, such as V_2O_3, VO_2, and V_2O_5 are bolometers. A bolometer is a thermal infrared detector. Therefore, bolometers are used in infrared imaging applications such as thermal camera, night vision camera, mine detection, early fire detection, medical imaging and gas leakage detection [84]. Materials which are used in bolometers require high temperature coefficient of resistance (TCR) and a small noise constant (1/f) [84]. Vanadium oxides belong to this category. Although pure and stoichiometric binary oxides such as VO_2, V_2O_3, and V_2O_5 have high TCR, they are difficult to synthesize as single crystals. V_2O_3 is an excellent candidate due to the critical temperature of its IMT transition which is far below the room temperature and, thus, the level of noise is low. However, the actual strategy is to use systems mixing different single-valence vanadium oxides in order to design stable microbolometric materials with high TCR and resistivity [85]. The use of vanadium oxides for such bolometric applications appeared after 1992 since, fprior to this date, it was classified by the US government.

3. Structures and Physical Properties of Binary and Ternary Vanadium Oxides

3.1. Case of Binary Vanadium Oxides

As most of the d-transition metals, vanadium has different oxidation states which are present in oxides as either single or mixed valence states. The vanadium oxides existing in a single valence state are typically $V^{II}O$, $V^{III}{}_2O_3$, $V^{IV}O_2$, and $V^{V}{}_2O_5$ while couples of mixed valence oxides exist such as V_3O_5, V_4O_7, V_5O_9, V_6O_{11}, V_6O_{13}, V_7O_{13}, and V_8O_{15}. These latter oxides mix mainly two valence states of vanadium [22]. The formation of vanadium oxide of particular oxidation state(s) is highly dependent on the preparation method, i.e., the experimental parameters such as the temperature, the partial pressure of the oxidant/reducer [73]. For instance, the following phases are formed and transformed subsequently in an oxidative atmosphere in the order: VO_2, V_6O_{13}, V_4O_9, V_3O_7, and V_2O_5. This order of appearance during the synthesis is closely related to the increasing oxidation

state. For these oxides, the oxidation states for the vanadium is 4.0, 4.3, 4.5, 4.7, and 5.0, respectively [86,87]. Such vanadium oxides ranging from V_2O_5 to VO_2 belong to the Wadsley series, i.e., oxides of general formula V_nO_{2n+1} [72]. Another important category of vanadium oxides is the so-called Magnéli phases with a general formula V_nO_{2n-1} [72].

The structure of the most important vanadium oxides are described below along with their properties. The rich coordination-style configurations for the vanadium ions, which is also one reason why vanadium has various valence states, leads to the formation of numerous and varied frameworks [88]. The control of vanadium oxide structures is not an easy task. Usually in transition metal oxides, the electronic properties are related to the s-band associated with the transition metal ion and the p-band associated with the oxygen ion. As a consequence, these orbitals are pushed away from the Fermi level while the remaining d-orbitals are close to this level [89]. Thus, the d-orbitals of the metal are of significant importance in the explanation of electronic properties using either crystal field theory or conventional band theory. In the crystal field theory, the splitting energy for 3d-series ions in oxides has a value of 1–2 eV and this value increases as cation oxidation state increases. In conventional band theory, which treats the electrons as extended plane wave, the metal d-orbitals form the conduction band. According to this theory, the semiconductors are defined as materials having completely filled valence band and an empty conduction band separated by a short energy band gap (E_g). The structure and the morphology of solid state materials are mainly responsible of the observed properties [37]. In other words, the physical properties of a material depend strongly on its structure. The various atom-stacking style form the numerous crystal structures of vanadium oxides [90,91], thus providing the foundation to understand the interplay between the properties and the structures. In this section, binary vanadium oxides with both single and mixed valence states are discussed.

3.1.1. Structure of VO_2, V_2O_5, and V_2O_3

The oxides of formula VO_2, V_2O_5, and V_2O_3 are formed of vanadium in one valence state. Their melting points are 1967, 690, and 1970 °C, respectively, while metallic vanadium melts at 1910 °C. The two ends of the Wadsley series, that are VO_2 and V_2O_5, are known layered vanadium oxides [73]. For the highest valence state of vanadium (V^{5+}), there is only one V_2O_5 phase which is the orthorhombic crystal system (space group of P_{mmn}) [92]. Indeed, as long as the reaction temperature is high enough and the oxygen is sufficiently provided, orthorhombic V_2O_5 would be exclusively formed [93]. The orthorhombic lattice of vanadium pentoxide is composed of *[VO_5]* pyramids which form alternating double chains (pyramids-up/pyramids-down) along the *b*-axis. These double chains are connected laterally by bridging oxygens to form a sheet or a ribbon in the *a*–*b* plane. The planes themselves are connected by Van der Waals bonds [83]. The Van der Waals bonds are weak and create easy cleavage along these planes [83]. Since V_2O_5 has a layered structure it is, therefore, possible to extract few layers (of nanometer thickness) or even a monolayer of vanadium pentoxide [22]. Although the sheets/ribbons along the *b*-axis direction are very robust, the V_2O_5 lattice is fairly open and permeable to smaller intercalating cations. In addition, the surface of the Van der Waals planes is polar, thus allowing hydration phenomenon [94]. Theoretically, in the crystal structure of V_2O_5, the nominal valence state of vanadium atoms is +V, but thermal agitation and crystal defects create a small concentration of V (IV) in the solid. Therefore, electronic conduction occurs by means of electron hopping. This is equivalent to the motion of the +IV valent vanadium states. The presence of V (IV) in V_2O_5 also creates local lattice distortion [83].

For VO_2, more than 10 types of V (IV) oxide phases have been reported and the preparation of the desired structure is hard since the structures are very similar. Among these vanadium dioxides, VO_2(M), VO_2(R) and VO_2(B) are the three main phases, from which VO_2(B) is metastable. The other vanadium dioxide polymorphs are metastable phases including VO_2(A), VO_2(B), VO_2(C), and VO_2(D), but also mineral phases such as paramontroseite and nsutite-type structures [95,96]. Compared to VO_2(M) and VO_2(R),

the synthesis of metastable phases usually requires a lower temperature. The VO_2(M/R) exhibits an IMT where VO_2(M) and VO_2(R) are the insulating and the metallic phases, respectively. Below the phase transition temperature (T_C), vanadium dioxide has a monoclinic structure (VO_2(M)) [97] while above T_C, VO_2 is in rutile form (VO_2(R)) [22]. In rutile phase, each vanadium is coordinated to six nearest oxygens, thus forming *[VO_6]* octahedra [83]. These *[VO_6]* octahedra are symmetrical and form edge-sharing chains along the *c*-axis of the crystal lattice. This tetragonal lattice has a space group $P4_2/mnm$ while the monoclinic phase, VO_2(M), has a space group $P2_1/c$. At room temperature, the metastable phases also exist and VO_2(B) is the most investigated one. Eventually, VO_2(B) can be converted to metastable VO_2(A) or VO_2(M) by heat treatment [98]. VO_2(B) is sometimes named as VO_2(M2) since it has a monoclinic structure. The main difference between the VO_2(M) and VO_2(B) monoclinic structures is based on the β angle of the lattice structure which is 122.62° in VO_2(M) and 92.88° in VO_2(B). In addition, VO_2(B) does not exhibit an insulating-to-metal transition, neither the tetragonal VO_2(A) phase. The IMT in VO_2(M/R) is induced by temperature gradient leading to a huge change in resistivity. The structural changes involve small distortions of the infinitely linear V–V chains (with a V–V distance of 0.288 nm along the *c*-axis) in VO_2(R), thus giving rise to the dimerization of V–V pairs (with two values of 0.262 nm and 0.316 nm between V–V) in VO_2(M) [72]. In the rutile phase, the electrons from d-orbitals are shared by all of the vanadium atoms along the *c*-direction of the lattice, thus leading to the metallic behavior. In the monoclinic phase, the vanadium atoms form dimers, thus resulting in the insulating behavior (i.e., semiconducting VO_2(M)) [99]. Furthermore, during the phase transition to VO_2(R), the V–V pairs in the chains in VO_2(M) do not only undergo dimerization, but also a twist from linear to zigzag-type chains [72] (Figure 5). The local structural rearrangement around the V atoms during the insulator-to-metal transition provides a key factor to modify the band–gap value [72]. It is important to note that monoclinic and rutile VO_2 phases have different crystal systems, but their crystal lattices are of great similarity. The only difference between these two structures is the displacement of the vanadium atoms in the chains. Therefore, this structural similarities between the metallic and insulating phases makes the understanding of the IMT more difficult.

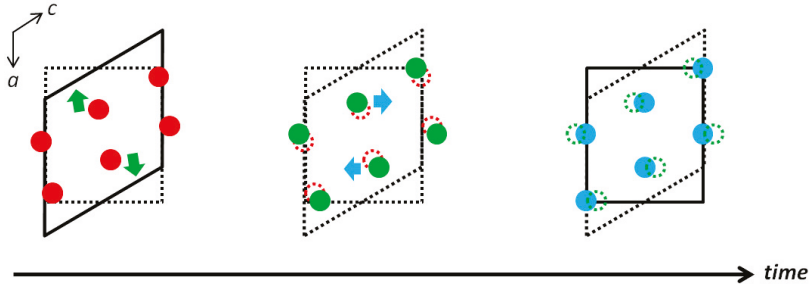

Figure 5. Changes in the crystalline structure during VO_2 phase transition. The schematized sequence occurs in the picoseconds scale.

Concerning V_2O_3, there are very limited numbers of phases. This is mainly related to the chemical instability of the low valence state vanadium ions, here V (III). However, there is still intense research in searching for new V_2O_3 crystal polymorphs. Similar to iron(III) oxides (Fe_2O_3) which is known as either hematite (α-Fe_2O_3), beta phase (β-Fe_2O_3), gamma phase (γ-Fe_2O_3), maghemite (δ-Fe_2O_3), or epsilon phase (ε-Fe_2O_3) [100], only δ-V_2O_3 and ε-V_2O_3 have not been discovered up to now. Vanadium sesquioxide (V_2O_3) also exhibits an IMT where V_2O_3 has a monoclinic/rhombohedral structure below T_C, and a corundum structure above T_C [22]. In its insulating phase (below T_C), V_2O_3 has body

centered monoclinic structure with space group $I2/a$. The metallic phase of V_2O_3 (above T_C) has a trigonal corundum structure with space group $R\bar{3}c$.

3.1.2. Properties of VO_2, V_2O_5, and V_2O_3

The control of the synthesis of binary vanadium oxides of particular structure is a key parameter to tailor the desired electronic properties [72]. It is well known that the charge carrier concentration in the prepared materials is crucial to understand and explain the performance of different vanadium oxides in various applications such as energy conversion, in particular photocatalysis and water photosplitting (Section 4). Indeed, the electronic properties are usually discussed using the band structure of the semiconductor materials, which is the plot of electron energies against the wave vector. Prior to further process in this section on the properties (especially electronic ones) of binary vanadium oxides with single vanadium valence, it is important to introduce some notions of the band structure theory. The number of bands (in a band structure diagram) is equal to the number of atomic orbitals in the unit cell of the compound. The overlap integral, which is the overlap between the interacting orbitals, determines the bandwidth (or the band dispersion), i.e., it is the difference in energy between the lowest and highest levels in a band. The greater is the overlap between neighboring orbitals, the greater is the bandwidth (and vice versa). Therefore, the behavior of electrons in a solid can be studied microscopically from its electronic band structure (Figure 6) [101]. From these electronic properties, and more particularly from the band structure diagram, it is possible to extract additional important information about the material such as optical properties. Indeed, in a material, optical properties originate from the response of electrons to a stimulus which is the transition between energy levels under an incident radiation. The energy band gap calculation and the absorption edge estimation are of high interest in many research fields due to potential applications in optical, electronic, and optoelectronic devices. The electronic band structure of a material is dependent on the crystal structure of the material.

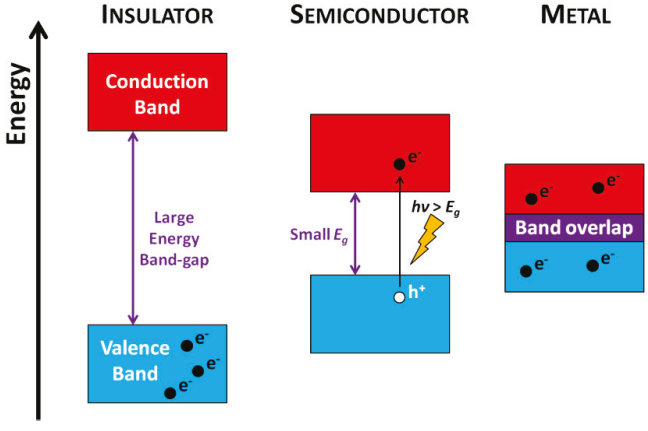

Figure 6. The band structures of insulator, semiconductor and metal.

Concerning the main single valence state of binary vanadium oxides (VO_2, V_2O_5, and V_2O_3), their electronic structure are all characterized by a strong hybridization between the 2p oxygen and 3d vanadium bands, which are the valence orbitals. Their optical properties can be explained using their electronic properties. Since most of the binary vanadium oxides exhibit an insulator-to-metal transition which leads to electrochromic and thermochromic properties, such oxides are very interesting for the design of advanced materials. Indeed, the IMT can be triggered using different stimuli including voltage and heat. Since the vanadium–oxygen bonds are highly ionic in vanadium oxides, the value of

transition temperature of the IMT strongly depends on the oxidation state of the vanadium ion, i.e., T_C increases with oxidation states of the vanadium atom [22]. The resulting phase transitions in vanadium oxides are reversible and are accompanied by changes in structural, magnetic, optical and electrical properties. The structural change is a key factor since it leads to a displacement of the atoms in the crystal lattice and to a redistribution of electronic charges and, hence, the observed physico-chemical properties change [102].

In V_2O_5, the Fermi energy, which corresponds to the highest occupied electronic band, is calculated at 1.62 eV. This Fermi level is separated from higher conduction band by about 0.6 eV [103] while the valence band is at about 2.7 eV. Vanadium pentoxide has an indirect bandgap of 1.7 eV calculated by DFT (Density Functional Theory) but this value is smaller than the experimental one (2.3 eV). This underestimation of the bandgap is a common problem using the DFT. Concerning the indirect E_g, it is the result of the split-off of oxygen 2p band up to the vanadium 3d band [83]. In addition, there are two discrete intermediate bands (situated within the bandgap) with narrow bandwidth of about 0.7 eV [103], and they can make significant contribution to charge transport phenomena or mediate optical transitions from valence to conduction bands. Concerning the optical and electrical properties, V_2O_5 exhibits significant optical anisotropy in the visible region [22]. This anisotropy is due to the bands which are dispersive to various extents, and this is a clear indication of the crystal structure anisotropies. For instance, the electronic conduction within the $a-b$ planes of V_2O_5 crystal lattice is considerably higher than that perpendicular to these planes [83]. The electron hopping (resulting from small concentration of V^{4+} in V_2O_5) is much easier within the *a*–*b* planes due to the shorter distances between vanadium atoms compared to the perpendicular direction to these planes. This leads to in-plane/out-of-plane conduction anisotropy [83]. In the form of films, the electrical conductivity of V_2O_5 remains low (from 10^{-2} to 10^{-3} $S{\cdot}cm^{-1}$) [104]. Apart from the anisotropic behavior observed in vanadium pentoxide, the presence of dispersive bands is also an indication of strong hybridization, since the more bands are dispersive, the stronger is the hybridization, and vice versa. In addition, in the semiconducting state, vanadium pentoxide exhibits high transmittance in near-UV and blue part of the visible spectrum, and low transmittance in near-IR and red part of the visible spectrum. The most known/popular property associated with V_2O_5 is its electrochromic effect, which can produce series of different colours of the material. Concerning the electrochemical properties of V_2O_5, the voltammograms of V_2O_5 films exhibit only one couple of redox peaks at around 0.70 V and -0.4 V, and these peaks are ascribed to the V^{5+}/V^{4+} pair (the voltammograms were obtained at a scan rate of 0.030 $V{\cdot}s^{-1}$ over a potential range of ± 1 V). As the number of deposited layers increases, the produced current linearly increases as well as the optical modulation. Indeed, a voltage of -1 V is required to color the films while the color is subsequently bleached under a voltage of 1 V. The electrochromic transitions in V_2O_5 films have an excellent reversibility [105]. However, it is difficult to classify V_2O_5 in the cathodic or anodic electrochromism category. The cathodic electrochromism refers to a decrease in transmittance caused by charge injection (the case of Ti and W oxides), while anodic electrochromism refers to an increase in the transmittance (for instance Cr, Mn, and Fe oxides). Vanadium pentoxide is unique since it exhibits a transmittance increase in the near-UV and blue part of the visible spectrum and, simultaneously, a transmittance decrease in the near-IR and red part of the visible by charge injection [106]. The charge injection in V_2O_5 can be performed by intercalation into the van der Waals planes of small cation such as H^+, Li^+, and Na^+, which cause electrochemical charge transfer reactions. The electrochromic properties of V_2O_5 have been developed for the design smart windows. On the other hand, vanadium pentoxide is also a thermochromic material with a transition at 530 K [107]. The resulting IMT is only observed when V_2O_5 is deposited in the form of thin films (nanostructure effect). However, the observed transition does not involve structural change. In the bulk phase, there is not IMT since vanadium pentoxide remains semiconducting at all temperatures [108].

In VO_2, the metallic rutile and the monoclinic insulating phases have a Fermi level at almost the same energy level, i.e., 7.47 eV, and 7.44 eV, respectively [22]. Vanadium dioxide is transparent in the IR region above *Tc* and the optical transmittance changes by about two orders of magnitude during the transition [109]. The IR transmittance of VO_2 exhibits hysteresis loops around the transition temperature: upon heating the optical switching occurs around 80 °C while upon cooling, it is at about 60 °C. Both phases of VO_2 (metallic and insulating) absorb in the visible. Indeed, the material in insulating phase has a brown-yellow color, which turns into reddish-brown when deposited in the form of thin films, while the metallic state exhibits a greenish blue color [110]. The optical and electronic properties of VO_2 can be explained by the band theory, where the number of band groups in the insulating phase is exactly the same as in the metallic phase, but in the latter, each band group is doubled. Therefore, in the rutile metallic structure, there is a finite overlapping of valence and conduction bands, which is a characteristic of metallic behavior [22]. In the monoclinic insulating structure, there is a gap of energy between the bands resulting from the oxygen 2p orbitals and the vanadium 3d orbitals. As a consequence, the observed energy band gap (E_g) in the rutile structure is 0.6 eV [111], while for the monoclinic structure, E_g is 2.5 eV. These properties of VO_2 (M/R) can be also described (and, thus, better understood) using the crystal field theory [22]. In the metallic rutile phase ($T > T_C$), vanadium (IV) is at the center of an oxygen octahedron. Therefore, in a symmetry point of view, the 3d orbitals are split into doubly-degenerated e_g and triply-degenerated t_{2g} levels. The e_g orbitals are directed towards the 2p orbitals of the oxygen ligand and they form the $e_g{}^{\sigma}$ bands in Figure 7. Regarding the monoclinic and rutile symmetries, the t_{2g} orbitals, which are not directed toward the 2p orbitals of oxygens but between them, form the $e_g{}^{\pi}$ and a_{1g} bands (Figure 7). The t_{2g} orbitals are also responsible for pairing between vanadium (IV) creating dimer resulting in the splitting of a_{1g} into two bands. However, this dimerization effect in the metallic rutile phase is weak and pairing of vanadium (IV) does not happen. That is why the overlapping between a_{1g} and $e_g{}^{\pi}$ bands occurs at the Fermi level and it results in the metallic properties of rutile VO_2 (Figure 7). In the insulating monoclinic phase, the distortion of the lattice results in stronger dimerization effect between vanadium (IV) pairs, thus splitting the a_{1g} into two bands without overlap between a_{1g} and $e_g{}^{\pi}$ at Fermi level (Figure 7). In addition, in the monoclinic phase, the $e_g{}^{\pi}$ band is destabilized by V-O overlapping and thus pushes this band upwards from the Fermi level [112,113].

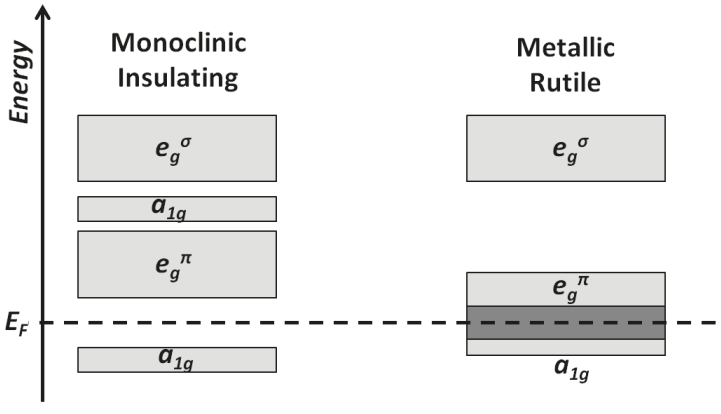

Figure 7. Energy diagrams of monoclinic insulating and metallic rutile phases of VO_2.

Concerning the optical properties, VO_2 shows significant anisotropy in the infrared region [22]. Similar to V_2O_5, VO_2 can also change its optical properties in a persistent and reversible way in response to a voltage [114]. Although VO_2 is electrochromic, it is

rather used as thermochormic materials with an IMT at 340 K [115], since V_2O_5 exhibits better electrochromic performance. In addition, the optical excitation through laser pulses is also an effective method (compared to excitation using heat gradient, i.e., by change of temperature) to control the phase transition in VO_2(M/R) [116]. Indeed, laser pulses of sufficiently high energy could trigger a non-thermal sub-picosecond structural phase transition [117]. During this optical excitation, electrons are promoted from the VB to the CB of VO_2. Subsequently, the collapse of the band gap occurs, thus leading to the transition into metallic phase. After depopulation of the e_g^{σ} bonding orbitals, the reversible transition occurs.

On the other hand, the strains present in VO_2 is also a way to regulate the physical and chemical properties of the VO_2(M/R) material. Indeed, deposited in the form of films, the source of strain is from the lattice and elastic mismatches between the VO_2 material and the substrate. According to the relative size of the mismatch, the strain can be divided into tensile stress and compressive stress. For VO_2 thin films, the induced strain can effectively adjust the IMT due to the presence of lattice mismatch between the sample and the substrate, thus causing a change of the transition point of VO_2 IMT [118]. In addition to the different physical excitation detailed just above, the doping is also an effective method to affect the IMT in VO_2(M/R) by either decreasing or increasing T_C [117]. Doping is a typical chemical method to control the carrier concentration in semiconducting materials by insertion of discrete energy levels within the energy band gap. Depending on the nature of the doped elements (i.e., p- or n-type dopants), electrons injection (in the conduction band) or holes injection (in the valence band) in the host material is performed. In the case of W (VI) doping which has a much larger size than vanadium, injection of electrons in the parent materials occurs as well as an additional effect: the induction of lattice strain. This structural change plays an important role in the decrease of the phase-transition temperature [119]. Indeed, the insertion of W atoms not only breaks the lattice symmetry but also increases the spacing between the metal cations [120]. On the other hand, low-valence metal ions such as Cr^{3+}, Ga^{3+}, and Al^{3+} are used to increase the temperature of the VO_2 phase transition [121,122].

Another possibility to induce IMT transition is the use of an electric field through the Joule heating effect (from leakage/loss of current) [117]. However, it is important to rule out the electric and thermal effects from other processes. By applying an electric field transverse to the material's interface with a gate electrode, i.e., metal oxide semiconductor field effect transistor (MOSFET) (Figure 8), it is observed that the IMT is suppressed at high bias [73].

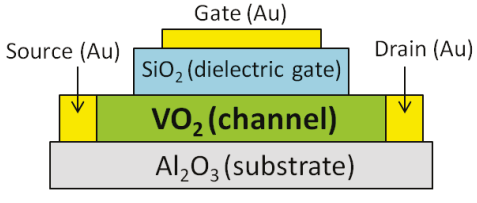

Figure 8. Scheme of a MOSFET using thermochromic VO_2.

In V_2O_3, a striking IMT occurs at 150 K which is marked by a jump in the resistivity by seven orders of magnitude and an antiferromagnetic ordering of spins. V_2O_3 also shows electrochromism with a transition at about 160 K. The Fermi level of V_2O_3 is at 9.2 eV while the observed energy gap is about 0.66 eV. At temperature below 150 K, vanadium trioxide exists in its insulating phase with a monoclinic structure [72]. At a temperature above 150 K, the high-temperature paramagnetic V_2O_3 phase exists with a corundum crystal structure that exhibits metallic behavior. Therefore, at room temperature, there is a finite overlapping of valence and conduction bands, thus giving its metallic behavior of the corundum structure. Similar to VO_2, the crystal field, which is generated by the

oxygen on vanadium in the octahedra $[VO_6]$, leads to the splitting of the d-orbitals into two sets of bands: t_{2g} (lower band) and ${e_g}^{\sigma}$ (upper band). In V_2O_3, the upper band is doubly degenerated and it consists in fact of d_{xz} and d_{yz} bands. Concerning the lower band, the non-cubic arrangement of vanadium ions in the lattice combined with the trigonal distortion leads to the degeneration of t_{2g} orbitals into a_{1g} singlet (d_{3z2-r2}) and doubly-degenerated ${e_g}^{\pi}$ bands (d_{xy} and d_{x2-y2}) as shown in Figure 9 [123]. In the insulating monoclinic phase, the symmetry of the crystal field is lower than in corundum phase. Therefore, the a_{1g} and ${e_g}^{\pi}$ bands are split, thus creating an energy gap between a_{1g} and ${e_g}^{\pi}$ bands while, in the metallic corundum phase, the a_{1g} and ${e_g}^{\pi}$ bands overlap at the Fermi level (Figure 9) [124].

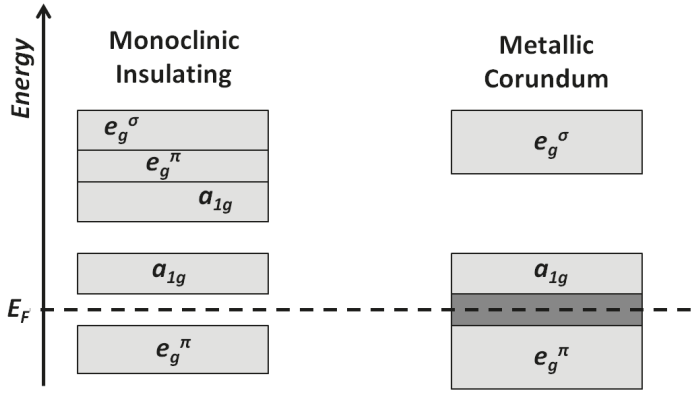

Figure 9. Energy diagrams of monoclinic insulating and metallic corundum phases of V_2O_3.

It is worth noting that the degree of anisotropy in binary vanadium oxides of single vanadium valence increases in the following order: $V_2O_3 < VO_2 < V_2O_5$. Finally, vanadium monoxide (VO) also exists but it is usually a non-stoichiometric oxide. Vanadium monoxide crystallizes in cubic rock salt structure (NaCl) where all the $[VO_6]$ distorted octahedra are connected by the edges [125].

3.1.3. Binary Vanadium Oxides with Mixed Valence States

The oxides of the general formula $V_nO_{(2n+1)}$, i.e., the Wadsley phases, exist between V_2O_5 and VO_2. This means that these phases have a mixture of vanadium (IV) and (V) because of oxygen vacancies. On the other hand, the Magnéli phases, i.e., oxides of the general formula $V_nO_{(2n-1)}$, point out the vanadium oxides which exist between VO_2 and V_2O_3. This means that these phases have a mixture of vanadium (IV) and (III). The compounds of Magnéli and Wadsley series are intermediate oxides with vanadium in a mixed valence state formed from slabs of rutile-like structure sharing faces [126]. This is also known as the "shear structure" concept. These binary vanadium oxides have interesting electromagnetic properties due to strong electron correlation. It includes the insulator-to-metal transition (IMT), which is one of the most important parameters in strongly correlated electron systems [126]. In the Magnéli phases, i.e., oxides between V_2O_3 and VO_2, the arrangement of atomic planes in the rutile VO_2 structure is $[ABAB\ldots]$, where A = O and B = VO. By applying the shear operations which are (i) to periodically eliminate one A-plane every n B-planes, and (ii) to close the resulting gaps by operating a shear vector, the formula nVO + $(n-1)$O = $V_nO_{(2n+1)}$ is obtained [126]. The structure of Magnéli phases includes n VO_2 units between shear planes. Until now, six compounds (n = from 3 to 8) have been isolated. Almost all $V_nO_{(2n+1)}$ compounds (n = 4, 5, 6, 8) show an IMT accompanied by sharp reduction of the magnetic susceptibility due to the formation of spin-singlet V^{4+}–V^{4+} pairs in the low temperature insulating phase [126]. For n = 3 and 7, the insulating compound V_3O_5 has an antiferromagnetic state below T_N = 75 K,

while the metallic compound V_7O_{13} has a rare antiferromagnetic groundstate [126]. On the other hand, in the Wadsley series which contain oxides between VO_2 and V_2O_5, only two compounds, V_3O_7 and V_6O_{13}, have been obtained in both powder and single crystal [126]. In addition, the $V_nO_{(2n+1)}$ compounds exhibit interesting electronic properties like V_2O_5, i.e., electron hopping [126].

The structure of V_6O_{13} can be explained by the shear structure concept and this vanadium oxide undergoes insulator-to-metal transition at −123 °C. V_6O_{13} contains a mixture of vanadium at a valence of +IV and +V, which is beneficial to the electronic conductivity. At room temperature, i.e., high temperature phase, V_6O_{13} is in its metallic state with a layered structure belonging to space group $C2/m$. In the low temperature insulating state, the structure of V_6O_{13} belongs to space group $P2_1/a$. In addition to its IMT, V_6O_{13} also exhibits an antiferromagnetic transition [126]. As mentioned above, the IMT in V_6O_{13} is accompanied by a sharp reduction of magnetic susceptibility, which highlights the formation of spin-singlet V^{4+}–V^{4+} pairs in the insulating phase. V_6O_{13}, as most of the Wadsley compounds (including V_2O_5, V_6O_{13}, V_3O_7, and VO_2(B)), are promising materials for cathodes in rechargeable Li-ion batteries (LIBs) mainly due to their stable layered structure but also to their high specific capacity [126,127]. Furthermore, V_6O_{13} has additional advantages such as higher rate capability, better reversible capacity, smaller volume expansion and safer lithiation potential. Indeed, at room temperature, V_6O_{13} could manage high rate of charge and discharge because of the metallic character of this oxide at ambient temperatures. In term of molar ratio of inserted lithium ions into the layered material, the theoretical specific capacity of the cathode material is 8 mol Li^+ in 1 mol V_6O_{13}. However, the preparation of V_6O_{13} is complicated to achieve owing to the valence fluctuation of vanadium atoms, i.e., it is hard to control the ratio between +IV and +V valence states [77].

Concerning V_3O_7, it is also an intermediate phase between VO_2 and V_2O_5 which is often reported in the literature as hydrate compound ($V_3O_7{\cdot}H_2O$) at room temperature, i.e., in its insulating phase [128]. V_3O_7 is a mixed valence oxide with a ratio of $V^{4+}/V^{5+} = 0.5$. This vanadium oxide has a bandgap of 2.5 eV at room temperature, and it is rather considered as a semiconductor as most of the vanadium oxides in their insulating phase [129]. The structure of crystalline $V_3O_7{\cdot}H_2O$ is orthorhombic with a space group *Pnam* [127,128]. This phase has a layered structure similar to orthorhombic V_2O_5 since $V_3O_7{\cdot}H_2O$ is mostly prepared from vanadium (V) oxide [127]. $V_3O_7{\cdot}H_2O$ is composed of layers of $[VO_6]$ octahedra and $[VO_5]$ trigonal bipyramids sharing corners [126,128,129]. In the structure of $V_3O_7{\cdot}H_2O$, the water molecule is bound to vanadium by replacing one of the oxygen atoms in the $[VO_6]$ octahedron, thus forming hydrogen bonds with the octahedron in the next layer which gives a 3D structure [128]. Like V_6O_{13}, $V_3O_7{\cdot}H_2O$ is also a promising cathode material in LIBs since these materials have high initial capacity which is closely related to their layered structure together with the presence of mixed valence states of vanadium ions [127]. In addition, $V_3O_7{\cdot}H_2O$ exhibits excellent electrochromic performance because of optical modulation in both anodic and cathodic reactions, thus making $V_3O_7{\cdot}H_2O$ an excellent candidation cathode material for electrochromic applications [129]. For instance, in the form of films, $V_3O_7{\cdot}H_2O$ can switch reversibly between a reduced blue state (at −1.2 V) and an oxidized orange state (at +1.9 V) [130]. These reversible changes are accompanied by changes of reflectance, especially at 590 nm. Therefore, similar to V_2O_5, $V_3O_7{\cdot}H_2O$ is characterized by a typical muli-electrochromism but with faster kinetics. The fast kinetics observed in the $V_3O_7{\cdot}H_2O$ film can be explained by its unique structure combined with mixed valence states of V (V) and V (IV). That contributes to higher electronic conductivity and more active redox sites during the reduction and oxidation processes [130]. On the other hand, non-hydrated V_3O_7 has received less attention than its hydrate form. This fact is mainly due to its metastable behavior. Indeed, the non-hydrated phase can be formed by heat treatment of $V_3O_7{\cdot}H_2O$ which leads to removal of the water molecule starting at 75 °C and finishing at about 305 °C. However, the formed V_3O_7 is metastable and plays the role of growing seeds for the formation of V_2O_5. In orther words, although $V_3O_7{\cdot}H_2O$

can be prepared from V_2O_5, its heating in air gives rise to both dehydration and oxidation into V_2O_5. It is possible to synthesize directly V_3O_7 (with a stable structure) by using spray pyrolysis technique on substrate heated at 400 °C [129]. The crystalline phase of V_3O_7 has a monoclinic structure belonging to space group *Pmmn* [129]. In addition, V_3O_7 exhibits higher intercalation capability, fast switching intercalation/extraction rate and better reversibility than V_2O_5 [129].

Another interesting phase in the Wadsley series is V_4O_9. The synthesis of this $V_nO_{(2n+1)}$ with $n = 4$ is a real challenge since it has a formal valence ratio $V^{4+}/V^{5+} = 1$. In addition, V_4O_9 is a special compound in the Wadsley series in the sense that its structure and properties are still not clear (although its existence has been recognized), thus, this phase is often called "the missing link" in binary vanadium oxides [126]. Usually, V_4O_9 is synthesized by a solid state reaction in a reducing atmosphere of an appropriate mixture of binary vanadium oxides with single valence state: V_2O_5 and V_2O_3 (or VO_2). As reducing agents, carbon and SO_2 are the most used and the synthesis is carried out under ultra-high vacuum. However, the best method to prepare single phase V_4O_9 is by using sulfur (S) as a reducing agent (Equation (10)), but an excess of S leads to the formation of VO_2(B) phase [126]. The structure of V_4O_9 is not a plane fault type but a tunnel defect type. The crystal system of V_4O_9 is orthorhombic and belongs to the space group *Cmcm*. Since V_4O_9 is prepared from V_2O_5 reduction where an excess of reductant gives VO_2(B), this suggests that V_4O_9 has a layered structure similar to those from V_2O_5 and VO_2(B).

$$4V_2O_5 + S \rightarrow 2V_4O_9 + SO_2 \tag{10}$$

To better explain the structure of V_4O_9, the shear structure concept can be used. The lattice of V_2O_5 is formed of layers of *[V_2O_3]* (called "*a*") which are stacked and sharing *[O_2]* units in the *c*-direction (layers called "*b*"), thus V_2O_5 has a layered structure of *[VO_5]* pyramids-up/pyramids-down along the *ab*-plane (Section 3.1.1). Hence, the structure of V_2O_5 has the stacking of layers as *[ababa . . .]* in the c-direction (or parallel to the *ab*-plane). On the other hand, the crystal structure of VO_2(B) has a *[abaaba . . .]* stacking which can be regarded as a daughter structure of V_2O_5. Indeed, this stacking manner of *[abaaba . . .]* is obtained from V_2O_5 stacking by using the following shear operation: to periodically eliminate one *b*-layer every two *a*-layers, so the arrangement is *[abaxabaxa . . .]* (*x* = gap) where the gaps are closed by connecting each *[aba]*-block, thus giving the stacking manner of *[abaabaa . . .]*. For V_4O_9, it is supposed that its stacking structure has a cleavage plane. This suggests that the *ab*-plane of V_4O_9 is a cleavage plane with a lattice similar to that of V_2O_5 or VO_2(B). If the structure of V_4O_9 were a shear structure derived from V_2O_5, it would have a stacking manner of *[abababaababababaab . . .]*. This stacking manner is derived by two operations: the periodic elimination of one *b*-layer every four *a*-layers, so the arrangement is *[abababaxababababaxab . . .]* with closing the gaps and thus obtaining the composition of $8V_2O_3 + 6O_2 = 4V_4O_9$. However, the observed *c*-parameter is much shorter than the calculated value for the stacking periodicity of *[abababaababababaab . . .]*. To obtain the composition of V_4O_9, half of oxygen atoms should be removed from half of *b*-layers in this stacking periodicity. This model has stacking periodicity of *[abab'abaab'a . . .]* in which half of oxygen atoms in *b'*-layers are deficient in an ordered manner to form tunnel defects. Hence, the composition is $4V_2O_3$ (*a*-layers) + $2O_2$ (*b*-layers) + 2O (*b'*-layers) = $2V_4O_9$ [126]. In other words, the obtained structure is composed of *[VO_5]* pyramids, *[VO_6]* distorted octahedra and *[VO_4]* tetrahedra that is very similar to the structure of vanadyl pyrophosphate $(VO)_2P_2O_7$ (by replacing *[PO_4]* tetrahedra by *[VO_4]* tetrahedra). The similarities of V_4O_9 to $(VO)_2P_2O_7$ are even lager, especially in magnetic properties. Indeed, the excitation gap between the singlet groundstate and the excited triplet state is approximately 73 K. Therefore, the resemblance of magnetic properties between V_4O_9 and $(VO)_2P_2O_7$ strongly supports the reliability of the structure [126].

3.2. Case of Ternary Vanadium Oxides

Ternary vanadium oxides are interesting materials since their properties can be tuned according to the third element composing them. In terms of modifying the photoinduced properties of materials, it was observed that metal impurities in homometallic oxide can modify the energy bandgap by the overlapping of outer s- and d-orbitals of the p- and d-block metals ions, respectively, thus giving rise to smaller energy band gap (E_g) [131]. Therefore, it was assumed that p- and d-block metals could be used to design single phase heterometallic and nowadays, many visible light-responsive photoactive materials are heterometallic oxides, e.g., ternary and quaternary oxides [131]. Concerning the oxides based on vanadium, one promising class of material is the metal orthovanadates which are composed of VO_4^{3-} tetrahedral. Several orthovanadates including $BiVO_4$, $FeVO_4$, $Mn_3(VO_4)_2$, $CeVO_4$, $NdVO_4$, and $GdVO_4$ have been widely studied during the last decades due to their promising properties and ease of preparation. Other metal vanadates such as, for instance, $Cu_2V_2O_7$, $Cu_3V_2O_8$, $Co_3V_2O_8$, FeV_3O_8, $Ag_4V_2O_7$ have received also a strong interest from the scientific community. Indeed, these vanadium based oxides can be used in (photo)catalysis, lithium-ion batteries, solar cells, gas sensors, water splitting technologies, optoelectronics, etc. [132–134]. Such an interest for transition metal vanadates is due to their interesting optical, electric and magnetic properties, thus being useful in the above mentioned applications [135]. Although most of the ternary vanadium oxides are not thermochromic and/or electrochromic as the binary vanadium oxides, these transition metal vanadates have attracted considerable attention for environmental applications since they are semiconductors which can be activated under UV or visible light radiations. Therefore, ternary vanadium oxide based materials can trigger photoinduced chemical reactions such as photocatalysis and photo-Fenton process for contaminant removal or photosplitting of water (for O_2 and/or H_2 production) as discussed in Section 4 [135].

3.2.1. Bismuth Vanadates

Bismuth vanadates are ternary oxides which exhibit a wide variety of structures [136]. The most promising one is $BiVO_4$. This oxide is a n-type semiconductor that exists in three polymorphs: monoclinic scheelite-like, tetragonal scheelite-like, and tetragonal zircon-like structures with an energy band gap (E_g) of 2.40, 2.34, and 2.90 eV, respectively [137–139]. All these crystal structures are built up with *[VO_4]* tetrahedra and *[BiO_8]* polyhedra where V (V) and Bi (III) are in the center of these units. In both scheelite phases, each *[BiO_8]* is surrounded by eight vanadium units, whereas in zircon structure, Bi units are surrounded by only six *[VO_4]* [139]. Comparing the scheelite structures, the difference between monoclinic and tetragonal phases is based on the local environment, where vanadium and bismuth units are more distorted in the monoclinic structure [139]. In addition, a reversible phase transition between monoclinic scheelite-like (low temperature phase) and tetragonal scheelite-like (high temperature phase) structures occurs at 255 °C [138,139]. However, between tetragonal zircon-like and tetragonal scheelite-like structure, an irreversible phase transition is observed at about 400–500 °C [138,139]. Therefore, at room temperature, there are two $BiVO_4$ polymorphs which are stable. Among them, the monoclinic scheelite-like structure exhibits the best photoactivity under solar light, e.g., longer lifetime of photogenerated charge carriers and higher photocurrent. This is due to better photon absorption and charge carrier transport resulting from smaller E_g and distorted *[VO_4]* and *[BiO_8]* units, respectively [138,139].

The crystalline structure and the energy band gap of $BiVO_4$ have an influence on the efficiency of photo-induced processes triggered by this semiconductor, e.g., photocatalytic reactions. However, the exposed crystal facets are maybe more important since they can affect the thermodynamic and the kinetic of a chemical reaction [137]. By designing a particular crystal, the crucial parameters of photo-induced chemical reactions in heterogeneous phase can be tuned such as the preferential adsorption of a reactant, the surface transfer of photo-generated charge carriers and the desorption of products [137,140]. In the case of bismuth vanadate where the monoclinic structure is the most photoactive one, the *{010}*

and *{110}* crystal facets has redox functions since they provide reduction and oxidation sites, respectively, in which photogenerated electrons and holes are available [141,142]. The effect of these crystal facets on the efficiency of $BiVO_4$ in photo-induced processes is often investigated by photoelectrochemical (PEC) and transient absorption spectroscopy (TAS) analyses [143]. PEC measurements could explain the charge carriers' behavior at the surface of $BiVO_4$, especially the surface recombination which could be evaluated by amperometry, i.e., by analyzing the shape of photogenerated current curve at potential near the onset of steady state photocurrent (larger is the current "spike", higher is the recombination). TAS is another powerful tool (which is detailed hereafter) to understand the charge carriers' dynamics including relaxation rate, recombination rate, and mechanism of recombination [143,144]. The operation of this fast spectroscopy is based on the excitation of the sample by a pulse followed by the optical measurement (using a spectrophotometer) and the analysis of spectral differences between excited and the ground state levels of the sample as a function of time [144]. Since the delay between excitation and measurement sets the time scales that can be studied, TAS is considered as a fast spectroscopic technique [144]. The advantage of TAS studies resolved in time (compared to PEC studies) is the possibility to investigate the dynamics of photogenerated holes. Indeed, TAS allows the observation of these dynamics where h^+ is responsible, for instance, to water oxidation or generation of hydroxyl radicals while in PEC analysis, the hole dynamics is indirectly deduced from the current signal which is monitored via external circuit. In the future, studies based on transient absorption spectroscopy will surely developed since currently, TAS studies of transition metal oxides are limited [143,144]. To date, the dynamics of photogenerated holes in $BiVO_4$ was studied using transient absorption spectroscopy coupled to photoelectrochemical measurement. In such a study (in aqueous medium), the constant of decay time of spectroscopic signal of h^+ is dependent to the applied bias due to kinetic competition between water oxidation and charge carrier recombination. In addition, the time constant for charge carriers' recombination (measured with transient absorption spectroscopy) is different to the time constant of back electron transfer (measured with transient photocurrent measurements using chopped light), thus indicating two distinct recombination processes which limit the photocurrent generation in $BiVO_4$ photoanodes. One recombination process is fast (occurring within microseconds) and assigned to direct bulk electron/hole recombination, while the other one is slow (occurring within milliseconds) and identified as recombination of surface-accumulated holes with bulk electrons. The latter process, also called back electron transfer, can be avoided at strong anodic bias which provides a large energetic barrier to prevent this recombination process [143]. With regard to TAS and PEC analyses of $BiVO_4$ photoanaode, a model of carrier dynamics can be schematized (Figure 10). After the electron/hole separation under simulated solar light, hole trapping process in energy levels closed to VB occurs at 5 picoseconds. At 40 ps and 2.5 ns, electron relaxation and trapping, respectively, are in competition with direct recombination with trapped holes. The relaxation and trapping processes are expected to be dominant over recombination. After 10 ns to 10 µs, recombination of trapped charge carriers can occur (Figure 10). In addition, at such time scales, no spectral or kinetic differences are observed between systems under a bias voltage or not, thus indicating that the effects of bias voltage occur on longer time scales [144].

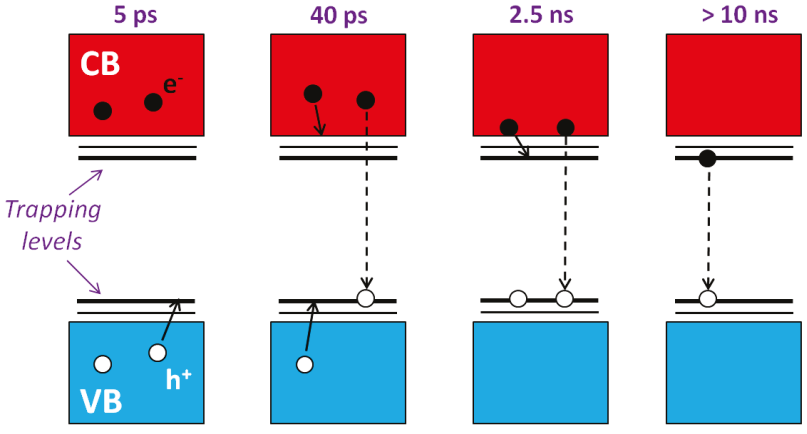

Figure 10. Scheme of charge carriers dynamics within the first stages of $BiVO_4$ photoactivation.

The main advantages of $BiVO_4$ are its non-toxicity and its energy band gap located in the visible region. However, several drawbacks are responsible of the low efficiency of bismuth vanadate in photo-induced chemical reactions such as its poor electron mobility and high e^-/h^+ recombination rate [137,138]. In addition, $BiVO_4$ has a short hole diffusion length (70−100 nm) that compromises the optimization of film thickness and light harvesting according to the optical penetration depth principle [138]. All these disadvantages are mainly due to the structure of $BiVO_4$ and the vanadium 3d orbitals which constitute the conduction band, since *[VO_4]* tetrahedra are not connected to each other and the V 3d orbitals are strongly localized, respectively [138].

On the other hand, there are many other bismuth vanadates in the ternary system Bi–V–O. These bismuth vanadates exhibit different crystalline structures, from which the most known are the Aurivillius-type $Bi_4V_2O_{11}$ phase (and also, its reduced form: $Bi_4V_2O_{10}$) [145–149]. Beside $Bi_4V_2O_{11}$, there are also hollandite-type $Bi_8V_2O_{17}$ structure, $Bi_{3.33}(VO_4)_2O_2$, $Bi_2VO_{5.5}$, etc. [136]. However, $Bi_4V_2O_{11}$ and $Bi_{3.33}(VO_4)_2O_2$ compounds are the most studied materials in photo-induced processes.

Concerning $Bi_{3.33}(VO_4)_2O_2$, it crystallizes in the triclinic system (space group $P\bar{1}$) with the following lattice parameters: a = 7.114 Å, b = 7.844 Å, c = 9.372 Å, α = 106.090°, β = 94.468°, and γ = 112.506° [136]. This crystal structure could be described by the alternative stacking along the b-axis of two types of layer (layers I and II). The layer I has four distinct Bi sites and *[VO_4]* tetrahedra while the layer II has three distinct Bi sites and *[VO_4]* tetrahedra. It is worth noting the deformation of coordination environments for all Bi atoms (due to lone pair of Bi^{3+}), but the *[VO_4]* tetrahedra remain regular. In the two types of tetrahedral (in $Bi_{3.33}(VO_4)_2O_2$), the mean V–O distance is 1.715 Å which is slightly shorter than 1.74 Å for tetrahedra in $BiVO_4$. About the four Bi atoms in layer I, the coordination number is 8 while for the three Bi atoms in layer II, it is 6. Therefore, the mean interatomic distances Bi–O is between 2.39 Å and 2.61 Å and it is consistent to those in $BiVO_4$ (2.48 Å). $Bi_{3.33}(VO_4)_2O_2$ has a yellow color and its optical band gap is estimated at 2.36 eV, which is similar to the monoclinic scheelite $BiVO_4$ [136].

Concerning $Bi_4V_2O_{11}$, it is a material which was discovered in the 1980s. It is defined as an intermediate compound in the system Bi_2O_3-V_2O_5. This bismuth vanadate material is particularly interesting due to its physical properties, e.g., dielectric properties, ferroelectricity and pyroelectricity at room temperature. The crystalline structure of $Bi_4V_2O_{11}$ is the parent structure of the *BIMEVOX* family materials (*BI* = bismuth, *ME* = metal subtitution, *VOX* = vanadates) which have attractive conduction properties at moderate temperature [146]. $Bi_4V_2O_{11}$ has also attracted interest due to its photo-induced properties for organic pollutants removal in water (Section Bismuth Vanadates in Section 4.2.3) [148].

$Bi_4V_2O_{11}$ exhibits two reversible phase transitions at 430 °C and at 570 °C while the melting temperature is 870 °C [145,146,148]. Therefore, there are three phases of $Bi_4V_2O_{11}$ which are the low-temperature α-form, the intermediate β-form, and the high-temperature γ-form which crystallize in the monoclinic, orthorhombic and tetragonal system, respectively [147]. The tetragonal gamma phase belongs to the *I4/mmm* space group while the orthorhombic beta polymorph has *Amam* space group [146]. For the alpha $Bi_4V_2O_{11}$, it is more complicated to assign a space group since its monoclinic structure is a three-fold supercell [147]. However, the sructure was refined recently in the *A2* space group [147]. All these three modifications can be described from a mean orthorhombic subcell having $a_m \approx 5.53$ Å, $b_m \approx 5.61$ Å and $c_m \approx 15.29$ Å (c being the stacking direction). The relationships between the unit cell parameters of the three phases and those of the subcell are: $a_\gamma = b_\gamma = a_m/(2)^{1/2}$, $c_\gamma = c_m$; $a_\beta = 2a_m$, $b_\beta = b_m$, $c_\beta = c_m$; $a_\alpha = 6a_m$, $b_\alpha = b_m$ and $c_\alpha = c_m$ [146]. From a structural point of view, the structure of the three $Bi_4V_2O_{11}$ phases is built from $[Bi_2O_2]^{2+}$ layers separated by vanadium–oxygen deficient perovskite slabs $[VO_{3.5}]$ [145]. Therefore, $Bi_4V_2O_{11}$ has the general formula $[Bi_2O_2][A_{m-1}B_mO_{3m+1}]$ consisting of an intergrowth between $[Bi_2O_2]^{2+}$ sheets and $[A_{m-1}B_mO_{3m+1}]^{2-}$ perovskite-like slabs with m as the number of $[BO_6]$ octahedra stacked along the direction perpendicular to the sheets. Therefore, $Bi_4V_2O_{11}$ (or $Bi_2VO_{5.5}$) is the corresponding oxygen deficient structure with $m = 1$ i.e., $[Bi_2O_2][VO_{3.5}\square_{0.5}]$ ("□" symbolizes the oxygen deficiency) [146]. A deepened comparison between the polymorphs, based on their structure and their conductivity, can be also discussed. Structurally, the alpha structure mainly differs from the two high temperature polymorphs by a specific vanadium-oxygen surroundings. Indeed, the vanadium-oxygen slabs exhibit vanadium with three different oxygen environments [147]. About conductive properties, the gamma polymorph has the highest conductivity compared to the two other phases, i.e., 0.2 $S{\cdot}cm^{-1}$ is observed at 600 °C with a strong drop during the phase transition from gamma to beta and beta to alpha [145]. The conductivity of beta and alpha phases is 0.01 $S{\cdot}cm^{-1}$ at 500 °C and 10–5 $S{\cdot}cm^{-1}$ at 300 °C, respectively. The observed drop in electrical performance is obviously due to the crystal structure, and particularly to the ordering of the oxygen vacancies in the V-O slabs [145]. These slabs are the components that mainly differ (strucrurally and electrically) from one phase to another [145]. For example, in the gamma phase, there is a large disorder of the oxygen atoms in V-O slabs which leads to fast diffusion properties. In addition to the electrical conductivity, $Bi_4V_2O_{11}$ has interesting optical properties with an energy band gap of 2.15 eV. This low E_g makes $Bi_4V_2O_{11}$ a promising visible-light-active material in photocatalysis. In addition, since $Bi_4V_2O_{11}$ has a layered structure (Aurivillius-related phase), the separation of photogenerated carriers is favored in the stacking direction, thus improving its photocatalytic efficiency. However, within the layers, the photogenerated electrons and holes are easily recombined because of the short band gap (2.15 eV) [149]. Another characteristic of $Bi_4V_2O_{11}$ is its ability to be easily reduced and re-oxidized as, for example, through $Bi_4V_2O_{10}$. In this reduced phase, there are also high and low temperature polymorphs where the structure of the low temperature one (α-$Bi_4V_2O_{10}$) is similar to α-$Bi_4V_2O_{11}$: $[Bi_2O_2]$ and $[VO_3]$ layers are identified but the latter one, $[VO_3]$, is built up by $[VO_5]$ square pyramids sharing basal corners.

3.2.2. Iron Vanadates

In the last decade, many scientists have focused on iron vanadates due to their versatile properties (photocatalysis, Fenton-based process, etc.). Among these ternary oxides, $FeVO_4$, FeV_3O_8, Fe_2VO_4, FeV_2O_4, $Fe_2V_4O_{13}$, $Fe_4(VO_4)_4$ have been successfully synthesized using different routes [134]. Usually, vanadates exhibit higher melting point and lower decomposition rate (at high temperatures) than V_2O_5. This is particularly the case of iron vanadates where the incorporation of Fe leads to stabilization of the material, thus decreasing the volatility of V. The most studied iron vanadate is $FeVO_4$ (also called iron orthovanadate) which has a stoichiometric ratio V:Fe = 1. $FeVO_4$ is also paramagnetic at room temperature with a saturation magnetization of 0.15 $emu{\cdot}g^{-1}$ [132]. This stoichiometric iron vanadate exhibits four different phases usually labeled as $FeVO_4$-I, $FeVO_4$-II,

$FeVO_4$-III, and $FeVO_4$-IV. The $FeVO_4$-I polymorph is the only stable phase formed at room temperature while other ones are all metastable phases formed at high pressures and/or high temperatures. Pure $FeVO_4$-I crystallizes in triclinic system with space group $P\bar{1}$ [133]. Structurally, this polymorph is built from distorted *[FeO_6]* octahedra and distorted *[FeO_5]* trigonal bipyramids linked together according the following sequence: two octahedra and one trigonal bypiramid. These Fe–O polyhedra are arranged in doubly-bent chains which are joined together by *[VO_4]* tetrahedral in order to form a 3D framework. The other forms of iron orthovanadates, i.e., $FeVO_4$-II, -III, and -IV, crystallize in the orthorhombic $CrVO_4$, orthorhombic α-PbO_2 and monoclinic wolframite $NiWO_4$ structures, respectively [150,151]. It is worth noting that hydrated $FeVO_4$ is amorphous, but after prolonged reaction time at normal pressure and low temperature, crystalline monoclinic $FeVO_4 \cdot xH_2O$ can be obtained. Concerning the physico-chemical properties of crystalline $FeVO_4$-I, it is a stable n-type semiconductor with a narrow energy band gap (E_g). The E_g has been estimated between 2.70 (direct) and 2.05 (indirect) eV depending on the synthesis parameters and the size and morphology of the prepared material [150–154]. The energetic position of the conduction band is above zero and more precisely at −0.4 eV [155]. This means that $FeVO_4$ semiconductor can theoretically produce hydrogen ($E^0(H^+/H_2) = 0$ V) under appropriate irradiation ($h\nu > E_g$), and the theoretical STH (solar-to-hydrogen) efficiency is relatively high (16%). Concerning the photophysical properties, the photocurrent density in undoped $FeVO_4$ is low (less than 0.1 $mA \cdot cm^{-2}$) at 1.23 V vs. RHE (reversible hydrogen electrode) [154]. However, to improve the photophysical properties of $FeVO_4$, synthesis of nanostructured materials and their modification using dopants can increase the specific surface area and improve the electronic properties (by modifying the band structure of $FeVO_4$), respectively [156]. In the case of Mo-doped $FeVO_4$, the photocurrent under simulated solar irradiation increases with increasing the dopant concentration with a maximum value of 0.2 $mA \cdot cm^{-2}$ for 2% of Mo at 1.6 V vs. RHE [154]. The produced photocurrent is improved of about 90% compared to undoped $FeVO_4$. At higher percentage of Mo, the photocurrent decreases since the presence of high amount of intrinsic defects act as recombination centers. Regarding the IPCE, 2% Mo-doped $FeVO_4$ exhibits an efficiency of 7% at 400 nm, while it is only 1% for undoped $FeVO_4$ at the same experimental conditions. Since the IPCE remains low at longer wavelength, the direct band gap appears to contribute more to the photocurrent than the indirect E_g [154]. In order to enhance the electronic properties without the use of dopants, quaternary oxides can be designed. Indeed, bismuth-substituted iron vanadate ($Fe_{1-x}Bi_xVO_4$) has improved charge carrier mobility and exhibits a shift of E_g towards higher energies with an increase of Bi content [154]. However, during the synthesis of either pristine or modified iron vanadates, particular attention is required to limit the formation of secondary phases like $Fe_2V_4O_{13}$ [154]. Concerning metastable $FeVO_4$ phases, few works are reported but $FeVO_4$-II has shown better properties than stable $FeVO_4$-I in gas sensing and photocatalytic activity. Indeed, metastable phases usually exhibit unique properties which are better than the pure phase. Such a fact is also observed in the case of vanadium oxides with metasable VO_2(B) which has better photo-induced properties than stable VO_2(M), especially in the degradation of organic pollutants. Finally, although there are numerous PEC studies of $FeVO_4$, TAS has not been performed yet, in contrary to one of the most popular vanadate, $BiVO_4$ (Section 3.2.1).

Another widely studied iron vanadate is $Fe_2V_4O_{13}$. This compound has a monoclinic structure which consists of tetrahedrally coordinated *[VO_4]* and octahedrally coordinated *[Fe_2O_{10}]* units, where tetrahedra are linked to octahedra through edge sharing, thus forming an unusual horseshoe-like chain structure [157,158]. It is quite difficult to prepare pure $Fe_2V_4O_{13}$ since $FeVO_4$ is always observed as an impurity. In addition, during the crystallization of $Fe_2V_4O_{13}$ (from the amorphous material), the specific surface area of $Fe_2V_4O_{13}$ calculated by BET was found to significantly decrease from 52 to 22 $m^2 \cdot g^{-1}$ while the color of the material changed from brown to light green [159]. In the structure of $Fe_2V_4O_{13}$, there is the presence of holes and channels which are interesting for many applications. Indeed, this iron vanadate has been investigated as an efficient cathode for lithium ion batteries as

well as catalyst for either photooxidation of organic pollutants or photoreduction of CO_2. For LIB, $Fe_2V_4O_{13}$ can deliver a discharge capacity of about 154 $mA{\cdot}h{\cdot}g^{-1}$ between 1.5 and 4.0 V after 50 cycles [157]. However, under irradiation, its photocurrent density is about 16 $\mu A{\cdot}cm^{-2}$ at 1.23 V vs. RHE in sodium borate electrolyte. This low value is due to the poor charge transport of this iron vanadate [158]. As a consequence, the IPCE is only 1.5% under 1.4 V at 350 nm [158]. $Fe_2V_4O_{13}$ is n-type semiconductor with an optical band gap of 2.3 eV with an absorption edge extending toward the visible light region. The conduction band minimum (CBM) of $Fe_2V_4O_{13}$ is determined to be −0.55 eV (vs. RHE) [160] while the valence band maximum (VBM) is located at 1.69 eV.

A less known iron vanadate is FeV_2O_4. This spinel compound crystallizes in cubic face-centered structure and belongs to the space group $Fd\bar{3}m$. The lattice parameters are as the following: a = 8.32 Å, b = 8.32 Å, c = 8.32 Å and $\alpha = \beta = \gamma = 90°$ with a cell volume of 588.77 $Å^3$ [161]. The iron cations are located in eight tetrahedral sites *[FeO_4]* while vanadium ions are situated in 16 octahedral *[VO_6]* (the cubic-closed packing structure is based on oxygen anions) [161]. FeV_2O_4 is a semiconductor which has a yellow color and it exhibits a direct energy band gap at about 1.9 eV and an indirect one at approximately 2.6 eV [162]. Comparing to iron (III) oxide (Fe_2O_3) and vanadium (V) oxide (V_2O_5), FeV_2O_4 is a material exhibiting much better electronic properties, i.e., with effective separation of photo-generated charge carriers, thus leading to better and faster charge transfer process at the interface with the liquid or gaseous medium [162]. In addition, the charge transfer resistance (RCT) is 23 KΩ which is a relatively low value. Therefore, FeV_2O_4 is considered as a suitable photo-electrode material for PEC cell [162]. The photocurrent of this iron vanadate under UV-visible illumination (100 $mW{\cdot}cm^{-2}$) can reach 0.18 $mA{\cdot}cm^{-2}$ at 1.2 V with an IPCE of 22% at 320 nm (in sulfate electrolyte) [162]. Finally, another underrated iron vanadate is FeV_3O_8. It has a monoclinic structure with lattice parameters of a = 12.13 Å, b = 3.679 Å and c = 6.547 Å and a direct optical band gap of 2.23 eV, thus suggesting a potential and promising photoactivity under visible light [163].

3.2.3. Copper Vanadates

Different polymorphs of copper vanadate (CVO) have been studied including CuV_2O_6, $Cu_2V_2O_7$, $Cu_3V_2O_8$, etc. The preparation of different types of copper vanadate with different stoichiometries can be achieved using different synthesis techniques and different experimental conditions [164,165]. The value of stoichiometric ratio strongly influences both physical and chemical properties. This stoichiometry is often determined by the ratio between copper (II) and vanadium (V) oxides, since the crystal structures of many copper vanadates are considered to be composed of CuO and V_2O_5. For example, CuV_2O_6, $Cu_2V_2O_7$, and $Cu_3V_2O_8$ exhibit molar ratio of CuO and V_2O_5 of 1:1, 2:1, and 3:1, respectively, and other combinations of copper oxide with V_2O_5 can lead to various phases of copper vanadate. In addition to the pure phase, surface modifications can be performed using metals and nonmetals, thus improving electrical, optical, and structural properties of the materials by enhancement of charge carrier transport, tuning of the band gap energy, etc. Initially, copper vanadates attracted the interest of scientists due to their high lithiated characteristics and their potential application as cathode in LIB [164]. This is particularly the case of $Cu_3V_2O_8$ and its composites and doped forms [164]. Crystalline copper vanadates have interesting layered structures which are composed of Cu-O layers in octahedral coordination joined by V-O tetrahedral layers. In addition, copper vanadates are also semidonductors with interesting optical properties, i.e., the absorption of a large part of natural solar light [164].

$Cu_3V_2O_8$ is one of the most investigated CVO. It can crystallized in either monoclinic, triclinic, or orthorhombic system, all with a low symmetry. Usually, most of the CVO structures offers a large range of phases [164]. The monoclinic gamma phase (γ-$Cu_3V_2O_8$) consists of *[VO_4]* tetrahedra and two distinct Cu units: square-planar *[CuO_4]* and square-pyramidal *[CuO_5]*. It is the most stable phase of this type of copper vanadate. The oxidation states for copper, vanadium and oxygen in $Cu_3V_2O_8$ are +2, +5 and −2, respectively, thus

the electronic band structure is mainly composed of Cu $3d^9$, V $3d^0$, and O $2p^6$ orbitals [166]. Indeed, γ-$Cu_3V_2O_8$ is a n-type semiconductor with an indirect band gap of about 1.8 eV and a direct band gap at approximately 2.7 eV [135]. The predicted E_g transitions are from O 2p to Cu 3d orbitals for direct E_g and from O 2p to V 3d orbitals for indirect energy band gap (Figure 11) [166]. It is worth noting that the valence band exhibits a high degree of hybridization with strong involvement of O 2p orbitals. Furthermore, the Fermi level (E_F) is located at 4.57 eV while VBM and CBM lay at 6.03 and 4.23 eV, respectively [166]. These values are relative to the vacuum level (e.g., $E^0(H^+/H_2)$ is situated at 4.5 eV). Regarding these properties, γ-$Cu_3V_2O_8$ is attractive for photochemical and electrochemical applications such as lithium ion batteries and photocatalysis [164,165].

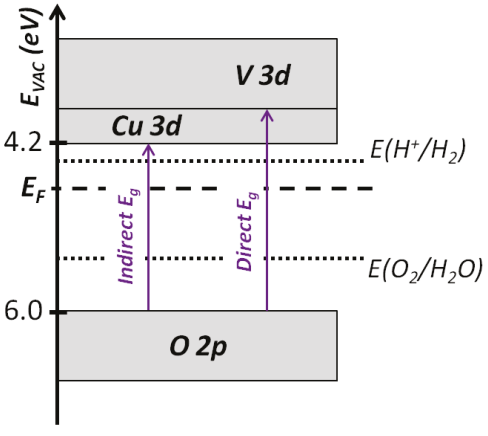

Figure 11. The electronic band structure of γ-$Cu_3V_2O_8$ (related to the vacuum energy).

Concerning the photoelectrochemical properties of γ-$Cu_3V_2O_8$, the photocurrent density is measured at 62 μA·cm^{-2} at 1.23 V vs. RHE under simulated solar irradiation. In addition, the IPCE of γ-$Cu_3V_2O_8$ reaches only 3% at 360 nm [166]. Due to a relatively low energy band gap, there is a fast recombination between the photogenerated charge carriers, thus leading to the weak photoactivity of γ-$Cu_3V_2O_8$. The recombination process, which dominates this copper vanadate, is worsened by short diffusion length. Therefore, although the energy band gap and the physico-chemical stability of γ-$Cu_3V_2O_8$ appear promising, the performance of this material as a photoelectrode in PEC applications is not yet suitable. Further work is required to improve the properties and performance of γ-$Cu_3V_2O_8$ in order to design a next-generation photoanode [166].

Another famous copper vanadate which is also an n-type semiconductor is $Cu_2V_2O_7$. Indeed, it has been already used as a cathode material for rechargeable LIB, photoelectrode in PEC technologies (for water oxidation) and as a photocatlyst [167]. $Cu_2V_2O_7$ has a monoclinic crystal structure where V^{5+} ion is surrounded by four oxygen while Cu^{2+} ion is coordinated with five oxygens [168]. This semiconductor copper vanadate is also a promising candidate for visible light-driven photocatalysis because of its narrow energy band-gap (2.0 eV) which is an indirect E_g [167,168]. The photocurrent density achieved by $Cu_2V_2O_7$ reaches about 120 μA·cm^{-2} at 1.58 V vs. RHE while the IPCE is 4% at 400 nm under 1.23 V vs. RHE [168]. However, as in the case of $Cu_3V_2O_8$, the photocatalytic efficiency of $Cu_2V_2O_7$ is limited because of the fast recombination of photogenerated holes and electrons. Therefore, composites with a Z-scheme structure have been designed in order to prevent this recombination i.e., to efficiently separate the e^-/h^+ pairs in the composite [167]. Indeed, a direct Z-scheme system is similar to a type-II heterojunction (Figure 12), but the electrons of the holes of semiconductor No1 (SC1) recombine by physical

contact with the electrons of semiconductor No2 (SC2), thus the remaining photogenerated electrons and holes of SC1 and SC2, respectively, are spatially separated.

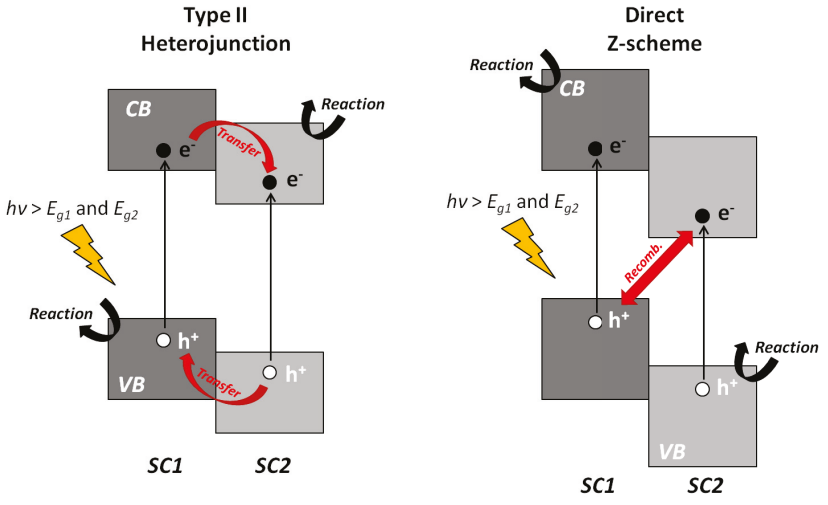

Figure 12. Electronic band structure of type-II heterojunction and direct Z-scheme with the different charge carriers migrations.

3.2.4. Silver Vanadates

Among the ternary vanadium oxides that are investigated for photochemical applications, silver vanadates have attracted much attention, mainly because of their narrow band gap and highly dispersed and hybridized valence band. The valence band in silver vanadates is composed of 2p orbitals of oxygen and 4d orbitals of silver and the hydbridization between the $2p^6$ orbitals with completely filled $4d^{10}$ orbitals leads to a VB located at a more positive energy level than VB in most of the other ternary vanadium oxides. That feature increases the oxidation power of the material. On the other hand, the conduction band consists of hybridized 5s orbital of silver with 3d orbitals of vanadium. Therefore, silver vanadates exhibit good absorption of low energy photon (e.g., visible light) and high mobility of photogenerated holes, which are crucial characteristics for application in photochemical processes, especially the degradation of organic pollutants (Section 4.2.2) [169].

A variety of ternary oxides based on silver, like $AgSbO_3$, $AgInO_2$, $Ag_2Ti_4O_9$, etc., have been recently developed as visible-light responsive photoactive materials [169]. In addition, ternary oxides based on vanadium and with a perovskite structure, such as $SrVO_3$ and $CaVO_3$, are highly stable and transparent oxides. Therefore, silver vanadates have attracted much interest due to their potential applications ranging from photocatalysis to batteries and sensors, and passing through antibacterial agents [170]. Silver vanadates have excellent electrochemical properties making them suitable for primary lithium ion batteries. Indeed, in the form of electrodes, $Ag_2V_4O_{11}$ nanowires and α-$AgVO_3$ microrods have exhibited high discharge capacities of 366 mA·h·g^{-1} and 324.1 mA·h·g^{-1}, respectively [135]. Silver vanadates have also interesting optical properties with intense absorption bands in the visible region, especially for α-$AgVO_3$, β-$AgVO_3$, $Ag_4V_2O_7$, $Ag_2V_4O_{11}$, and Ag_3VO_4 [171].

Concerning $AgVO_3$, this ternary vanadium oxide exists in two stable phases, both having a monoclinic structure: α-$AgVO_3$ and β-$AgVO_3$. The alpha and beta polymorph belong to space group *C2/c* and *Cm*, respectively [135,170,172]. In addition, α-$AgVO_3$ phase can be irreversibly transformed to β-$AgVO_3$ at around 200 °C [170]. The structure of crystalline $AgVO_3$ exhibits silver ions with three different local coordinations corresponding to $[AgO_x]$ clusters (x = 5, 6, and 7) and vanadium ions coordinated to four oxygen,

thus forming tetrahedron *[VO_4]* [170]. $AgVO_3$ materials are p-type semiconductors with a direct energy band gap. The E_g of the most stable polymorph, i.e., β-$AgVO_3$ is estimated to be about 2.2 eV [169,173]. That clearly indicates that β-$AgVO_3$ is a visible-light driven photoactive material with promising applications under natural sunlight. As reported in the previous paragraph, the narrow energy band gap of silver vanadates is mainly due to hydridization of O 2p and Ag 4d orbitals which compose the valence band [169]. In addition, in β-$AgVO_3$, there are intermediate energy levels within the band gap which arise from the structural disorder of the building blocks, i.e., *[VO_4]* and *[AgO_x]* clusters. This disorder also enhances the separation of photogenerated electron/hole pairs and implies highly mobile charge carriers [170]. Therefore, the electrochemical performance of β-$AgVO_3$ is better than α-$AgVO_3$. This better performance is further improved by the tunnel structure of the beta polymorph, thus allowing better cation insertion, i.e., higher specific capacity values [172].

Another silver vanadate, $Ag_2V_4O_{11}$, is widely used as efficient cathode in LIB for advanced biomedical devices such as implantable cardiac defibrillators [172]. Indeed, $Ag_2V_4O_{11}$ is a silver vanadate which been successfully commercialized for use as cathode material in LIB [174]. $Ag_2V_4O_{11}$ has a monoclinic structure with the space group *C2/m* [135]. The crystal structure of this silver vanadate is made of *[V_4O_{16}]* units which are composed of distorted *[VO_6]* octahedra sharing corners in order to form an infinite *[V_4O_{12}]$_n$* quadruple strings [135]. These chains are linked by corner-shared oxygen to provide continuous *[V_4O_{11}]$_n$* layers which are separated by silver atoms [135]. $Ag_2V_4O_{11}$ is a semiconductor with an indirect band of about 2.0 eV. Indeed, the absorption band of $Ag_2V_4O_{11}$ almost covers the region from UV to about 600 nm which corresponds to the visible portion of the natural sunlight [175]. Therefore, $Ag_2V_4O_{11}$ is not only an excellent electrochemical material, but also a promising photoactive material. The conduction band of $Ag_2V_4O_{11}$ is composed of the V 3d and Ag 5s5p orbitals while the valence band is the result of O 2p and Ag 4d hydribization as in most of silver vanadates [175]. The energy position of VBM and CBM can be determined theoretically by using the equation related to Mulliken electronegativity and the band gap value of the semiconductor oxide (Equation (11). As a result, the conduction band minimum is determined to be 4.4 eV relative to the vacuum level (which is close to $E(H^+/H_2)$ = 4.5 eV) while the valence band maximum is calculated to be 6.4 eV (using E_g = 2.0 eV) [175].

$$E_{CBM} = X - 0.5E_g \quad (11)$$

where E_{CBM} and E_g are the CB edge and band gap energies relative to the vacuum level, respectively, and X is the mean of the Mulliken electronegativity of the constituent atoms in the semiconductor [175].

Concerning the other silver vanadates, pure $Ag_4V_2O_7$ is difficult to prepare since this phase often coexists with Ag_3VO_4 during the synthesis. $Ag_4V_2O_7$ crystallizes in the orthorhombic system and it exhibits a band gap of about 2.5 eV. On the other hand, Ag_3VO_4 has also a band gap in the visible region with a value estimated to be 2.2 eV [176]. This phase crystallizes in the monoclinic system [176]. Compared to $Ag_4V_2O_7$, the energy position of the conduction band in Ag_3VO_4 is less negative, thus leading to less efficient reduction ability [177]. Despite most of silver vanadates have narrow energy band gaps, the separation rate of photo-generated electrons and holes remain low, that is the main drawback of these ternary vanadium oxides [176].

3.2.5. Manganese and Other Transition Metal Vanadates

There are many other transition metal vanadates, of which manganese ones are among the most documented. Most of manganese vanadates have been firstly studied for their electrochemical properties in LIBs [178]. However, $Mn_2V_2O_7$ has attracted attention not only for its electrochemical performance but also for its optical properties. There are two phases of this manganese vanadate: monoclinic β-$Mn_2V_2O_7$ and triclinic α-$Mn_2V_2O_7$ [178,179]. β-$Mn_2V_2O_7$ exhibits an energy band gap of about 1.2 eV while α-$Mn_2V_2O_7$ has a larger E_g

(1.8 eV) [178,180]. The structure of β-$Mn_2V_2O_7$ is composed of *[MnO_6]* octahedra sharing edges with *[V_2O_7]* interlayer while for α-$Mn_2V_2O_7$, it is often reported as impurity [178]. Another interesting manganese vanadate is $Mn(VO_3)_2$. It crystallizes in monoclinic structure and exhibits a direct energy band gap of about 3.0 eV [181].

For the other transition metal vanadates, the Table 1 summarizes the most important optical characteristics of such materials, i.e., their photocurrent and band gap energy values, since such properties are crucial for photo-induced chemical processes [180].

Table 1. Measured and calculated energy band gap for different transition metal vanadates along with their produced photocurrent.

Phase	Measured (eV)		Calculated (eV)		Photocurrent ($mA \cdot cm^{-2}$)
	Direct E_g	Indirect E_g	Direct E_g	Indirect E_g	
$Cr_2V_4O_{13}$	2.56	2.55	2.52	2.30	0.139
α-CoV_2O_6	2.17	2.16	2.25	2.25	0.015
$Co_3V_2O_8$	2.06	2.03	2.34	2.22	0.006
$Ni_2V_2O_7$	2.75	2.72	2.73	2.50	0.003
$Ni_3V_2O_8$	2.55	2.54	2.66	2.50	0.003
$Cu_{11}V_6O_{26}$	1.41	1.38	2.49	1.87	0.950
α-Ag_3VO_4	2.07	1.70	2.38	2.14	0.062
β-Ag_3VO_4	1.91	1.61	2.51	2.51	0.410

4. Vanadium Oxides in Photochemical Processes for Environmental Applications

4.1. Production of Sustainable Energy

One of the major concerns for humanity in the 21st century is the environmental changes [164,182]. Therefore, the production of renewable and sustainable energy is a crucial problematic throughout the world. Renewable energy sources can fulfil the requirements of energy without any production of pollution (toxic air pollutants and greenhouse gases), thus it is the best alternative to overcome the currently existing problems [183,184]. One of the main sustainable and renewable sources of energy is solar light with its utilization in photocatalysis, photovoltaic cell, etc. [164]. Therefore, besides the degradation of pollutant which is developed in Section 4.2, binary and ternary vanadium oxides can be used in the field of sustainable energy. The two main applications using vanadium oxide based materials in this field are the production of hydrogen by water splitting and the production of electricity using photovoltaic devices. Hydrogen (H_2), as a fuel, has a great energy yield (122 $KJ \cdot g^{-1}$) compared to fossil fuels (40 $KJ \cdot g^{-1}$) which are known to produce greenhouse gases and particulate matter (PM). A green and sustainable way to produce hydrogen is from the splitting of water molecule for two main reasons: (i) water is abundant on the planet (70% of Earth area is covered by water); and (ii) such a technology does not produce wastes (only hydrogen and oxygen). Using vanadium oxides materials as semiconductor photocatalysts, water splitting can be photo-assisted. The photosplitting of water has attracted the interest of many environmental chemists since it is considered as the "Holy Grail" in the field of energy: conversion of solar energy into chemical energy [9]. However, since the overall reaction of water splitting (Equations (12)–(14)) has relatively high Gibbs energy (ΔG^0 = 237.2 $KJ \cdot mol^{-1}$), the use of only solar energy is not enough to trigger the production of both hydrogen and oxygen using the actual commercial photocatalysts. Therefore, unless the discovery of an extraordinary green, efficient and inexpensive material, additional energy should be supplied to efficiently break H_2O molecules into molecular oxygen and hydrogen [185–188]. Therefore, electrical energy coupled to an irradiation (especially solar light) can be used in a photoelectrochemical (PEC) system containing a photoactive electrode (Figure 13). This strategy appears the best solution (so far) to produce green energy by water splitting. PEC is also called electrochemically assisted photocatalysis (electrophotocatalysis). To produce H_2 in an economically viable way and to reduce production cost, the electrical energy can derive from renewable sources, such as photovoltaic systems, so the produced hydrogen is entirely "green". In other words,

photoelectrochemical (PEC) cell is the most advanced way to produce chemical energy (hydrogen) by converting solar energy.

$$2H^+ + 2e^- \rightarrow H_2; \quad E^0 = 0 \text{ V} \tag{12}$$

$$2H_2O + 4h^+ \rightarrow O_2 + 4H^+; \quad E^0 = 1.23 \text{ V} \tag{13}$$

$$2H_2O + h\nu \rightarrow 2H_2 + O_2; \quad \Delta E = 1.23 \text{ V} \tag{14}$$

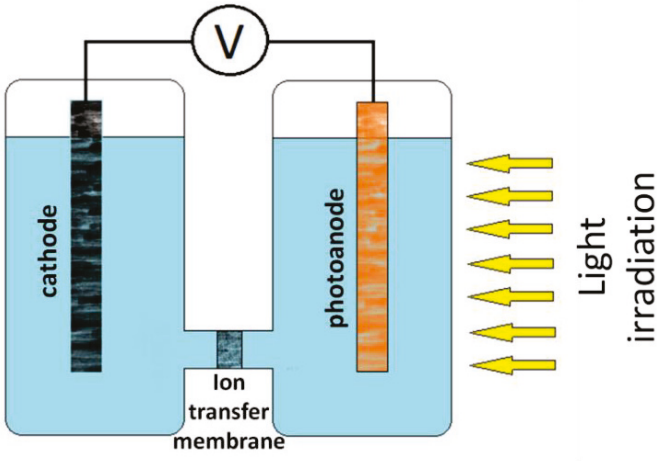

Figure 13. Two-compartment photoelectrochemical cell: the case of photoactive anode.

A PEC system is basically a cell coupled to a potentiostat. The PEC cell is composed of an anode and a cathode in contact with an electrolyte. An electrical voltage is applied between the electrodes. There are several cell configurations with either electrodes in the same compartment or separated by an ion-transfer membrane. For water splitting, the two-compartment PEC cell is the most suitable since O_2 and H_2 evolve separately, thus avoiding potential explosive mixture and water recombination (Figure 13) [189]. The electrophotocatalytic process for the production of hydrogen by water splitting using a PEC cell and a semiconductor photocatalyst such as vanadium oxides requires that the redox potentials for both water oxidation (Equation (13)) and reduction (Equation (12)) should lie within the energy band gap of the photoactive material (Figure 14) [186–190]. This photo-active material is often an n-type semiconductor photocatalyst like vanadium oxides and it constitutes the anode which is irradiated (photoanode). Since $\Delta E = 1.23$ V (for overall water splitting), the energy band gap of a photocatalyst candidate should be theoretically 1.23 eV in order to photogenerate e^- and h^+ species of enough energy to trigger the reactions (Equations (13) and (14)) [190]. However, due to overpotential losses, the E_g value should be at least 2 eV [185–188]. After the generation of e^-/h^+ pair under suitable irradiation, the PEC water splitting process using a photoanode is composed of three main steps: (i) water oxidation in the photoanode compartment, (ii) e^- transfer through external circuit toward the cathode compartment, where (iii) reduction of water occurs [186,189].

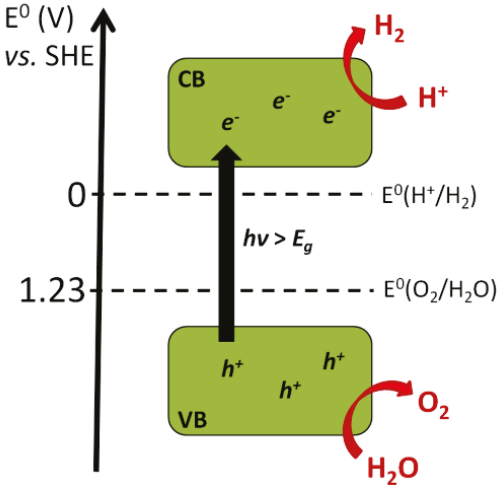

Figure 14. Mechansim of overall water splitting using heterogeneous semiconductor photocatalysis.

The first report on PEC water splitting dates 1972 [191]. In this work, Fujishima and Honda used rutile TiO_2 photoanode which is irradiated by UV light in a two-compartment cell. Unlike titanium dioxide which is the most popular photocatalytic material, vanadium oxides are promising candidates for PEC water splitting. One reason is that many vanadium oxides can be photoactivated by visible light. Although Fe_2O_3, WO_3, or CdS are also visible light driven photocatalyst, they cannot be used in this sustainable process due to inappropriate band structure, low photostability, high recombination rate, or high toxicity [185,186]. Another reason why vanadium oxides are interesting is their band structure. Indeed, the energy band gap of many vanadium oxides has the suitable energetic position, thus enclosing the redox potentials for water splitting, especially for the production of H_2 [192,193] while most of semiconductor transition metal oxides are efficient in partial water splitting, especially water oxidation (oxygen production). Therefore, vanadium oxide photocatalysts can be used without any electrical voltage for the production of hydrogen where V_6O_{13}, VO_2(M), and VO_2(B) could produce until 35 µmol of hydrogen per gram of catalyst after 12 h [192]. Supported VO_2 nanorods with energy band gap of 2.7 eV are also able to photocatalytically produce hydrogen by water splitting under UV light at room temperature. Indeed, in the presence of ethanol, a maximum value of H_2 production rate of 800 $mmol \cdot m^{-2} \cdot h^{-1}$ is obtained when the light is incident to the axis of the nanorods (due to vertical alignment of the nanorods) [194]. V_2O_5 has also shown interesting photo-induced properties with the generation of 8.9 $mm^3 \cdot h^{-1}$ of hydrogen by water splitting under visible light and in the presence of methanol. The role of alcohols is to trap photogenerated holes, thus improving the electron-hole pair separation where electrons can be efficiently used in the production of hydrogen (Figure 15A). The high efficiency of V_2O_5 in photocatalytic water splitting is also explained by the high specific surface area which is controlled by the sol-gel technique where vanadium triethoxide precursor and structure directing agent are employed [195]. In the case of using photo-sensitization process, i.e., using Eosin Y dye, the production of hydrogen can reach almost 20 $mm^3 \cdot h^{-1}$ [195]. Indeed, under irradiation, the excited dye can transfer its electrons to the conduction band of V_2O_5 photocatalyst where reduction reaction for the formation of hydrogen occurs (Figure 15B).

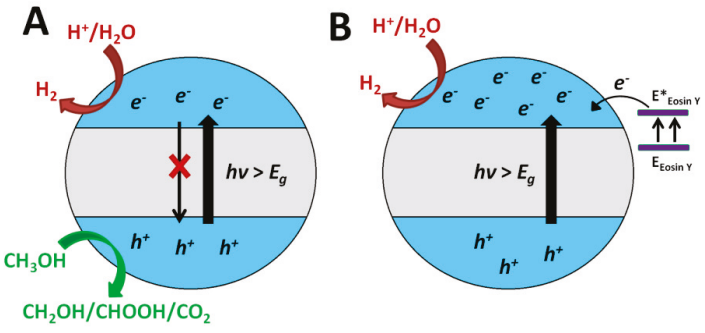

Figure 15. Improvement of hydrogen production using semiconductor photocatalyst by (**A**) sacrificial agent method (here, methanol) and (**B**) by dye photosensitization (here, Eosin Y).

However, the production rate of hydrogen using only light energy (without electrical bias) is low. This poor efficiency is mainly due to kinetic issues, limited solar energy conversion (photon to electron), and important charge recombination [196,197]. In addition, some binary and ternary vanadium oxides have a conduction band minimum which is not suitable for hydrogen production via the water splitting. For instance, $BiVO_4$ has a CBM at 0 V vs. SHE which makes the generation of H_2 experimentally impossible due to overpotential losses. However, $BiVO_4$ is an efficient photocatalyst for water oxidation which is a more challenging reaction than water reduction (four photogenerated holes are required compared to two photogenerated electrons for hydrogen production) [198]. There are potential alternatives to overcome these drawbacks by, for instance, the surface modification of photocatalysts. Indeed, the use of a synergistic co-catalyst is able to decrease the activation energy for H_2 production or to improve the charge carriers separation. Another example is the use of a suitable composite photocatalyst (especially a type-II heterojunction) since the photogenerated electrons are accumulated in one semiconductor while the photogenerated holes are collected in the other semiconductor, thus improving the e^-/h^+ pair separation under irradiation. This is the case of $FeVO_4$/CdS where 400 µM of hydrogen H_2 is produced after 5 h under visible light [197] and of $BiVO_4$/CdS nanoparticles with a hydrogen production rate of 0.57 mmol·h^{-1} under visible light [199]. However, the solution which appears the most efficient (so far) is to set up a PEC system (i.e., the use of electric bias) since relatively simple materials with low production cost can be used while the electric bias improves the e^-/h^+ pair separation by enforcing the movement of electrons oppositely to that of holes.

In such a PEC configuration, vanadium oxide photoanodes are more efficient, especially $BiVO_4$ due to its appropriate electronic band structure, excellent chemical and thermal stabilities, and environmental friendliness [193,200,201]. Its band gap of 2.4–2.5 eV (absorption edge: 500–520 nm) allows the production of 6.2–7.5 mA·cm^{-2} photocurrent under simulated solar light. In addition, its valence band maximum which is located at 2.5 V vs. RHE provides a strong driving force for water oxidation by photogenerated holes [143]. Concerning the production of hydrogen by water splitting, bismuth vanadate photoanode can produce up to 2.5 µmol·min^{-1} of hydrogen depending on the experimental conditions [202]. Since $BiVO_4$ has poor separation ability and slow mobility of carriers, it has limited efficiency in practical applications [200]. Therefore, modifications such as doping, coupling to oxygen evolution cocatalysts (OECs) and fabricating heterostructure composites (using for example $FeVO_4$ [203,204]) are considered to be the most promising techniques for improving the efficiency of vanadium oxide based materials [200]. Indeed, co-doping of metal and non-metal into ternary iron vanadium oxide could increase the carriers' concentration and decrease the energy band gap, thus enhancing the PEC activities [205]. $BiVO_4$/$FeVO_4$ heterostructured photoanode exhibits a photocurrent density of 2.5 mA·cm^2 at 1.23 V vs. RHE, which might be attributed to excellent charge trans-

fer/transport phenomena (Figure 16) [206]. In addition to thermodynamic parameters, the physical factors including specific surface area, exposed crystal facets, etc., are also crucial to obtain the best photo-induced efficiency. The design of nanostructured vanadium oxides in the form of ultrafine powder, hierarchical structure and porous material is an efficient approach to reach high rates in hydrogen production [207,208].

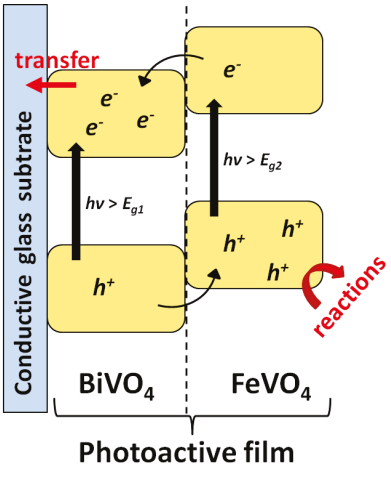

Figure 16. Charge transport of photogenerated holes and electrons in layered $BiVO_4/FeVO_4$ photoanode.

On the other hand, PEC processes using photoanode are also interesting for the degradation of pollutants [185,186]. The main advantage in the use of a PEC cell is the reaching of higher mineralization rates [140,185]. Since the charge carrier recombination in the photoanode is limited by the vector charge transport along the electrochemical potential gradient, the activation energy for full mineralization is easily achieved [140,185]. However, vanadium oxides have high oxidation power, thus, non-assisted photocatalysis is sufficient for efficient degradation of pollutants (Section 4.2).

Another environmental application using the photoinduced properties of vanadium oxides under solar light is the photovoltaic technology. Such devices, especially in the form of organic solar cells, are composed of an anode, a cathode, an active organic layer and interfacial layers [209]. In these latter ones, vanadium oxides are promising. The interfacial layers cover the electrode and are in contact to the organic layer. Their function is to support the transport of photogenerated charges [209]. Usually, as interfacial layer, poly(3,4-ethylenedioxythiophene) poly(styrenesulfonate) (PEDOT:PSS) is employed but its poor long-term stability has pushed the scientists to consider other possibilities to replace PEDOT:PSS such as V_2O_5. Vanadium pentoxide can be deposited in ambient conditions, thus avoiding high temperature annealing and other post-treatments [210]. Recently, it is in perovskite solar cells that vanadium oxides exhibited outstanding performance as hole-transport layers [211].

4.2. Photo-Induced Degradation of Organic Contaminants

The organic contamination is a critical issue for the natural environment, especially for the hydrosphere. Indeed, many pollutants are accumulated in in the aqueous media, especially the persistent organic pollutants (POPs) and the contaminants of emerging concern (CECs), i.e., pharmaceuticals and personal care products (PPCPs), endocrine-disrupting compounds (EDCs), flame retardants (FRs), pesticides, herbicides, and fungicides, etc. These CECs are frequently detected in wastewater treatment plant (WWTP) effluents. Indeed, the use of conventional treatments are not enough efficient to remove the CECs while these contaminants have a well-known harmful impact not only on the environment, but

also on the human health. Therefore, the discharge of WWTP effluents (i.e., treated wastewaters) is the main source of contamination of CECs and POPs into the natural environment, thus being a real threat for drinking water source (ground and surface water) [212].

The properties of vanadium oxides are versatile mainly due to the multivalent character of vanadium. Thank to these properties, it is possible to design efficient photo-induced processes (photocatalysis, photo-Fenton, etc.) for environmental remediation, including the removal of organic pollution [83].

4.2.1. Generalities of Photo-Induced Processes

One of the most efficient techniques to remediate the environment, especially for the removal of organic contaminants from water, is the advanced oxidation process (AOP). The AOPs are based on the generation of reactive oxygen species (ROS) including inorganic radicals, such as $HO^{\bullet}$. AOPs usually enhance the biodegradation of organic pollutants but it could also lead to degradation intermediates which are more toxic than the original targeted molecules [212]. The activation of the AOPs can be performed either by catalysis, heat, light, or a combination of these means (e.g., photocatalysis and photo-Fenton). It is the technology based on the use of coupled catalysis and solar radiation which is highlighted in this section since the resulting process can reach high remediation efficiency along with sustainable development (i.e., efficient and environmentally friendly process).

In AOPs, the most important active species are hydroxyl radicals ($HO^{\bullet}$). $HO^{\bullet}$ has two main characteristics. First, it is a strong oxidant with a redox potential $E^0(HO^{\bullet}/H_2O)$ of 2.8 V vs. NHE. Second, it is a nonselective oxidant which is able to react with most of the organic contaminants with high bimolecular kinetic constants (10^8–10^{11} $M^{-1}{\cdot}s^{-1}$). These characteristics are responsible for the high efficiency of AOPs in the removal of POPs and CECs [213]. The reaction between hydroxyl radicals and organic molecules proceeds mainly by hydrogen abstraction (from C–H, N–H, or O–H bonds) and by hydroxyl addition to unsaturated bonds. It is worth noting that the involvement of hydroxyl radicals in organic decontamination process is not easy to demonstrate since the half-life of $HO^{\bullet}$ is in the order of nanosecond. Therefore, most of their identification are performed using indirect methods such as fluorescence spectroscopy or electron paramagnetic resonance in the presence of suitable probe molecules. In addition to hydroxyl radicals, the photo-induced degradation of organic pollutants involve other radicals like superoxide anion ($O_2^{\bullet -}$) and its conjugated form, hydroperoxyl radical ($HO_2^{\bullet}$). These radicals are, however, less reactive than $HO^{\bullet}$ [213].

These photo-induced AOPs are suitable techniques for the degradation of organic contaminants. Among them, direct photolysis, photocatalysis and photo-Fenton reaction are the most used processes. Direct photolysis is based on the sole use of light to break the chemical bonds in the contaminant molecule. Since UVB and UVC irradiations are the most used lights in direct photolysis, this method cannot be considered as sustainable process (and it is not discussed in this section) while photocatalytic and photo-Fenton processes are developed hereafter.

Photocatalysis

The photocatalysis is a photo-induced process combining the use light irradiation and catalysis. Therefore, the compounds which are employed in such a process are called photocatalysts like vanadium oxide based materials. In this case, the process is referred as heterogeneous photocatalysis since solid semiconductors are used. Prior to describe how heterogeneous photocatalysis is operating, a brief historical background, and some basic principles should be introduced. Although the definition of a semiconductor is in Section 3.1.2, the term semiconducting was first used by Alessandro Volta in 1782 and it is at the beginning of the 20th century that Johan Koenigsberger classified materials into conductor, insulator, and semiconductor. On the other hand, the concept of photoconductivity appeared in 1874 [164]. Indeed, an electron can move from valence band (VB) to conduction band (CB) when the supplied energy to the semiconductor is higher than the

energy band gap (E_g)—also known as forbidden energy band—which is the energy gap between the VB and the CB. The value of the energy band gap is an intrinsic value, thus varying from one material to another. In other words, under incident light of sufficient energy, the electrons move from VB to CB while holes have an opposite motion, thus generating a current [164].

A key parameters in the selection of a semiconductor photocatalyst is the value of the energy band gap along with the stability of the material. The principle of heterogeneous photocatalysis using semiconductors is based on the generation of electrons and holes, i.e., the e^-/h^+ pairs (Equation (15)). Indeed, once the e^-/h^+ pairs are photogenerated under an incident irradiation of energy ($h\nu$) equal or larger than the energy band gap, these charge carriers are responsible in the formation of reactive oxygen species (Equations (16)–(22)) which, subsequently, degrade organic contaminants. The primary ROS are formed by the reaction of electron and hole with oxygen and water, respectively. However, the mechanism of hydroxyl radical generation is still the matter of discussions since the photogenerated holes can react also with surface hydroxyl function present at the surface of the photocatalyst. The degradation of pollutants can also occur directly through photogenerated holes (which are oxidant), but this reaction is not kinetically favored due to the strong reactivity of ROS with organic molecules. The formation of ROS does not only include the generation of superoxide and hydroxyl radicals, but also other species such as hydroperoxyl radicals and hydrogen peroxide, which is an important precursor of $HO^\bullet$ (Equations (16)–(22)) [33]. H_2O_2 is also a key precursor in Fenton-based processes (Section Photo-Fenton and Fenton-Based Processes).

$$Semiconductor + h\nu \rightarrow e^- + h^+ \quad (15)$$

$$OH^- + h^+ \rightarrow HO^\bullet \quad (16)$$

$$H_2O + h^+ \rightarrow HO^\bullet + H^+ \quad (17)$$

$$O_2 + e^- \rightarrow O_2^{\bullet -} \quad (18)$$

$$O_2^{\bullet -} + H^+ \rightarrow HO_2^\bullet \quad (19)$$

$$2HO^\bullet \rightarrow H_2O_2 \quad (20)$$

$$H_2O_2 + e^- \rightarrow HO^\bullet + OH^- \quad (21)$$

$$H_2O + O_2^{\bullet -} \rightarrow HO_2^\bullet + OH^- \quad (22)$$

However, several conditions should be fulfilled to observe the above mentioned photocatalytic reactions. In addition to the fact that the e^-/h^+ pair generation is in competition with the recombination process (releasing the absorbed energy in the form of either light or heat), the photogeneation of the charge carriers (electrons and holes) should reach the surface of the photocatalyst where they react with adsorbed reactants, since the photocatalysis is a surface dependent process (Langmuir–Hinshelwood model). In addition, the redox potential of the photocatalytic reaction (e.g., the generation of ROS) has to lie within the energy band gap (Figure 17). Therefore, the feasibility of a photocatalytic reaction depends mainly on the energetic position of the valence band maximum (VBM) and the conduction band minimum (CBM) of the semiconductor photocatalyst [33].

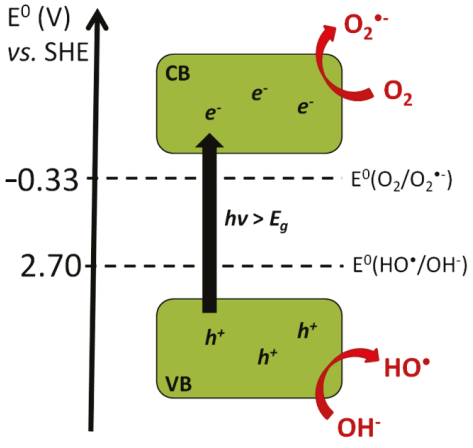

Figure 17. Mechanism of primary ROS generation by heterogeneous semiconductor photocatalysis.

Photo-Fenton and Fenton-Based Processes

Another important photo-induced process is the photo-Fenton reaction. Usually, this process describes the generation of ROS in the presence of iron. Indeed, the classical Fenton reaction was discovered in 1894 by H. J. H. Fenton whom observed the oxidation of tartaric acid in the presence of iron and hydrogen peroxide [214]. About 100 years later, the heterogeneous Fenton reaction was observed (Equations (23) and (24)). Compared to the homogeneous system, heterogeneous Fenton reaction can be used over a wider range of pH (e.g., environmental pH) since there is no need to use acidic condition to avoid the production of sludge (from iron coagulation/precipitation). However, the mechanism of heterogeneous Fenton is still unresolved. This complexity is due to various interactions between the surface of the material with hydrogen peroxide, organic molecules (and their degradation byproducts), and the generated ROS [213]. It is admitted the main ROS are $HO^{\bullet}$ and $HO_2^{\bullet}/O_2^{\bullet-}$ which are either generated at the surface of the materials or at the close surroundings of the surface through possibly leached iron (i.e., homogeneous Fenton reaction) [213].

$$\equiv Fe^{II} + H_2O_2 \rightarrow \equiv Fe^{III}OH + HO^{\bullet} \quad (23)$$

$$\equiv Fe^{III} + H_2O_2 \rightarrow \equiv Fe^{II} + H^+ + HOO^{\bullet} \quad (24)$$

On the other hand, heterogeneous photo-Fenton reaction is considered as viable alternative to classical heterogeneous Fenton, since there is no need to add hydrogen peroxide to the system (Equation (25)). Indeed, the generation of inorganic radicals such as hydroxyl and superoxide radicals occurs via the photolysis of iron (III) where electron transfers occur with adsorbed water molecules, i.e., a ligand to metal charge transfer (LMCT). The AOPs generated by heterogeneous photo-Fenton reaction are efficient in the degradation of organic contaminants including pharmaceuticals, pesticides/herbicides, etc. [215,216]. Furthermore, it allows the possibility of using natural solar light, thus increasing the sustainibility of such a process.

$$\equiv Fe^{III} + H_2O + h\nu \rightarrow \equiv Fe^{II} + H^+ + HO^{\bullet} \quad (25)$$

However, other transition metals can also trigger Fenton-type reactions. To increase the environmentally friendliness of these processes, it is possible to use elements that are abundant in the Earth's crust. Intense research is actually focused on these iron-free Fenton processes [217]. One important element is aluminum which has a stronger ability to convert H_2O_2 to $HO^{\bullet}$ through e^- transfer due to more negative redox potential ($E^0(Al^{3+}/Al^0) = -1.66$ V) than iron ($E^0(Fe^{3+}/Fe^{2+}) = +0.776$ V). However, the main disad-

vantage of using zero-valent aluminum is the formation of Al_2O_3 layer which is hard to remove, thus requiring strong acidic conditions to avoid the inhibition of the Fenton process. The generation of ROS in such a system mainly occurs through the in situ production of hydrogen peroxide by electron transfer to dissolved oxygen. The hydrogen peroxide is then subsequently decomposed to generate hydroxyl radicals (Figure 18) [217].

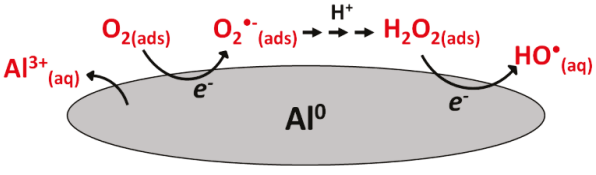

Figure 18. Generation of primary ROS at the surface of aluminum.

Another interesting element with high natural occurrence is manganese due to its versatility in oxidation states ranging from 0 to +VII. Among them, only Mn (II), Mn (III), and Mn (IV) can be used in Fenton-based processes. Mn (II) species are predominantly present in soluble form while Mn (III) and Mn (IV) exist in the form of oxides and hydroxides, such as Mn_3O_4, Mn_2O_3, MnOOH, and MnO_2. The latter is already known as oxidizing material for direct degradation (neither light nor radical precursor assistance) of adsorbed organic contaminants. In this iron-free Fenton process involving manganese, the mechanism is complex and it is not yet resolved. However, it is assumed that hydrogen peroxide is activated by interconversion between Mn^{2+} and Mn^{4+} via intermediate Mn^{3+}. According to the type and the form of the oxide used, the main ROS are either hydroxyl radicals or superoxide radicals. The main advantage of this Mn-based Fenton process is a significant efficiency at circum-neutral conditions, especially for pH ranging from 4 to 8 [217].

Copper is the element which is the most analogeous to iron in Fenton-based processes. Indeed, like Fe (II) and Fe (III), monovalent and divalent copper can activate hydrogen peroxide to generate reactive oxygen species, especially $HO^\bullet$ and $HO_2^\bullet$ (Equations (26) and (27)). The main advantage of copper oxides over iron ones is their stability (Cu leaching is limited), thus allowing this iron-free Fenton reaction to run out at circum-neutral pH. However, Cu (I) is readily oxidized into Cu (II) by oxygen, thus, its reaction with hydrogen peroxide is inhibited. This is a strong drawback which limits practical application of this system. Excess of H_2O_2 has to be used which increases the cost of this iron-free Fenton process but decrease the oxidation efficiency (by scavenging the generated $HO^\bullet$) [217].

$$\equiv Cu^{II} + H_2O_2 \rightarrow \equiv Cu^{I} + H^+ + HOO^\bullet \quad (26)$$

$$\equiv Cu^{I} + H_2O_2 \rightarrow \equiv Cu^{II} + OH^- + HO^\bullet \quad (27)$$

Finally, vanadium is also an element which is active in Fenton-type reactions. Among the multiple oxidation states of vanadium, only V (V) to V (IV) can trigger a Fenton-like reaction (Equation (28)), but in the form of oxo-cations. Such reactions are observed in biochemical process involving vanadium [134], but also at the surface of vanadium oxide based materials [218]. It is worth noting that cerium, a lanthanide element, in soluble or solid form ($Ce^{3+}/^{4+}$ or CeO_2) can trigger Fenton-based processes on the same scheme as in the case of iron (Equations (29) and (30)). However, considering the toxicity of cerium, it cannot be implemented in applications for the treatment of water from organic contaminants [217].

$$VO^{2+} + H_2O_2 \rightarrow VO_2^{+} + H^+ + HO^\bullet \quad (28)$$

$$\equiv Ce^{III} + H_2O_2 \rightarrow \equiv Ce^{IV} + OH^- + HO^\bullet \quad (29)$$

$$\equiv Ce^{IV} + H_2O_2 \rightarrow \equiv Ce^{III} + H^+ + HOO^\bullet \quad (30)$$

The mechanism using these transition metals in the photo-Fenton process has not been yet clearly demonstrated. However, since hydrogen peroxide can be in situ photochemically generated (e.g., by photocatalysis), the iron-free Fenton-based processes appear to have a significant contribution in photocatalytic systems based, for instance, on binary and ternary vanadium oxides.

4.2.2. Binary Vanadium Oxides

V_2O_5

As discussed in Section 3.1, V_2O_5 materials are usually studied for applications in electrochemical devices, especially for Li-ion batteries. However, during the last decades, there is a growing interest of the use of vanadium pentoxide in photocatalytic applications, especially for the degradation of organic pollutants and the production of hydrogen by water splitting. In order to be thermodynamically feasible, the valence band maximum should be more positive than the redox potential of hydroxyl radical generation ($E^0(HO^\bullet/H_2O)$ = 2.8 V) and the conduction band minimum should be more negative than the redox potential of hydrogen formation ($E^0(H^+/H_2)$ = 0 V), respectively [219]. Indeed, the VBM and CBM of V_2O_5 is about 2.6–3.0 V and from −0.1 to +1.0 V, respectively. Therefore, the band structure of V_2O_5 is suitable for these photocatalytic processes. It is worth noting that the generation of superoxide radical is theoretically not feasible ($E^0(O_2/O_2^{\bullet-})$ = −0.33 V), but V_2O_5 presents surface defects in the form of V^{4+} which allows the generation of superoxide radicals [219].

Vanadium pentoxide can be synthesized using different experimental methods and prepared in different forms (powders, films, etc.). Most of the preparation techniques involved wet chemical methods which allow the use of structure directing agent (Triton X-100, polyvinylpyrrolidone, polyethylen glycol, etc.) in order to design a particular morphology. Whatever the method employed, all the prepared V_2O_5 photocatalysts require an annealing process in order to get crystalline materials, usually at temperature about 500 °C.

Supported photocatalysts can be prepared using the sol-gel method along with the vanadium triisopropoxide oxide as precursor [220,221]. Another preparation procedure of supported V_2O_5 is the hydrothermal method [222]. Such a solvothermal method often implies ammonium metavanadate (NH_4VO_3) as precursor, but bulk V_2O_5 powder can be also directly used as precursor. Indeed, in the presence of a reducing agent such as oxalic acid, VO_2(B) film is prepared (Equations (31) and (32)) which is subsequently converted into V_2O_5 with the appropriate morphology [222].

$$V_2O_5 + 3H_2C_2O_4 \rightarrow 2VOC_2O_4 + 3H_2O + 2CO_2 \quad (31)$$

$$VOC_2O_4 \rightarrow VO_2 + CO_2 + CO \quad (32)$$

By this mean, V_2O_5 films with different morphologies (including hierarchical nanostructures, nanorods, nanowires, etc.) can be deposited on different substrates such as sapphire, indium tin oxide (ITO) coated glass, etc. [220,222]. The thickness of the films can be regulated by the number of deposited layers on the substrate, and that can have an impact on the quality and the efficiency of the supported photocatalyst [220]. The calculated energy band gap (E_g) is about 2.1 eV, so the V_2O_5 photocatalytic films can be used in the degradation of organic pollutants in aqueous or gaseous phases under simulated sunlight [220–222]. For instance, V_2O_5 nanowires films can degrade around 98% of toluidine blue O, an organic dye, after 50 min under UV light [220]. Flower like nonastructure films are able to remove up to 74% and 63% of methylene blue under UV and visible light, respectively, after 200 min [222]. In addition, 51% of this organic dye is mineralized into CO_2 and H_2O in the case of UV irradiation. Gaseous pollutants can be also efficiently degraded by V_2O_5 photocatalysis, such as for example 1,2-dichlobenzene [221]. Under visible light, about 45% of this organic contaminants can be degraded after 7 h

irradiation in presence of V_2O_5 [221]. The excellent photocatalytic properties of V_2O_5 films are ascribed to large specific surface area and efficient visible light utilization [221,222].

On the other hand, V_2O_5 powders can be also preprared. As in the case of supported photocatalysts, sol-gel, and hydrothermal methods are often chosen to synthesize V_2O_5 powders using NH_4VO_3 and H_2O_2 as precursors [223,224]. In addition, co-precipitation can be also used in the presence of NH_4VO_3 and HNO_3 [225]. The energy band gap of the synthesized V_2O_5 powders is about 2.3 eV while the specific surface area is high for nanostructured powders [223–225]. Nanostructured powders can degrade efficiently rhodamine 6G, congo red, and methyl orange under visible light with removal extents of 78%, 99%, and 82%, respectively, after 180 min irradiation time [223,224]. Phenolic contaminants such as phenol, pyrocatechol (2-HP), 2-chlorophenol (2-CP) 2-nitrophenol (2-NP), and 2-aminophenol (2-AP) are also degraded by V_2O_5 photocatalysis under natural sunlight [225]. Although the degradation extents for phenol, 2-HP, 2-CP, 2-NP, and 2-AP are 13%, 40%, 68%, 81%, and 37%, the mineralization is lower with extents about 8%, 16%, 42%, 29%, and 27%, respectively [225]. The high efficiency of V_2O_5 powder photocatalysts is due mainly to the high specific surface area, relatively good utilization of visible light and excellent electron-hole pair separation [223,224]. Indeed, based on the produced photocurrent and compared to commercial micro-sized V_2O_5 powder, the number of charge carriers reaching the surface of the nanostructured materials (where reactions occur) is higher [224]. In addition, the exposition of V_2O_5 to irradiation induces the formation of surface defects which are composed of V^{4+} states, thus improving the lifetime of charge carriers by electron trapping phenomenon [225]. Moreover, the reproducibility of the photocatalytic experiments is also excellent with almost no change in removal rate after repeated runs [223]. Furthermore, V_2O_5 nanopowders are also efficient antimicrobial agents with improved removal of *Escherichia coli* and *Staphylococcus aureus* bacteria [223]. Recently, the effect of various extra-drying process (e.g., vacuum, freeze, oven) during the preparation of V_2O_5 nanoparticles through wet chemical methods has shown a limitation in the particle aggregation, thus increasing the reactivity of the photocatalyst [226]. Indeed, the nanoparticles size are in the range of 30–40 nm and the specific surface area is in the range of 125–205 $m^2 \cdot g^{-1}$ [226]. Therefore, the synthesis procedure is crucial in the preparation of efficient photocatalysts.

Concerning the mechanism of any photo-induced degradation of organic contaminants, the blank and dark experiments should be always performed, i.e., direct photolysis and adsorption, respectively. V_2O_5 cannot efficiently remove organic pollution via adsorption processes while solar and visible light has not enough energy to photolyze most of the organic contaminants [220]. The photocatalytic mechanism is a surface-dependent process following the model of Langmuir–Hinshelwood, thus requiring the adsorption of the target molecule onto the surface of the photocatalyst. Many studies have shown that the photocatalytic degradation of organic contaminants using V_2O_5 occurs mainly via the primary ROS which are superoxide and hydroxyl radicals [221,223–225]. Indeed, hydroxyl radicals are form by reaction of photogenerated holes with surface hydroxyl group or adsorbed water molecule [221,225]. However, the involvement of $O_2^{\bullet -}$ species is contradictory among the published works. Some scientists claim the reaction of photogenerated electrons with dissolved oxygen and subsequently, hydrogen peroxide and hydroxyl radicals can be formed by a cascade of reactions (Equations (19), (33)–(35)) according to the pH [221,224,225]. However, regarding the band structure of V_2O_5, especially the conduction band minimum, the formation of $O_2^{\bullet -}$ is not thermodynamically feasible [225]. A viable tool for the identification of ROS, particularly for $HO^{\bullet}$ and $O_2^{\bullet -}$, is the electron paramagnetic resonance (EPR). Indeed, the signals of DMPO-$HO^{\bullet}$ and DMPO-O_2^{-} spin adducts have a characteristics hyperfine structure [224]. By this mean, the photocatalytic degradation of organic contaminant in the presence of V_2O_5 suggests a negligible contribution of the superoxide radicals [224].

$$HO_2^{\bullet} + HO_2^{\bullet} \rightarrow H_2O_2 + O_2 \quad (33)$$

$$O_2^{\bullet -} + H_2O_2 \rightarrow OH^{\bullet} + OH^{-} + O_2 \quad (34)$$

$$H_2O_2 + h\upsilon \rightarrow 2OH^{\bullet} \quad (35)$$

The degradation of aromatic compounds results in ring opening through the oxidation by $HO^{\bullet}$, and ultimately leads to smaller species such as acetate and maleate [221]. In the case of organic dye, degradation occurs via *N*-deethylation, thus giving rise to smaller intermediates such as benzoic acid, hydroxybenzoic acid, etc. [223]. It is important to mention that the pH of the system is a crucial parameter [223,225]. Indeed, the ionic form of the organic pollutants (which is related to its pK_a) and the charge surface properties of the material are dependent to the pH, thus impacting the interactions pollutant/photocatalyst. In addition, the pH affect also the generation of ROS [225]. For instance, at low pH, superoxide radicals form hydroperoxyl radicals (Equation (19)) and subsequently hydrogen peroxide (Equations (33) and (37)) which is a precursor for the generation of hydroxyl radicals (Equations (21), (34), and (35)) [225].

To resume, vanadium pentoxide nanostructured materials are promising solar light driven photocatalysts for the remediation of water from organic contaminants. So far, many studies have been focused on the removal of organic dyes, thus, the self-sensitization of the photocatalyst for the generation of ROS is possibly involved. Therefore, further works on colorless POPs and CECs are necessary in order to draw a better overview on the efficiency of V_2O_5 photocatalysis.

VO_2

Vanadium dioxide is thoroughly investigated for applications as smart windows due to its thermochromic properties (Section 2.2). The study of its photocatalytic properties is not yet well documented although it is a promising photoactive material. Among the different polymorphs of vanadium dioxide, VO_2(B) exhibits interesting photocatalytic properties although it is a semiconductor which is not thermochromic and which has a slightly larger energy band gap than that of V_2O_5, with a value of 2.8 eV [227]. Supported VO_2(B) can be prepared by an aqueous sol-gel method using V_2O_5 and hydrogen peroxide as precursors. The deposition of the sol-gel should be performed on substrates that will not react with the vanadium oxide layer (such as Si/SiO_2 and sapphire) since on lime glass, contamination by ion diffusion could occur during the annealing process [228]. Layered VO_2(B) is obtained by annealing in reducing conditions, e.g., in H_2/Ar atmosphere or in vacuum in order to reduce V_2O_5 to mixed valence V_4O_9 and ultimately to VO_2. The photocatalytic activity of VO_2(B) films is considerably better than that of V_2O_5 with a more efficient removal of Rhodamine B under UVA light [227]. The higher photocatalytic efficiency could be ascribe to the defect at the surface of vanadium oxide since the reductive annealing leads to more oxygen vacancies which are beneficial for the e^-/h^+ pairs separation.

Since the literature on single phase VO_2 photocatalysts is scarce, composites containing VO_2 is also discussed in this section. Usually, the synthesis procedure of such materials involves hydrothermal methods using V_2O_5 and a reducing agent such as citric and oxalic acid [229–233]. By this mean, VO_2(B) and VO_2(M) can be prepared according to the experimental conditions. Then heterojunctions with another semiconductor metal oxide can be formed using, for instance, dispersion of VO_2 powder into a metal alkoxide sol-gel [230,231,233]. VO_2(B)/CeO_2 photocatalysts in the form of nanoparticles exhibit efficient photo-induced properties for the removal of Rhodamine B with a removal extent reaching up to 66% in 180 min under UV irradiation. Similarly, VO_2 alone can remove only 29% of this dye under the same experimental conditions [229]. The better photocatalytic properties of VO_2(B)/CeO_2 is explained by a smaller energy band gap (E_g = 3.25 eV) compared to that of pure VO_2 (E_g = 3.5 eV). This shift toward lower values is due to the presence of CeO_2 which absorbs larger extent of the visible light [229]. VO_2(M)/ZnO composite is a photocatalyst with high specific surface area and energy band gap of 2.67 eV [231]. Indeed, in the form of a hierarchical structure, VO_2(M)/ZnO gives rise to a specific surface area of about 70 $m^2 \cdot g^{-1}$ which is a two-fold increase compared to the single component, thus, increasing the number of photocatalytic sites. In such a composite, ZnO is responsible to the widening of E_g due its energy band gap of 2.7 eV

compared to 2.3 eV for pure VO_2. VO_2(M)/ZnO photocatalyst can degrade up to 80% Rhodamine B under solar like irradiation after 20 min, which is significantly better than the single components [231]. In addition, the reproducibility after repeated photocatalytic runs is excellent while the composite remains stable without any dissolution of the material. Another efficient composite photocatalyst is VO_2(M)/TiO_2 which is able to degrade completely methylene blue within 10 min under UV light and about 70% of Rhodamine B after 2.5 h under solar irradiation [230,231,233]. However, the purpose of this latter composite is to design thermochromic and self-cleaning coating by combining the properties of TiO_2 and VO_2. Therefore, the photocatalytic properties are ascribed only to TiO_2, thus, assuming a negligible contribution of VO_2 in the photocatalytic mechanism [230,233].

The mechanism of photocatalytic degradation of organic pollutant in the presence of VO_2 based photocatalysts involves the generation of primary ROS (i.e., $HO^{\bullet}$ and $O_2^{\bullet -}$) by reaction of water and oxygen with photogenerated holes and electrons, respectively [229]. These strong oxidizing radicals are the main reactive species in the mineralization of organic contaminants. In addition, in the case of VO_2(B)/CeO_2, CeO_2 plays the role of an electron trap, thus, the photogenerated e^- are accumulated in there, that improves the e^-/h^+ pairs separation [229]. It is also plausible that CeO_2 induces Fenton-type reactions which would explain the excellent efficiency of this composite photocatalyst. For VO_2(M)/ZnO photocatalyst, photocorrosion of ZnO was expected (Equation (36)) but in this type-II hetrojunction, the photogenerated holes are accumulated in VO_2 while electrons are transferred to ZnO, thus, reducing the photocorrosion and limiting the recombination of e^-/h^+ pairs [231].

$$ZnO + 2h^+ \rightarrow Zn^{2+} + 1/2O_2 \quad (36)$$

Vanadium dioxide can be also combined with ternary oxides such as silver vanadate (Ag_3VO_4) [232]. VO_2/Ag_3VO_4 composite prepared by hydrothermal method exhibits efficient utilization of both UVA and visible light (at $\lambda < 420$ nm) since about 73% of Rhodamine B is removed after 90 min irradiation time. The reproducibility and stability of this composite is also stable. To explain the excellent photocatalytic efficiency of VO_2/Ag_3VO_4, VO_2 is ascribed as the key component, since in this composite, it acts as electron trap, thus improving the e^-/h^+ pairs separation [232].

Mixed Valence Vanadium Oxides

Mixed valence vanadium oxides are attractive materials for many applications. Among these oxides, V_4O_9 and V_6O_{13} are the most investigated in photocatalytic applications. One of the first works about the photocatalytic properties of such bynary vanadium oxides appeared in 1990 where the photo-induced degradation of isopropanol was 2.5-fold enhanced under UV-visible light [234]. Indeed, V_2O_5 is already a good photocatalyst in the degradation of organic contaminants, but the amount of electronic defects (i.e., the presence of V^{4+} at V_2O_5 surface) is assumed to play a key role in the photocatalytic efficiency. Thus, by extending this hypothesis, vanadium oxides of mixed V (IV) and V (V) should exhibit improved photocatalytic properties [234,235]. Although such oxides are promising, they are much less studied than V_2O_5 and VO_2 [236]. Usually V_4O_9 and V_6O_{13} are synthesized from V (V) precursors such as V_2O_5 and NH_4VO_3 which are reduced by heat treatment in either vacuum or reducing atmosphere [234–236].

V_6O_{13} is probably the most documented mixed valence vanadium oxides [234–236]. This photocatalyst can oxidize completely 3-hexanol under visible light ($\lambda = 460$ nm) while in the dark or using photo-activated VO_2 and V_2O_5, the degradation of this alcohol is negligible [236]. In addition, the photocatalytic degradation of primary alcohols including 1-pentanol, 1-hexanol, 1-octanol, 1-nonanol, and 1-decanol is also efficient using V_6O_{13} photocatalyst. It is worth noting that this photocatalytic degradation is selective since about 70% of the alcohols is oxidized in aldehyde [236]. Furthermore, the photocatalytic degradation of secondary alcohols using V_6O_{13} leads to more than 70% selectivity in the formation of ketones. V_6O_{13} photocatalyst can also efficiently degrade saturated hydrocarbons, especially aromatics, such as xylene and toluene [236]. In the form of a composite,

V_6O_{13} is also an efficient photocatalyst [235]. Indeed, VO_2/V_6O_{13} can remove organic contaminants, such as atrazine and methylene blue under visible light with an excellent reproducibility after repeated runs, thus indicating the stability of the photocatalyst. This photoactive nanostructured VO_2/V_6O_{13} is able to completely mineralize atrazine after 2 h irradiation while 75% of methylene blue can be degraded within 1 h, which is significantly better than V_2O_5 and VO_2 photocatalysis [235]. The VO_2/V_6O_{13} exhibits high specific surface area (about 25 $m^2 \cdot g^{-1}$) and an energy band gap of 2.4 eV. It is worth noting that, in the VO_2/V_6O_{13}, the band structure is modified due to the formation of heterojunction, thus extending the light absorption in the visible part of the spectrum [235].

Concerning the degradation mechanisms, the presence of V (IV) leads to the formation of oxygen vacancies which (i) enhanced the adsorption of the organic molecule at the surface of the material and (ii) improved the e^-/h^+ pairs separation [234]. The photo-induced generation of primary ROS such as hydroxyl and superoxide radicals operates more efficiently due to the presence of V (IV) at the surface of the photocatalyst [234]. An alternative mechanism of photocatalytic degradation of organic molecules proceeds via chemisorption of the contaminant onto the surface of the material followed by excitation of the V-O-C bonding [236]. This phenomenon causes the elimination of protons in alpha position, and ultimately to the production of byproducts. This mechanistic scheme is different from the conventional photocatalytic mechanism [236]. In composite photocatalyst like VO_2/V_6O_{13}, the adsorption of organic pollutants at the surface of the material is improved, thus being one reason of the excellent photocatalytic efficiency. In addition, the presence of both V (IV) and V (IV) improves the separation of charge carriers, namely the photogenerated electrons and holes, thus giving rise to higher production of primary reactive oxygen species that lead to the mineralization of organic contaminants into CO_2 and H_2O [235].

Another popular mixed valence vanadium oxide is V_4O_9 [237]. This compound has shown efficient but smaller photo-induced properties than V_6O_{13}. Indeed, V_4O_9 photocatalyst can degrade Rhodamine B under visible light with a removal extent of 45% after 3 h irradiation. The energy band gap of V_4O_9 is about 2.13 eV. It is also interesting to note that this mixed valence oxide is not often mentioned in the literature as a photocatalyst for several reasons. The first one is that V_4O_9 has similar photocatalytic efficiency as V_2O_5 which is easier to prepare. The second one is the similar crystalline structure between V_2O_5 and V_4O_9 which both have an orthorhombic system, thus resulting in very similar diffractions during the characterization by XRD [237]. Consequently, it is plausible that V_4O_9 has been confused with V_2O_5. The mechanism of photocatalytic degradation of organic pollutants using V_4O_9 exhibits predominant role of superoxide radicals and photogenerated holes [237].

4.2.3. Ternary Vanadium Oxides

Bismuth Vanadates

Among ternary vanadium oxides based on vanadium, $BiVO_4$ is probably the most studied one due to bismuth which broadens the response of the material in the visible light, thus increasing its applicability for photocatalysis under sunlight. In addition, $BiVO_4$ is stable and non-toxic which highlight its environmental compatibility [149,238]. Bismuth vanadate exists in three polymoprhs (Section 2.1) where the monoclinic scheelite phase is the most photocatalytically efficient [33]. Indeed, it is a promising visible light driven semiconductor photocatalyst which is mainly investigated in suspended systems and supported materials. The latter is more convenient for environmental applications since the immobilization of the photocatalyst on supports such as glass and polymer is beneficial for post-treatment separation [33]. $BiVO_4$ with different morphologies can be designed using wet chemical methods, especially hydrothermal techniques [238]. By this mean, different hierarchical structures can be prepared by varying experimental conditions including pH, temperature, type of precursor, and presence of structure directing agent [238,239]. Prior to develop the applications of $BiVO_4$ in photo-induced processes for the degradation

of organic pollutants, it is worth mentioning that the photocatalytic efficiency in the degradation of organic pollutants differs from one work to another. These differences are due to the way of synthesis of $BiVO_4$, the type of incident radiation and the kind of targeted pollutant [33].

Most of the literature is devoted to the degradation of organic dyes. Although they are not considered as suitable model pollutants, organic dyes are environmentally relevant contaminants and they provide an overview on the feasibility of the tested material in the removal of organic pollutants. Nanostructured $BiVO_4$ with 1D and 2D morphology can degrade up to 93% of methylene blue and 86% of methyl orange after 60 and 150 min visible light irradiation, respectively. In addition, $BiVO_4$ nanotubes are able to completely remove Rhodamine B after only 15 min irradiation. These excellent removal extents are mainly ascribed to the high specific surface area which is ranging from 5 to 45 $m^2 \cdot g^{-1}$ for such nanostructures. These values are considerably higher than those of bulk $BiVO_4$ (about 0.5 $m^2 \cdot g^{-1}$) [238]. The high specific surface area is associated with the increase of active site number and better adsorption properties. Furthermore, the recombination rate between e^-/h^+ pairs is smaller than in bulk structure due to better transfer of charge carriers at the surface (i.e., shorter pathway resulted from smaller particle size) [238]. Other structures such as hierarchical ones are also efficient in the degradation of organic pollutants. For example, denditric, hollow sphere and olive-like $BiVO_4$ can degrade under visible light more than 80% of a wide range of organic dyes (e.g., Rhodamine B and methylene blue) after short irradiation times [238]. Like 1D and 2D nanostructured $BiVO_4$, the main advantage of hierarchical structures is their high specific surface area (higher than 2 $m^2 \cdot g^{-1}$) [238].

Since the decolorization of organic dyes provides only basic knowledge of the feasibility of the photocatalytic reactions using recent materials, deeper insights into $BiVO_4$ mediated photo-induced processes for the removal of organic contaminants are required [33]. To this end, two strategies are possible: (i) the study of the degradation pathway and mineralization extent of organic dyes; and (ii) the use of uncolored model pollutants in order to avoid self-sensitization process (i.e., in order to study the intrinsic properties of the photoactive material). The mineralization of the contaminants is crucial since incomplete removal could lead to more toxic intermediate byproducts [33]. Concerning the first strategy, total organic carbon and mass spectrometry studies have shown that $BiVO_4$ is able to mineralize 65% of methylene blue under visible light while the intermediate degradation products are composed of hydroxylated aromatics [33]. In addition, the complete removal of Rhodamine B by the visible light driven $BiVO_4$ photocatalyst is associated to only 40% mineralization extent after 100 h irradiation time [240]. The degradation of Rhodamine B follows two main pathways which are the deethylation process and the removal of the chromophore since the identified intermediates are ethylbenzene, xylene, etc. [240]. Concerning the second strategy, pharmaceutical compounds are often used such as ibuprofen (IBP) and ciprofloxacin (CIP) [241,242]. Indeed, under UVA light, $BiVO_4$ can degrade about 90% of IBP and 65% of CIP. $BiVO_4$ photocatalyst is also efficient in the degradation of phenolic compounds such as nonyl- and octyl-phenols which are well known endocrine disruptor compounds [243]. In this latter case, the alkyl chain of the phenolic compounds plays the role of an anchor on the surface of $BiVO_4$, thus improving its adsorption onto the surface of the photocatalyst and improving the degradation reaction. Apart from aqueous pollutants, $BiVO_4$ can also degrade contaminants in gaseous phase including isopropyl alcohol and nitrogen oxides [244,245]. For instance, under visible light, $BiVO_4$ is able to convert 25% of N_2O after 12 h irradiation time. To improve the photocatalytic efficiency of $BiVO_4$, besides doping and preparation of composite, an interesting strategy is to use simultaneously different contaminants which are removed by reduction and oxidation processes. Indeed, the case of dual phenol and chromium (VI) pollution can be efficiently treated using $BiVO_4$ since phenol can be oxidized and mineralized into CO_2 and H_2O while Cr (VI) can be reduced in Cr (III) (which is much less toxic) [246]. Concretely, after 3 h irrdiation time under visible light, complete removal of Cr (VI) is achieved and 60% of phenol is mineralized by the $BiVO_4$ photocatalysis. For comparison, at similar experimental condition and using

phenol alone, only 10% of the pollutant is completely removed. Another interesting strategy to enhance the photocatalytic ability of $BiVO_4$ is to prepare or anneal the material in reducing atmosphere (H_2) in order to generate oxygen vacancies which improve the charge carrier transport, thus resulting in better photocatalytic efficiency [247]. Under visible light, hydrogenated $BiVO_4$ can degrade up to 98% of tetracycline which is significantly higher than the 52% achieved using pristine $BiVO_4$.

The mechanism of degradation of organic pollutants using $BiVO_4$ is crucial and several contradictions are present in the literature. Indeed, the identification of the main reactive oxygen species gives rise to different results from one work to another. Some researchers have stated the main ROS are hydroxyl radicals while other ones have found the main contribution in organic pollutant degradation is from superoxide radicals. These differences are due to misinterpretation of results that arises from unreliable employed method to identify the primary ROS such as the scavenging method. Therefore, more sophisticated methods should be employed like for instance the electron paramagnetic resonance (EPR). By EPR, it has been proven that $BiVO_4$ photocatalytically generates neither hydroxyl radicals nor superoxide radicals [248]. Indeed, the theoretical band structure of monoclinic scheelite $BiVO_4$ (at normal conditions) exhibits a conduction band minimum and valence band maximum of 0 V and 2.4 V vs. NHE, respectively (Figure 19). Therefore, the redox potential for the formation of primary ROS, i.e., $E^0(O_2/O_2^{\bullet -})$ and $E^0(OH^{\bullet}/H_2O)$ are not within the energy band gap of $BiVO_4$, thus, the production of these radicals is thermodynamically not favored [33,198,239,248].

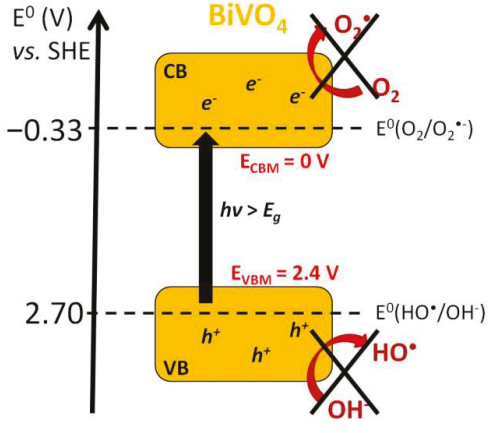

Figure 19. Energy diagram of the band structure of $BiVO_4$ photocatalyst.

However, why $HO^{\bullet}$ is often detected in $BiVO_4$ photocatalytic systems? One reason is the pH value of the reaction system. The theoretical band structure of $BiVO_4$ is for pH = 0 while in practice, the pH is so-called natural. Therefore, an increase of pH leads to a shift of the bands toward negative values, thus allowing the formation of superoxide radicals. These $O_2^{\bullet -}$ can be converted into $HO^{\bullet}$ via the generation of H_2O_2 during the photocatalytic process according to the chemical reaction (Equations (21) and (37)) [240,241,249]. It is worth noting that even at natural pH, the generation of hydroxyl radicals by photogenerated holes from $BiVO_4$ is even less favored [241].

$$O_2^{\bullet -} + 2H^+ + e^- \rightarrow H_2O_2 \quad (37)$$

The second reason is when organic dyes are used. In this case, sensitization of $BiVO_4$ occurs by transfer of electrons from the excited state of the dye to the conduction band of the photocatalyst (Equations (38) and (39)). Therefore, the resulted improvement of the

photocatalytic process is not due to the intrinsic photo-induced properties of $BiVO_4$. Indeed, the injected electrons in the $BiVO_4$ react with oxygen to produce superoxide radicals, thus following the reaction scheme above (Equations (18), (19), (33)–(35) and (37)), i.e., the generation of H_2O_2 and subsequently $HO^\bullet$ [240].

$$RhB + h\nu \rightarrow RhB^* \quad (38)$$

$$BiVO_4 + RhB^* \rightarrow RhB^{\bullet +} + BiVO_4(e^-) \quad (39)$$

The production of hydroxyl radicals is strongly dependent of the pH which is the key factor. Some researchers stated that the generation of hydroxyl radicals from superoxide radicals is favored at low pH while other scientists discussed that the alkaline pH might be more favorable due to the presence of OH^-, which is easily convertible into $HO^\bullet$ by reaction with photogenerated holes. However, the latter case has been demonstrated to be thermodynamically not feasible. Although $BiVO_4$ is a promising photocatalyst for environmental remediation, further studies are required to develop its application for degradation of a wider range of contaminants and to clear out the uncertainties of its degradation mechanism.

Other bismuth vanadates such as $Bi_4V_2O_{11}$ and $Bi_8V_2O_{17}$ are also used as visible light driven photocatalysts [250,251]. The preparation methods of these materials are similar to that for $BiVO_4$, thus $BiVO_4$ is often present as impurity, i.e., pure mixed valence bismuth vanadate is not easily prepared. However, their use in the removal of organic pollutants is efficient under visible light. For instance, $BiVO_4/Bi_4V_2O_{11}$ can be efficiently degrade and mineralize sulfamethazine with degradation and mineralization extents of 95% and 50%, respectively [250]. The main primary ROS are identified as superoxide radicals.

Iron Vanadates

Iron vanadates, especially $FeVO_4$, are interesting materials for the photo-induced degradation of organic pollutants. Indeed, due to their semiconducting properties and the presence of iron, both photocatalytic and photo-Fenton processes can be triggered using these photoactive materials. Although iron vanadates are gaining stronger interest within the photochemical community, few works on pure single phase are reported, thus, composite materials based on iron vanadates are also discussed in this section.

$FeVO_4$ is a semiconductor with an energy band gap of about 2.15 eV, thus absorbing visible light [156]. The conduction band minimum is positioned at −0.65 eV while the valence band maximum is at 1.50 eV. $FeVO_4$ can be synthesized by wet chemical methods using iron nitrate and ammonium metavanadate as precursors, and structure-directing agents (e.g., PEG and PVP) to design a particular morphology [132,156]. According to the morphology, the E_g varies from 2.1 to 3.0 eV where nanostructures exhibit higher energy band gap than bulk ones [132,156,252–254]. The specific surface area is found to vary between 15 and 30 $m^2 \cdot g^{-1}$ [132,254]. $FeVO_4$ photocatalysts are efficient for the removal of organic dyes under UVA light with removal extents of about 90% for Rhodamine B and 50% for phenol red after 300 min and 120 min irradiation time, respectively [156,252,254]. However, under visible light, the photocatalytic efficiency is lower [156,254]. Indeed, about 70% of Rhdomaine B can be degraded after 5 h irradiation time with less than 10% mineralization rate [151,156,253,254].

Due to the presence of iron in the material, $FeVO_4$ can also triggered Fenton-type reactions. For instance, in the presence of H_2O_2, the degaradtion of Rhodmaine B is almost completed under visible light [254]. Compared to classical heterogeneous Fenton catalysts such as hematite (α-Fe_2O_3), magnetite (Fe_3O_4), and goethite (γ-FeOOH), $FeVO_4$ is able to efficiently activate H_2O_2 into hydroxyl radicals with the removal of more than 90% of methyl orange after 1 h reaction [152]. Under visible light, photo-Fenton is also triggered by $FeVO_4$ with subsequent activation of peroxymonosulfate (HSO_5^-) into sulfate radicals ($SO_4^{\bullet -}$), thus leading, after 1 h of irradiation time, to the degradation of 96% of sulfamethoxazole, an antibiotic substance often detected in wastewater effluents [255].

However, the performance of this photo-induced process is rather low due to weak photolysis rates for iron and vanadium and unstable cycle between high and low valences species, i.e., Fe(III)/Fe(II) and V(V)/V(IV) [255].

Therefore, composite materials based on $FeVO_4$ can be prepared to increase the efficiency of the photo-induced processes. $ZnO/FeVO_4$ material triggers simultaneously, under UVA light and in the presence of H_2O_2, photocatalytic and Fenton processes with synergetic efficiency, thus achieving 93% degradation extent of sodium dodecyl sulfate within 1 h [256]. Similarly, $FeVO_4/CeO_2$ is also a material combining photocatalytic and photo-Fenton processes which are efficient in the removal of 4-nitrophenol [257]. In this case, the contribution of Fenton reaction, i.e., measured in the dark with the presence of hydrogen peroxide, has led to a 9% degradation extent after 1 h reaction while with both visible light and H_2O_2, the removal extent reached 94% [257]. In addition, such photoactive materials can be reused since efficiency after repeated runs is stable while the photo-induced processes, especially the Fenton reaction, do not required highly acidic conditions to be efficient. These multi-photoactive materials are efficient in the treatment of real wastewaters, thus highlighting their potential applications at industrial level [256]. On the other hand, many $FeVO_4$ based composites are studied regarding only the photocatalytic process without taking into account the potential contribution of the photo-Fenton process. $FeVO_4/V_2O_5$, $FeVO_4/BiVO_4$, and $FeVO_4/Fe_2O_3$ are interesting composites which have exhibited excellent photocatalytic activity in the removal of many organic dyes, including Rhodamine B, phenol red, methyl violet, and methylene blue [133,258,259]. In such composites, direct Z-scheme or type-II heterojunction (Figure 12 in Section 3.2.3) improves the e^-/h^+ pair separation, thus the photogenerated charge carriers react more efficiently (for the formation of ROS), but also enhances the absorption of visible light (i.e., a shift of the E_g toward shorter wavelengths). Compared to the single components, the use of composite photocatalysts under either UVA or visible light irradiation leads to an increase in the removal extents of organic pollutants from +10% to +80% according to the experimental conditions [133,258,259].

Concerning the photo-induced mechanisms for the degradation of organic pollutants, the photocatalytic and photo-Fenton are both involved. For photocatalysis using pure $FeVO_4$, the band structure of this semiconductor allows the formation of superoxide radicals from the reaction of dissolved oxygen with the photogenerated electron since $E^0(O_2^{\bullet-}/O_2)$ is situated within the energy band gap of $FeVO_4$. The photogenerated holes cannot produce hydroxyl radicals since $E^0(H_2O/HO^{\bullet})$ is more positive than the valence band maximum [132]. However, the h^+ can oxidize water to produce hydrogen peroxide (Equation (40)) which, subsequently, reacts with e^- to produce hydroxyl radicals (Equation (21)) [156]. The production of H_2O_2 following this reaction path is not significant in the presence of an organic dye due to the photo-sensitization process (Equations (38) and (39)). Therefore, $O_2^{\bullet-}$ is the main primary ROS in the degradation of organic contaminants.

$$2H_2O + 2h^+ \rightarrow H_2O_2 + 2H^+ \quad (40)$$

In $FeVO_4$ composites, the choice of the second component is crucial. In $FeVO_4/CeO_2$, the CBM of $FeVO_4$ and CeO_2 are −0.45 eV and −0.32 eV, respectively, and their VBM are at 1.55 eV and 2.45 eV [257]. Therefore, under UVA, the photogenerated e^- are accumulated in the CB of CeO_2 while h^+ are transferred in the VB of $FeVO_4$, thus defining the principle of the type-II heterojunction with increase of charge carriers' lifetime (Figure 12 in Section 3.2.3). If $FeVO_4$ is decorated by CeO_2, the latter acts rather as an electron scavenger, thus also enhancing the e^-/h^+ pair separation. Once the surface Ce (IV) trapped an electron, the reduced Ce (III) is an efficient ion for the generation of superoxide radicals from dissolved O_2 [257]. Therefore, the use of CeO_2 with its Ce^{3+}/Ce^{4+} cycle is an efficient method to improve the photocatalytic efficiency of $FeVO_4$ for the degradation of organic compounds. Additionally, a type-II heterojunction, direct Z-scheme like $FeVO_4/Fe_2O_3$ works on the same principle: to limit the charge carrier recombination. In a direct Z-scheme, the mechanism could be viewed as an "extreme" type-II heterojunction but with

the energetic level of CBM of the first component close to that of the VBM of the second component (Figure 12 in Section 3.2.3). In $FeVO_4/Fe_2O_3$, under incident light of suitable energy, the photogenerated electrons and holes in the CB of $FeVO_4$ and VB of Fe_2O_3 can react rapidly to generate primary ROS since the e^- and h^+ in the CB of Fe_2O_3 and VB of $FeVO_4$ are combined fastly. This direct Z-scheme mechanism was confirmed by scavenging experiments, where the main active species for the degradation of organic pollutants are identified as $HO^\bullet$ and h^+ (Figure 20). Indeed, such results could not be observed in the case of a type-II heterojunction mechanism, where the configuration would lead to the inability to generate any primary ROS (Figure 20) [259].

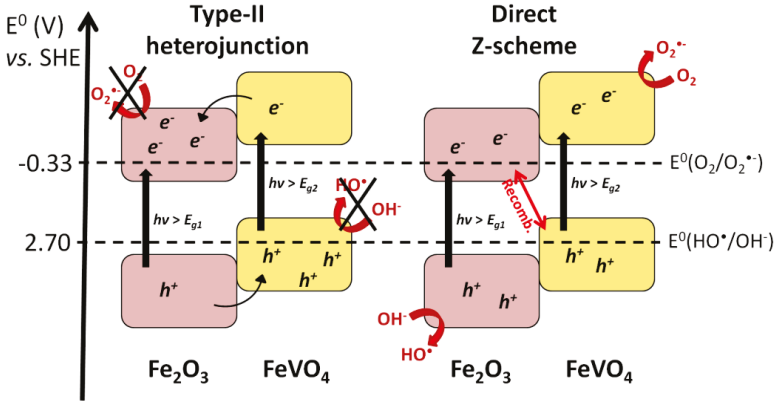

Figure 20. The band structure of $FeVO_4/Fe_2O_3$ composite and the generation of primary ROS following either a type-II heterojunction or a direct Z-scheme mechanism.

The photo-Fenton mechanism, in presence of H_2O_2 and $FeVO_4$, occurs by following a two-way reaction scheme [152,257]. Indeed, the activation of hydrogen peroxide into peroxyl radicals is performed using surface iron (III) and vanadium (V) according to the Fenton-like reactions (Equations (24) and (42)). Subsequently, the reduced species, i.e., Fe (II) and V (IV) generate hydroxyl radicals (Equations (23) and (41)). These Fenton-type pathways are still the matter of discussion within the photochemical community since the use of light irradiation could play a preponderant role [152]. Indeed, since the Fenton-like reaction are slower than Fenton reactions, the recycling of iron and vanadium species is slow, thus requiring the presence of incident light which could increase the photolysis of Fe (III) and V (V) into reduced species [152,255]. The main active species during the degradation of organic contaminants using $FeVO_4/H_2O_2$/light system are $HO^\bullet$ [152,255]. In addition, the generation of hydroxyl radicals increases by increasing the amount of surface vanadium (V) [152]. It is worth noting that instead of H_2O_2, peroxymonosulfate (HSO_5^-) could be used to generate other efficient radicals for the degradation of organic pollutants: the sulfate radicals ($SO_4^{\bullet-}$) [255]. The production of the sulfate radicals (Equation (43)) could also lead to the generation of hydroxyl radicals by reaction with hydroxide anions (Equation (44)). In addition, singlet oxygen which is an excellent oxidant could be formed in such a photochemical system (Equations (45) and (46)) [255]. From these reactions, it is clear that there is a synergy with the photocatalytic process since photogenerated electrons are involved in several crucial reaction steps. In the form of a composite, especially $FeVO_4/CeO_2$, a third reaction pathway appears [152,257]. Indeed, surface Ce (IV) in CeO_2 can activate Fenton-type processes (Equations (29) and (30)), thus generating hydroxyl radicals [257].

$$\equiv V^{IV} + H_2O_2 \rightarrow \equiv V^{V} + OH^- + HO^\bullet \quad (41)$$

$$\equiv V^{V} + H_2O_2 \rightarrow \equiv V^{IV} + H^+ + HOO^\bullet \quad (42)$$

$$Fe^{2+}/V^{4+} + HSO_5^- \rightarrow SO_4^{\bullet -} + OH^- + Fe^{3+}/V^{5+} \quad (43)$$

$$SO_4^{\bullet -} + OH^- \rightarrow SO_4^{2-} + HO^{\bullet} \quad (44)$$

$$HSO_5^- + SO_5^{\bullet -} + e^- \rightarrow HSO_4^- + SO_4^{2-} + {}^1O_2 \quad (45)$$

$$2SO_5^{\bullet -} + H_2O \rightarrow 3/2\,{}^1O_2 + 2HSO_4^- \quad (46)$$

Regarding the combined photo-induced processes in $FeVO_4$ based systems, most of the published works referred to addition of H_2O_2 which requires the use of chemical and potentially increases the cost of implementation (or scale up) of such a photo-induced process for the removal of organic contaminants. Therefore, a key point in the research of simultaneously combined photocatalytic and photo-Fenton processes is to focus on in situ generation of H_2O_2 and to study the contribution of each involved process and their potential synergy.

On the other hand, other iron vanadates are gaining stronger interest in the photochemical community. It is the case of $Fe_2V_4O_{13}$ which is a visible light driven photocatalyst with an energy band gap in the range of 2.2–2.8 eV [260,261]. The energy levels of conduction band minimum and valence band maximum are −2.05 eV and 0.15 eV, respectively [261]. Therefore, the photoctalytic reduction ability of $Fe_2V_4O_{13}$ is relatively strong. Indeed, this iron vanadate is able to remove Cr (VI) by reduction reaction using photogenerated electrons (Equation (47)) [260]. The conversion extent of Cr (VI) into non-toxic Cr (III) reaches up to 98% which is significantly higher than that in presence of TiO_2 (about 40%). The performance of $Fe_2V_4O_{13}$ can be also ascribed to its higher specific surface area [260,261].

$$Cr_2O_7^{2-} + 14H^+ + 6e^- \rightarrow 2Cr^{3+} + 7H_2O \quad (47)$$

In the form of composite, $Fe_2V_4O_{13}/ZnO$ can degrade 90% of methyl orange under simulated solar light [261]. This enhanced removal extent compared to pristine $Fe_2V_4O_{13}$ is due to the formation of a type-II heterojunction where, under light irradiation, the photogenerated electrons are accumulated in the conduction band of ZnO while h^+ are transferred into the valence band of $Fe_2V_4O_{13}$. Since the CBM of ZnO in this system is at −0.35 eV, the production of superoxide radicals is favored. However, the VBM are not enough positive to allow the production of hydroxyl radical by reaction with the photogenerated holes. Furthermore, the h^+ has weak oxidation ability to directly degrade the organic dye and, therefore, the main primary ROS are $O_2^{\bullet -}$.

$Fe_2V_4O_{13}$ can also act as a multi-Fenton catalyst. Similar to $FeVO_4$, a two way reaction scheme occurs in the presence of H_2O_2 which is activated into reactive oxygen species as described above (Equations (23), (24), (41), and (42)). Therefore, $Fe_2V_4O_{13}$ can degrade more than 90% of methyl orange associated with a mineralization extent of 40% [159]. The mechanism involves the cycle of redox couples Fe(III)/Fe(II) and V(V)/V(IV). By comparison with $FeVO_4/V_2O_5$ and Fe_2O_3/V_2O_5 systems where two compounds are combined, the best results are achieved using $Fe_2V_4O_{13}$, thus highlighting a synergy in the Fenton activity induced by iron and vanadium species [159]. $Fe_2V_4O_{13}$ has been also tested in the degradation of real wastewater effluents spiked by organic dyes. As expected, a decrease of efficiency is observed compared to synthetic wastewater (removal extent < 50%) due to the consumption of H_2O_2 by the organic matter which is present in higher extents [159].

Finally, another interesting iron vanadate is FeV_3O_8. This materials is a semiconductor which is a promising visible light driven photocatalyst (E_g = 2.23 eV) [163]. Indeed, depending on its morphology, the specific surface area can reach more than 150 $m^2 \cdot g^{-1}$ (for ultrathin nanostructured material), thus giving rise to good adsorption properties. In addition, under visible light, FeV_3O_8 can remove up to 92% of methyl orange after only 30 min irradiation time [163]. In such a photoactive system, the main primary ROS are identified as both superoxide and hydroxyl radicals, but further studies are required to confirm this observation since the exact role of photogenerated holes are not clearly elucidated.

Other Transition Metal Vanadates

Among the other transition metal vanadates, the most promising ones are summarized in the Table 2. These ternary oxides are semiconductor photocatalysts which could be activated either under visible or UVA light. Although they are promising materials, their use in photo-induced processes for the removal of organic contaminants are far less documented than bismuth and iron vanadates. In addition, these atypic vanadates are often coupled with another oxide to form a composite. Therefore, deeper research is necessary to elucidated the photocatalytic mechanism (of both pure and composite materials) and to highlight potentially other photo-induced processes like the Fenton-type reactions which probably occur in metal vanadates based on Ce, Cu, and Mn.

Table 2. Overview of different transition metal vanadate in the photo-induced degradation of organic pollutants.

System	E_g (eV)	Pollutant	Incident Irradiation	Degradation Extent	Ref.
ZnV_2O_4	2.1	CO_2	Visible light	~80% conversion into CO	[262]
$AgVO_3/BiVO_4$	2.32–2.43	Rhodamine B	Visible light	93% after 120 min	[263]
$CeO_2/CeVO_4/V_2O_5$	2.26–2.93	Methylene blue	Visible light	93% after 4 h (189 μmol of produced H_2)	[264]
$Ag_4V_2O_7/BiVO_4$	2.36–2.41	Methylene blue and NO	Visible light	98% for MB and 53% for NO after 30 min	[265]
$Cu_3V_2O_7(OH)_2{\cdot}2H_2O$	2.1	Methylene blue	Visible light	~90% after 150 min	[266]
$Cu_3V_2O_8$	-	Methyl orange	UVA light	72% after 100 min	[267]
$Cu_2V_2O_7$ (+H_2O_2)	2.17	Evans blue	UVA light	77% after 120 min	[268]
$Cu_2V_2O_7$/g-C_3N_4	2.0–2.7	CO_2	Visible light	-	[167]
$Cu_3V_2O_8$	2.05–2.10	Methyl orange	UVA light	78% after 120 min	[135]
$Mn(VO_3)_2$	3.05	Methyl orange	UVA light	84% after 80 min	[181]
$Mn_2V_2O_7$	2.79	Methylene blue	Solar light	90% after 4 h	[179]

5. Conclusions

Binary and ternary vanadium oxides in single and mixed valence states are promising materials for environmental applications. Based on the versatile behaviour of vanadium, the electronic and optical properties of semiconducting vanadium oxides can be tuned, thus giving rise to interesting photo-induced properties. Therefore, vanadium oxide-based materials can trigger photochemical processes for the environmental purposes including the splitting of water for hydrogen production and the photocatalytic and photo-Fenton processes for the removal of organic pollutants in water. Such problematics are highly relevant for the current and next generations. This review article provides a useful tool for scientific research and pedagogical knowledge where the comprehensive description of the structure and intrinsic properties of vanadium oxides are related to their photochemical efficiency in environmental processes.

Author Contributions: Conceptualization, writing: original draft preparation, writing: review and editing, supervision, O.M.; writing: original draft preparation, writing: review and editing, P.P. All authors have read and agreed to the published version of the manuscript.

Funding: This research received no external funding.

Institutional Review Board Statement: Not applicable.

Informed Consent Statement: Not applicable.

Data Availability Statement: No new data were created or analyzed in this study. Data sharing is not applicable to this article.

Conflicts of Interest: The authors declare no conflict of interest.

References

1. Weeks, M.E. The Discovery of the Elements. VII. Columbium, Tantalum, and Vanadium. *J. Chem. Educ.* **1932**, *9*, 863–884. [CrossRef]
2. Gustafsson, J.P. Vanadium geochemistry in the biogeosphere speciation, solid-solution interactions, and ecotoxicity. *Appl. Geochem.* **2019**, *102*, 1–25. [CrossRef]
3. Safstrom, N.G. Sur Le Vanadium, Métal Nouveau, Trouvé Dans Du Fer En Barres De Eckersholm, Forge Qui Tire Sa Mine De Taberg, Dans Le Smaland. *Ann. Chim. Phys.* **1831**, *46*, 105–111.
4. Baharum, H.; Chu, W.C.; Teo, S.S.; Ng, K.Y.; Rahim, R.A.; Ho, C.L. Molecular cloning, homology modeling and site-directed mutagenesis of vanadium-dependent bromoperoxidase (GcVBPO1) from Gracilaria changii (Rhodophyta). *Phytochemistry* **2013**, *92*, 49–59. [CrossRef] [PubMed]
5. Adriano, D.C. *Trace Elements in the Terrestrial Environment*; Springer: New York, NY, USA, 1986; pp. 470–501.
6. Moskalyk, R.R.; Alfanti, A.M. Processing of vanadium: A review. *Miner. Eng.* **2003**, *16*, 793–805. [CrossRef]
7. Imtiaz, M.; Rizwan, M.S.; Xiong, S.; Li, H.; Ashraf, M.; Shahzad, S.M.; Shahzad, M.; Rizwan, M.; Tu, S. Vanadium, recent advancements and research prospects: A review. *Environ. Int.* **2015**, *80*, 79–88. [CrossRef] [PubMed]
8. Baroch, E.F. Vanadium and vanadium alloys. In *Kirk-Othmer Encyclopedia of Chemical Technology*; Wiley: New York, NY, USA, 2013; pp. 1–18.
9. Liu, M.; Su, B.; Tang, Y.; Jiang, X.; Yu, A. Recent Advances in Nanostructured Vanadium Oxides and Composites for Energy Conversion. *Adv. Energy Mater.* **2017**, *7*, 1700885. [CrossRef]
10. Rehder, D. The potentiality of vanadium in medicinal applications. *Future Med. Chem.* **2012**, *4*, 1823. [PubMed]
11. World Health Organization. International Programme on Chemical Safety, Environmental Health, Criteria 61, Vanadium. Available online: http://www.inchem.org/documents/ehc/ehc/ehc81.htm (accessed on 26 December 2020).
12. Korbecki, J.; Baranowska-Bosiacka, I.; Gutowska, I.; Chlubek, D. Biochemical and medical importance of vanadium compounds. *Acta Biochim. Pol.* **2012**, *59*, 195. [CrossRef]
13. Barceloux, D.G. Vanadium. *J. Toxicol. Clin. Toxicol.* **1999**, *37*, 265–278. [CrossRef]
14. Rehder, D. Vanadium. Its role for humans. *Met. Ions Life Sci.* **2013**, *13*, 139–169. [PubMed]
15. Wright, M.T.; Belitz, K. Factors controlling the regional distribution of vanadium in groundwater. *Groundwater* **2010**, *48*, 515–525. [CrossRef] [PubMed]
16. Vouk, V.B.; Piver, W.T. Metallic elements in fossil fuel combustion products. *Environ. Health Perspect.* **1983**, *47*, 2111–2225.
17. Miramand, P.; Fowler, S.W. Bioaccumulation and transfer of vanadium in marine organisms. In *Vanadium in the Environment: Part 1. Chemistry and Biochemistry*; Nriagu, S.W., Ed.; Wiley: New York, NY, USA, 1998; pp. 167–169.
18. Kiss, T.; Kiss, E.; Garribba, E.; Sakurai, H. Speciation of insulin-mimetic VO (IV)-containing drugs in blood serum. *J. Inorg. Biochem.* **2000**, *80*, 65–73. [CrossRef]
19. Hansen, T.V.; Aaseth, J.; Alexander, J. The effect of chelating agents on vanadium distribution in the rat body and on uptake by human erythrocytes. *Arch. Toxicol.* **1982**, *50*, 195–202. [CrossRef]
20. Rehder, D. The bioinorganic chemistry of vanadium. Angew. *Chem. Int. Ed. Engl.* **1991**, *30*, 148–167.
21. Granqvist, C.G. Spectrally selective coatings for energy efficiency and solar applications. *Phys. Scr.* **1985**, *32*, 401–407. [CrossRef]
22. Lamsal, C.; Ravindra, N.M. Vanadium Oxides: Synthesis, Properties, and Applications. In *Semiconductors*; Pech-Canul, M., Ravindra, N., Eds.; Springer Nature: Cham, Switzerland, 2019; pp. 127–218.
23. Parker, J.C., Jr.; Geiser, U.W.; Lam, D.J.; Xu, Y.; Ching, W.Y. Optical properties of the vanadium oxides VO_2 and V_2O_5. *J. Am. Ceram. Soc.* **1990**, *73*, 3206–3208. [CrossRef]
24. Chang, T.C.; Cao, X.; Bao, S.H.; Ji, S.D.; Luo, H.J.; Jin, P. Review on thermochromic vanadium dioxide based smart coatings: From lab to commercial application. *Adv. Manuf.* **2018**, *6*, 1–19. [CrossRef]
25. Azenha, E.; Romeiro, A.; Sarakha, M. Photodegradation of pesticides and photocatalysis in the treatment of water and waste. In *Applied Photochemistry*; Evans, R.C., Douglas, P., Burrows, H.D., Eds.; Springer: Dordrecht, The Netherlands, 2013; pp. 247–266.
26. Gaya, U.I. *Heterogeneous Photocatalysis Using Inorganic Semiconductor Solids*; Springer: Dordrecht, The Netherlands, 2014.
27. Hinojosa-Reyes, L.; Guzman-Mar, J.L.; Villanueva-Rodriguez, M. Semiconductormaterials for photocatalytic oxidation of organic pollutants in wastewater. In *Photocatalytic Semiconductors*; Hernandez-Ramirez, A., Medina-Ramirez, I., Eds.; Springer: Cham, Switzerland, 2015; pp. 187–228.
28. Larsson, D.G.J. Pollution from drug manufacturing: Review and perspectives. *Philos. Trans. R. Soc. B* **2014**, *369*, 71–78. [CrossRef]
29. Sauvé, S.; Desrosiers, M. A review of what is an emerging contaminant. *Chem. Cent. J.* **2014**, *8*, 15–21. [CrossRef] [PubMed]
30. Deblonde, T.; Cossu-Leguille, C.; Hartemann, P. Emerging pollutants in wastewater: A review of the literature. *Int. J. Hyg. Environ. Health* **2011**, *214*, 442–448. [CrossRef] [PubMed]
31. Bolong, N.; Ismail, A.F.; Salim, M.R.; Matsuura, T. A review of the effects of emerging contaminants in wastewater and options for their removal. *Desalination* **2009**, *239*, 229–246. [CrossRef]

32. Petrie, B.; Barden, R.; Kasprzyk-Hordern, B. A review on emerging contaminants in watewaters and the environment: Current knowledge, understudied areas and recommendations for future monitoring. *Water Res.* **2015**, *72*, 3–27. [CrossRef] [PubMed]
33. Monfort, O.; Plesch, G. Bismuth vanadate-based semiconductor photocatalysts: A short critical review on the efficiency and the mechanism of photodegradation of organic pollutants. *Environ. Sci. Pollut. Res. Int.* **2018**, *25*, 19362–19379. [CrossRef]
34. Langeslay, R.R.; Kaphan, D.M.; Marshall, C.L.; Stair, P.C.; Sattelberger, A.P.; Delferro, M. Catalytic Applications of Vanadium: A Mechanistic Perspective. *Chem. Rev.* **2019**, *119*, 2128–2191. [CrossRef]
35. Cotton, F.A.; Wilkinson, G.; Murillo, C.A.; Bochmann, M. *Advanced Inorganic Chemistry*, 6th ed.; Wiley: New York, NY, USA, 1999.
36. Baess, C.F.; Mesmer, R.E. Hydrolysis of cations. *Ber. Bunsen. Phys. Chem.* **1976**, *81*, 245–246.
37. Livage, J. Hydrothermal Synthesis of Nanostructured Vanadium Oxides. *Materials* **2010**, *3*, 4175–4195. [CrossRef]
38. Sadoc, A.; Messaoudi, S.; Furet, E.; Gautier, R.; Le Fur, E.; Le Pollès, L.; Pivan, J.Y. Structure and stability of VO_2^+ in aqueous solution: A car-parrinello and static ab initio study. *Inorg. Chem.* **2007**, *46*, 4835–4843. [CrossRef]
39. Bouhedja, L.; Steunou, N.; Maquet, J.; Livage, J. Synthesis of polyoxovanadates from aqueous solutions. *J. Solid State Chem.* **2001**, *162*, 315–321. [CrossRef]
40. Thompson, K.H.; Orvig, C. Metal complexes in medicinal chemistry: New vistas and challenges in drug design. *Dalton Trans.* **2006**, 761–764. [CrossRef] [PubMed]
41. Rehder, D. The coordination chemistry of vanadium as related to its biological functions. *Coord. Chem. Rev.* **1999**, *182*, 297–322. [CrossRef]
42. Pessoa, J.C.; Etcheverry, S.; Gambino, D. Vanadium compounds in medicine. *Coord. Chem. Rev.* **2005**, *301–302*, 24–48. [CrossRef] [PubMed]
43. Kanamori, K.; Tsuge, K. Inorganic Chemistry of Vanadium. In *Vanadium Biochemical and Molecular Biological Approaches*; Michibata, H., Ed.; Springer: Dordrecht, The Netherlands, 2012; pp. 3–31.
44. Mukherjee, B.; Patra, B.; Mahapatra, S.; Banerjee, P.; Tiwari, A.; Chatterjee, M. Vanadium—An element of atypical biological significance. *Toxicol. Lett.* **2004**, *150*, 135–143. [CrossRef]
45. Almeida, M.; Filipe, S.; Humanes, M.; Maia, M.F.; Melo, R.; Severino, N.; Silva, J.A.L.; Fraústo da Silva, J.J.R.; Wever, R. Vanadium haloperoxidases from brown algae of the Laminariaceae family. *Photochemistry.* **2001**, *57*, 633–642. [CrossRef]
46. Menon, A.S.; Rau, M.; Ramasarma, T.; Crane, F.L. Vanadate inhibits mevalonate synthesis and activates NADH oxidation in microsomes. *FEBS Lett.* **1980**, *114*, 139–141. [CrossRef]
47. Golden, M.H.; Golden, B.E. Trace Elements: Potential Importance in Human Nutrition with Particular Reference to Zinc and Vanadium. *Br. Med. Bull.* **1981**, *37*, 3731–3736. [CrossRef]
48. Byrne, A.R.; Kosta, L. Vanadium in foods and in human body fluids and tissues. *Sci. Total Environ.* **1978**, *10*, 17–30. [CrossRef]
49. Heinemann, G.; Fichtl, B.; Vogt, W. Pharmacokinetics of vanadium in humans after intravenous administration of a vanadium containing albumin solution. *Br. J. Clin. Pharmacol.* **2003**, *55*, 241–245. [CrossRef]
50. Willsky, G.R.; Chi, L.H.; Godzala, M.; Kostyniak, P.J.; Smee, J.J.; Trujillo, A.M.; Alfano, J.A.; Ding, W.J.; Hu, Z.H.; Crans, D.C. Anti-diabetic effects of a series of vanadium dipicolinate complexes in rats with streptozotocin-induced diabetes. *Coord. Chem. Rev.* **2011**, *255*, 2258–2269. [CrossRef]
51. Thompson, K.H.; Lichter, J.; LeBel, C.; Scaife, M.C.; McNeil, J.H.; Orvig, C. Vanadium treatment of type 2 diabetes: A view to the future. *J. Inorg. Biochem.* **2009**, *103*, 554. [CrossRef] [PubMed]
52. Ray, R.S.; Basu, M.; Ghosh, B.; Samanta, K.; Chatterjee, M. Vanadium, a Versatile Biochemical Effector in Chemical Rat Mammary Carcinogenesis. *Nutr. Cancer.* **2005**, *51*, 184–196. [CrossRef] [PubMed]
53. Ray, R.S.; Rana, B.; Swami, B.; Venu, V.; Chatterjee, M. Vanadium mediated apoptosis and cell cycle arrest in MCF7 cell line. *Chem.-Biol. Interact.* **2006**, *163*, 239–247. [CrossRef]
54. Parasuraman, A.; Lim, M.T.; Menictas, C.; Kazacos, M.S. Review of material research and development for vanadium redox flow battery applications. *Electrochim. Acta* **2013**, *101*, 27–40.
55. Swette, L.; Jalan, V. *Development of Electrodes for the NASA Iron/Chromium Redox System and Factors Affecting Their Performance*; Giner Inc.: Waltham, MA, USA, 1984. Available online: https://ntrs.nasa.gov/api/citations/19850027158/downloads/19850027158.pdf (accessed on 26 December 2020).
56. Savinell, R.F.; Liu, C.C.; Galasco, R.T.; Chiang, S.H.; Coetzee, J.F. Discharge characteristics of a soluble Iron–Titanium battery system. *J. Electrochem. Soc.* **1979**, *126*, 357. [CrossRef]
57. Kioseoglou, E.; Petanidis, S.; Gabriel, C.; Salifoglou, A. The chemistry and biology of vanadium compounds in cancer therapeutics. *Coord. Chem. Rev.* **2015**, *301–302*, 87–105. [CrossRef]
58. Schwendt, P.; Tatiersky, J.; Krivosudsky, L.; Simunekova, M. Peroxido complexes of vanadium. *Coord. Chem. Rev.* **2016**, *318*, 135–157. [CrossRef]
59. Nomura, K.; Zhang, S. Design of Vanadium Complex Catalysts for Precise Olefin Polymerization. *Chem. Rev.* **2011**, *111*, 2342–2362. [CrossRef]
60. Nomura, K.; Zhang, W. (Imido)vanadium(V)-alkyl, -alkylidene complexes exhibiting unique reactivity towards olefins and alcohols. *Chem. Sci.* **2010**, *1*, 161–173. [CrossRef]
61. Wischang, D.; Brucher, O.; Hartung, J. Bromoperoxidases and Functional Enzyme Mimics as Catalysts for Oxidative Bromination-A Sustainable Synthetic Approach. *Coord. Chem. Rev.* **2011**, *255*, 2204–2217. [CrossRef]

62. Kumar, S.; Jain, A.; Ichikawa, T.; Kojima, Y.; Dey, G.K. Development of vanadium based hydrogen storage material: A review. *Renew. Sust. Energy Rev.* **2017**, *72*, 791–800. [CrossRef]
63. Sakintuna, B.; Lamari-Darkrim, F.; Hirscher, M. Metal hydride materials for solid hydrogen storage: A review. *Int. J. Hydrogen Energy* **2007**, *32*, 1121–1140. [CrossRef]
64. Marban, G.; Solis, T.V. Towards the hydrogen economy? *Int. J. Hydrogen Energy* **2007**, *32*, 1625–1637. [CrossRef]
65. Ma, Y.D.; Dai, Y.; Guo, M.; Niu, C.W.; Zhu, Y.T.; Huang, B.B. Evidence of the existence of magnetism in pristine VX2 monolayers (X = S, Se) and their strain-induced tunable magnetic properties. *ACS Nano* **2012**, *6*, 1695–1701. [CrossRef] [PubMed]
66. Chmiola, J.; Largeot, C.; Taberna, P.L.; Simon, P.; Gogotsi, Y. Monolithic Carbide-Derived Carbon Films for Micro-Supercapacitors. *Science* **2010**, *328*, 480. [CrossRef]
67. Miller, J.R.; Outlaw, R.A.; Holloway, B.C. Graphene Double-Layer Capacitor with ac Line-Filtering Performance. *Science* **2010**, *329*, 1637. [CrossRef]
68. Bae, S.; Kim, H.; Lee, Y.; Xu, X.; Park, J.S.; Zheng, Y.; Balakrishnan, J.; Lei, T.; Kim, R.H.; Song, Y.I.; et al. Roll-to-roll production of 30-inch graphene films for transparent electrodes. *Nat. Nanotechnol.* **2010**, *5*, 574. [CrossRef]
69. Weckhuysen, B.M.; Keller, D.E. Chemistry, spectroscopy and the role of supported vanadium oxides in heterogeneous catalysis. *Catal. Today* **2003**, *78*, 25–46. [CrossRef]
70. Dummer, N.F.; Bartley, J.K.; Hutchings, G.J. Vanadium Phosphate Materials as Selective Oxidation Catalysts. *Adv. Catal.* **2011**, *54*, 189–247.
71. Khodakov, A.; Olthof, B.; Bell, A.T.; Iglesia, E. Structure and catalytic properties of supported vanadium oxides: Support effects on oxidative dehydrogenation reactions. *J. Catal.* **1999**, *181*, 205–216. [CrossRef]
72. Wu, C.; Feng, F.; Xie, Y. Design of vanadium oxide structures with controllable electrical properties for energy applications. *Chem. Soc. Rev.* **2013**, *42*, 5157–5183. [CrossRef] [PubMed]
73. Prasadam, V.P.; Bahlawane, N.; Mattelaer, F.; Rampelberg, G.; Detavernier, C.; Fang, L.; Jiang, Y.; Martens, K.; Parkin, I.P.; Papakonstantinou, I. Atomic layer deposition of vanadium oxides: Process and application review. *Mater. Today Chem.* **2019**, *12*, 396–423. [CrossRef]
74. Delmas, C.; Cognacauradou, H.; Cocciantelli, J.M.; Menetrier, M.; Doumerc, J.P. The LixV2O5 system—An overview of the structure modifications induced by the lithium intercalation. *Solid State Ion.* **1994**, *69*, 257–264. [CrossRef]
75. Ostreng, E.; Gandrud, K.B.; Hu, Y.; Nilsen, O.; Fjellvag, H. High power nanostructured V2O5 thin film cathodes by atomic layer deposition. *J. Mater. Chem.* **2014**, *2*, 15044–15051. [CrossRef]
76. Xie, Y.; Wu, C.Z. Design of nanoarchitectured electrode materials applied in new-generation rechargeable lithium ion batteries. *Dalton Trans.* **2007**, *5235*, 5235. [CrossRef]
77. Wan, Z.; Zou, Z.; Wang, J.; Long, F.; Wu, Y. Synthesis and Electrochemical Properties of Flower-like Na-doped V6O13 Cathode Materials for Li-ion Batteries. *Int. J. Electrochem. Sci.* **2018**, *13*, 6565–6576. [CrossRef]
78. Kucharczyk, D.; Niklewski, T. Accurate X-ray determination of the lattice parameters and the thermal expansion coefficients of VO2 near the transition temperature. *J. Appl. Cryst.* **1979**, *12*, 370–373. [CrossRef]
79. Jerominek, H.; Picard, F.; Vincent, D. Vanadium oxide films for optical switching and detection. *Opt. Eng.* **1993**, *32*, 2092–2099. [CrossRef]
80. Cavalleri, A.; Dekorsy, T.; Chong, H.H.W.; Kieffer, J.C.; Schoenlein, R.W. Evidence for a structurally-driven insulator-to-metal transition in VO_2: A view from the ultrafast timescale. *Phys. Rev. B* **2004**, *70*, 161102. [CrossRef]
81. Granqvist, C.G. Recent progress in thermochromics and electrochromics: A brief survey. *Thin Solid Films* **2016**, *614*, 90–96. [CrossRef]
82. Gupta, A.; Aggarwal1, R.; Gupta, P.; Dutta, T.; Narayan, R.J.; Narayan, J. Semiconductor to metal transition characteristics of VO2 thin films grown epitaxially on Si (001). *Appl. Phys. Lett.* **2009**, *95*, 111915. [CrossRef]
83. Darling, R.B.; Iwanaga, S. Structure, properties, and MEMS and microelectronic applications of vanadium oxides. *Sadhana* **2009**, *34*, 531–542. [CrossRef]
84. Niklaus, F.; Decharat, A.; Jansson, C.; Stemme, G. Performance model for uncooled infrared bolometer arrays and performance predictions of bolometers operating at atmospheric pressure. *Infrared Phys. Technol.* **2008**, *51*, 168–177. [CrossRef]
85. Wood, R.A.; Han, C.J.; Kruse, P.W. Integrated uncooled infrared detector imaging arrays. *IEEE Workshop Solid-State Sencor Actuator* **1992**. [CrossRef]
86. Mattelaer, F.; Geryl, K.; Rampelberg, G.; Dobbelaere, T.; Dendooven, J.; Detavernier, C. Atomic layer deposition of vanadium oxides for thin-film lithium-ion battery applications. *RSC Adv.* **2006**, *6*, 114658–114665. [CrossRef]
87. Mattelaer, F.; Geryl, K.; Rampelberg, G.; Dendooven, J.; Detavernier, C. Amorphous and crystalline vanadium oxides as high-energy and high-power cathodes for three-dimensional thin-film lithium ion batteries. *ACS Appl. Mater. Interfaces* **2017**, *9*, 13121–13131. [CrossRef]
88. Cao, A.M.; Hu, J.S.; Liang, H.P.; Wan, L.J. Self-Assembled Vanadium Pentoxide (V_2O_5) Hollow Microspheres from Nanorods and Their Application in Lithium-Ion Batteries. *Angew. Chem. Int. Ed.* **2005**, *44*, 4391. [CrossRef]
89. Adler, D. Mechanisms for metal-nonmetal transitions in transition-metal oxides and sulfides. *Rev. Mod. Phys.* **1968**, *40*, 714–736. [CrossRef]
90. Muhr, H.J.; Krumeich, F.; Schonholzer, U.P.; Bieri, F.; Niederberger, M.; Gauckler, L.J.; Nesper, R. Vanadium Oxide Nanotubes—A New Flexible Vanadate Nanophase. *Adv. Mater.* **2000**, *12*, 231. [CrossRef]

91. Pinna, N.; Wild, U.; Urban, J.; Schlogl, R. Divanadium Pentoxide Nanorods. *Adv. Mater.* **2003**, *15*, 329. [CrossRef]
92. Eyert, V.; Hoch, K.-H. Electronic structure of V_2O_5: Role of octahedral deformations. *Phys. Rev. B* **1998**, *57*, 12727–12737. [CrossRef]
93. Zhang, X.F.; Wang, K.X.; Wei, X.; Chen, J.S. Carbon-Coated V_2O_5 Nanocrystals as High Performance Cathode Material for Lithium Ion Batteries. *Chem. Mater.* **2011**, *23*, 5290. [CrossRef]
94. Hermann, K.; Chakrabarti, A.; Druzinic, R.; Witko, M. Ab initio density functional theory studies of hydrogen adsorption at the V_2O_5(010) surface. *Phys. Stat. Sol.* **1999**, *173*, 195–208. [CrossRef]
95. Liu, L.; Cao, F.; Yao, T.; Xu, Y.; Zhou, M.; Qu, B.; Pan, B.; Wu, C.; Wei, S.; Xie, Y. New-phase VO2 micro/nanostructures: Investigation of phase transformation and magnetic property. *New J. Chem.* **2012**, *36*, 619. [CrossRef]
96. Xie, J.; Wu, C.; Hu, S.; Dai, J.; Zhang, N.; Feng, J.; Yang, J.; Xie, Y. Ambient rutile VO2(R) hollow hierarchitectures with rich grain boundaries from new-state nsutite-type VO2, displaying enhanced hydrogen adsorption behavior. *Phys. Chem. Chem. Phys.* **2012**, *14*, 4810. [CrossRef] [PubMed]
97. Cavalleri, A.; Toth, C.; Siders, C.W.; Squier, J.A.; Raksi, F.; Forget, P.; Kieffer, J.C. Femtosecond structural dynamics in VO_2 during an ultra fast solid-solid phase transition. *Phys. Rev. Lett.* **2001**, *87*, 237401. [CrossRef] [PubMed]
98. Zhang, S.; Shang, B.; Yang, J.; Yan, W.; Wei, S.; Xie, Y. From VO2 (B) to VO2 (A) nanobelts: First hydrothermal transformation, spectroscopic study and first principles calculation. *Phys. Chem. Chem. Phys.* **2011**, *13*, 15873. [CrossRef] [PubMed]
99. Liu, M.; Hwang, H.Y.; Tao, H.; Strikwerda, A.C.; Fan, K.B.; Keiser, G.R.; Sternbach, A.J.; West, K.G.; Kittiwatanakul, S.; Lu, J.W.; et al. Terahertz-field-induced insulator-to-metal transition in vanadium dioxide metamaterial. *Nature* **2012**, *487*, 345–348. [CrossRef]
100. Cornell, R.M.; Schwertmann, U. *The Iron Oxides: Structure, Properties, Reactions, Occurrences and Uses*, 2nd ed.; Wiley VCH: Weinheim, Germany, 2003.
101. Yu, P.; Cardona, M. *Fundamentals of Semiconductors: Physics and Materials Properties*; Springer: Heidelberg, Germany, 2010; pp. 17–106.
102. Batista, C.; Ribeiro, R.M.; Teixeira, V. Synthesis and characterization of VO2-based thermochromic thin films for energy-efficient windows. *Nanoscale Res. Lett.* **2011**, *6*, 301. [CrossRef]
103. Parker, J.C.; Lam, D.J.; Xu, Y.N.; Ching, W.Y. Optical properties of vanadium pentoxide determined from ellipsometry and band-structure calculations. *Phys. Rev. B* **1990**, *42*, 5289–5293. [CrossRef]
104. Wang, Y.; Takahashi, K.; Shang, H.; Cao, G. Synthesis and Electrochemical Properties of Vanadium Pentoxide Nanotube Arrays. *J. Phys. Chem. B Lett.* **2005**, *109*, 3085–3088. [CrossRef] [PubMed]
105. Alsawafta, M.; Almoabadi, A.; Badilescu, S.; Truong, V.V. Improved Electrochromic Properties of Vanadium Pentoxide Nanorods Prepared by Thermal Treatment of Sol-Gel Dip-Coated Thin Films. *J. Electrochem. Soc.* **2015**, *162*, H466–H472. [CrossRef]
106. Talledo, A.; Andersson, A.M.; Granqvist, C.G. Structure and optical absorption of $Li_yV_2O_5$ thin films. *J. Appl. Phys.* **1991**, *69*, 3261–3265. [CrossRef]
107. Nadkarni, G.S.; Shirodkar, V.S. Experiment and theory for switching in Al/V2O5/Al devices. *Thin Solid Films* **1983**, *105*, 115–129. [CrossRef]
108. Chain, E.E. Optical properties of vanadium dioxide and vanadium pentoxide thin films. *Appl. Opt.* **1991**, *30*, 2782–2787. [CrossRef]
109. Livage, J. Optical and electrical properties of vanadium oxides synthesized from alkoxides. *Coord. Chem. Rev.* **1999**, *190*, 391–403. [CrossRef]
110. Xu, G.; Jin, P.; Tazawa, M.; Yoshimura, K. Thickness dependence of optical properties of VO_2 thin films epitaxially grown on sapphire (0001). *Appl. Surf. Sci.* **2005**, *244*, 449–452. [CrossRef]
111. Borisov, B.S.; Koretkaya, S.T.; Mokerov, V.G.; Rakov, A.V.; Solovev, S.G. Electrical and optical properties of VO2 near semiconductor-semimetal transition point. *Sov. Phys. Solid State (Engl. Transl.)* **1971**, *12*, 1763–1766.
112. Biermann, S.; Poteryaev, A.; Lichtenstein, A.I.; Georges, A. Dynamical singlets and correlation-assisted peierls transition in VO_2. *Phys. Rev. Lett.* **2005**, *94*, 026404. [CrossRef]
113. Adler, D.; Brooks, H. Theory of semicondutor to metal transitions. *Phys. Rev.* **1967**, *155*, 826–840. [CrossRef]
114. Granqvist, C.G. *Handbook of Inorganic Electrochromic Materials*; Elsevier: Amsterdam, The Netherlands, 1995; pp. 237–295.
115. Zylbersztejn, A.; Mott, N.F. Metal-insulator transition in vanadium dioxide. *Phys. Rev. B* **1975**, *11*, 4383–4395. [CrossRef]
116. Becker, M.; Buckman, A.B.; Walser, R.M. Femtosecond laser excitation dynamics of the semiconductor-metal phase transition in VO_2. *Appl. Phys. Lett.* **1996**, *79*, 2404–2408. [CrossRef]
117. Shao, Z.; Luo, H.; Jin, P. Recent progress in the phase-transition mechanism and modulation of vanadium dioxide materials. *NPG Asia Mater.* **2018**, *10*, 581–605. [CrossRef]
118. Aetukuri, N.B.; Aetukuri, N.B.; Gray, A.X.; Drouard, M.; Cossale, M.; Gao, L.; Reid, L.; Kukreja, R.; Ohldag, H.; Jenkins, C.A.; et al. Control of the metal-insulator transition in vanadium dioxide by modifying orbital occupancy. *Nat. Phys.* **2013**, *9*, 661–666. [CrossRef]
119. Ardakani, A.H.; Nie, A.; Marley, P.M.; Zhu, Y.; Phillips, P.J.; Singh, S.; Mashayek, M.; Sambandamurthy, G.; Low, K.; Klie, R.B.; et al. Atomic origins of monoclinic-tetragonal (rutile) phase transition in doped VO2 nanowires. *Nano Lett.* **2015**, *15*, 7179–7188. [CrossRef]
120. Booth, J.M.; Casey, P.S. Anisotropic structure deformation in the VO2 metalinsulator transition. *Phys. Rev. Lett.* **2009**, *103*, 086402. [CrossRef]

121. Marezio, M.; McWhan, D.B.; Remeika, J.P.; Dernier, P.D. Structural aspects of the metal-insulator transitions in Cr-doped VO2. *Phys. Rev. B* **1972**, *5*, 2541. [CrossRef]
122. Brückner, W.; Gerlach, U.; Thuss, B. Phase diagram of V1-xAlxO2. *Phys. Status Solidi* **1977**, *40*, K131–K134. [CrossRef]
123. Thomas, G.A.; Rapkine, D.H.; Carter, S.A.; Millis, A.J.; Rosenbaum, T.F.; Metcalf, P.; Honig, J.M. Observation of the gap and kinetic energy in a correlated insulator. *Phys. Rev. Lett.* **1994**, *73*, 1529–1532. [CrossRef]
124. Saha-Dasgupta, T.; Andersen, O.K.; Nuss, J.; Poteryaev, A.I.; Georges, A.; Lichtenstein, A.I. Electronic structure of V2O3: Wannier orbitals from LDA-NMTO calculations. *arXiv* **2009**, arXiv:0907.2841.
125. Surnev, S.; Ramsey, M.G.; Netzer, F.P. Vanadium oxide surface studies. *Prog. Surf. Sci.* **2003**, *73*, 117–165. [CrossRef]
126. Yamazaki, S.; Li, C.; Ohoyama, K.; Nishi, M.; Ichihara, M.; Ueda, H.; Ueda, Y. Synthesis, structure and magnetic properties of V4O9—A missing link in binary vanadium oxides. *J. Solid State Chem.* **2010**, *183*, 1496–1503. [CrossRef]
127. Zhang, Y.; Liu, X.; Xie, G.; Yu, L.; Yi, S.; Hu, M.; Huang, C. Hydrothermal synthesis, characterization, formation mechanism and electrochemical property of V3O7·H2O single-crystal nanobelts. *Mater. Sci. Eng. B* **2010**, *175*, 164–171. [CrossRef]
128. Zakharova, G.S.; Volkov, V.L.; Täschner, C.; Hellmann, I.; Leonhardt, A.; Klingeler, R.; Büchner, B. Synthesis and characterization of V3O7.H2O nanobelts. *Solid State Commun.* **2009**, *149*, 814–817. [CrossRef]
129. Cristopher, M.; Karthick, P.; Sivakumar, R.; Gopalakrishnan, C.; Sanjeeviraja, C.; Jeyadheepan, K. On the preparation of Tri-vanadium hepta-oxide thin films for electrochromic applications. *Vacuum* **2019**, *160*, 238–245. [CrossRef]
130. Mjejri, I.; Rougier, A. Color Switch in V3O7.H2O cycled in Li and Na based electrolytes: Novel vanadium oxide based electrochromic material. *J. Mater. Chem. C* **2020**, *8*, 3631–3638. [CrossRef]
131. Chen, X.; Shen, S.; Guo, L.; Mao, S.S. Semiconductor based photocatalytic hydrogen generation. *Chem. Rev.* **2010**, *110*, 6503. [CrossRef] [PubMed]
132. Mosleh, M. Nanocrystalline iron vanadate: Facile morphology-controlled preparation, characterization and investigation of optical and photocatalytic properties. *J. Mater. Sci. Mater. Electron.* **2017**, *28*, 5866–5871. [CrossRef]
133. Ghiyasiyan-Arani, M.; Salavati-Niasari, M.; Naseh, S. Enhanced photodegradation of dye in waste water using iron vanadate nanocomposite; ultrasound-assisted preparation and characterization. *Ultrason. Sonochem.* **2017**, *39*, 494–503. [CrossRef]
134. Heydari, A.; Sheykhan, M.; Sadeghi, M.; Radfar, I. Nano-Rods of FeVO4: An Efficient Heterogeneous Catalyst for Chemo-Selective Oxidation of Benzylic Alcohols. *Inorg. Nano-Metal Chem.* **2016**, *47*, 248–255. [CrossRef]
135. Zhang, S.; Sun, Y.; Li, C.; Ci, L. Cu3V2O8 hollow spheres in photocatalysis and primary lithium batteries. *Solid State Sci.* **2013**, *25*, 15–21. [CrossRef]
136. Kumada, N.; Takei, T.; Haramoto, R.; Yonesaki, Y.; Dong, Q.; Kinomura, N.; Nishimoto, S.; Kameshima, Y.; Miyake, M. Preparation and crystal structure of a new bismuth vanadate, Bi3.33(VO4)2O2. *Mater. Res. Bull.* **2011**, *46*, 962–965. [CrossRef]
137. Gan, J.; Lu, X.; Tong, Y. Towards highly efficient photoanodes: Boosting sun light-driven semiconductor nanomaterials for water oxidation. *Nanoscale* **2014**, *6*, 7142. [CrossRef] [PubMed]
138. Tolod, K.R.; Hernandez, S.; Russo, N. Recent advances in the BiVO4 photo catalyst for sun-driven water oxidation: Top-performing photoanodes and scale-up challenges. *Catalysts* **2017**, *7*, 13. [CrossRef]
139. Park, Y.; McDonald, K.J.; Choi, K.-S. Progress in bismuth vanadate photo anodes for use in solar water oxidation. *Chem. Soc. Rev.* **2013**, *42*, 2321. [CrossRef]
140. Teoh, W.Y.; Scott, J.A.; Amal, R. Progress in heterogeneous photocatalysis: From classical radical chemistry to engineering nanomaterials and solar reactors. *J. Phys. Chem. Lett.* **2012**, *3*, 629–639. [CrossRef]
141. Tachikawa, T.; Ochi, T.; Kobori, Y. Crystal-face-dependent charge dynamics on a BiVO4 photocatalyst revealed by single-particle spectroelectrochemistry. *ACS Catal.* **2016**, *6*, 2250–2256. [CrossRef]
142. Tan, H.L.; Wen, X.; Amal, R.; Ng, Z.H. BiVO4 {010} and {110} relative exposure extent: Governing factor of surface charge population and photocatalytic activity. *J. Phys. Chem. Lett.* **2016**, *7*, 1400–1405. [CrossRef]
143. Ma, Y.; Pendlebury, S.R.; Reynal, A.; Le Formal, F.; Durrant, J.R. Dynamics of photogenerated holes in undoped BiVO4 photoanodes for solar water oxidation. *Chem. Sci.* **2014**, *5*, 2964–2973. [CrossRef]
144. Ravensbergen, J.; Abdi, F.F.; Santen, J.H.; Frese, R.N.; Dam, B.; Krol, R.; Kennis, J.T.M. Unraveling the Carrier Dynamics of BiVO4: A Femtosecond to Microsecond Transient Absorption Study. *J. Phys. Chem. C* **2014**, *118*, 27793–27800. [CrossRef]
145. Vannier, N.; Pernot, E.; Anne, M.; Isnard, O.; Nowogrocki, G.; Mairesse, G. Bi4V2O11 polymorph crystal structures related to their electrical properties. *Solid State Ion.* **2003**, *157*, 147–153. [CrossRef]
146. Mairesse, G.; Roussel, P.; Vannier, R.N.; Anne, M.; Pirovano, C.; Nowogrocki, G. Crystal structure determination of α, β and γ-Bi4V2O11 polymorphs. Part I: γ and β-Bi4V2O11. *Solid State Sci.* **2003**, *5*, 851–859. [CrossRef]
147. Mairesse, G.; Roussel, P.; Vannier, R.N.; Anne, M.; Nowogrocki, G. Crystal structure determination of α, β and γ-Bi4V2O11 polymorphs. Part II: Crystal structure of α-Bi4V2O11. *Solid State Sci.* **2003**, *5*, 861–869. [CrossRef]
148. Lakkepally, S.; Kalegowda, Y.; Ramarao, V.; Hanumantharayappa, E.; Siddaramanna, A. Room temperature synthesis of amorphous Bi4V2O11 as cathode material for Li secondary batteries. *Mater. Res. Express* **2018**, *5*, 115501. [CrossRef]
149. Liang, M.; Yang, Z.; Mei, Y.; Zhou, H.; Yang, S. Dye-Sensitized-Assisted, Enhanced Photocatalytic Activity of TiO2/Bi4V2O11. *NANO Brief Rep. Rev.* **2018**, *13*, 1850028. [CrossRef]
150. Nithya, V.D.; Selvan, R.K.; Sanjeeviraja, C.; Radheep, D.M.; Arumugam, S. Synthesis and characterization of FeVO4 nanoparticles. *Mater. Res. Bull.* **2011**, *46*, 461654–461658. [CrossRef]

151. Baeis, M.G.; Mousavi, S.H.; Jeddy, M.R. Controlled synthesis and characterization of iron vanadate magnetic nanoparticles: Investigation it's photodegradation of Rhodamine B. *J. Mater. Sci. Mater. Electron.* **2017**, *28*, 1480–1484. [CrossRef]
152. Deng, J.H.; Jiang, J.Y.; Zhang, Y.Y.; Lin, X.P.; Du, C.M.; Xiong, Y. FeVO4 as a highly active heterogeneous Fenton-like catalyst towards the degradation of Orange II. *Appl. Catal. B* **2008**, *84*, 468–473. [CrossRef]
153. Ozturk, B.; Soylu, G.S.P. Synthesis of surfactant-assisted FeVO4 nanostructure: Characterization and photocatalytic degradation of phenol. *J. Mol. Catal. A Chem.* **2015**, *398*, 65–71. [CrossRef]
154. Zhang, M.; Ma, Y.; Friedrich, D.; Krol, R.; Wong, L.H.; Abdi, F.F. Elucidation of opto-electronic and photoelectrochemical properties of FeVO4 photoanodes for solar water oxidation. *J. Mater. Chem. A* **2018**, *6*, 548–555. [CrossRef]
155. Arunachalam, M.; Yun, G.; Ahn, K.S.; Kang, S.H. Revealing the beneficial effects of FeVO4 nanoshell layer on the BiVO4 inverse opal core layer for photoelectrochemical water oxidation. *J. Phys. Chem. C* **2017**, *121*, 7625–7634. [CrossRef]
156. Dutta, D.P.; Ramakrishnan, M.; Roy, M.; Kumar, A. Effect of transition metal doping on the photocatalytic properties of FeVO4 nanoparticles. *J. Photochem. Photobiol. A* **2017**, *335*, 102–111. [CrossRef]
157. Lakkepally, S.; Kalegowda, Y.; Ganganagappa, N.; Siddaramanna, A. A new and effective approach for Fe2V4O13 nanoparticles synthesis: Evaluation of electrochemical performance as cathode for lithium secondary batteries. *J. Alloy. Compd.* **2018**, *737*, 665–671. [CrossRef]
158. Tang, D.; Rettie, A.J.E.; Mabayoje, O.; Wygant, B.R.; Lai, Y.; Liu, Y.; Mullins, C.B. Facile Growth of Porous Fe2V4O13 Films for Photoelectrochemical Water Oxidation. *J. Mater. Chem. A* **2016**, *4*, 3034–3042. [CrossRef]
159. Zhang, Y.Y.; Deng, J.H.; He, C.; Huang, S.S.; Tian, S.H.; Xiong, Y. Application of Fe2V4O13 as a new multi-metal heterogeneous Fenton-like catalyst for the degradation of organic pollutants. *Environ. Technol.* **2010**, *31*, 145–154. [CrossRef]
160. Li, P.; Zhou, Y.; Li, H.; Xu, Q.; Meng, X.; Wang, X.; Xiao, M.; Zou, Z. All-solid-state Z-scheme system arrays of $Fe_2V_4O_{13}$/RGO/CdS for visible light-driving photocatalytic CO_2 reduction into renewable hydrocarbon fuel. *Chem. Commun.* **2015**, *51*, 800–803. [CrossRef]
161. Maggay, I.V.B.; Juan, L.M.Z.; Lu, J.S.; Nguyen, M.T.; Yonezawa, T.; Chan, T.S.; Liu, W.R. Electrochemical properties of novel FeV2O4 as an anode for Na-ion batteries. *Sci. Rep.-UK* **2018**, *8*, 8839. [CrossRef]
162. Mandal, H.; Shyamal, S.; Hajra, P.; Bera, A.; Sariket, D.; Kundu, S.; Bhattacharya, C. Development of ternary iron vanadium oxide semiconductors for their applications in Photoelectrochemical Water Oxidation. *RSC Adv.* **2016**, *6*, 4992–4999. [CrossRef]
163. Zhang, L.F.; Zhou, J.; Zhang, C.Y. pH-controlled growth of ultrathin iron vanadium oxide (FeV3O8) nanoplatelets with high visible-light photo-catalytic activity. *J. Mater. Chem. A* **2014**, *2*, 14903. [CrossRef]
164. Hassan, A.; Iqbal, T.; Tahir, M.B.; Afsheen, S. A review on copper vanadate-based nanostructures for photocatalysis energy production. *Int. J. Energy Res.* **2019**, *43*, 9–28. [CrossRef]
165. Ghiyasiyan-Arani, M.; Masjedi-Arani, M.; Salavati-Niasari, M. Facile synthesis, characterization and optical properties of copper vanadate nanostructures for enhanced photocatalytic activity. *J. Mater. Sci. Mater. Electron.* **2016**, *27*, 4871–4878. [CrossRef]
166. Jiang, C.M.; Farmand, M.; Wu, C.H.; Liu, Y.S.; Guo, J.; Drisdell, W.S.; Cooper, J.K.; Sharp, I.D. Electronic Structure, Optoelectronic Properties, and Photoelectrochemical Characteristics of γ-Cu3V2O8 Thin Films. *Chem. Mater.* **2017**, *29*, 3334–3345. [CrossRef]
167. Truc, N.T.T.; Hanh, N.T.; Nguyen, M.V.; Chi, N.T.P.L.; Noi, N.V.; Tran, D.T.; Ha, M.N.; Trung, D.Q.; Pham, T.D. Novel direct Z-scheme Cu2V2O7/g-C3N4 for visible light photocatalytic conversion of CO2 into valuable fuels. *Appl. Surf. Sci.* **2018**, *457*, 968–974. [CrossRef]
168. Guo, W.; Chemelewski, W.D.; Mabayoje, O.; Xiao, P.; Zhang, Y.; Mullins, C.B. Synthesis and Characterization of CuV2O6 and Cu2V2O7: Two Photoanode Candidates for Photoelectrochemical Water Oxidation. *J. Phys. Chem. C* **2015**, *119*, 27220–27227. [CrossRef]
169. Shi, H.; Zhou, C.; Zhang, C. Silver vanadate nanowires: Photocatalytic properties and theoretical calculations. *Res. Chem. Intermed* **2015**, *41*, 7725–7737. [CrossRef]
170. Oliveira, C.R.; Assis, M.; Teixeira, M.M.; Silva, M.D.P.; Li, M.S.; Andres, J.; Gracia, L.; Longo, E. An Experimental and Computational Study of β-AgVO3: Optical Properties and Formation of Ag Nanoparticles. *J. Phys. Chem. C* **2016**, *120*, 12254–12264. [CrossRef]
171. Hu, X.; Hu, C.; Qu, J. Preparation and visible-light activity of silver vanadate for the degradation of pollutants. *Mater. Res. Bull.* **2008**, *43*, 2986–2997. [CrossRef]
172. McNulty, D.; Ramasse, Q.; O'Dwyer, C. The Structural Conversion from α-AgVO3 to β-AgVO3: Ag Nanoparticle Decorated Nanowires with Application as Cathode Materials for Li-ion Batteries. *Nanoscale* **2016**, *8*, 16266–16275. [CrossRef]
173. Xu, J.; Hu, C.; Xi, Y.; Wan, B.; Zhang, C.; Zhang, Y. Synthesis and visible light photocatalytic activity of b-AgVO3 nanowires. *Solid State Sci.* **2012**, *14*, 535–539. [CrossRef]
174. Cao, X.; Zhan, H.; Xie, J.; Zhou, Y. Synthesis of Ag2V4O11 as a cathode material for lithium battery via a rheological phase method. *Mater. Lett.* **2006**, *60*, 435–438. [CrossRef]
175. Shi, H.; Li, Z.; Kou, J.; Ye, J.; Zou, Z. Facile Synthesis of Single-Crystalline Ag2V4O11 Nanotube Material as a Novel Visible-Light-Sensitive Photocatalyst. *J. Phys. Chem. C* **2011**, *115*, 145–151. [CrossRef]
176. Xu, H.; Li, H.; Sun, G.; Xia, J.; Wu, C.; Ye, Z.; Zhang, Q. Photocatalytic activity of La2O3-modified silver vanadates catalyst for Rhodamine B dye degradation under visible light irradiation. *Chem. Eng. J.* **2010**, *160*, 33–41. [CrossRef]
177. Ren, C.; Fan, J.; Liu, S.; Li, W.; Wang, F.; Li, H.; Liu, X.; Chang, Y. One-step hydrothermal synthesis of the novel Ag3VO4/Ag4V2O7 composites for enhancing visible-light photocatalytic performance. *RSC Adv.* **2016**, *6*, 95156–95164. [CrossRef]

178. Xia, D.; Xu, S.; Wang, W.; Wang, D.; Wu, M.; Gong, F. Pure-phase β-Mn2V2O7 interconnected nanospheres as high performance lithium ion battery anode. *Chem. Commun.* **2020**, *56*, 8043–8046. [CrossRef]
179. Pei, L.Z.; Lin, N.; Wei, T.; Yu, H.Y. Synthesis of manganese vanadate nanobelts and their visible light photocatalytic activity for methylene blue. *J. Exp. Nanosci.* **2016**, *11*, 197–214. [CrossRef]
180. Yan, Q.; Yu, J.; Suram, S.K.; Zhou, L.; Shinde, A.; Newhouse, P.F.; Chen, W.; Li, G.; Persson, K.A.; Gregoire, J.M.; et al. Solar fuels photoanode materials discovery by integrating high-throughput theory and experiment. *Proc. Natl. Acad. Sci.* **2017**, *114*, 3040–3043. [CrossRef] [PubMed]
181. Nasiri, A.; Nasiri, M. Manganese vanadate nanostructure: Facile precipitation preparation, characterization, and investigation of their photocatalyst activity. *J. Mater. Sci. Mater. Electron.* **2017**, *28*, 9096–9101. [CrossRef]
182. Tsai, Y.C. Desalination plants and renewables combined to solve power and water issues. *Energy* **2016**, *113*, 1018–1030. [CrossRef]
183. Yaqoot, M.; Diwan., P.; Kandpal, T.C. Review of barriers to the dissemination of decentralized renewable energy systems. *Renew. Sustain. Energy Rev.* **2016**, *58*, 477–490. [CrossRef]
184. Benedek, J.; Sebestyén, T.T.; Bartók, B. Evaluation of renewable energy sources in peripheral areas and renewable energy-based rural development. *Renew. Sustain. Energy Rev.* **2018**, *90*, 516–535. [CrossRef]
185. Arnaut, L.G.; Barroso, M.; Serpa, C. Solar energy conversion. In *Applied Photochemistry*; Giacomo, B., Serena, S., Eds.; Springer: Dordrecht, The Netherlands, 2013; pp. 267–304.
186. Chiarello, G.L.; Selli, E. Photocatalytic hydrogen production. *Recent Pat. Eng.* **2010**, *4*, 155. [CrossRef]
187. Ismail, A.A.; Bahnemann, D.W. Photochemical splitting of water for hydrogen production by photocatalysis: A review. *Sol. Energy Mater. Sol. Cells* **2014**, *128*, 85. [CrossRef]
188. Gholipour, M.R.; Dinh, C.-T.; Beland, F.; Do, T.-O. Nanocomposite hetero junctions as sunlight-driven photocatalysts for hydrogen production from water splitting. *Nanoscale* **2015**, *7*, 8187. [CrossRef]
189. Liao, C.-H.; Huang, C.-W.; Wu, J.C.C. Hydrogen production from semicon ductor-based photocatalysis via water splitting. *Catalysts* **2012**, *2*, 490–516. [CrossRef]
190. Ibhadon, A.O.; Fitzpatrick, P. Heterogeneous photocatalysis: Recent advances and applications. *Catalysts* **2013**, *3*, 189–218. [CrossRef]
191. Fujishima, A.; Honda, K. Electrochemical photolysis of water at a semicon ductor electrode. *Nature* **1972**, *238*, 37–38. [CrossRef]
192. Shena, T.F.-R.; Lai, M.H.; Yang, T.C.K.; Fu, I.P.; Liang, N.Y.; Chen, W.T. Photocatalytic production of hydrogen by vanadium oxides under visible light irradiation. *J. Taiwan Inst. Chem. Eng.* **2012**, *43*, 95–101. [CrossRef]
193. Monfort, O.; Lianos, O.; Plesch, G. Design of Bismuth Vanadate-Based Materials: New Advanced Photoanodes for Solar Hydrogen Generation. In *Photoelectrochemical Solar Cells*; Sankir, N.D., Sankir, M., Eds.; Wiley-Scrivener: Beverly, MA, USA, 2019; pp. 219–249.
194. Wang, Y.; Zhang, Z.; Zhu, Z.; Li, Z.; Vajtai, R.; Ci, L.; Ajayan, P.M. Nanostructured VO2 Photocatalysts for Hydrogen Production. *ACS Nano* **2008**, *2*, 1492–1496. [CrossRef]
195. Puangpetch, T.; Chavadej, S.; Sreethawong, T. Mesoporous-assembled V2O5 nanosheet synthesized via a surfactant-modified sol–gel technique and its photocatalytic H2 production activity under visible light irradiation. *Powder Technol.* **2011**, *208*, 37–41. [CrossRef]
196. Ran, J.; Zhang, J.; Yu, J.; Jaroniec, M.; Qiao, S.Z. Earth-abundant cocatalysts for semiconductor-based photocatalytic water splitting. *Chem. Soc. Rev.* **2014**, *43*, 7787. [CrossRef]
197. Zhang, L.; Jin, Z.; Ma, X.; Zhang, Y.; Wang, H. Property of iron vanadate over CdS nanorod for efficient photocatalytic hydrogen production. *New J. Chem.* **2019**, *43*, 3609–3618. [CrossRef]
198. Tan, H.L.; Amal, R.; Ng, Y.H. Alternative Strategies in Improving the Photocatalytic and Photoelectrochemical Activities of Visible Light-driven BiVO4: A Review. *J. Mater. Chem. A* **2017**, *5*, 16498–16521. [CrossRef]
199. Zou, L.; Wang, H.; Wang, X. High Efficient Photodegradation and photocatalytic Hydrogen Production of CdS/BiVO4 Heterostructure through Z-Scheme Process. *ACS Sustain. Chem. Eng.* **2017**, *5*, 303–309. [CrossRef]
200. Li, N.; Wu, X.; Wang, M.; Huang, K.; He, J.; Ma, W.; Chen, H.; Li, Y.; Feng, S. Facile preparation of BiVO4/FeVO4 heterostructure for efficient water-splitting applications. *Int. J. Hydrogen Energy* **2019**, *44*, 23046–23053. [CrossRef]
201. Abdi, F.F.; Han, L.; Smets, A.H.M.; Zeman, M.; Dam, B.; Krol, R. Efficient solar water splitting by enhanced charge separation in a bismuth vanadate-silicon tandem photoelectrode. *Nat. Commun.* **2013**, *4*, 2195. [CrossRef]
202. Monfort, O.; Pop, L.-C.; Sfaelou, S.; Plecenik, T.; Roch, T.; Dracopoulos, V.; Stathatos, E.; Plesch, G.; Lianos, P. Photoelectrocatalytic hydrogen production by water splitting using BiVO4 photoanodes. *Chem. Eng. J.* **2016**, *286*, 91. [CrossRef]
203. Biswas, S.K.; Baeg, J.O. Enhanced photoactivity of visible light responsive W incorporated FeVO4 photoanode for solar water splitting. *Int. J. Hydrogen Energy* **2013**, *38*, 14451–14457. [CrossRef]
204. Morton, C.D.; Slipper, I.J.; Thomas, M.J.K.; Alexander, B.D. Synthesis and characterisation of Fe-V-O thin film photoanodes. *Photochem. Photobiol.* **2010**, *216*, 209–214. [CrossRef]
205. Wang, W.; Zhang, Y.; Wang, L.; Bi, Y. Facile synthesis of Fe3+/Fe2+ self-doped nanoporous FeVO4 photoanodes for efficient solar water splitting. *J. Mater. Chem. A* **2017**, *5*, 2478–2482. [CrossRef]
206. Moniz, S.J.A.; Zhu, J.; Tang, J. 1D Co-Pi modified BiVO4/ZnO junction cascade for efficient photoelectrochemical water cleavage. *Adv. Energy Mater.* **2014**, *4*, 1301590. [CrossRef]

207. Li, G.; Zhang, D.; Yu, J.C. Ordered Mesoporous BiVO4 through Nanocasting: A Superior Visible Light-Driven Photocatalyst. *Chem. Mater.* **2008**, *20*, 3983. [CrossRef]
208. Monfort, O.; Sfaelou, S.; Satrapinskyy, L.; Plecenik, T.; Roch, T.; Plesch, G.; Liano, P. Comparative study between pristine and Nb-modified BiVO4 films employed for photoelectrocatalytic production of H2 by water splitting and for photocatalytic degradation of organic pollutants under simulated solar light. *Catal. Today* **2017**, *280*, 51–57. [CrossRef]
209. Gunes, S.; Neugebauer, H.; Sariciftci, N.S. Conjugated Polymer-Based Organic Solar Cells. *Chem. Rev.* **2007**, *107*, 1324. [CrossRef] [PubMed]
210. Zilberberg, K.; Trost, S.; Meyer, J.; Kahn, A.; Behrendt, A.; Lützenkirchen-Hecht, D.; Frahm, R.; Riedl, T. Inverted Organic Solar Cells with Sol–Gel Processed High Work-Function Vanadium Oxide Hole-Extraction Layers. *Adv. Funct. Mater.* **2011**, *21*, 4776. [CrossRef]
211. Sun, H.; Hou, X.; Wei, Q.; Liu, H.; Yang, K.; Wang, W.; An, Q.; Rong, Y. Low-temperature solution-processed p-type vanadium oxide for perovskite solar cells. *Chem. Commun.* **2016**, *52*, 8099.
212. Salimi, M.; Esrafili, A.; Gholami, M.; Jafari, A.J.; Kalantary, R.R.; Farzadkia, M.; Kermani, M.; Sobhi, H.R. Contaminants of emerging concern: A review of new approach in AOP Technologies. *Environ. Monit. Assess.* **2017**, *189*, 414.
213. He, J.; Yang, X.; Men, B.; Wang, D. Interfacial mechanisms of heterogeneous Fenton reactions catalyzed by iron-based materials: A review. *J. Environ. Sci.* **2016**, *39*, 97–109. [CrossRef]
214. Fenton, H.J.H. Oxidation of tartaric acid in the presence of iron. *J. Chem. Soc. Trans.* **1894**, *65*, 899–910. [CrossRef]
215. Clarizia, L.; Russo, D.; Di Somma, I.; Marotta, R.; Andreozzi, R. Homogeneous photo-Fenton processes at near neutral pH: A review. *Appl. Catal. B* **2017**, *209*, 358–371. [CrossRef]
216. Pouran, S.R.; Aziz, A.R.A.; Daud, W.M.A.W. Review on the main advances in photo-Fenton oxidation system for recalcitrant wastewaters. *J. Ind. Eng. Chem.* **2015**, *21*, 53–69. [CrossRef]
217. Bokare, A.D.; Choi, W. Review of iron-free Fenton-like systems for activating H2O2 in advanced oxidation processes. *J. Hazard. Mater.* **2014**, *275*, 121–135. [CrossRef] [PubMed]
218. Zhang, M.; Niu, Y.; Xu, Y. Heterogeneous Fenton-like magnetic nanosphere coated with vanadium oxide quantum dots for enhanced organic dyes decolorization. *J. Colloid Interface Sci.* **2020**, *579*, 269–281. [CrossRef]
219. Le, T.K.; Kang, M.; Kim, S.W. A review on the optical characterization of V2O5 micro-nanostructures. *Ceram. Int.* **2019**, *45*, 15781–15798. [CrossRef]
220. Shahid, M.; Rhen, D.S.; Shakir, I.; Patole, S.P.; Yoo, J.B.; Yang, S.J.; Kang, D.J. Facile synthesis of single crystalline vanadium pentoxide nanowires and their photocatalytic behavior. *Mater. Lett.* **2010**, *64*, 2458–2461. [CrossRef]
221. Liu, B.; Li, X.; Zhao, Q.; Liu, J.; Liu, S.; Wang, S.; Tade, M.O. Insight into the Mechanism of Photocatalytic Degradation of Gaseous o-dichlorobenzene over Flower-Type V2O5 Hollow Spheres. *J. Mater. Chem. A* **2015**, *3*, 15163–15170. [CrossRef]
222. Liu, H.; Gao, Y.; Zhou, J.; Liu, X.; Chen, Z.; Cao, C.; Luo, H.; Kanehira, M. Growth of oriented vanadium pentaoxide nanostructures on transparent conducting substrates and their applications in photocatalysis. *J. Solid State Chem.* **2014**, *214*, 79–85. [CrossRef]
223. Jayaraj, S.K.; Sadishkumar, V.; Arun, T.; Thangadurai, P. Enhanced photocatalytic activity of V2O5 nanorods for the photodegradation of organic dyes: A detailed understanding of the mechanism and their antibacterial activity. *Mater. Sci. Semicon. Proc.* **2018**, *85*, 122–133. [CrossRef]
224. Sajid, M.M.; Shad, N.A.; Javed, Y.; Khan, S.B.; Zhang, Z.; Amin, N.; Zhai, H. Preparation and characterization of Vanadium pentoxide (V2O5) for photocatalytic degradation of monoazo and diazo dyes. *Surfaces Interfaces* **2020**, *19*, 100502. [CrossRef]
225. Aslam, M.; Ismail, I.M.I.; Salah, N.; Chandrasekaran, S.; Qamar, M.T.; Hameed, A. Evaluation of Sunlight Induced Structural Changes and Their Effect on the Photocatalytic Activity of V2O5 for the Degradation of Phenols. *J. Hazard. Mater.* **2015**, *286*, 127–135. [CrossRef]
226. Sahraeian, N.; Esmaeilzadeh, F.; Mowla, D. Hydrothermal synthesis of V2O5 nanospheres as catalyst for hydrogen sulfide removal from sour water. *Ceram. Int.* **2021**, *47*, 923–934. [CrossRef]
227. Monfort, O.; Roch, T.; Satrapinskyy, L.; Gregor, M.; Plecenik, T.; Plecenik, A.; Plesch, G. Reduction of V2O5 thin films deposited by aqueous sol–gel method toVO2(B) and investigation of its photocatalytic activity. *Appl. Surf. Sci.* **2014**, *322*, 21–27. [CrossRef]
228. Monfort, O.; Roch, T.; Gregor, M.; Satrapinskyy, L.; Plecenik, T.; Plecenik, A.; Plesch, G. Formation of vanadium oxide thin films prepared from aqueous sol-gel system. *Key Eng. Mater.* **2014**, *605*, 79–82. [CrossRef]
229. Saini, M.; Dehiya, B.S.; Umar, A. VO2(M)@CeO2 core-shell nanospheres for thermochromic smart Windows and photocatalytic applications. *Ceram. Int.* **2020**, *46*, 986–995. [CrossRef]
230. Chen, Z.; Cao, C.; Chen, S.; Luo, H.; Gao, Y. Crystallised mesoporous TiO2(A)–VO2(M/R) nanocomposite films with self-cleaning and excellent thermochromic properties. *Mater. Chem. A* **2014**, *2*, 11874. [CrossRef]
231. Li, W.; Ji, S.; Sun, G.; Ma, Y.; Guo, H.; Jin, P. Novel VO2(M)–ZnO heterostructured dandelions with combined thermochromic and photocatalytic properties for application in smart coatings. *New J. Chem.* **2016**, *40*, 2592–2600. [CrossRef]
232. Tao, X.; Hang, Q.; Wu, T.; Liao, F. Quasi-Hexagonal VO2/Ag3VO4 Microcrystals for Photo-Catalytic Degradation of Rhodamine B. *Asian J. Chem.* **2014**, *26*, 8291–8294. [CrossRef]
233. Li, Y.; Ji, S.; Gao, Y.; Luo, H.; Kanehira, M. Core-shell VO2@TiO2 nanorods that combine thermochromic and photocatalytic properties for application as energy-saving smart coatings. *Sci. Rep.* **2013**, *3*, 1370. [CrossRef]
234. Moshfegh, A.Z.; Ignatiev, A. Photo-Enhanced Catalytic Decomposition Of Isopropanol On V205. *Catal. Lett.* **1990**, *4*, 113–122. [CrossRef]

235. Jiang, B.; Peng, X.; Qu, Y.; Wang, H.; Tian, C.; Pan, Q.; Li, M.; Zhou, W.; Fu, H. A New Combustion Route to Synthesize Mixed Valence Vanadium Oxide Heterojunction Composites as Visible-Light-Driven Photocatalysts. *ChemCatChem* **2014**, *6*, 2553–2559. [CrossRef]
236. Zavahir, S.; Xiao, Q.; Sarina, S.; Zhao, J.; Bottle, S.; Wellard, M.; Jia, J.; Jing, L.; Huang, Y.; Blinco, J.P.; et al. Selective Oxidation of Aliphatic Alcohols using Molecular Oxygen at Ambient Temperature: Mixed-Valence Vanadium Oxide Photocatalysts. *ACS Catal.* **2016**, *6*, 3580–3588. [CrossRef]
237. Arunadevi, R.; Kavitha, B.; Rajarajan, M.; Suganthi, A. Synthesis of Ce/Mo-V4O9 nanoparticles with superior visible light photocatalytic activity for Rhodamine-B degradation. *J. Environ. Chem. Eng.* **2018**, *6*, 3349–3357. [CrossRef]
238. Malathi, A.; Madhavan, J.; Ashokkumar, M.; Arunachalam, P. A review on BiVO4 photocatalyst: Activity enhancement methods for solar photocatalytic applications. *Appl. Catal. A* **2018**, *555*, 47–74.
239. Samsudin, M.F.R.; Sufian, S.; Hameed, B.H. Epigrammatic progress and perspective on the photocatalytic properties of BiVO4-based photocatalyst in photocatalytic water treatment technology: A review. *J. Mol. Liq.* **2018**, *268*, 438–459. [CrossRef]
240. de la Martinez Cruz, A.; Perez, U.M.G. Photocatalytic properties of BiVO4 prepared by the co-precipitation method:Degradation of rhodamine B and possible reaction mechanisms under visible Irradiation. *Mater. Res. Bull.* **2010**, *45*, 135–141. [CrossRef]
241. Li, F.; Kang, Y.; Chen, M.; Liu, G.; Lv, W.; Yao, K.; Chen, P.; Huang, H. Photocatalytic degradation and removal mechanism of ibuprofen via monoclinic BiVO4 under simulated solar light. *Chemosphere* **2016**, *150*, 139–144. [CrossRef] [PubMed]
242. Shi, W.; Yan, Y.; Yan, X. Microwave-assisted synthesis of nano-scale BiVO4 photocatalysts and their excellent visible-light-driven photocatalytic activity for the degradation of ciprofloxacin. *Chem. Eng. J.* **2013**, *215–216*, 740–746. [CrossRef]
243. Kohtani, S.; Koshiko, M.; Kudo, A.; Tokumura, K.; Ishigaki, Y.; Toriba, A.; Hayakawa, K.; Nakagaki, R. Photodegradation of 4-alkylphenols using BiVO4 photocatalyst under irradiation with visible light from a solar simulator. *Appl. Catal. B* **2003**, *46*, 573–586. [CrossRef]
244. Huang, C.-M.; Pan, G.-T.; Peng, P.-Y.; Yang, T.C.K. In situ DRIFT study of photocatalytic degradation of gaseous isopropanol over BiVO4 under indoor illumination. *J. Mol. Catal. A Chem.* **2010**, *327*, 38–44. [CrossRef]
245. Wang, L.; Liu, J.; Song, W.; Wang, H.; Li, Y.; Liu, J.; Zhao, Z.; Tan, J.; Duan, Z.; Deng, J. Experimental and DFT insights of BiVO4 as an effective photocatalytic catalyst for N2O decomposition. *Chem. Eng. J.* **2019**, *366*, 504–513. [CrossRef]
246. Xie, B.; Zhang, H.; Cai, P.; Qiu, R.; Xiong, Y. Simultaneous photocatalytic reduction of Cr(VI) and oxidation of phenol over monoclinic BiVO4 under visible light irradiation. *Chemosphere* **2006**, *63*, 956–963. [CrossRef]
247. Jiang, L.; Chen, D.; Qin, L.; Liang, J.; Sun, X.; Huang, Y. Enhanced photocatalytic activity of hydrogenated BiVO4 with rich surface-oxygen-vacancies for remarkable degradation of tetracycline hydrochloride. *J. Alloys Compd.* **2019**, *783*, 10–18. [CrossRef]
248. Saison, T.; Chemin, N.; Chaneac, C.; Durupthy, O.; Mariey, L.; Mauge, F.; Brezova, V.; Jolivet, J.-P. New Insights Into BiVO4 Properties as Visible Light Photocatalyst. *J. Phys. Chem. C* **2015**, *119*, 12967–12977. [CrossRef]
249. Monfort, O.; Roch, T.; Gregor, M.; Satrapinskyy, L.; Raptis, D.; Lianos, P.; Plesch, G. Photooxidative properties of various BiVO4/TiO2 layered composite films and study of their photocatalytic mechanism in pollutant degradation. *J. Environ. Chem. Eng.* **2017**, *5*, 5143–5149. [CrossRef]
250. Li, J.; Lu, P.; Deng, W.; Zeng, Z.; Lin, L.; Zhao, G. Facile synthesis of sheet-like BiVO4/Bi4V2O11 composite for enhanced photocatalytic properties. *Mater. Chem. Phys.* **2020**, *254*, 123489. [CrossRef]
251. Pu, Y.; Liu, T.; Huang, Y.; Chen, C.; Kim, S.I.; Seo, H.J. Optical properties and visible-light-driven photocatalytic activity of Bi8V2O17 nanoparticles. *J. Nanopart. Res.* **2015**, *17*, 202. [CrossRef]
252. Ghiyasiya-Arani, M.; Salavati-Niasari, M.; Masjedi-Arani, M.; Mazloom, F. An easy sonochemical route for synthesis, characterization and photocatalytic performance of nanosized FeVO4 in the presence of aminoacids as green capping agents. *J. Mater. Sci. Mater. Electron.* **2018**, *29*, 474–485. [CrossRef]
253. Liu, Z.; Lu, Q.; Wei, M.; Guo, E. $FeVO_4$ nanobelts: Controllable synthesis by electrospinning and visible-light photocatalytic properties. *J. Sol-Gel Sci. Technol.* **2017**, *82*, 67–74. [CrossRef]
254. Tan, G.; Xu, C.; Ren, H.; Yang, W.; Zhao, C.; Xia, A. Synthesis and Photocatalytic Activities of Bamboo-Like $FeVO_4$ Nanocrystalline. *J. Nano Res.* **2017**, *46*, 123–134. [CrossRef]
255. Zhang, J.; Zhao, W.; Li, Z.; Lu, G.; Zhu, M. Visible-light-assisted peroxymonosulfate activation over Fe(II)/V(IV) selfdoped FeVO4 nanobelts with enhanced sulfamethoxazole degradation: Performance and mechanism. *Chem. Eng. J.* **2021**, *403*, 126384. [CrossRef]
256. Rahimpour, R.; Chaibakhsh, N.; Zanjanchi, M.A.; Moradi-Shoeili, Z. Fabrication of ZnO/FeVO4 heterojunction nanocomposite with high catalytic activity in photo-Fenton-like process. *J. Alloys Compd.* **2020**, *817*, 152702. [CrossRef]
257. Eshaq, G.H.; Wang, S.; Sun, H.; Sillanpaa, M. Superior performance of FeVO4@CeO2 uniform core-shell nanostructures in heterogeneous Fenton-sonophotocatalytic degradation of 4-nitrophenol. *J. Hazard. Mater.* **2020**, *382*, 121059. [CrossRef] [PubMed]
258. Sajid, M.M.; Khan, S.B.; Shad, N.A.; Amin, N.; Zhang, Z. Visible light assisted photocatalytic degradation of crystal violet dye and electrochemical detection of ascorbic acid using a BiVO4/FeVO4 heterojunction composite. *RSC Adv.* **2018**, *8*, 23489. [CrossRef]
259. Wang, Q.; Liu, Z.; Lu, Q.; Guo, E.; Wei, M. Fabrication of Direct Z-scheme a-Fe2O3/FeVO4 Nanobelts with Enhanced Photoelectrochemical Performance. *ChemistrySelect* **2018**, *3*, 809–815. [CrossRef]
260. Marikkani, S.; Vinoth Kumar, J.; Muthuraj, V. Design of novel solar-light driven sponge-like Fe2V4O13 photocatalyst: A unique platform for the photoreduction of carcinogenic hexavalent chromium. *Sol. Energy* **2019**, *188*, 849–856. [CrossRef]

261. Gowthami, K.; Krishnakumar, B.; Thirunarayanan, G.; Swaminathan, M.; Muthuvel, I. Novel Fe2V4O13/ZnO nano-heterojunction: Effective decomposition of methyl orange under solar light irradiation. *Mater. Today-Proc.* **2020**, *29*, 1199–1203. [CrossRef]
262. Tahir, M. Hierarchical 3D VO2/ZnV2O4 microspheres as an excellent visible light photocatalyst for CO2 reduction to solar fuels. *Appl. Surf. Sci.* **2019**, *467–468*, 1170–1180. [CrossRef]
263. Wang, R.; Cao, L. Facile synthesis of a novel visible-light-driven AgVO3/BiVO4 heterojunction photocatalyst and mechanism insight. *J. Alloys Compd.* **2017**, *722*, 445–451. [CrossRef]
264. Cui, X.; Liu, Z.; Li, G.; Zhang, M.; Song, Y.; Wang, J. Self-generating CeVO4 as conductive channel within CeO2/CeVO4/V2O5 to induce Z-scheme charge-transfer driven photocatalytic degradation coupled with hydrogen production. *Int. J. Hydrogen Energy* **2019**, *44*, 23921–23935. [CrossRef]
265. Hu, Y.; Fan, J.; Pu, C.; Li, H.; Liu, E.; Hu, X. Facile synthesis of double cone-shaped Ag4V2O7/BiVO4 nanocomposites with enhanced visible light photocatalytic activity for environmental purification. *J. Photochem. Photobiol. A* **2017**, *337*, 172–183. [CrossRef]
266. Wang, P.; Yang, H.; Wang, D.; Chen, A.; Dai, W.L.; Zhao, X.; Yang, J.; Wang, X. Activation of Kagome lattice-structured Cu3V2O7(OH)2·2H2O volborthite via hydrothermal crystallization for boosting visible light-driven water oxidation. *Phys. Chem. Chem. Phys.* **2018**, *20*, 24561–24569. [CrossRef]
267. Min, W.; Qiong, L. Synthesis and Photocatalytic Property of Cu3V2O8 Prepared by Liquid Phase Precipitation. *Adv. Mater. Res.* **2011**, *236–238*, 1675–1678.
268. Kalal, S.; Pandey, A.; Ameta, R.; Punjabi, P.B. Heterogeneous photo-Fenton-like catalysts Cu2V2O7 and Cr2V4O13 for an efficient removal of azo dye in water. *Cogent Chem.* **2016**, *2*, 1143344. [CrossRef]

processes

MDPI

Article

Degradation of Direct Blue 1 through Heterogeneous Photocatalysis with TiO_2 Irradiated with E-Beam

Elvia Gallegos [1,2], Florinella Muñoz Bisesti [3], Katherine Vaca-Escobar [1], Cristian Santacruz [4], Lenys Fernández [1], Alexis Debut [5] and Patricio J. Espinoza-Montero [1,*]

1 Escuela de Ciencias Químicas, Pontificia Universidad Católica del Ecuador, Av. 12 de Octubre 1076, P.O. Box 17-01-2184, Quito, Ecuador; elvia.gallegosc@epn.edu.ec (E.G.); krvaca@puce.edu.ec (K.V.-E.); lmfernandez@puce.edu.ec (L.F.)

2 Departamento de Ingeniería Civil y Ambiental, Escuela Politécnica Nacional, Ladrón de Guevara E11·253, P.O. Box 17-01-2759, Quito, Ecuador

3 Departamento de Ciencias Nucleares, Escuela Politécnica Nacional, Ladrón de Guevara E11·253, P.O. Box 17-01-2759, Quito, Ecuador; florinella.munoz@epn.edu.ec

4 Departamento de Física, Escuela Politécnica Nacional, Ladrón de Guevara E11-253, P.O. Box 17-01-2759, Quito, Ecuador; cristian.santacruz@epn.edu.ec

5 Centro de Nanociencia y Nanotecnología, Universidad de las Fuerzas Armadas ESPE, Av. Gral. Rumiñahui s/n, P.O. Box 171-5-231B, Sangolquí, Ecuador; apdebut@espe.edu.ec

* Correspondence: pespinoza646@puce.edu.ec; Tel.: +593-2299-1700 (ext. 1929)

Received: 1 April 2020; Accepted: 7 September 2020; Published: 18 September 2020

Abstract: Most dyes used in the textile industry are chemically stable and poorly biodegradable, therefore, they are persistent in the environment and difficult to degrade by conventional methods. An alternative treatment for this kind of substance is heterogeneous photocatalysis using TiO_2, so, in this work, it is proposed to degrade Direct Blue 1 (DB1) using microparticulate TiO_2 irradiated with e-beam at three different doses: 5, 10 and 20 kGy (J/kg). The DB1 degradation was implemented in a batch reactor (DB1 initial concentration = 50 mg L^{-1}, pH 2.5, TiO_2 concentration = 200 mg L^{-1}). We have demonstrated that the photocatalytic power of TiO_2, when irradiated with e-beam (5, 10, 20 kGy), varies slightly, with minor effects on photodegradation performance. However, the dose of 10 kGy showed a slightly better result, according to the DB1 photodegradation rate constant. Adsorption process was not affected by irradiation; its isotherm was fitted to Freundlich's mathematical model. The DB1 photodegradation rate constants, after one hour of treatment, were: 0.0661 and 0.0742 min^{-1} for irradiated (10 kGy) and nonirradiated TiO_2, respectively. The degradation rate constant has an increase of 12.3% for irradiated TiO_2. Finally, there was no evidence of mineralization in the degradation process after 60 min of treatment. According to the results, the irradiation of microparticulate TiO_2 with e-beam (10 kGy) slightly improves the photodegradation rate constant of DB1.

Keywords: Direct Blue 1; irradiated TiO_2; heterogeneous photocatalysis; electron-beam; adsorption

1. Introduction

Effluents from the textile industry are considered an important environmental problem because it is difficult to treat due to their high nonbiodegradable load, partially attributed to the dye presence. At present, 100,000 different types of dyes are produced, of which about 36,000 tons dye/year are consumed by the textile industries [1]. The dyes are used in the dyeing stage, where up to 30% of them come off, becoming part of the industrial discharge [2].

Among the most used dyes are those of the azo type, which constitute around 70% of world production [3], due to their ease of preparation and the wide range of colors in which they are offered. These dyes have chromophore groups formed by double bonds –N=N– and have high stability to light

and washing. Most of them are sulfonic acids or their salts [4]. Its high stability determines properties of difficult degradation by conventional treatment methods; therefore, they are an important source of chemical and esthetic contamination [2]. Among the environmental problems caused by azo dyes are: color in effluents, visual pollution and eutrophication of water bodies, effects on gases solubility in water [5], generation of toxic, carcinogenic or mutagenic amines under specific conditions [6] and alterations in soil microbial biological activity of populations when they have been subjected to irrigation [7], among others.

One of the azo dyes used in the staining of denim fabrics in Ecuador, particularly in Pelileo (city located in the country center), is Direct Blue 1 (DB1), whose structure is shown in Figure 1, and it has two azo groups in its composition, it has a molecular weight of 992.82 g mol^{-1}, which resists temperatures of up to 300 °C, and is difficult to degrade by conventional methods.

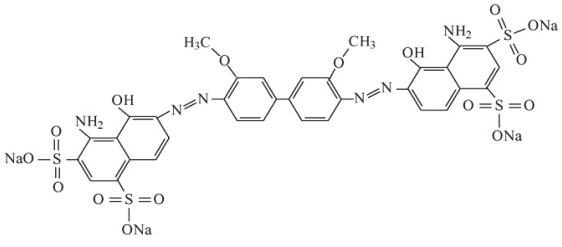

Figure 1. Direct Blue 1 (DB1) structure [8].

As an alternative treatment for compounds of difficult degradation, there are Advanced Oxidation Processes (AOPs), which are characterized by the oxidation reactions promoted by the hydroxyl radical (•OH) [9,10]. AOPs have been extensively studied for the oxidation of persistent compounds in water [11], such as dyes. Its advantages are simple handling, the relatively low cost of the reagents [9], as well as the oxidation of organic matter, even reaching its total mineralization (CO_2, H_2O and inorganic salts) [1]. A brief summary of some AOPs and other methodologies used for DB1 degradation are shown in Table 1:

Table 1. DB1 degradation using Advanced Oxidation Processes (AOPs) and other methodologies.

Treatment	Operating Conditions	DB1 Concentration	Removal	Other Results	Ref.
Photocatalysis with C_5N_4 irradiated	V = 20 mL; pH = 7; catalyst concentration = 100 mg L^{-1}; reactor batch.	50 mg L^{-1}	Complete discoloration after 60 min of treatment	Low percentages of mineralization (10%)	[12]
Ozonation and electrocoagulation	V = 200 L, Q = 10 L min^{-1}; ozone injection = 5.21 mg min^{-1}; 1100 L tank capacity; $\frac{3}{4}$ in hydraulic line pipe. V = 1 L; electrode area = 160 cm^2; i = 5 mA cm^{-2}; aluminum anodes; iron cathodes.	50 mg L^{-1}	50% color removal after 210 min 99% color removal after 20 min	Electrocoagulation is more economically viable than ozonation, since it promotes greater dye removal and requires less energy consumption	[13]
AOPs using pulsed corona discharge from water.	V = 300 mL; Q = 100 mL min^{-1}, peroxide rate = 8.8×10^{-4} mol L^{-1}, pH = 3.5–10.3; conductivity = 100 µS cm^{-1}	10 mg L^{-1}	75–80% color removal after 60 min.	The addition of hydrogen peroxide improves the discoloration rate.	[14]
Photocatalysis with TiO_2 films	V = 250 mL; pH = 2–10; 200 W mercury lamp	4–10 mg L^{-1}	98% degradation after 1800 min at pH = 2	Decrease 12 to 46% removal of COD at a pH of 2 by varying dye concentration	[15]
Photocatalysis with TiO_2 and ZnO supported on polystyrene and polyethylene terephthalate	pH = 2.5 y 6 (TiO_2) y 7–11 (ZnO), 8 W UV lamps	50 mg L^{-1}	100% degradation after 50 min with the two catalysts	The immobilized catalyst mass reached 0.399 mg cm^{-3} for TiO_2 and 0.689 mg cm^{-2} for ZnO in PET. The highest photocatalytic degradation was at pH = 2.5 using TiO_2.	[16]
Photocatalytic degradation using rutile TiO_2	-	-	Discoloration and removal of COD 60%	The rutile activity improves making a composite of it with polyaniline.	[17]
Photocatalysis with Fe_2O_3 compounds, surrounded by C_3N_4 and amorphous carbon.	V = 20 mL, T = 20 °C; pH = 7; catalyst mass = 50 mg; H_2O_2 30% solution; 35 W Xe lamp	500 mg L^{-1}	Degradation greater than 99% after 50 min with C_3N_4 and the same value after 35 min with the CN-Fe compound	TOC removal does not exceed 15%. Three cycle catalyst reuses with 99% removal results.	[18]
Peroxidase-mediated discoloration	H_2O_2 concentration = 2.4 mM; nano enzyme concentration = 150 nM	10 µM L^{-1}	Complete discoloration of DB1 after three days.	-	[19]
Photocatalytic degradation with biogenic copper synthesized from native *Escherichia* sp.	V = 100 mL; catalyst mass = 100 mg; use of solar radiation	25–100 mg L^{-1}	Discoloration of 88.42% after 5 h of exposure.	The concentrations of total dissolved solids, COD, hardness, chlorides, sulfates, electrical conductivity, total suspended solids, turbidity, and pH decreased.	[20]
Biosorptions using biomass of *Trametes versicolor*	V = 50 mL; biomass = 250 mg; pH = 2–9; T = 25 °C; batch system	25–800 mg L^{-1}	Maximum biosorptions of 101.1 mg g^{-1} for the native fungus and 152.3 mg g^{-1} for the treated fungus.	Technology projection on a large scale.	[8]
Biotransformation by *Marinonacter* sp.	V = 100 mL; T = 37 °C; pH = 8; concentration NaCl = 70 g L^{-1}	100 mg L^{-1}	Complete discoloration after 6 h	Less toxicity of the metabolites with respect to the dye.	[21]
Adsorption, using low-cost adsorbents	V = 50 mL; T = 28 ± 2 °C; batch mode;	21%	Appreciable decrease in COD (70–90%) in samples treated for 1 h.	Cane bagasse is better absorbent than sawdust by 10% and brick dust by 25%	[22]
Discoloration by *Bacillus* sp.	NaCl concentration = 0–9%, pH = 5–9; T = 20–35 °C	150 mg L^{-1}	47% discoloration after 24 h, 57% after 48 h and 73% after 72 h, all at pH = 7	The discoloration for the treatment in which the initial concentration was 25 mg L^{-1}, was 25.10% and 29.51% higher, for 1 h and 5 h, respectively.	[23]
Degradation by laccase	V = 10 mL; laccase mass = 0.5 g; T = 30 °C	50 mg L^{-1}	54 and 68% degradation for 18 h for the free and immobilized enzyme, respectively.	-	[24]
Discoloration by laccase from *Pycnoporus cinnabarinus*	V = 3.1 mL; pH = 4.9; laccase mass = 0.82–25 µg	25 mg L^{-1}	The disappearance of the dye is confirmed after contact with oxygen.	-	[25]
Degradation by azoreductase and laccase	-	0.6 mol L^{-1}	80% discoloration after 24 h.	Production of toxic by-products in some cases, for example 3,3 dimethoxybenzidine in the case of DB1.	[26]
Adsorption using cement kiln powder	V = 250 mL, cement mass = g; Stirring speed = rpm	800 mg L^{-1}	The removal is greater than the one carried out with activated carbon.	When washing the cement with colorant, it does not return to the water.	[27]

A widely used AOP is heterogeneous photocatalysis with TiO_2, which consists of an electron-hole pair (e^--h^+) generation, by excitation of the electron from a semiconductor through UV radiation. The holes oxidize the hydroxyl ion in water to generate hydroxyl radicals (•OH), and electrons are transferred to adsorbed molecular oxygen to generate a superoxide ion. The •OH generation allows the degradation of the target pollutant [10].

TiO_2 is a cheap, chemically stable, and nontoxic semiconductor. Several studies have been developed to improve its photocatalytic activity [28], for instance: doping with metal ions, doping with nonmetals, formation of compounds with TiO_2 and with less energetic band gap semiconductors or with noble gases, dye sensitization, or rare earth modifications [10]. Some studies have applied ionizing radiation, particularly accelerated electrons (e-beam), to TiO_2 nanoparticles, improving their photocatalytic activity [8,9]. There are few studies on this last modification, therefore, in this work the photocatalytic degradation of the DB1 dye is studied using a TiO_2 microparticulate irradiated with accelerated electrons.

2. Materials and Methods

2.1. Reagents and Equipment

TiO_2 Hombitan (commercial grade, 325 μm microparticulate) previously sieved, DB1 Dyetex, Quito-Ecuador and H_2SO_4 1 N (Merck, Quito-Ecuador) were used. The equipment used was: ELU6U linear electron accelerator with 8 MeV power, EMPIREAN model PANanalytical diffractometer, Shimadzu TOC-5 total organic carbon meter, Hitachi U 1900, Tokio-Japan spectrophotometer, HACH 2800, Loveland-USA spectrophotometer, LABEC magnetic stirrer VELP, 15 W Sylvania Mercury.

2.2. TiO_2 Irradiation

A total of 2 g of TiO_2 Hombitan by Venator Materials was placed in LDPE low-density polyethylene bags, and those bags were irradiated in a linear electron accelerator (ELU6U) at three doses: 5, 10 and 20 kGy (J/kg) [29,30].

2.3. TiO_2 Characterization

TiO_2 was characterized by X-Ray Diffraction (XRD), operating in a θ-2θ configuration (Bragg–Brentano geometry) equipped with a copper X-ray tube (Kα-λ = 1.54056 Å) at 45 kV and 40 mA. The diffractograms analysis was performed on the average of four measurements between the angles 5° to 90° (θ-2θ) using the High Score Plus software.

Diffuse Reflectance Spectroscopy (DRS) was obtained at room temperature using a UV–VIS spectrometer equipped with an integrating sphere (Perkin Elmer, Lambda 365). The energy band gap of TiO_2 samples was determined by extrapolating the slope to R→0 in the plot $(R{\cdot}h\upsilon)^n$ versus $h\upsilon$, where R is the reflectance, $h\upsilon$ is the photon energy and n = 2 corresponds to direct allowed transitions [31–34]. The best fit to a straight line near the absorption edge was used to determine the energy band gap.

Infrared absorption of TiO_2 powder samples was obtained by measuring the Fourier transform infrared (FTIR) in a Jasco FT/IR 4700 spectrometer. Samples were analyzed at room temperature in a region of 4000–400 cm^{-1}. Spectral resolution was 1 cm^{-1}. Adsorbed water was removed from TiO_2 powder by heating the samples to 50 °C for 24 h. TiO_2 powder was mixed with KBr and pressed into pellets.

Finally, elemental analysis by Energy-Dispersive X-ray Spectroscopy (EDS) was performed in a RESCAN MIRA 3 scanning electron microscope.

2.4. DB1 Degradation Tests with Irradiated TiO_2

The photocatalysis process was implemented in a batch reactor equipped with two Sylvania 15 W mercury lamps, with a working wavelength of 254 nm (UV region), two acrylic chambers and a water-cooling system (Figure 2), which allowed for keeping the temperature constant.

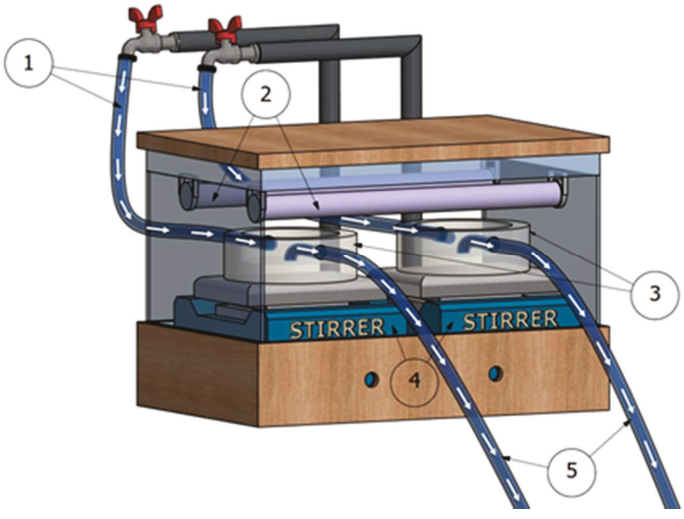

Figure 2. Diagram of the photoreactor used in the degradation of the DB1 dye. (1) Water inlet, (2) UV lamps, (3) Samples, (4) Magnetic stirrers, (5) Water outlet.

The effluent used was water with an initial concentration of 50 mg L^{-1} of DB1 dye, and 200 mg L^{-1} of both irradiated and nonirradiated TiO_2 [16,17]. Then, ultrasound was applied for 10 min to the mixture.

Photodegradation was performed for 60 min, with stirring at 200 rpm [35] using a magnetic stirrer, Figure 2, and the change in pH was also followed by taking measurements at the beginning and at the end of the process. To verify degradation, aliquots were taken at different times, which were centrifuged (6000 rpm) to separate the catalyst from the sample. The sample was filtered through a Whatman filter with a pore diameter of 0.45 µm. The DB1 concentration decrease was followed by spectrophotometry, at a wavelength of 565 nm [18]. The concentrations were obtained from a previously prepared calibration curve.

The DB1 degradation reaction constant was determined after one hour of photodegradation by fitting the experimental data to a kinetic model.

The irradiation dose effect on reaction rate was analyzed using a completely randomized design (CRD), the independent variable was irradiation dose and the response variable was the reaction constant. Statistical analyzes were developed in STATGRAPHICS Centurion XVIII software. The experiments were made in triplicate.

2.5. Adsorption Kinetics

DB1 adsorption in nonirradiated and irradiated TiO_2 was studied for different doses (5, 10 and 20 kGy). This study was made using the Figure 2 reactor, in the same photodegradation conditions ($C_{o,\,DB1}$ = 50 mg L^{-1}; catalyst dose = 200 mg L^{-1}; pHo = 2.5; T_{amb}) in light absence. Samples were taken every 10 min, during 50 min and were analyzed by spectrophotometry. With the experimental data of DB1 concentration, DB1 adsorption kinetics on TiO_2 were determined, with which the adsorption equilibrium time was established.

2.6. Adsorption Isotherms

Solutions with different DB1 concentrations, in a range of 25 to 250 mg L^{-1}, were prepared. The conditions established in the previous section were used (Catalyst dose = 200 mg L^{-1}; pH = 2.5; T_{amb}). Samples were taken after reaching the equilibrium time, previously determined, these samples were filtered through 0.45 µm filters and measured by UV-vis spectrophotometry.

Experimental data were analyzed to identify if they fit Langmuir or Freundlich mathematical models, and the irradiation dose influence in adsorption onto TiO_2 was studied using a CRD, in which the design variable was the irradiation dose (0 kGy and best dose) and the response variable was the best adjusted kinetic constant. Statistical analyzes were done in STATGRAPHICS Centurion XVIII software. The samples were taken in triplicate.

2.7. Contact Angles

The static contact angles were measured following the procedure described by [31–35]. Dried titanium dioxide samples were stored at ambient conditions before measurement. TiO_2 powder was sprinkled uniformly on a 2 × 2 cm clean flat surface. A glass microscope slide (20 × 10 × 2 mm) was covered with double-sided adhesive tape. The tape was pressed to the powder with a 500 g weight for 10 s. The excess of powder was removed by using a razor blade. Finally, the slide was shaken to remove nonadhered material. This preparation technique produces a uniform powder surface. Measurements were taken immediately at ambient conditions, 20 °C and 60% relative humidity. For the static contact angle, an 8 µL droplet of deionized water was placed on the slide, and within 30 s three contact angle readings were measured (Dataphysics, OCA 25 equipped with electronic syringe module ESr-N). Each measurement was taken on three different positions of the slide and repeated on three slides. The average value is reported.

2.8. Mineralization Levels through TOC

Dye mineralization levels were measured at the beginning and ending of the process, through the determination of Total Organic Carbon (TOC), using method 5310 of the Standard Methods for the Examination of Water and Wastewater.

3. Results

3.1. X-ray Diffraction, Band Gap by DRS and FTIR Spectroscopy

Figure 3 show the two samples analyzed patterns (TiO_2 nonirradiated and TiO_2 irradiated).

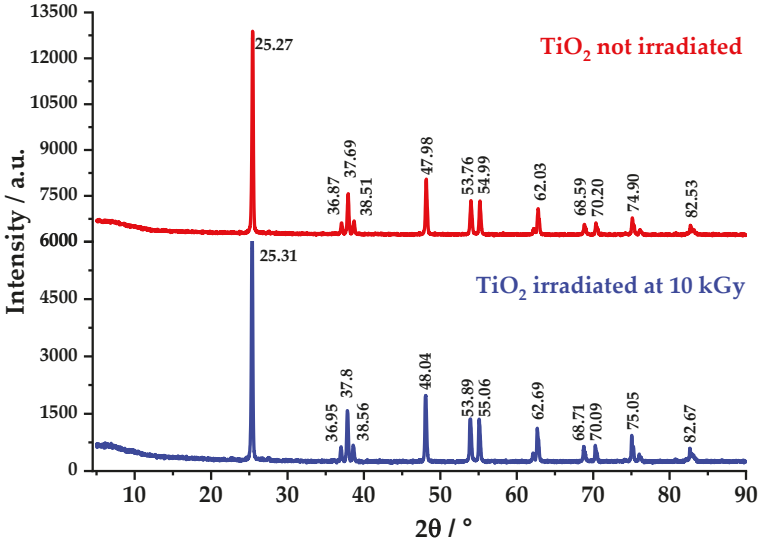

Figure 3. TiO_2 X-ray diffraction with and without irradiation.

Figure 4 shows the FTIR spectra of TiO_2 samples, with and without e-beam treatment measured under ambient pressure conditions at the same humidity.

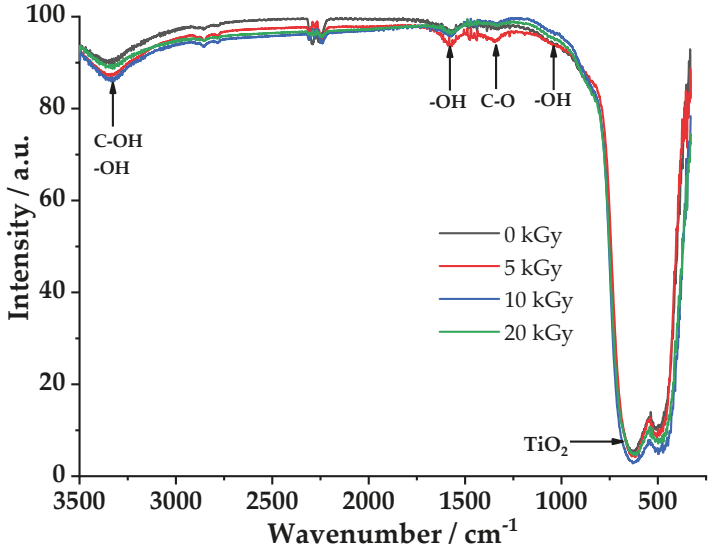

Figure 4. FT-IR spectra of TiO_2 with and without e-beam treatment measured under ambient conditions. Inset, a magnified view of the spectrum of the samples.

Band gap measurements were performed using DRS to determine if there were any changes in the optical properties of TiO_2 caused by e-beam treatment (5, 10, and 20 kGy) (Figure 5).

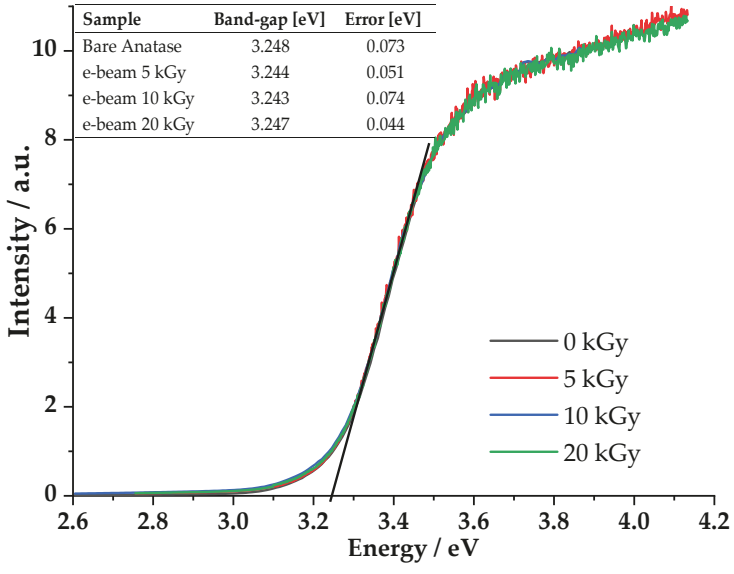

Figure 5. Diffuse Reflectance Spectroscopy (DRS) spectra of TiO_2 with and without e-beam treatment are displayed. Inset, the band gaps estimated from the DRS spectra are summarized.

In order to verify the presence of C in the samples of TiO_2, EDS analysis was performed. Figure 6 shows an analysis based on mapping that identifies the elements that conform the sample. It is noted that the elements of the sample are O, Ti and C. The presence of C is attributed to the impurities in the sample. The averages of each element were 48.74%, 48.26%, and 3.00%, respectively.

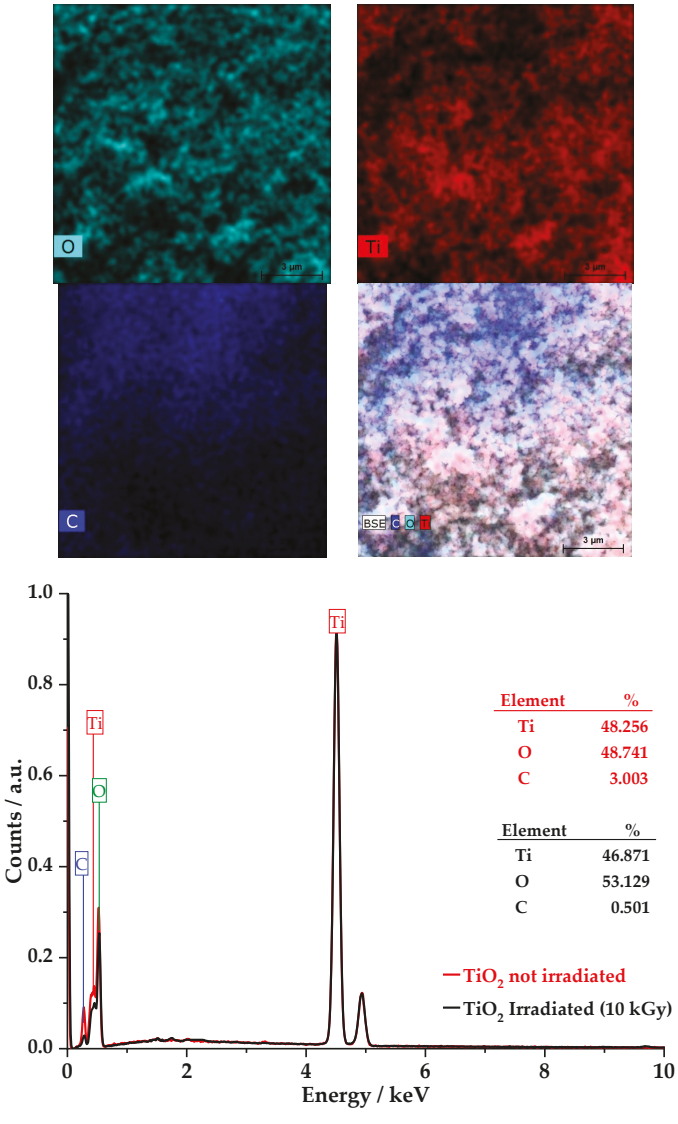

Figure 6. Energy-Dispersive X-ray Spectroscopy (EDS) mapping of composition of sample of TiO_2 without irradiation, and EDS spectrum of irradiated and unirradiated TiO_2.

3.2. Heterogeneous Photocatalysis

The curves obtained from DB1 dye degradation by heterogeneous photocatalysis with TiO_2 irradiated at various doses and nonirradiated are shown in Figure 7.

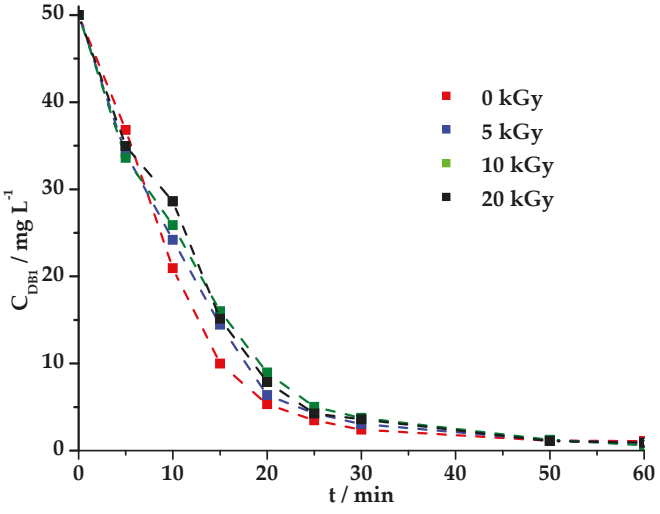

Figure 7. DB1 photodegradation on TiO_2 with and without e-beam treatment is displayed. Conditions: $C_{o,\,DB1}$ = 50 mg L^{-1}; catalyst dose = 200 mg L^{-1}; pH_o = 2,5; $T_{amb} \approx 20$ °C.

To determine the dye degradation reaction constants, a linear fit was performed as shown in Figure 8. The experimental data were adapted to a pseudo first order kinetic model which is consistent with what was reported in other studies [16,36]. Results are shown in Table 2. Subsequently, an ANOVA was performed (Figure 9) in order to analyze dye degradation constant rates.

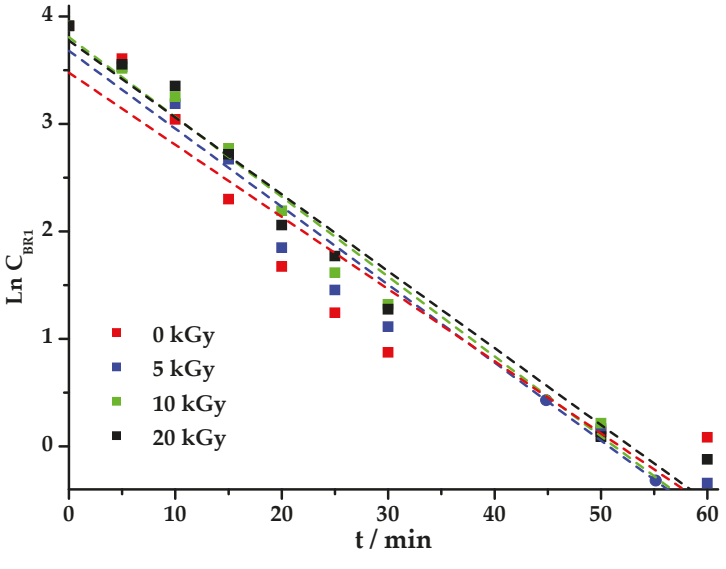

Figure 8. DB1 linear adjustment according to pseudo first order kinetics, data from Figure 7.

Table 2. Rate constants for pseudo first order reaction at different irradiation doses.

Radiation Dose (kGy)	Constant Rate	r^2
Not irradiated	0.0661	0.8826
5	0.0677	0.9273
10	0.0742	0.9818
20	0.0715	0.9644

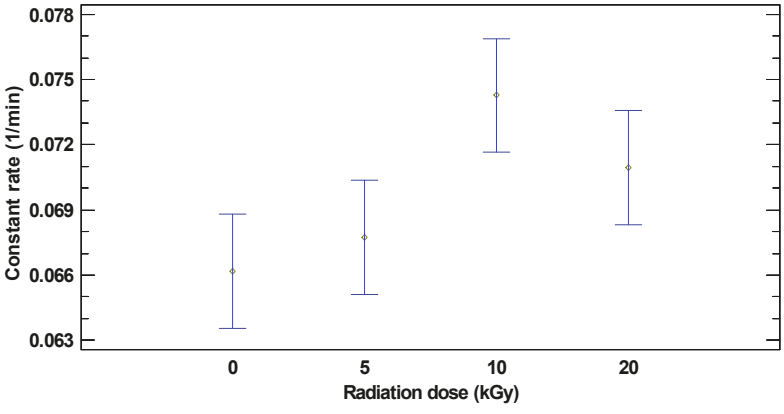

Figure 9. Statistical analysis of irradiation dose effect on the photodegradation of DB1. Conditions: $C_{o,\,DB1}$ = 50 mg L^{-1}; catalyst dose = 200 mg L^{-1}; pH_o = 2.5; $T_{amb} \approx 20$ °C.

3.3. Isotherms of Adsorption

Adsorption isotherms obtained were "S" type, they can be observed in Figure 10:

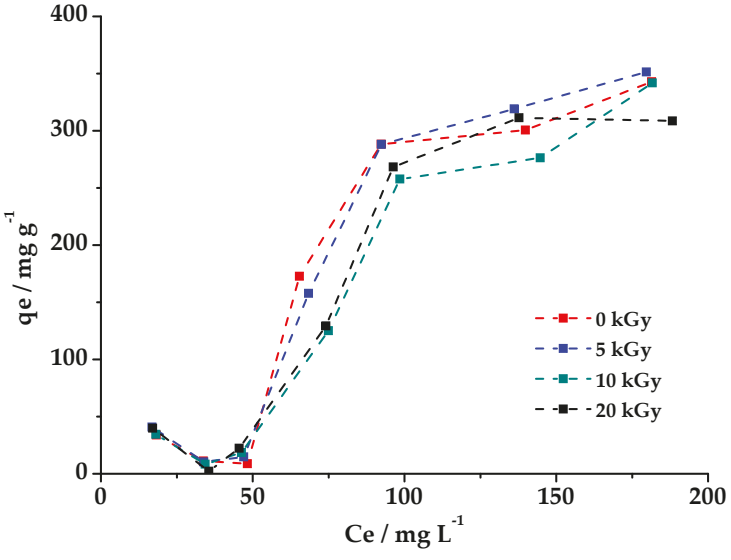

Figure 10. Adsorption DB1 dye isotherms of unirradiated and irradiated TiO_2 at different doses (5, 10 y 20 kGy).

With increasing concentrations, isotherms took a trend that was later adapted to the Freundlich mathematical model (Equation (1)) with high correlations (Table 3). With the experimental data from this linearization, adsorption constant K_f was obtained for each adsorption dose. Their average values are detailed in Table 3. In addition, a statistical analysis of the K_f was performed using CRD as shown in Figure 11.

$$\log(Q_e) = \log(K_f) + \frac{1}{n}\log(C_e) \quad (1)$$

Table 3. Freundlich isotherm parameters.

Doses (kGy)	Parameters		
	r^2	K_f (mg g^{-1})	N
0	0.947	1.897	0.959
5	0.970	2.913	1.047
10	0.968	1.810	0.981
20	0.945	2.962	1.084

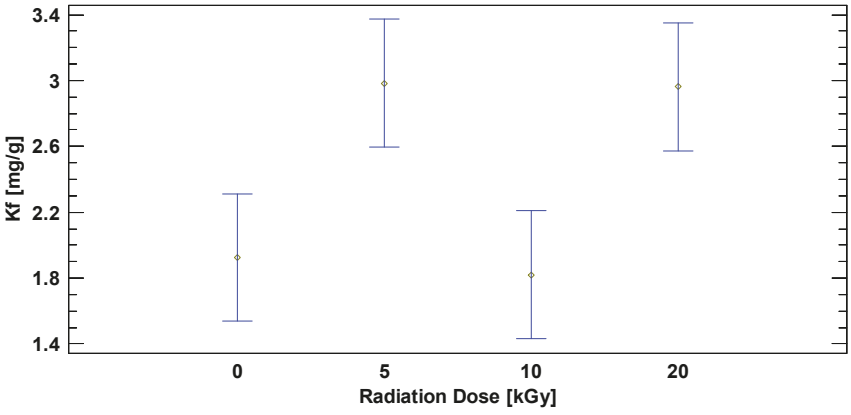

Figure 11. Statistical analysis of irradiation dose effect on DB1 adsorption. ($C_{O,\,DB1}$ = 50 mg L^{-1}; catalyst dose = 200 mg L^{-1}; pH_o = 2.5; T_{amb}).

3.4. Mineralization

In Table 4, the percentages of DB1 mineralization levels achieved after one hour of treatment are presented.

Table 4. % Total Organic Carbon (TOC) removal during DB1 degradation after 60 min of treatment.

Doses kGy	%TOC
0	2.48
10	1.61

3.5. Contact Angles

The contact angle by sessile drop of the nonirradiated and irradiated TiO_2 samples are shown in Figure 12 (insert).

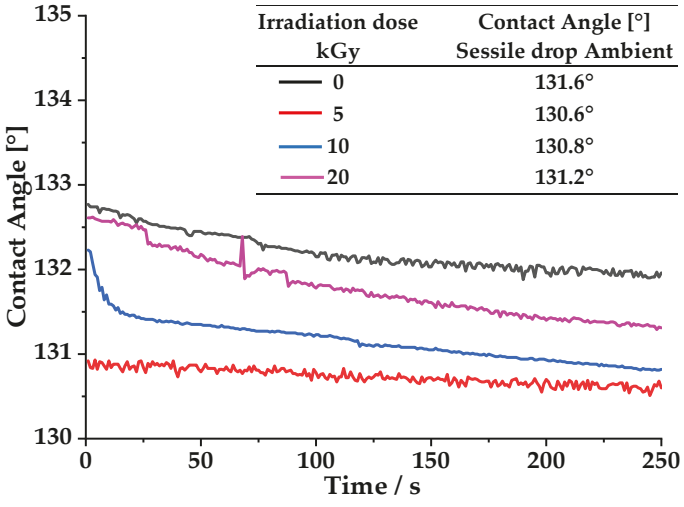

Figure 12. Contact angle by sessile drop without drying the sample (ambient), of the nonirradiated and irradiated TiO_2. Insert, contact angle.

4. Discussion

4.1. X-ray Diffraction, Band Gap by DRS and FTIR Spectroscopy

Figure 3 shows TiO_2 X-ray diffraction patterns with and without irradiation. The main features of the XRD pattern of the two samples are similar, peaks at 25 and 48 degrees, which are anatase phase characteristic peaks [37], and it shows that the crystalline phase used for the photocatalyst when it was irradiated with accelerated electrons did not change. This result is in agreement with the ones found in other studies. A study has pointed out that there were no significant changes in the TiO_2 phase composition and crystal lattice when it was subjected to gamma irradiation at different doses (30–150 kGy) [38]. Another study shows that there were no changes in TiO_2 when it was irradiated with e-beam with an energy of 5 MeV and a current of 200 μA [39]. Also, the peaks in Figure 3 are in good agreement with the standard spectrum and XRD patterns were similar, indicating that there was no change in the crystallinity of TiO_2 caused by the e-beam treatment [39,40]. However, reports that changes in structure and improvement in photocatalytic activity were obtained at highest doses (5 MGy) [41].

The FTIR analysis results of the four TiO_2 samples with and without e-beam treatment, obtained under similar environmental conditions (same humidity), are shown in Figure 4. The samples treated at 5 and 10 kGy clearly show an increased signal corresponding to water. Signals at 3300, 1600 and 900 cm^{-1} can be attributed to the OH-stretching, bending and vibrational water modes, respectively [42–44]. It is difficult to discriminate OH on C groups in IR spectra, because the C-O-H stretch overlaps the OH stretch of water adsorbed on the surface. However, in the electron beam-treated samples, especially at 5 kGy, the peak of the C–O stretching at 1400 cm^{-1} is more intense, and this does not happen with other samples. This result was confirmed by the contact angle (Figure 12), where the sample treated at 5 kGy has the lowest contact angle (that is the highest wettability). In line with these results, it can be confirmed that the amount of water adsorbed on the TiO_2 surfaces increased after e-beam treatment, i.e., the TiO_2 surfaces became more hydrophilic [29]. Therefore, partial oxidation of C impurities on TiO_2 could be responsible for the slight improvement of photocatalytic activity. While, the TiO_2 reticular vibration signal can be assigned to the band between 600–700 cm^{-1} [44]. The e-beam treatment had almost no influence on the geometric and electronic structures of TiO_2.

To corroborate the presence of residual carbon in TiO_2, from its synthesis, studies of EDS of the samples treated and not treated with e-beam were carried out. According to the results found,

the percentage of carbon decreased from 3.00% for the untreated sample to 0.50 % for the sample treated at 10 kGy (Figure 6). This leads us to presume that part of the impure C is released from the surface of TiO_2 with radiation, however this does not occur with the carbon that is within the TiO_2 crystalline structure. Apparently, the TiO_2 treatment with e-beam causes the carbon to acquire different oxidation states, which influences the photocatalytic behavior of TiO_2.

Diffuse Reflectance Spectroscopy (DRS) was used to determine band gap, which was obtained by the Kubelka–Munk function. It was plotted as a wavelength function, where the intercept on the x-axis (energy) of the linear extrapolation of the Kubelka–Munk function corresponds to the material's band-gap (Figure 5) [45]. The energy band gap for all TiO_2 samples, irradiated and unirradiated, was around 3.25 eV (Insert of the Figure 5) which corresponds to reported value of anatase [34]. The value of the band gap does not change significantly up to irradiation, indicating that the change in optical properties cannot be the reason for the slight variation in photocatalytic activity. These results are consistent with those reported in the literature [29].

Furthermore, XPS studies reported by Kim M. J. et al., for the TiO_2 surface, show that Ti 2p spectra for untreated and e-beam-treated TiO_2 samples (5, 10, and 15 kGy) show no structural changes. In contrast, the C 1s spectrum was significantly influenced by the e-beam treatment, i.e., the existing C as an impurity underwent a noticeable structural change in front of the e-beam. Finally, it has been shown that when 5 and 10 kGy e-beam doses were used to irradiate TiO_2 samples, the absolute intensity of the C 1s state increases with respect to the untreated sample. The center of the C 1s peak shifts to a higher binding energy after e-beam treatment. In the case of e-beam exposure at 15 kGy, the intensity of the C 1s peak decreases. The change in C 1s state after e-beam treatment is due to the formation of C-O bonds, causing the TiO_2 surface to become more hydrophilic [29,46]. The literature is complemented by the results shown in this paper, with regard to contact angle, band gap, EDS and FTIR.

In the case of TiO_2 irradiated at 20 kGy, C 1s is removed, provoking a slightly decrease in the FTIR signals intensity and an increase in the contact angle (reduces hydrophilicity). The decrease of C 1s is due to the elimination of C by oxidizing agents created in the atmosphere by the e-beams and may become more dominant than the C deposition from the atmosphere, or oxidation of existing ones [29].

4.2. Effect of Irradiation on Heterogeneous Photocatalysis

According to Figure 7, the degradation of the DB1 in the first 5 min is slightly faster in the case of TiO_2 irradiated at 10 kGy, however, after this time the degradation of the dye is slightly faster with nonirradiated TiO_2. Unexpectedly, after 50 min of treatment, there is again a breaking point, where the irradiated TiO_2 becomes lighter faster. Therefore, a statistical analysis of the degradation rate constant is convenient, and it is shown later. A degradation of around 98% is reached for all cases at 60 min of treatment.

A linear fit was performed to determine the dye degradation rate constants, as shown in Figure 8. The experimental data were adapted to a pseudo first order kinetic model. The rate constant averages for three replications are detailed in Table 2. Subsequently, an ANOVA was performed, Figure 9, in which we determined that there is a statistically significant difference ($p < 0.05$) in the reaction rate constants. This analysis indicates that the 10 kGy dose is the one that presents an improvement in the reaction rate constant, which is due an increase in the concentration of C-O bonds coming from impurities on the surface of TiO_2 [29].

4.3. Effect of Irradiation Dose on Adsorption

The adsorption isotherms obtained were "S" type; that is, at low concentrations of adsorbate (DB1), the surface (TiO_2) presents collateral associations, a process known as "cooperative adsorption" [47]. This kind of adsorption behavior implies a moderate intermolecular attraction between the adsorbate and the adsorbent, where there is a strong competition for the adsorption centers with solvent molecules or other adsorbates [48]. This process is identified in the isotherm as a turning point in the low concentration zone (Figure 10), as the adsorbate concentration increases, it presents better affinity

towards the surface, and can be seen as an increase in the curve slope until saturation of available sites is reached (maximum adsorption).

With increasing concentrations, isotherms take a trend that is later adapted to the Freundlich mathematical model with high correlations, Table 3. With the experimental data from this linearization, the adsorption constant K_f was obtained for each adsorption dose; this constant is an approximate indicator of the maximum adsorption capacity on TiO_2 [49]. Their average values are detailed in Table 3.

Using a CRD, in which the independent variable was the irradiation dose and the response variable was the adsorption constant, it was determined that there was a statistically significant difference between these values ($p < 0.05$). Figure 11 reflects that there is no a statistically significant difference between 0 and 10 kGy doses, nor between 5 and 20 kGy doses, but there is a statistically significant difference between 0 and 5 kGy doses, 0 and 20 kGy doses, 10 and 5 kGy doses, and between 10 and 20 kGy doses.

Particle size is a determining factor for the adsorption process, since it is related to the specific surface area, while the particle size decreases, the specific surface area increases and therefore, the number of active sites [50]. The TiO_2 particle size used in this work was around 325 μm (considered a micrometric size), which means that it could improve the adsorption capacity if the particle size decreases.

Nevertheless, an excessive adsorption might block the way of the light towards the nanoparticle and provoke a decrease in the photocatalytic efficiency, especially when there are big molecules such as DB1 [2]. This can be confirmed with the experimental results of K_f, for TiO_2 without irradiation and TiO_2 irradiated at 10 kGy, where the lowest value of K_f is obtained.

4.4. Contac Angle

Contact angle refers to the angle that the surface of a liquid makes when it encounters a solid. The value of the contact angle depends mainly on the relationship between the adhesive forces between the liquid and the solid and the cohesive forces of the liquid. When the adhesive forces with the surface of the solid are very large in relation to the cohesive forces, the contact angle is less than 90 degrees, resulting in the liquid wetting the surface. Contact angle measurement is useful in the evaluation of surface macroscopic properties, such as surface energy and wettability [51].

The variation of the contact angle between irradiated and nonirradiated TiO_2 samples is small. The e-beam produces a change on the surface that affects the contact angle variation, which goes down from 131.6° (TiO_2, 0 kGy) to 130.8° (TiO_2, 10 kGy), Figure 12; this slight decrease can be attributed to the increase in C-OH, as discussed above, which causes a slight increase of the wettability. That is likely related to the slight increase of the photocatalytic activity of the TiO_2 irradiated at 10 kGy. However, studies show that to achieve a change in the oxidation state of Ti, an increase in the Ti^{3+}/Ti^{4+} ratio, and irradiation with an MeV electron beam is required [52]. There are some studies that compares the photocatalytic activity and the super-hydrophilicity of TiO_2 induced by UV irradiation. The results are inconclusive, however, the composition and the processing of the material increases the photocatalytic activity and reduces the super-hydrophilic character, or vice versa [53–55]. According to Yu et al., the mechanism of photoinduced super-hydrophilicity of the films is different from that of photocatalytic oxidation, super-hydrophilicity is attributed to formation of surface trapped electrons and Ti^{3+} defective sites [56]. All these studies show that the photoinduced super-hydrophilicity is not permanent and reduces when the sample is stored in the dark for a couple of days.

4.5. Mineralization

According to Table 4, the mineralization after 60 min of treatment with TiO_2, not irradiated and irradiated at 10 kGy, is very low. However, it is important to note that the interest of this research was not to achieve total mineralization, but to study the effect of irradiation on the degradation of the DB1. However, in a study developed with azo dyes, it was determined that total mineralization occurs at longer times, around 5 h [57], which means that this low percentage could be caused by the time taken

to mineralize the dye. Other studies attribute the low TOC to structure cleavage and to the production of organic molecular small fragments that are not fully mineralized under the prevailing oxidative conditions [58,59].

5. Conclusions

TiO_2 irradiated at 10 kGy allows a slightly faster degradation of DB1, compared to the degradation with TiO_2 irradiated at 0, 5, and 20 kGy; in this sense, the rate constant of degradation of DB1, on TiO_2 irradiated at 10 kGy, is slightly higher statistically, according to ANOVA analysis. The results of XRD and band gap are identical for the irradiated and unirradiated TiO_2 with e-beam, showing that e-beam irradiation show no changes in the crystalline structure of the TiO_2 samples. However, EDS and XPS results from similar e-beam irradiation show that its surface properties suffer slight modifications, and the residual carbon on the TiO_2 structure is oxidized by irradiation, forming oxygenated species (C-O), which causes an increase in the TiO_2 hydrophilicity. This was corroborated experimentally by decreasing the contact angle, increasing the FT-IR (signals to the C-OH). In the case of TiO_2 irradiated at 20 kGy, C-OH groups are lost; causing a decrease in the intensity of the corresponding signals in FTIR intensity and an increase in the contact angle (reduces wettability). Regarding the absorption, the TiO_2 irradiated at 10 kGy absorbs less than the other materials used (TiO_2 irradiated at 0, 5 and 20 kGy); this apparently slightly favors the degradation of DB1, since an excessive adsorption would prevent the adequate passage of light towards the photocatalyst, causing a decrease in the speed of the degradation.

Author Contributions: Conceptualization, P.J.E.-M. and F.M.B.; methodology, P.J.E.-M. and F.M.B.; software, K.V.-E., A.D. and C.S.; validation, E.G., F.M. and P.J.E.-M.; formal analysis, E.G., C.S. and A.D.; investigation, E.G.; resources, F.M.B. and P.J.E.-M.; data curation, K.V.-E.; writing—original draft preparation, E.G., P.J.E.-M., L.F. and F.M.B.; writing—review and editing, E.G., P.J.E.-M., K.V.-E., L.F. and F.M.B.; visualization, P.J.E.-M. and F.M.B.; supervision, P.J.E.-M. and F.M.B.; project administration, P.J.E.-M. and F.M.B.; funding acquisition, P.J.E.-M. and F.M.B. All authors have read and agreed to the published version of the manuscript.

Funding: This research was funded by ESCUELA POLITÉCNICA NACIONAL, grant number PIMI-14-13.

Acknowledgments: The authors wish to thank the Laboratorio de Investigaciones Aplicadas de la Escuela Politécnica Nacional for the support receive during this research and the Centro de Nanociencia y Nanotecnología, Universidad de las Fuerzas Armadas ESPE for the X-ray and EDS analysis.

Conflicts of Interest: The authors declare no conflict of interest.

References

1. Reza, K.M.; Kurny, A.; Gulshan, F. Parameters affecting the photocatalytic degradation of dyes using TiO2: A review. *Appl. Water Sci.* **2017**, *7*, 1569–1578. [CrossRef]
2. Kordouli, E.; Bourikas, K.; Lycourghiotis, A.; Kordulis, C. The mechanism of azo-dyes adsorption on the titanium dioxide surface and their photocatalytic degradation over samples with various anatase/rutile ratios. *Catal. Today* **2015**, *252*, 128–135. [CrossRef]
3. Bafana, A.; Devi, S.S.; Chakrabarti, T. Azo dyes: Past, present and the future. *Environ. Rev.* **2011**, *19*, 350–371. [CrossRef]
4. Denisov, E.T.; Denisova, T.G.; Pokidova, T.S. *Handbook of Free Radical Initiators*; John Wiley & Sons: Hoboken, NJ, USA, 2005; ISBN 0471281832.
5. Nigam, P.; Banat, I.M.; Singh, D.; Marchant, R. Microbial process for the decolorization of textile effluent containing azo, diazo and reactive dyes. *Process Biochem.* **1996**, *31*, 435–442. [CrossRef]
6. Poyatos, J.M.; Muñio, M.M.; Almecija, M.C.; Torres, J.C.; Hontoria, E.; Osorio, F. Advanced Oxidation Processes for Wastewater Treatment: State of the Art. *Water Air Soil Pollut.* **2010**, *205*, 187. [CrossRef]
7. Topaç, F.O.; Dindar, E.; Uçaroğlu, S.; Başkaya, H.S. Effect of a sulfonated azo dye and sulfanilic acid on nitrogen transformation processes in soil. *J. Hazard. Mater.* **2009**, *170*, 1006–1013. [CrossRef]
8. Bayramoğlu, G.; Arıca, M.Y. Biosorption of benzidine based textile dyes "Direct Blue 1 and Direct Red 128" using native and heat-treated biomass of Trametes versicolor. *J. Hazard. Mater.* **2007**, *143*, 135–143. [CrossRef]

9. Oturan, M.A.; Aaron, J.-J. Advanced oxidation processes in water/wastewater treatment: Principles and applications. A review. *Crit. Rev. Environ. Sci. Technol.* **2014**, *44*, 2577–2641. [CrossRef]
10. Nevárez-Martínez, M.C.; Espinoza-Montero, P.; Quiroz-Chávez, F.; Ohtani, B. Fotocatálisis: Inicio, actualidad y perspectivas a través del TiO_2. *Av. Química* **2017**, *12*, 45–59.
11. Daghrir, R.; Drogui, P.; Robert, D. Modified TiO2 for environmental photocatalytic applications: A review. *Ind. Eng. Chem. Res.* **2013**, *52*, 3581–3599. [CrossRef]
12. Picho-Chillán, G.; Dante, R.C.; Muñoz-Bisesti, F.; Martín-Ramos, P.; Chamorro-Posada, P.; Vargas-Jentzsch, P.; Sánchez-Arévalo, F.M.; Sandoval-Pauker, C.; Rutto, D. Photodegradation of Direct Blue 1 azo dye by polymeric carbon nitride irradiated with accelerated electrons. *Mater. Chem. Phys.* **2019**, *237*, 121878. [CrossRef]
13. Lambert, J.; Vega, M.M.; Isarain-Chavez, E.; Peralta-Hernandez, J.M. Ozone and electrocoagulation processes for treatment of dye in leather industry wastewater: A comparative study. *IJ Emerg. Technol. Adv. Eng.* **2011**, *3*, 1–9.
14. Sugiarto, A.T.; Ohshima, T.; Sato, M. Advanced oxidation processes using pulsed streamer corona discharge in water. *Thin Solid Films* **2002**, *407*, 174–178. [CrossRef]
15. Mohammed, A.K.; Mckenzie, K.T. Photocatalityc degradation of Chicago Sky Blue 6B and Benzopurpurin 4B using titanium dioxide thin film. *J. Environ. Sci.* **2005**, *17*, 869–872.
16. Sandoval, C.; Molina, G.; Jentzsch, P.V.; Pérez, J.; Munoz, F. Photocatalytic degradation of azo dyes over semiconductors supported on polyethylene terephthalate and polystyrene substrates. *J. Adv. Oxid. Technol.* **2017**, *20*. [CrossRef]
17. Yazhini, K.B.; Savitha, K.U.; Prabu, H.G. Photocatalytic Degradation of Dyes using Rutile TiO_2-Pani Composite Prepared by One Pot Method. *Environ. Pollut. Control Res.* **2014**, *1*, 1–6.
18. Dante, R.C.; Sánchez-Arévalo, F.M.; Huerta, L.; Muñoz-Bisesti, F.; Marquez, D.; Martín-Ramos, P.; Lartundo-Rojas, L.; Chamorro-Posada, P.; Solorza-Feria, O. Photocatalytic activity of a new composite material of Fe (III) oxide nanoparticles wrapped by a matrix of polymeric carbon nitride and amorphous carbon. *Fuller. Nanotub. Carbon Nanostruct.* **2017**, *25*, 630–636. [CrossRef]
19. ten Brink, H.B.; Dekker, H.L.; Schoemaker, H.E.; Wever, R. Oxidation reactions catalyzed by vanadium chloroperoxidase from Curvularia inaequalis. *J. Inorg. Biochem.* **2000**, *80*, 91–98. [CrossRef]
20. Noman, M.; Shahid, M.; Ahmed, T.; Niazi, M.B.K.; Hussain, S.; Song, F.; Manzoor, I. Use of biogenic copper nanoparticles synthesized from a native Escherichia sp. as photocatalysts for azo dye degradation and treatment of textile effluents. *Environ. Pollut.* **2020**, *257*, 113514. [CrossRef]
21. Prasad, A.S.A.; Satyanarayana, V.S.V.; Rao, K.V.B. Biotransformation of Direct Blue 1 by a moderately halophilic bacterium Marinobacter sp. strain HBRA and toxicity assessment of degraded metabolites. *J. Hazard. Mater.* **2013**, *262*, 674–684. [CrossRef] [PubMed]
22. Kaushik, C.P.; Tuteja, R.; Kaushik, N.; Sharma, J.K. Minimization of organic chemical load in direct dyes effluent using low cost adsorbents. *Chem. Eng. J.* **2009**, *155*, 234–240. [CrossRef]
23. Mahmood, F.; Shahid, M.; Hussain, S.; Shahzad, T.; Tahir, M.; Ijaz, M.; Hussain, A.; Mahmood, K.; Imran, M.; Babar, S.A.K. Potential plant growth-promoting strain Bacillus sp. SR-2-1/1 decolorized azo dyes through NADH-ubiquinone: Oxidoreductase activity. *Bioresour. Technol.* **2017**, *235*, 176–184. [CrossRef] [PubMed]
24. Karagoz, B.; Bayramoglu, G.; Altintas, B.; Bicak, N.; Arica, M.Y. Amine functional monodisperse microbeads via precipitation polymerization of N-vinyl formamide: Immobilized laccase for benzidine based dyes degradation. *Bioresour. Technol.* **2011**, *102*, 6783–6790. [CrossRef]
25. Schliephake, K.; Mainwaring, D.E.; Lonergan, G.T.; Jones, I.K.; Baker, W.L. Transformation and degradation of the disazo dye Chicago Sky Blue by a purified laccase from Pycnoporus cinnabarinus. *Enzym. Microb. Technol.* **2000**, *27*, 100–107. [CrossRef]
26. Mendes, S.; Farinha, A.; Ramos, C.G.; Leitão, J.H.; Viegas, C.A.; Martins, L.O. Synergistic action of azoreductase and laccase leads to maximal decolourization and detoxification of model dye-containing wastewaters. *Bioresour. Technol.* **2011**, *102*, 9852–9859. [CrossRef]
27. Saraya, M.E.-S.I.; Aboul-Fetouh, M.E.-S.; Nassar, H.S.; Abd-El-Rahman, A.M. Removal of direct dyes with cement kiln dust. *J. Mater. Sci. Eng. B* **2011**, *1*, 97.
28. Zaleska, A. Doped-TiO_2: A review. *Recent Pat. Eng.* **2008**, *2*, 157–164. [CrossRef]
29. Kim, M.J.; Kim, K.-D.; Tai, W.S.; Seo, H.O.; Luo, Y.; Kim, Y.D.; Lee, B.C.; Park, O.K. Enhancement of Photocatalytic Activity of TiO_2 by High-Energy Electron-Beam Treatment Under Atmospheric Pressure. *Catal. Lett.* **2010**, *135*, 57–61. [CrossRef]

30. Latthe, S.S.; An, S.; Jin, S.; Yoon, S.S. High energy electron beam irradiated TiO2 photoanodes for improved water splitting. *J. Mater. Chem. A* **2013**, *1*, 13567–13575. [CrossRef]
31. Köferstein, R.; Jäger, L.; Ebbinghaus, S.G. Magnetic and optical investigations on LaFeO3 powders with different particle sizes and corresponding ceramics. *Solid State Ion.* **2013**, *249*, 1–5. [CrossRef]
32. Nowak, E.; Combes, G.; Stitt, E.H.; Pacek, A.W. A comparison of contact angle measurement techniques applied to highly porous catalyst supports. *Powder Technol.* **2013**, *233*, 52–64. [CrossRef]
33. Braginsky, L.; Shklover, V. Light absorption in TiO2 nanoparticles. In *The European Physical Journal D*; Springer: Berlin, Germany, 1999; pp. 627–630.
34. Reddy, S.S.; Kotaiah, B. Decolorization of simulated spent reactive dye bath using solar/TiO_2/H_2O_2. *Int. J. Environ. Sci. Technol.* **2005**, *2*, 245–251. [CrossRef]
35. Rodríguez Mora, J.A. *Estudio del Efecto del Uso de Dióxido de Titanio Asistido con Carbón Activado, Obtenido a Partir de un Residuo Industrial, en la Foto-Degradación del Colorante Azul BRL*; EPN: Quito, Ecuador, 2016.
36. Konstantinou, I.K.; Albanis, T.A. TiO_2-assisted photocatalytic degradation of azo dyes in aqueous solution: Kinetic and mechanistic investigations. *Appl. Catal. B Environ.* **2004**, *49*, 1–14. [CrossRef]
37. Thamaphat, K.; Limsuwan, P.; Ngotawornchai, B. Phase characterization of TiO_2 powder by XRD and TEM. *Kasetsart J. (Nat. Sci.)* **2008**, *42*, 357–361.
38. Lamo, M.P.B.; Williams, P.; Reece, P.; Lumpkin, G.R.; Sheppard, L.R. Study of gamma irradiation effect on commercial TiO2 photocatalyst. *Appl. Radiat. Isot.* **2014**, *89*, 25–29. [CrossRef]
39. Hou, X.G.; Gu, X.N.; Hu, Y.; Zhang, J.F.; Liu, A.D. Enhanced Pt/TiO2 thin films prepared by electron beam irradiation. *Nucl. Instrum. Methods Phys. Res. Sect. B Beam Interact. Mater. At.* **2006**, *251*, 429–434. [CrossRef]
40. Hou, X.G.; Liu, A.D. Modification of photocatalytic TiO_2 thin films by electron beam irradiation. *Radiat. Phys. Chem.* **2008**, *77*, 345–351. [CrossRef]
41. Jun, J.; Dhayal, M.; Shin, J.H.; Kim, J.C.; Getoff, N. Surface properties and photoactivity of TiO2 treated with electron beam. *Radiat. Phys. Chem.* **2006**, *75*, 583–589. [CrossRef]
42. Du, P.; Bueno-López, A.; Verbaas, M.; Almeida, A.R.; Makkee, M.; Moulijn, J.A.; Mul, G. The effect of surface OH-population on the photocatalytic activity of rare earth-doped P25-TiO_2 in methylene blue degradation. *J. Catal.* **2008**, *260*, 75–80. [CrossRef]
43. Warren, D.S.; McQuillan, A.J. Influence of adsorbed water on phonon and UV-induced IR absorptions of TiO_2 photocatalytic particle films. *J. Phys. Chem. B* **2004**, *108*, 19373–19379. [CrossRef]
44. Martra, G.; Coluccia, S.; Marchese, L.; Augugliaro, V.; Loddo, V.; Palmisano, L.; Schiavello, M. The role of H_2O in the photocatalytic oxidation of toluene in vapour phase on anatase TiO_2 catalyst: A FTIR study. *Catal. Today* **1999**, *53*, 695–702. [CrossRef]
45. Sakthivel, S.; Kisch, H. Daylight Photocatalysis by Carbon-Modified Titanium Dioxide. *Angew. Chem. Int. Ed.* **2003**, *42*, 4908–4911. [CrossRef] [PubMed]
46. Moulder, J.F.; Stickle, W.F.; Sobol, P.E.; Bomben, K.D.; Chastain, J. *Handbook of X-ray Photoelectron Spectroscopy AReference Book of Standard Spectra for Identification and Interpretation of XPS Data*; Physical Electronics: Chanhassen, MN, USA, 1995.
47. Giles, C.H.; Smith, D.; Huitson, A. A general treatment and classification of the solute adsorption isotherm. I. Theoretical. *J. Colloid Interface Sci.* **1974**, *47*, 755–765. [CrossRef]
48. Asenjo, V.N.G. Una Nueva Generación de Carbones Activados de Altas Prestaciones Para Aplicaciones Medioambientales. Ph.D. Thesis, Universidad de Oviedo, Oviedo, Spain, 2014.
49. Voudrias, E.; Fytianos, K.; Bozani, E. Sorption–desorption isotherms of dyes from aqueous solutions and wastewaters with different sorbent materials. *Glob. NEST Int. J.* **2002**, *4*, 75–83.
50. Zhang, Z.; Wang, C.-C.; Zakaria, R.; Ying, J.Y. Role of particle size in nanocrystalline TiO2-based photocatalysts. *J. Phys. Chem. B* **1998**, *102*, 10871–10878. [CrossRef]
51. Lamour, G.; Hamraoui, A.; Buvailo, A.; Xing, Y.; Keuleyan, S.; Prakash, V.; Eftekhari-Bafrooei, A.; Borguet, E. Contact angle measurements using a simplified experimental setup. *J. Chem. Educ.* **2010**, *87*, 1403–1407. [CrossRef]
52. Kim, M.S.; Jo, W.J.; Lee, D.; Baeck, S.; Shin, J.H.; Lee, B.C. Enhanced Photocatalytic Activity of TiO_2 Modified by e-Beam Irradiation. *Bull. Korean Chem. Soc.* **2013**, *34*, 1397–1400. [CrossRef]
53. Guan, K. Relationship between photocatalytic activity, hydrophilicity and self-cleaning effect of TiO_2/SiO_2 films. *Surf. Coat. Technol.* **2005**, *191*, 155–160. [CrossRef]

54. Fujishima, A.; Rao, T.N.; Tryk, D.A. Titanium dioxide photocatalysis. *J. Photochem. Photobiol. C Photochem. Rev.* **2000**, *1*, 1–21. [CrossRef]
55. Lee, Y.C.; Hong, Y.P.; Lee, H.Y.; Kim, H.; Jung, Y.J.; Ko, K.H.; Jung, H.S.; Hong, K.S. Photocatalysis and hydrophilicity of doped TiO_2 thin films. *J. Colloid Interface Sci.* **2003**, *267*, 127–131. [CrossRef]
56. Jimmy, C.Y.; Yu, J.; Ho, W.; Zhao, J. Light-induced super-hydrophilicity and photocatalytic activity of mesoporous TiO_2 thin films. *J. Photochem. Photobiol. A Chem.* **2002**, *148*, 331–339.
57. Karkmaz, M.; Puzenat, E.; Guillard, C.; Herrmann, J.M. Photocatalytic degradation of the alimentary azo dye amaranth: Mineralization of the azo group to nitrogen. *Appl. Catal. B Environ.* **2004**, *51*, 183–194. [CrossRef]
58. Koch, M.; Yediler, A.; Lienert, D.; Insel, G.; Kettrup, A. Ozonation of hydrolyzed azo dye reactive yellow 84 (CI). *Chemosphere* **2002**, *46*, 109–113. [CrossRef]
59. Neamţu, M.; Zaharia, C.; Catrinescu, C.; Yediler, A.; Macoveanu, M.; Kettrup, A. Fe-exchanged Y zeolite as catalyst for wet peroxide oxidation of reactive azo dye Procion Marine H-EXL. *Appl. Catal. B Environ.* **2004**, *48*, 287–294. [CrossRef]

processes

MDPI

Article

Visible Light-Driven Photocatalytic Rhodamine B Degradation Using CdS Nanorods

Haseeb Ullah [1,*], Eva Viglašová [2] and Michal Galamboš [2,*]

[1] Department of Chemistry, Quaid-i-Azam University, Islamabad 45320, Pakistan
[2] Department of Nuclear Chemistry, Faculty of Natural Sciences, Comenius University in Bratislava, Mlynská Dolina, Ilkovičova 6, 84215 Bratislava, Slovakia; eva.viglasova@uniba.sk
* Correspondence: chemist.ktk.06@gmail.com (H.U.); michal.galambos@uniba.sk (M.G.)

Abstract: In this work, highly crystalline CdS nanorods (NRs) were successfully synthesized by a facile, one-step solvothermal method. The as-prepared CdS NRs powder was characterized by XRD, FESEM, Raman, PL, XPS, BET, and UV-visible techniques to evaluate the structural, morphological, and optical properties. The photocatalytic performance of the as-synthesized CdS NRs was investigated for the photodegradation of RhB dye under visible light irradiations. It has been found that CdS NRs show maximum RhB degradation efficiency of 88.4% in 120 min. The excellent photodegradation ability of the CdS NRs can be attributed to their rod-like structure together with their large surface area and surface state. The kinetic study indicated that the photodegradation process was best described by the pseudo-first-order kinetic model. The possible mechanism for the photodegradation of RhB dye over CdS NRs was proposed in this paper.

Keywords: CdS; rhodamine B; photocatalysis; pseudo-first order kinetics

Citation: Ullah, H.; Viglašová, E.; Galamboš, M. Visible Light-Driven Photocatalytic Rhodamine B Degradation Using CdS Nanorods. *Processes* **2021**, *9*, 263. https://doi.org/10.3390/pr9020263

Academic Editor: Olivier Monfort
Received: 30 November 2020
Accepted: 24 January 2021
Published: 29 January 2021

1. Introduction

In recent years, the ever-increasing global population, unplanned urbanization, and rapid industrialization have caused enormous environmental pollution, becoming an increasingly serious threat to the survival of human beings [1,2]. Organic dyes are considered a major class of environmental hazards, extensively produced by some industries such as the manufacture of plastics, papers, textile, food, cosmetic, drugs, and printing industries [3–5]. Most of the dyes have xenobiotic properties and complex aromatic structures and are resistant to degradation. Inhalation of organic dyes can cause eye burns, profuse sweating, vomiting, nausea, and mental confusion [6,7]. Nowadays, around 100,000 different types of synthetic dyes are produced with a production rate of 7×10^5 tons per year, and around 15% of the dyes are released into the natural ambiance [8]. The presence of dyes in waterbodies, even in a small amount, is a very concerning problem, as it not only affects the aesthetic nature but also reduces the photosynthetic activity of aquatic plants and algae in aqueous environments [9].

Various treatment methods, e.g., advanced oxidation processes [10], ion flotation [11], ozonation [12], membrane separation [13], anaerobic and aerobic treatment [14], biological treatment [15], and adsorption [16] have been used to treat wastewater containing organic dyes. However, these methods have several limitations, such as high cost, slow kinetics, and low performance. Therefore, it is important to develop an efficient and cost-effective technique for the decontamination of wastewater containing organic dyes. Recently, semiconductor-based photocatalysis has shown great potential in the remediation of the degradation of organic dyes as it can partially mineralize macromolecular organic dyes into small molecules such as H_2O and CO_2 [17]. During the photocatalysis process under visible light irradiation, the electrons excites from the filled valence band (VB) of a semiconductor to the empty conduction band (CB), generates excited electron-hole pairs, which reacts with the oxygen and hydroxyl ions to generate active radicals that can degrade

water contaminants readily and quickly [18]. Among the known semiconductor photocatalysts, titanium oxide (TiO_2) has been extensively studied and used [19]. The traditional photocatalysts such as ZnO andTiO_2 have been extensively used due to their low-cost, reusability, stability, and availability. However, their practical application as photocatalyst has been severely restricted due to their high bandgap (TiO2 ~ 3.2 eV, ZnO ~ 3.37 eV) and ultraviolet (UV) light activity that accounts only for 4% of the total UV-visible light [20–22]. Therefore, there is an imminent need to develop an efficient, low-cost visible-light active materials to tackle environmental pollution.

Among the semiconductor photocatalysts, cadmium sulfide (CdS) is the most extensively used photocatalyst in environmental remediation and one of the most important semiconductor materials (bandgap ~ 2.4 eV), absorbs in the visible region [23,24]. However, the practical usage of CdS in photocatalysis is limited due to some serious shortcomings, including particle aggregation, photo corrosion, and a short lifetime of photo-generated carriers [25,26]. In this context, various efforts have been made to improve CdS photocatalytic activity and stability, such as morphological and structural modification, ion doping, and semiconductors hybridization, etc. It is widely known that the photocatalytic properties of the semiconductor nanomaterials significantly depend on their specific properties such as size, bandgap, morphology, spatial architectures, and especially the specific surface area [27,28]. Therefore various synthetic methods have been investigated for the synthesis of 1D to 3D CdS nanostructures photocatalysts such as hydrothermal/solvothermal method, colloidal method, template method, thermal evaporation, electrochemically induced deposition method, and laser-assisted catalytic growth process [29,30]. Among all these methods, a solvothermal method is the most promising and cost-effective technique to direct and control the nanocrystalline properties of the resultant nanomaterials such as morphology, crystal phase, luminescence, and size [31]. It has been reported that CdS nanorods (NRs) with a hexagonal crystal structure, good crystallinity, and large surface area have proved higher photocatalytic activity compared to the pure cubic phases [32]. CdS NRs with a high aspect ratio showed higher photocatalytic activity due to the restrained electrons in a specific direction that influences the electronic and optical properties of the photocatalyst [33]. Liu et al. found the improved CdS photocatalytic performance due to the increase of exposed 002 facets [34].

Herein, by taking the above consideration and discussion, the main aim of our work was established. The morphology-controlled synthesis of hexagonal phase CdS NRs with high-aspect ratio, high surface area, and exposed 002 facets was performed. The photocatalytic activity of the CdS NRs for the photodegradation of rhodamine B (RhB) was investigated using visible light irradiation. Besides, the effect of several experimental parameters, viz., the catalyst dosage and the initial RhB concentration, were also examined.

2. Materials and Methods

2.1. Chemicals

Cadmium acetate dihydrate ($Cd(CH_3COO)_2{\cdot}2H_2O$), sodium diethyldithiocarbamate tetrahydrate ($C_5H_{10}NNaS_2{\cdot}4H_2O$), diethylenetriamine ($HN(CH_2CH_2NH_2)_2$), and ethanol ($C_2H_5OH$) were purchased from Sigma-Aldrich (Islamabad, Pakistan). Rhodamine B (RhB) dye was chosen as a model for the environmental pollutant. All chemicals were of reagent grade and were used as received.

2.2. Synthesis of CdS NRs

In a typical synthesis procedure, $Cd(CH_3COO)_2{\cdot}2H_2O$ (7.379 g), $C_5H_{10}NNaS_2{\cdot}4H_2O$ (5.25 g), and diethylenetriamine (120 mL) were added to a clean Teflon-lined autoclave. The mixture was vigorously stirred for 30 min to form a homogenous dispersion. The autoclave was then sealed and heated at 180 °C for 24 h in an oven and subsequently air cooled naturally. The resulting yellow product of CdS NRs was collected after centrifugation and washed with ethanol and distilled water, followed by drying at 80 °C for 10 h.

2.3. Characterization

The crystal phase identification of the photocatalyst was performed by X-ray diffraction (XRD) analysis. The XRD measurement was done using Bruker D2 Phaser diffractometer with Cu-Kα radiation (λ = 1.5406 Å) in the 2θ range between 10–80°. The structure and morphology were examined by a field emission scanning electron microscope (FESEM-EDS, Zeiss Ultra Plus), and the photoluminescence (PL) measurement was performed on a PL lifetime spectrometer (Edinburgh Instruments). The optical property was determined by using a UV-visible spectrophotometer (Shimadzu UV-1800). The electron binding energies and surface chemical composition were determined by X-ray photoelectron spectroscopy (XPS, Thermo K alpha). The pore size and surface area of the sample were measured by Brunauer–Emmett–Teller (BET) nitrogen adsorption measurement (BET Micromeritics ASAP 2020). Raman spectrum of the sample was recorded on an inVia Renishaw spectrometer.

2.4. Photocatalytic Degradation of RhB

The photocatalytic ability of the as-synthesized CdS NRs was assessed by the photocatalytic degradation of RhB under visible light irradiation using a 300 W incandescent lamp (Philips) placed at a working distance of 30 cm above the surface of the reaction medium. For RhB degradation, 10 mg sample of the CdS NRs catalyst was added into 80 mL of a 10 mg/L RhB solution. Before light illumination, the mixture was stirred continuously in the dark for 30 min to ensure desorption-adsorption equilibrium. During the subsequent irradiations, 4-mL of suspension was drawn at regular interval of time and centrifuged to obtain a clear solution. The remaining concentration of RhB dye was measured by a UV-vis spectrophotometer.

3. Results and Discussions

3.1. Structural, Chemical, and Optical Analysis of CdS NRs

The phase purity and crystallographic structure of the as-synthesized CdS NRs catalyst were investigated by using the XRD technique. The XRD pattern of CdS NRs is shown in Figure 1a. The observed diffraction peaks at 2θ 25.06°, 26.67°, 28.40°, 36.96°, 43.92°, 48.10°, 52.23°, 54.94°, and 67.31° and were assigned to the (100), (002), (101), (102), (110), (103), (112), (004), and (210) crystal planes of the hexagonal CdS, respectively (ICCD, PDF, 00-001-0780). The sharp diffraction peaks indicate the higher crystallinity of the as-synthesized CdS photocatalyst. The XRD peak intensities of the CdS NRs differ from the bulk material. It is noted that XRD peak intensity at 26.67° corresponding to (002) facet of CdS, is much more intense with a small width than all the other peaks, indicating the orientation growth of the nanorods along the c-axis [35], in agreement with FESEM results. Moreover, the XRD pattern of the as-synthesized CdS NRs did not show any peaks except for CdS, which confirms the high purity of the catalyst. The crystalline phase, homogeneity, and surface condition of the CdS NRs was further confirmed by Raman spectroscopy, as shown in Figure 1b. The CdS shows two characteristic peaks at 300 and 603 cm^{-1} corresponded to the 1LO and 2LO vibrational modes, respectively. The sharp Raman peaks indicate the high crystallinity of the synthesized photocatalyst, which is consistent with the XRD observations.

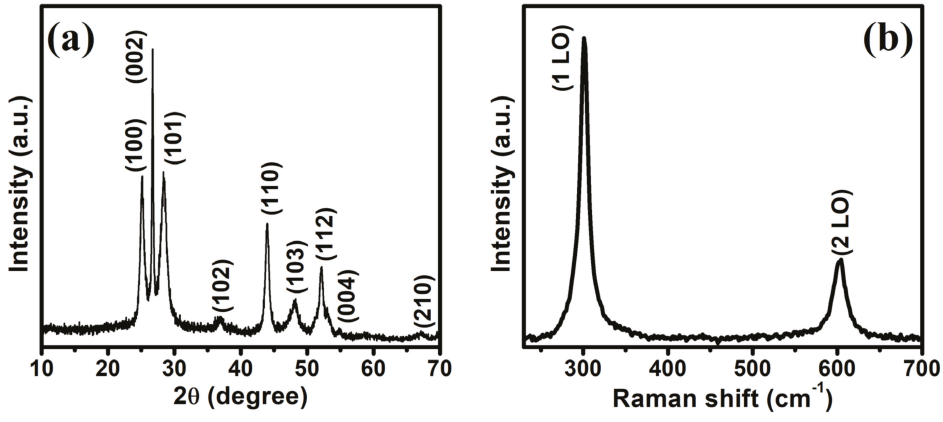

Figure 1. XRD patterns of CdS (**a**), Raman spectrum (**b**).

Field emission scanning electron microscopy (FESEM) was performed to determine the surface morphology and shape of the CdS nanostructures. The FESEM images of CdS nanostructures are shown in Figure 2, which provides clear evidence for the formation of a rod-like morphology of CdS.

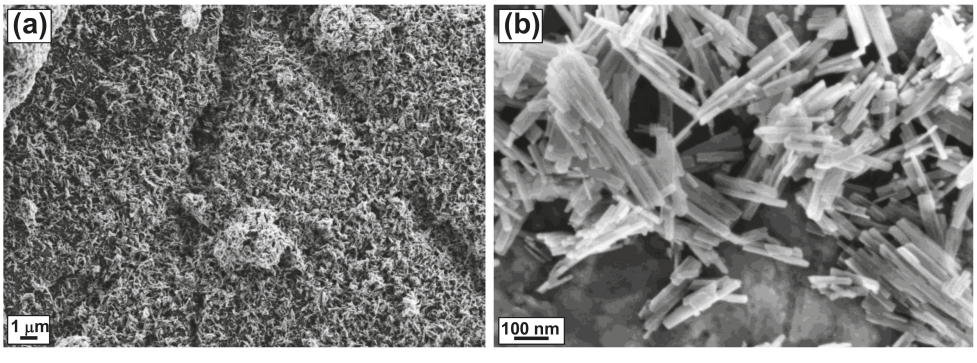

Figure 2. FESEM images of CdS NRs (**a**,**b**).

UV-visible spectrophotometric analysis (UV-vis) was performed to analyze the optical absorption properties of the as-prepared CdS NRs. Figure 3a shows the typical UV-vis spectrum of the CdS NRs in the 350–700 nm wavelength range with absorption edges at around 480 and 510 nm. The energy bandgap E_g was calculated from the following formula

$$\alpha h\nu = A\,(h\nu - E_g)^{1/2} \quad (1)$$

where α is the absorption coefficient, A is a constant, $h\nu$ is the photon energy, and E_g is the direct bandgap. The bandgap of the synthesized CdS NRs was calculated to be ~2.35 eV from the $(\alpha.E)^2$ vs. energy (eV) plot, and therefore, this nanomaterial can be used as an absorption photocatalyst over a wide range of the visible spectrum.

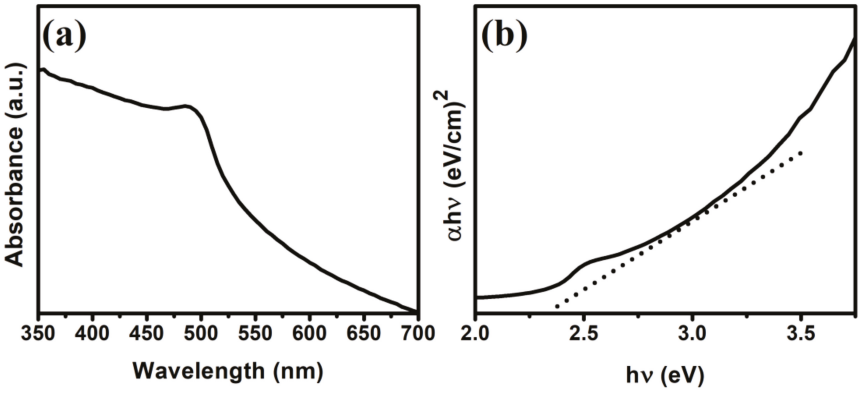

Figure 3. UV-vis DRS (**a**) and estimated bandgap energy (**b**) of CdS NRs.

The specific surface area and pore structure of CdS NRs were investigated. As shown in Figure 4, the observed isotherms can be assigned as type-IV sorption isotherms with an H3-type of hysteresis loop over a pressure range between 0.8 to 1.0 suggests the presence of slit-like pores [36]. The BET surface area of the CdS NRs was calculated as 51 m^2/g. The higher surface area of the as-synthesized CdS NRs photocatalyst compared to the reported CdS photocatalyst [37] makes the transfer of photo-generated charges easier due to the higher number of available active sites on the surface, resulting in improved photocatalytic performance. The average pore size was calculated as 32.7 nm.

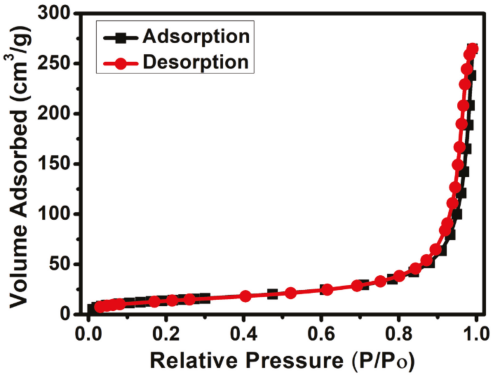

Figure 4. Nitrogen adsorption–desorption isotherm curve of CdS NRs.

The photoluminescence (PL) measurements were performed using an excitation wavelength of 380 nm to investigate the lifetime and separation of photo-induced electron-hole pairs in CdS NRs. The PL spectrum was recorded in the 425–600 nm spectral range (Figure 5a). It is well known that there is a close link between the PL data and the recombination process of photo-generated electron-hole pairs of the photocatalyst. Generally, a higher value of PL peak intensity indicates the rapid recombination of the photo-generated electron-hole pairs of the catalyst, while a lower value indicates the higher separation of photo-generated electron-hole pairs [38]. The PL emission spectrum of CdS NRs exhibits a broad emission peak around 510 nm due to the near-band-edge emission, which is consistent with the UV-vis spectroscopy results. Time-resolved PL spectrum was captured to calculate the lifetime of the photo-generated electron-hole pairs of the photocatalyst; this was found to be 1.83 ns (Figure 5b) [39].

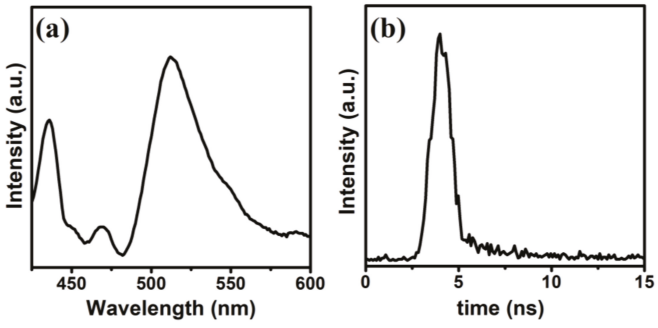

Figure 5. PL spectrum of CdS NRs (**a**), time-resolved PL spectrum (**b**).

The valence state and surface chemical composition of the CdS NRs were determined via XPS analysis. The XPS survey spectrum given in Figure 6a, show the presence of Cd and S in the majority, together with trace amount of C and O, which are probably due to contamination and adsorbed oxygen during sample exposure to the air. The two strong peaks located at 404.2 and 411.2 eV (Figure 6b) corresponds to the Cd 3d5/2 and Cd 3d3/2 states of Cd^{2+}, respectively [40]. The high-resolution S 2p spectrum in Figure 6c shows two strong peaks at 162.2 eV and 160.9 eV; and one weak peak at 168.3 eV. The strong peaks at 162.2 eV and 160.9 eV corresponds to the S 2p3/2 and S 2p1/2, respectively, which can be attributed to S^{2-} ions, while the weak peak at 168.3 eV is due to the higher valence state of S, which came from the hydrolysis of sulfur source. Figure 6d shows the binding energy of the O 1s peak of the surface adsorbed oxygen atoms on CdS.

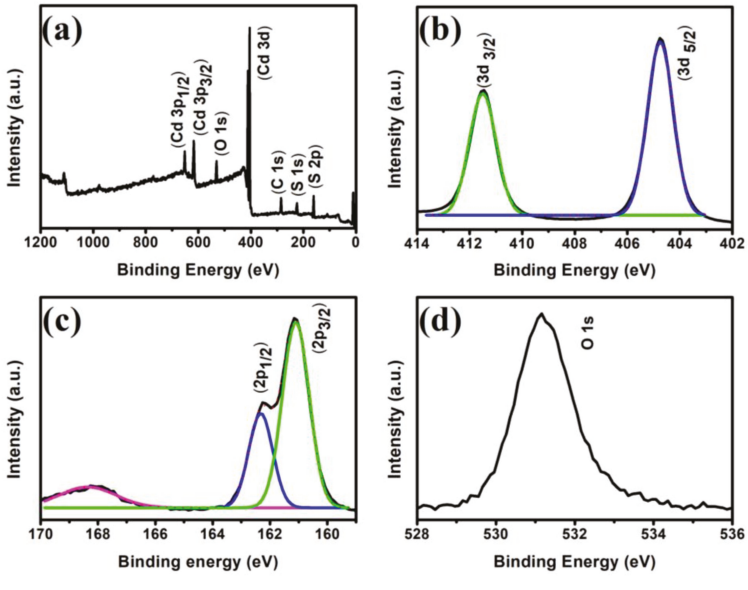

Figure 6. XPS survey spectrum of CdS NRs (**a**), high-resolution XPS spectra of Cd 3d (**b**), S 2p (**c**), and O 1s (**d**).

3.2. Photocatalytic Degradation of RhB

The photocatalytic ability of the as-prepared CdS NRs on the photodegradation of RhB in an aqueous solution under visible light illumination was investigated, and the results are shown in Figure 7. Before the photocatalytic reaction, a blank experiment without

adding photocatalyst was carried out to examine the self-degradation of RhB dye. It can be seen in Figure 7b, there is no obvious change in the concentration of dye in the absence of CdS, which suggested that the self-degradation of RhB dye during photocatalytic degradation reaction is negligible. However, by adding the photocatalyst in the solution, the absorption intensity of RhB decreases over time under visible light illumination, verifying that CdS NRs photocatalyst exhibits photocatalytic activity (Figure 7b). The photocatalytic decomposition of RhB reaches 88.4% in 120 min. However, it is very difficult to achieve the maximum degradation value during the photocatalysis process.

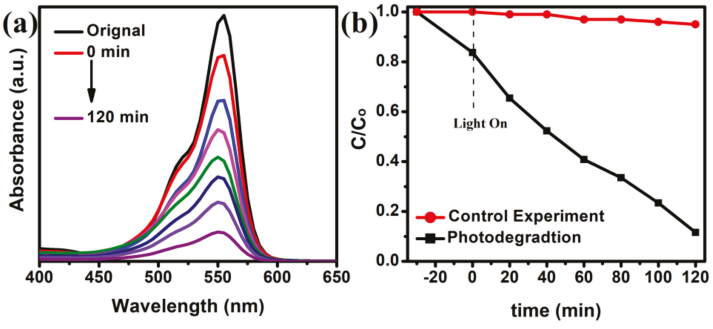

Figure 7. Time-dependent absorption spectra of RhB solution in visible light (**a**), and the degradation of RB in visible light (**b**).

The effect of photocatalyst dosage (5 mg, 7.5 mg, and 10 mg) on the photocatalytic activity was examined. As can be seen from Figure 8a, increasing the amount of CdS from 5 mg to 10 mg results in an increase in the photodegradation of RhB from 57 to 88.4%, respectively. This increase in photodegradation can be attributed to increases in the number of surface active sites and the total surface area of the catalyst available for the photocatalytic reaction [41].

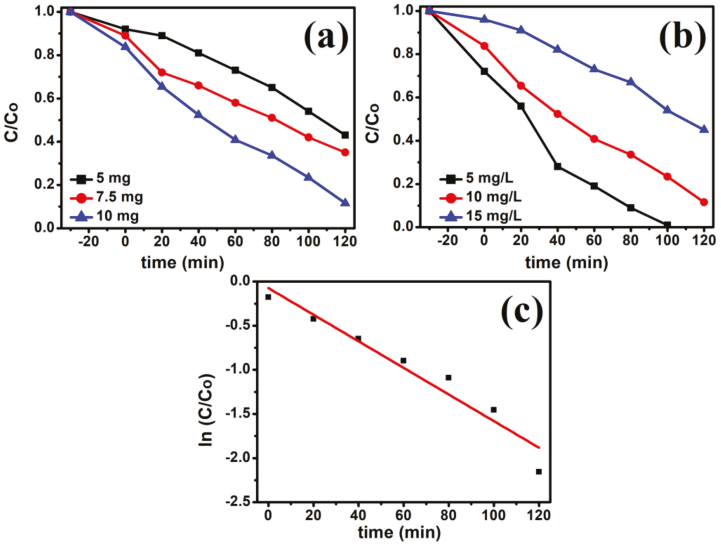

Figure 8. Effect of photocatalyst loading (**a**), Effect of initial RhB concentration (**b**), and Plot of ln (Co/C) vs. time (**c**) (10 mg photocatalyst, 10 mg/L RhB dye, Room temperature, 300 W incandescent lamp).

The effect of the initial RhB concentration on the photocatalytic activity was investigated by varying the concentration from 5 mg/L to 10 mg/L and 15 mg/L (Figure 8b), as it is an important parameter in the photodegradation of organic pollutants. The photocatalytic degradation efficiency decreases from 99 to 55% with the increase in the concentration of RhB from 5 mg/L to 15 mg/L. The reduced rate of degradation efficiency at higher concentrations is due to the unavailability of photoactive sites by increased adsorption of dye molecules and decreased rate of light penetration into the suspension [42,43]. At a high dye concentration, large portion of light is absorbed by the dye molecules, and only small portion of light is absorbed by the catalyst. As a result, the reduced photo flux reaching the catalyst surface causes a reduction in degradation efficiency.

The chemical kinetics of the photocatalytic reaction were studied to obtain some insight into the mechanism of the photodegradation process and to assess the feasibility and efficiency of treating the dye this way. The Langmuir–Hinshelwood kinetics and its pseudo-first-order reaction can be represented by the following equation as (Equations (2) and (3));

$$\frac{dC}{dt} = -K_{app}\, C \tag{2}$$

$$ln(\frac{Co}{C}) = K_{app}\, t \tag{3}$$

where K_{app} is the constant of degradation rate and t is the irradiation time. The $ln(C_o/C)$ versus t plot is shown in Figure 8c. A linear fit between $ln(C_o/C)$ and t was obtained for each plot supporting the conclusion that the photodegradation reaction follows pseudo-first-order kinetics with respect to dye concentration. The K_{app} values were calculated from the slopes of $ln(C_0/C)$ vs. t plots. For visible-light irradiation, the correlation coefficient was $R^2 = 0.945$ and the K_{app} value was 0.15×10^{-2} min^{-1}.

In addition, to study the photostability and reusability of the as-synthesized CdS NRs photocatalyst, an experiment of five consecutive cycles for the photodegradation of RhB dye was carried out. The photodegradation activity of the CdS NRs remained almost constant over five-cycles as shown in Figure 9a, suggests excellent cycling stability photocatalyst. The XRD pattern (Figure 9b) of the used photocatalyst after five cycles shows that no additional peak was observed and the crystal structure of the photocatalyst has been preserved, indicating the high stability and sustainability of the photocatalyst.

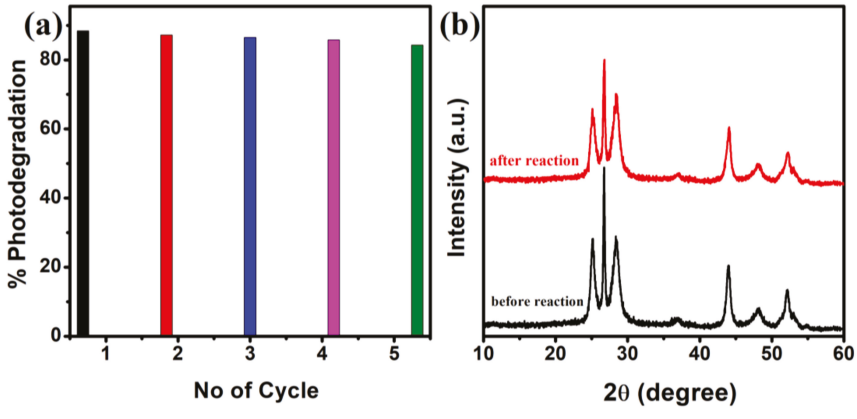

Figure 9. Stability test of CdS NRs for five cycles (**a**), XRD pattern for CdS NRs before the activity and after recycling five times for RhB photodegradation (**b**).

Figure 10, depicts the plausible mechanism for RhB dye degradation over CdS NRs. Upon visible light illumination, the electrons (ē) are excited from the filled valence band

(VB) of CdS to the conduction band (CB), creating a hole (h^+) in the VB. The generated electron from the conduction band is taken up by the adsorbed O_2 at the surface of the photocatalyst and produces superoxide radical ion ($^{\bullet}O_2^-$). The $^{\bullet}O_2^-$ further reacts with H_2O and produces hydroxyl radical ($^{\bullet}OH$) or can directly oxidize RhB dye. Simultaneously, some of the photo-induced holes (h^+) react with OH^- or H_2O to generate active specie $^{\bullet}OH$, which oxidize the adsorbed RhB dye.

$$\text{CdS NRs} + h\nu \rightarrow \text{CdS}\,(\bar{e} + h^+) \quad (4)$$

$$O_2 + \bar{e} \rightarrow O_2^- \quad (5)$$

$$O_2^- + \bar{e} + 2H^+ \rightarrow H_2O_2 \quad (6)$$

$$H_2O_2 + \bar{e} \rightarrow OH + OH^- \quad (7)$$

$$h^+ + OH^-/H_2O \rightarrow OH \quad (8)$$

$$OH + \text{RhB} \rightarrow \text{Decolourization} \quad (9)$$

$$h^+ + \text{RhB} \rightarrow \text{Decolourization} \quad (10)$$

$$O_2^- + \text{MB dye} \rightarrow \text{Decolourization} \quad (11)$$

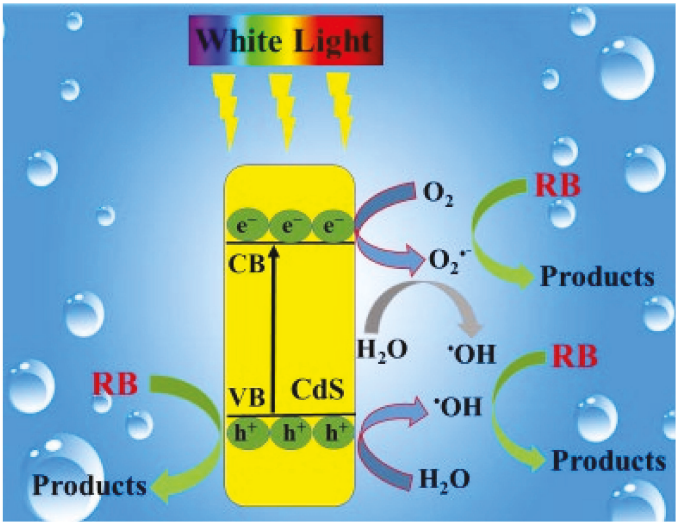

Figure 10. Proposed mechanism for the photocatalytic degradation of RB under visible light illumination.

4. Conclusions

In the present work, the highly crystalline CdS NRs were successfully synthesized by a one-step solvothermal method. The CdS NRs were characterized in terms of structure, morphological, and optical properties by XRD, Raman, FESEM, BET, PEL, UV-vis, and XPS techniques. The photocatalytic activity investigation was carried out by performing the photodegradation of RhB under visible light illumination over CdS NRs. Moreover, the photocatalytic activity of the CdS NRs depends on the various parameters such as initial dye concertation and the photocatalyst amount. It can be concluded that as-prepared CdS NRs show higher photocatalytic activity at a high dosage of photocatalyst and the low initial concentration of the RhB solution. The photodegradation of RhB follows a pseudo-first-order kinetic model.

Author Contributions: Conceptualization, H.U. and M.G.; investigation, H.U. and E.V. All authors have read and agreed to the published version of the manuscript.

Funding: This research was funded by the Higher Education Commission of Pakistan.

Institutional Review Board Statement: Not applicable.

Informed Consent Statement: Not applicable.

Data Availability Statement: The data presented in this study are available in the main text of the article.

Conflicts of Interest: The authors declare no conflict of interest.

References

1. Ferreira-Neto, E.P.; Ullah, S.; Da Silva, T.C.A.; Domeneguetti, R.R.; Perissinotto, A.P.; De Vicente, F.S.; Rodrigues-Filho, U.P.; Ribeiro, S.J. Bacterial nanocellulose/MoS2 hybrid aerogels as bifunctional adsorbent/photocatalyst membranes for in-flow water decontamination. *ACS Appl. Mater. Interfaces* **2020**, *12*, 41627–41643. [CrossRef] [PubMed]
2. Zhang, F.; Li, Y.-H.; Li, J.-Y.; Tang, Z.-R.; Xu, Y.-J. 3D graphene-based gel photocatalysts for environmental pollutants degradation. *Environ. Pollut.* **2019**, *253*, 365–376. [CrossRef] [PubMed]
3. Taghizadeh, M.T.; Siyahi, V.; Ashassi-Sorkhabi, H.; Zarrini, G. ZnO, AgCl and AgCl/ZnO nanocomposites incorporated chitosan in the form of hydrogel beads for photocatalytic degradation of MB, *E. coli* and *S. aureus*. *Int. J. Biol. Macromol.* **2020**, *147*, 1018–1028. [CrossRef] [PubMed]
4. Liu, Y.; Jin, W.; Zhao, Y.; Zhang, G.; Zhang, W. Enhanced catalytic degradation of methylene blue by α-Fe2O3/graphene oxide via heterogeneous photo-Fenton reactions. *Appl. Catal. B Environ.* **2017**, *206*, 642–652. [CrossRef]
5. Nie, L.; Zhang, Q. Recent progress in crystalline metal chalcogenides as efficient photocatalysts for organic pollutant degradation. *Inorg. Chem. Front.* **2017**, *4*, 1953–1962. [CrossRef]
6. Zhao, X.; Liu, S.; Tang, Z.; Niu, H.; Cai, Y.; Meng, W.; Wu, F.; Giesy, J.P. Synthesis of magnetic metal-organic framework (MOF) for efficient removal of organic dyes from water. *Sci. Rep.* **2015**, *5*, 11849. [CrossRef]
7. Asl, E.A.; Haghighi, M.; Talati, A. Sono-solvothermal fabrication of flowerlike Bi7O9I3-MgAl2O4 p-n nano-heterostructure photocatalyst with enhanced solar-light-driven degradation of methylene blue. *Sol. Energy* **2019**, *184*, 426–439.
8. Mahmoodi, N.M.; Abdi, J.; Oveisi, M.; Asli, M.A.; Vossoughi, M. Metal-organic framework (MIL-100 (Fe)): Synthesis, detailed photocatalytic dye degradation ability in colored textile wastewater and recycling. *Mater. Res. Bull.* **2018**, *100*, 357–366. [CrossRef]
9. Khalil, A.; Aboamera, N.M.; Nasser, W.S.; Mahmoud, W.H.; Mohamed, G.G. Photodegradation of organic dyes by PAN/SiO_2-TiO2-NH2 nanofiber membrane under visible light. *Sep. Purif. Technol.* **2019**, *224*, 509–514. [CrossRef]
10. Catalkaya, E.C.; Kargi, F. Color, TOC and AOX removals from pulp mill effluent by advanced oxidation processes: A comparative study. *J. Hazard. Mater.* **2007**, *139*, 244–253. [CrossRef]
11. Shakir, K.; Elkafrawy, A.F.; Ghoneimy, H.F.; Beheir, S.G.E.; Refaat, M. Removal of rhodamine B (a basic dye) and thoron (an acidic dye) from dilute aqueous solutions and wastewater simulants by ion flotation. *Water Res.* **2010**, *44*, 1449–1461. [CrossRef] [PubMed]
12. Zhang, J.; Lee, K.-H.; Cui, L.; Jeong, T. Degradation of methylene blue in aqueous solution by ozone-based processes. *J. Ind. Eng. Chem.* **2009**, *15*, 185–189. [CrossRef]
13. Pizzichini, M.; Russo, C.; Di Meo, C. Purification of pulp and paper wastewater, with membrane technology, for water reuse in a closed loop. *Desalination* **2005**, *178*, 351–359. [CrossRef]
14. Chan, Y.J.; Chong, M.F.; Law, C.L.; Hassell, D. A review on anaerobic–aerobic treatment of industrial and municipal wastewater. *Chem. Eng. J.* **2009**, *155*, 1–18. [CrossRef]
15. Paz, A.; Carballo, J.; Pérez, M.J.; Domínguez, J.M. Biological treatment of model dyes and textile wastewaters. *Chemosphere* **2017**, *181*, 168–177. [CrossRef]
16. Yao, X.; Ji, L.; Guo, J.; Ge, S.; Lu, W.; Cai, L.; Wang, Y.; Song, W.; Zhang, H. Magnetic activated biochar nanocomposites derived from wakame and its application in methylene blue adsorption. *Bioresour. Technol.* **2020**, *302*, 122842. [CrossRef]
17. Chen, X.; Wu, Z.; Liu, D.; Gao, Z. Preparation of ZnO Photocatalyst for the Efficient and Rapid Photocatalytic Degradation of Azo Dyes. *Nanoscale Res. Lett.* **2017**, *12*, 143. [CrossRef]
18. Li, M.; Song, C.; Wu, Y.; Wang, M.; Pan, Z.; Sun, Y.; Meng, L.; Han, S.; Xu, L.; Gan, L. Novel Z-scheme visible-light photocatalyst based on CoFe2O4/BiOBr/Graphene composites for organic dye degradation and Cr (VI) reduction. *Appl. Surf. Sci.* **2019**, *478*, 744–753. [CrossRef]
19. Romero-Saez, M.; Jaramillo, L.Y.; Saravanan, R.; Benito, N.; Pabon, E.; Mosquera, E.; Gracia Caroca, F. Notable photocatalytic activity of TiO2-polyethylene nanocomposites for visible light degradation of organic pollutants. *Express Polym. Lett.* **2017**, *11*, 899–909. [CrossRef]
20. Chen, X.; Dai, Y.; Wang, X. Methods and mechanism for improvement of photocatalytic activity and stability of Ag3PO4: A review. *J. Alloys Compd.* **2015**, *649*, 910–932. [CrossRef]

21. Li, J.; Fang, W.; Yu, C.; Zhou, W.; Zhu, L.; Xie, Y. Ag-based semiconductor photocatalysts in environmental purification. *Appl. Surf. Sci.* **2015**, *358*, 46–56. [CrossRef]
22. Hamid, S.B.A.; Teh, S.J.; Lai, C.W. Photocatalytic water oxidation on ZnO: A review. *Catalysts* **2017**, *7*, 93. [CrossRef]
23. Venkatesh, N.; Sabarish, K.; Murugadoss, G.; Thangamuthu, R.; Sakthivel, P. Visible light–driven photocatalytic dye degradation under natural sunlight using Sn-doped CdS nanoparticles. *Environ. Sci. Pollut. Res.* **2020**, *27*, 43212–43222. [CrossRef] [PubMed]
24. Nyamukamba, P.; Moloto, M.J.; Mungondori, H.H. Visible Light-Active CdS/TiO2 Hybrid Nanoparticles Immobilized on Polyacrylonitrile Membranes for the Photodegradation of Dyes in Water. *J. Nanotechnol.* **2019**, *2019*, 1–10. [CrossRef]
25. Yang, C.; Cheng, J.; Chen, Y.; Hu, Y. CdS nanoparticles immobilized on porous carbon polyhedrons derived from a metal-organic framework with enhanced visible light photocatalytic activity for antibiotic degradation. *Appl. Surf. Sci.* **2017**, *420*, 252–259. [CrossRef]
26. Hu, Y.; Gao, X.; Yu, L.; Wang, Y.; Ning, J.; Xu, S.; Ha, J.S. Carbon-Coated CdS Petalous Nanostructures with Enhanced Photostability and Photocatalytic Activity. *Angew. Chem. Int. Ed.* **2013**, *52*, 5636–5639. [CrossRef]
27. Dey, P.C.; Das, R. Enhanced photocatalytic degradation of methyl orange dye on interaction with synthesized ligand free CdS nanocrystals under visible light illumination. *Spectrochim. Acta Part A Mol. Biomol. Spectrosc.* **2020**, *231*, 118122. [CrossRef]
28. Reddy, C.V.; Vattikuti, S.P.; Shim, J. Synthesis, structural and optical properties of CdS nanoparticles with enhanced photocatalytic activities by photodegradation of organic dye molecules. *J. Mater. Sci. Mater. Electron.* **2016**, *27*, 7799–7808. [CrossRef]
29. Malik, R.; Singh, C.; Garg, R.; Kumar, V.; Singhal, S. Morphology Controlled CdS Nanostructures: A Proficient Visible-Light-Driven Photocatalyst. *Anal. Chem. Lett.* **2016**, *6*, 492–507. [CrossRef]
30. Zhang, Q.; Bu, X.; Zhang, J.; Wu, T.; Feng, P. Chiral semiconductor frameworks from cadmium sulfide clusters. *J. Am. Chem. Soc.* **2007**, *129*, 8412–8413. [CrossRef]
31. Thakur, S.; Das, P.; Mandal, S.K. Solvent-Induced Diversification of CdS Nanostructures for Photocatalytic Degradation of Methylene Blue. *ACS Appl. Nano Mater.* **2020**, *3*, 5645–5655. [CrossRef]
32. Yu, J.; Yu, Y.; Cheng, B. Enhanced visible-light photocatalytic H2-production performance of multi-armed CdS nanorods. *RSC Adv.* **2012**, *2*, 11829–11835. [CrossRef]
33. Singh, R.; Pal, B. Fine-tuning the photoluminescence and photocatalytic properties of CdS nanorods of varying dimensions. *Mater. Res. Bull.* **2013**, *48*, 1403–1410. [CrossRef]
34. Liu, Y.; Ma, Y.; Liu, W.; Shang, Y.; Zhu, A.; Tan, P.; Xiong, X.; Pan, J. Facet and morphology dependent photocatalytic hydrogen evolution with CdS nanoflowers using a novel mixed solvothermal strategy. *J. Colloid Interface Sci.* **2018**, *513*, 222–230. [CrossRef] [PubMed]
35. Ganesh, R.S.; Durgadevi, E.; Navaneethan, M.; Raji, P.; Ponnusamy, S.; Muthamizhchelvan, C.; Hayakawa, Y. Fabrication of bistable switching device using CdS nanorods embedded in PMMA (polymethylmethacrylate) nanocomposite. *J. Mater. Sci. Mater. Electron.* **2015**, *26*, 9010–9015. [CrossRef]
36. Chen, X.; Chen, W.; Lin, P.; Yang, Y.; Gao, H.; Yuan, J.; Shangguan, W. In situ photodeposition of nickel oxides on CdS for highly efficient hydrogen production via visible-light-driven photocatalysis. *Catal. Commun.* **2013**, *36*, 104–108. [CrossRef]
37. Ma, Y.; Zhao, Z.; Shen, Z.; Cai, Q.; Ji, H.; Meng, L. Hydrothermal carbonation carbon-coated CdS nanocomposite with enhanced photocatalytic activity and stability. *Catalysts* **2017**, *7*, 194. [CrossRef]
38. Rajendran, R.; Krishnakumar, V.; Jayaraman, V. Fabrication of tantalum doped CdS nanoparticles for enhanced photocatalytic degradation of organic dye under visible light exposure. *Colloids Surfaces A Physicochem. Eng. Asp.* **2019**, *580*, 123688. [CrossRef]
39. Singh, A.P.; Kumar, S.; Thirumal, M. Efficient Charge Transfer in Heterostructures of CdS/NaTaO3 with Improved Visible-Light-Driven Photocatalytic Activity. *ACS Omega* **2019**, *4*, 12175–12185. [CrossRef]
40. Cui, H.; Li, B.; Zhang, Y.; Zheng, X.; Li, X.; Li, Z.; Xu, S. Constructing Z-scheme based CoWO4/CdS photocatalysts with enhanced dye degradation and H2 generation performance. *Int. J. Hydrog. Energy* **2018**, *43*, 18242–18252. [CrossRef]
41. Devi, L.G.; Kumar, S.G. Exploring the critical dependence of adsorption of various dyes on the degradation rate using Ln3+-TiO2 surface under UV/solar light. *Appl. Surf. Sci.* **2012**, *261*, 137–146. [CrossRef]
42. Akbal, F. Photocatalytic degradation of organic dyes in the presence of titanium dioxide under UV and solar light: Effect of operational parameters. *Environ. Prog.* **2005**, *24*, 317–322. [CrossRef]
43. Salama, A.; Mohamed, A.; Aboamera, N.M.; Osman, T.A.; Khattab, A. Photocatalytic degradation of organic dyes using composite nanofibers under UV irradiation. *Appl. Nanosci.* **2018**, *8*, 155–161. [CrossRef]

processes

MDPI

Article

$CoFe_2O_4$ Nanomaterials: Effect of Annealing Temperature on Characterization, Magnetic, Photocatalytic, and Photo-Fenton Properties

Nguyen Thi To Loan [1,*], Nguyen Thi Hien Lan [1], Nguyen Thi Thuy Hang [2], Nguyen Quang Hai [3], Duong Thi Tu Anh [1], Vu Thi Hau [1], Lam Van Tan [4,5] and Thuan Van Tran [4,6,*]

1 Faculty of Chemistry, Thai Nguyen University of Education, Thai Nguyen City 24000, Vietnam; nguyenhienlan@dhsptn.edu.vn (N.T.H.L.); duongtuanh@dhsptn.edu.vn (D.T.T.A.); vuthihau-khoahoa@dhsptn.edu.vn (V.T.H.)
2 Thai Nguyen University of Technology, Thai Nguyen City 24000, Vietnam; thuyhangdhktcn@gmail.com
3 Faculty of Physics, Thai Nguyen University of Education, Thai Nguyen City 24000, Vietnam; nguyenquanghai@dhsptn.edu.vn
4 NTT Hi-Tech Institute, Nguyen Tat Thanh University, Ho Chi Minh City 700000, Vietnam; lamvantan101076@gmail.com
5 Ben Tre's Department of Science and Technology, Ben Tre Province 86000, Vietnam
6 Center of Excellence for Green Energy and Environmental Nanomaterials, Nguyen Tat Thanh University, Ho Chi Minh City 700000, Vietnam
* Correspondence: nguyentoloan@dhsptn.edu.vn (N.T.T.L.); tvthuan@ntt.edu.vn (T.V.T.)

Received: 23 October 2019; Accepted: 21 November 2019; Published: 28 November 2019

Abstract: In this research, structural, magnetic properties and photocatalytic activity of cobalt ferrite spinel ($CoFe_2O_4$) nanoparticles were studied. The samples were characterized by X-ray powder diffraction (XRD), energy dispersive X-ray (EDX), scanning electron microscopy (SEM), transmission electronic microscopy (TEM), Brunauer–Emmett–Teller (BET), Fourier transform infrared spectroscopy (FTIR), and UV-visible diffused reflectance spectroscopy (DRS) analysis. The XRD analysis revealed the formation of the single-phase $CoFe_2O_4$ with a cubic structure that is annealed at 500–700 °C in 3 h. The optical band gap energy for $CoFe_2O_4$ was determined to be in the range of 1.57–2.03 eV. The effect on the magnetic properties of cobalt ferrites was analyzed by using a vibrating sample magnetometer (VSM). The particle size and the saturation magnetization of cobalt ferrite nanoparticles increased with increasing annealing temperature. The photocatalytic activity of $CoFe_2O_4$ nanoparticles was investigated by using rhodamine B dye under visible light. The decomposition of rhodamine B reached 90.6% after 270 min lighting with the presence of H_2O_2 and CF500 sample.

Keywords: cobalt ferrite; magnetic properties; solution combustion method; rhodamine B; photocatalytic activity

1. Introduction

Among many ferrites, cobalt ferrite magnetic nanoparticles are attracting much attention because of their high coercivity, magnetocrystalline anisotropy, moderate saturation magnetization, chemical stability, wear resistance, electrical insulation, and structure [1]. Structurally, in the inverse spinel of the ferrite, tetrahedral sites are generally occupied by Fe^{3+} ions, whereas octahedral sites (B-sites) are inhabited by Co^{2+} and Fe^{3+} ions [2]. To alter structure and magnetic properties of ferrite nanoparticles, it is necessary to modify their composition and microstructures via different preparation routes [2]. $CoFe_2O_4$ nanoparticles were previously prepared by a wide array of synthesis routines, such as sol-gel [3,4], hydrothermal method [5], chemical co-precipitation [6,7], solvothermal [8], solid-state method [9], and solution combustion [10–13]. For each synthesis method, it was found that the

annealed temperature played a key role in determining the structure and properties of the obtained product. In recent years, photocatalytic oxidation of various dyes using ferrites has drawn a great deal of attention, opening new trends in the environmental remediation [14–16].

Currently, contamination of the water environment has been alarming due to the widespread use of organic compounds in manufacturing processes and the rapid development of dyeing industries. These dye compounds existing in water pose a direct threat to public health and to animal and aquatic life due to their toxicity, endocrine-disrupting capability, and mutagenic or potentially carcinogenic properties [17]. One of the most effective methods of solving this problem is advanced oxidation processes (AOPs). Among different AOPs, the photo-Fenton-like reaction was widely studied because it can produce more oxidative species such as hydroxyl radicals ($^{\bullet}OH$) to accelerate the reaction [18]. This method is based on the use of semiconductors and oxidant and light sources to perform the decomposition of organic matter. The advantages of the photo-Fenton processes consist of environmental friendliness and the ability to decompose completely organic pollutants into non-toxic inorganic substances, these being CO_2 and H_2O. Spinel ferrite materials have received wide application as photocatalysts due to their structural composition and thermal and chemical stability toward various reaction conditions [18]. The photo-Fenton reagent using ferrite can be easily recovered from the solution by an external magnetic field and is available for reutilization.

Abul Kalam et al. reported the photocatalytic activity of cobalt ferrite magnetic nanoparticles for degradation of methylene blue with H_2O_2 under visible light irradiation, and achieved very good performance [15]. P. Annie Vinosha et al. synthesized $NiFe_2O_4$ by co-precipitation technique. The photocatalytic application for the synthesized sample was studied for the degradation of methylene blue dye. In the presence of H_2O_2 and ferrites, methylene blue degradation efficiency reached ~30% in the dark but degradation improved to ~99% in the irradiation light [19]. $MgFe_2O_4$ nanoparticles synthesized by a solution combustion method exhibited a high ability for Photo-Fenton-like degradation of methylene blue [20]. In the photo-Fenton processes, hydrogen peroxide is used commonly as an oxidant. Hydrogen peroxide is safe and easy to handle and poses no lasting environmental threat because it readily decomposes to water and oxygen [17].

One of the major pollutants discharged from various industries is dyes [21–23]. Previous reports have revealed that thousands of new dyes have been synthesized and commercialized, with the total amount of approximately one million tons being consumed throughout the world [24,25]. Ever-increasing utilization and direct discharge without treatment of colored effluents have been considered as a problematic obstacle, affecting the photosynthesis of aquatic lives because of the reduction of the ability of light penetration [26]. Amid the most emergent synthetic dyes, rhodamine B (RhB) is a virtually hazardous and non-biodegradable dye [27]. In chemical essence, this compound is categorized as a cationic and soluble dye, in accordance with the existence of highly stable tertiary amine and carboxylic groups in its molecular structure. It is thus found to have a profound impact on living creatures as well as ambient environment via a range of approaches on direct or indirect exposure [28]. With such harmful and dangerous properties to many organisms, effective removal of dyes from wastewater is essential, but currently remains a challenge [29].

To eliminate the RhB contamination in wastewater, the adoption manifold feasible methods has been suggested, involving adsorption [30], electro-Fenton process [31], and microfiltration membrane [32]. For instance, Tawfik et al. synthesized the nano-sized polyamide-grafted carbon microspheres via interfacial polymerization, exhibiting a promising adsorption performance towards RhB at 19.9 mg/g [33]. Recently, Mustafa et al. have successfully attained a kind of eco-friendly activated carbon-based modified nanocomposite that combined carbon with bimetallic Fe and Ce nanoparticles [34]. Regardless of giving promising results in high surface area (~423 $m^2 \cdot g^{-1}$) and adsorption capacity (324.6 $m^2 \cdot g^{-1}$) towards RhB, the complicated preparation procedure limits applications of the synthesized nanocomposite. On the other hand, although the introduction of minerals as adsorbents for treating RhB have been developed, such approaches seem to confront many obstacles relating to material stability, recyclability, fabrication cost, and the reliance on post-treatment

separation [35–37]. With high stability, magnetism, and photocatalysis, $CoFe_2O_4$ nanoparticles are expected to deal with RhB pollution in water efficiently.

In this present report, the spinel cobalt ferrites nanoparticles are characterized for their structural, morphological, optical, and magnetic properties using various methods. In addition, the photocatalytic activity of samples was investigated by the degradation process of rhodamine B.

2. Materials and Methods

2.1. Materials

Cobalt nitrate hexahydrate ($Co(NO_3)_2{\cdot}6H_2O$), iron nitrate nonahydrate ($Fe(NO_3)_3{\cdot}9H_2O$), urea (CH_4N_2O), rhodamine B ($C_{28}H_{31}ClN_2O_3$), and hydrogen peroxide were obtained from Merck and used as received, without further purification.

2.2. Synthesis of $CoFe_2O_4$ Nanoparticles

The synthesis of cobalt ferrite was performed via solution combustion method using urea as fuel [11]. The process commenced with the dissolution of urea in the water, followed by the addition of $Co(NO_3)_2{\cdot}6H_2O$ and $Fe(NO_3)_3{\cdot}9H_2O$ at an appropriate amount and mole ratio under vigorous stirring. The resultant mixed solution was stirred further to afford a gel, which was then subjected to heating at 70 °C for 12 h in an oven. The obtained powder product was calcined at four different temperatures ranging from 500 to 800 °C for 3 h with a heat rate of 5 °C min^{-1}, and the subsequent products were labeled as CF500, CF600, CF700, and CF800 respectively.

2.3. Characterizations

The first characterization involved determining the crystallite size, r, of spinel using Scherrer's formula as follows:

$$r = \frac{k\lambda}{\beta \cos \theta} \quad (1)$$

where λ, k, β, and θ are the X-ray wavelength, Scherrer's constant (k = 0.89), the full width at half maximum observed in radians, and the angle of diffraction of the (311) peak with the highest intensity, respectively. θ and β were obtained via X-ray diffraction (XRD) results using a D8 Advance diffractometer (Brucker, Madison, WI, USA) instrument with CuK_α radiation (λ = 1.5406 Å) in a 2θ angle ranging from 20 to 70° with a step of 0.03°.

The second characterization regarding morphology of the particles was obtained via scanning electron microscope (SEM, Hitachi S-4800, Tokyo, Japan) and transmission electron microscopy (TEM, JEOL-JEM-1010, Tokyo, Japan). The composition of the samples was analyzed by energy dispersive X-ray spectroscopy (EDX, JEOL JED 2300 Analysis Station, Tokyo, Japan). N_2-sorption investigation was performed to obtain the Bet-specific surface area of the product. A surface analyzer instrument (a Quantachrome Nova 2200, Boynton Beach, FL, USA) was employed to obtain the isotherm at 77 K. The specific surface area was calculated via the Brunauer–Emmet–Teller (BET) method. The spinel structure was affirmed by Fourier transform infrared spectroscopy (FTIR Affinity-1S, Shimadzu, Tokyo, Japan). A UV-VIS absorption spectrometer (U-4100, Hitachi, Japan) was employed to obtain the optical absorption spectra. To elaborate magnetic properties of samples, a vibrating sample magnetometer (VSM, Ha Noi, Vietnam) operating at room temperature was utilized.

2.4. Photocatalytic Degradation of Rhodamine B

Multiple ferrite samples synthesized at different annealing temperatures were examined for photodegradation performance against Rhodamine B (RhB) aqueous solution. The irradiation source was 30 W LED lamps (Philips). The experiment commenced with the addition of 100 mg of ferrite sample into 100 mL of 10 mg. L^{-1} RhB aqueous solution. Following that, stirring was carried out in the dark for 30 min to allow the solution to reach the adsorption–desorption equilibrium state, followed

by the addition of 1.5 mL of 30% H_2O_2. Consequently, visible light irradiation started and the reaction took place under stirring. After specific periods, 5 mL of aliquots were removed and subjected to centrifugation for particle separation. RhB concentration was determined using an ultraviolet-visible spectrophotometer (UV-1700 Shimadzu, Tokyo, Japan) at 553 nm. The degradation efficiency of the ferrite against RhB (H) was calculated as follows:

$$H = \frac{C_o - C_t}{C_o} \times 100\% \quad (2)$$

where C is the concentration of RhB. The subscript 0 and t denote equilibrium state and time (t) after irradiation, respectively.

3. Results and Discussion

3.1. Structural Analysis

Different XRD patterns of cobalt ferrites corresponding to different annealing temperatures are shown in Figure 1. The reflection peaks corresponded to the characteristic spacing between (220), (311), (400), (511), and (440) plans of a cubic spinel structure, providing clear evidence of the formation of cobalt ferrite (JCPDS number 22–1086) [5]. α-Fe_2O_3 peaks corresponding to secondary impurities were observed for the sample annealed at 800 °C, which was possibly caused by sample decomposition [38]. Table 1 lists the average crystallite size (r), calculated using (1), and the lattice parameter (a), obtained using the formula $a^2 = d^2/(h^2 + k^2 + l^2)$ with inputs obtained from X-ray diffraction data. The mean crystallite size ranged from 9 to 29 nm and increased with elevated annealing temperature [29]. The lattice parameter for the samples of cobalt ferrites nanoparticles varied from 8.3347 to 8.3745 Å.

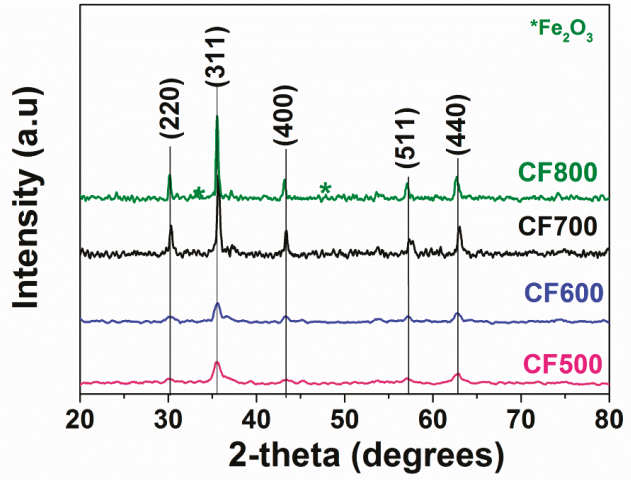

Figure 1. X-ray diffractions of $CoFe_2O_4$ nanoparticles annealed at 500–800 °C.

Table 1. Average crystallite size (r), lattice parameter (a), unit cell volume (V), wave number (ν_1 and ν_2) for the tetrahedral and octahedral site, respectively, and Brunauer–Emmet–Teller (BET) surface area of all the $CoFe_2O_4$ samples.

Samples	r (nm)	a (Å)	V (Å^3)	ν_1 (cm^{-1})	ν_2 (cm^{-1})	S_{BET} (m^2.g^{-1})
CF500	9	8.37	587.32	526	411	12.69
CF600	11	8.36	584.53	530	409	7.55
CF700	23	8.33	578.98	532	408	3.94
CF800	29	8.36	585.23	522	412	1.58

FTIR spectra of $CoFe_2O_4$ nanoparticles annealed at different temperatures are displayed in Figure 2. The cobalt ferrite samples exhibited two vibration bands at wave number 522–532 cm^{-1} (ν_1) and at 408–412 cm^{-1} (ν_2), corresponding to the stretching vibration of the M-O bond in tetrahedral and octahedral sites (Table 1). A. Kalam et al. [15] observed that the vibration mode between tetrahedral metal ion and oxygen complex gives rise to the high-frequency band in the range of 597–615 cm^{-1}, whereas stretching vibration between octahedral metal ion and oxygen complex gives rise to the weak frequency band in the range of 412–400 cm^{-1} in the case of cobalt ferrite, which is an inverse spinel ferrite.

The FTIR results confirmed that the samples had a spinel structure of $CoFe_2O_4$, which was revealed by the XRD results.

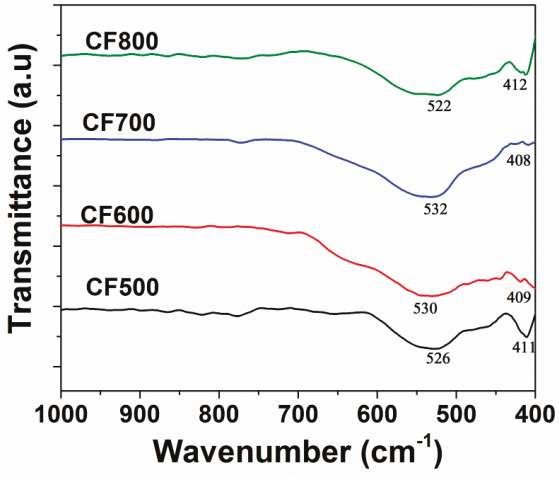

Figure 2. Fourier transform infrared (FTIR) spectrum of CF500–CF800 samples.

Figure 3 shows the SEM micrographs of $CoFe_2O_4$ nanoparticles annealed at different temperatures. The SEM images indicated that particles were agglomerated and spherical. In addition, the crystalline size of the samples seemed to increase proportionally with annealing temperature, which was consistent with the results of XRD analysis. The agglomeration could be explained by the interaction between magnetic particles that occurred during annealing under high temperatures. In addition, it was previously found that higher annealing temperature inevitably causes moderate agglomeration [2].

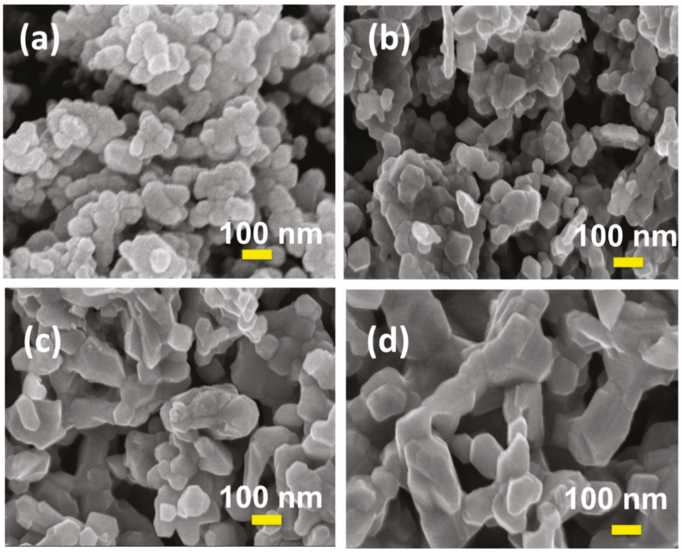

Figure 3. Scanning electron microscopy (SEM) of $CoFe_2O_4$ nanoparticles: (**a**) CF500, (**b**) CF600, (**c**) CF700, (**d**) CF800.

TEM images (Figure 4a) of the $CoFe_2O_4$ annealed at 500 °C revealed that the particle size was approximately 20 nm. Compositional determination was performed by energy dispersive X-ray spectroscopy (EDX) analysis, showing peaks corresponding to Co, Fe, and O elements of the CF500 sample (Figure 4b).

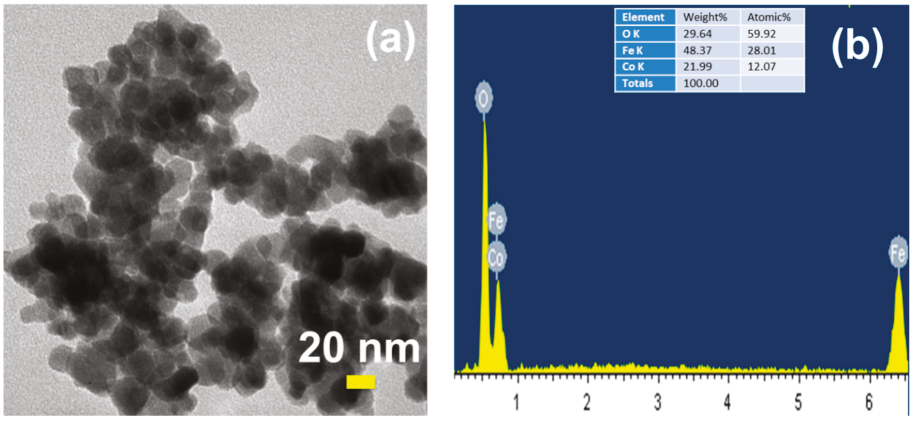

Figure 4. Transmission electronic microscopy (TEM) (**a**) and energy dispersive X-ray (EDX) (**b**) of the CF500 sample.

Isotherm of N_2 adsorption–desorption of products annealed at 500–800 °C are displayed in Figure 5. The decrease in the cobalt ferrites surface area was observed with the increase in annealing temperature (Table 1). The $CoFe_2O_4$ nanoparticles synthesized at 500 °C achieved the highest specific surface area of 12.69 $m^2 \cdot g^{-1}$.

Thus, annealing temperature affected the particle size, morphology, and surface area of cobalt ferrites.

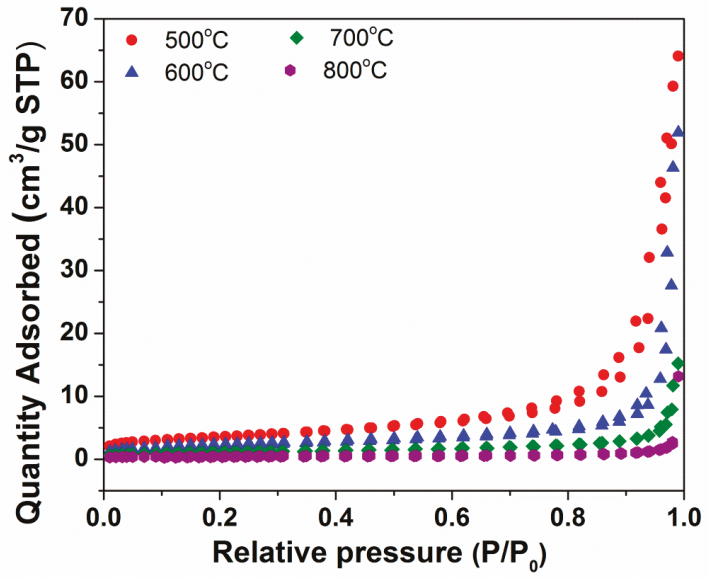

Figure 5. N_2 adsorption–desorption isotherm of CF500, CF600, CF700, and CF800.

Kubelka–Munk model was employed to calculate the band gaps (E_g) of $CoFe_2O_4$ nanoparticles using the absorption coefficient (α) calculated from diffuse reflectance spectra (DRS), as follows [39,40]:

$$F(R) = \alpha = \frac{(1-R)^2}{2R} \quad (3)$$

where F(R) is the Kubelka–Munk function, α is the absorption coefficient, and R is the reflectance. The band gap energy (E_g) of $CoFe_2O_4$ nanoparticles can be calculated by the following equation:

$$\alpha h\nu = A(h\nu - E_g)^n \quad (4)$$

where hν, α, A, and n represent energy of the photon, the absorption coefficient, the material parameter, and the transition parameter, respectively. n = 2 represents indirect transitions [41]. To determine the optical band gap energy (E_g), $(\alpha h\nu)^2$ was plotted against photon energy (hν) to produce multiple Wood–Tauc plots (Figure 6). The band gap values of CF500, CF600, CF700, and CF800 samples were found to be 1.57, 1.66, 1.90, and 2.03 eV, respectively. This indicated that the annealing affected the optical band gap energy of $CoFe_2O_4$ nanoparticles. The optical band gap energy value increased with increasing temperature in annealed samples.

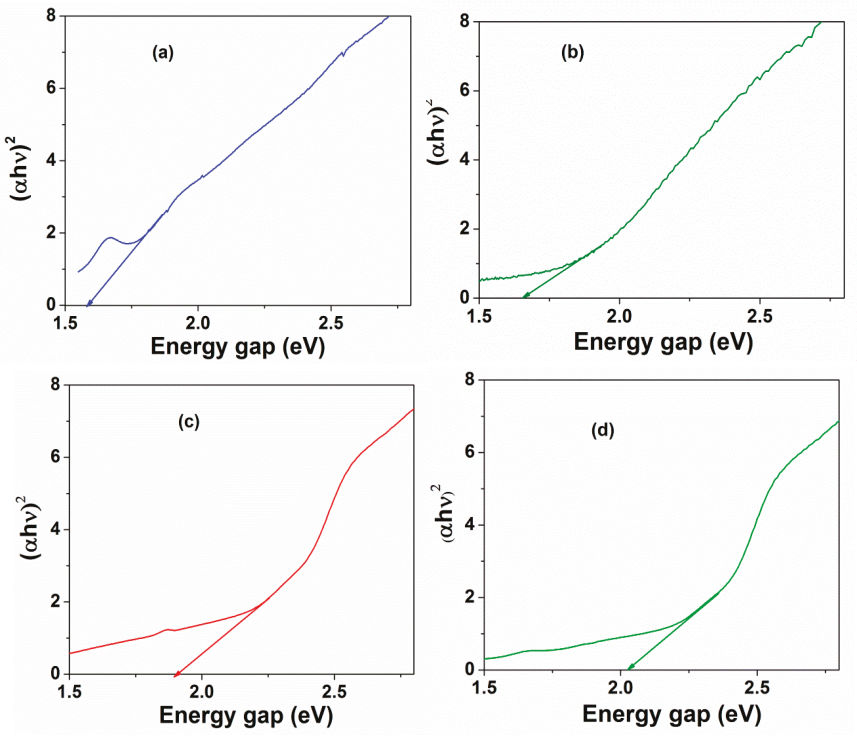

Figure 6. Wood–Tauc plots for $CoFe_2O_4$ nanoparticles: (**a**) CF500, (**b**) CF600, (**c**) CF700, (**d**) CF800.

3.2. Magnetic Properties

The magnetic properties of ferrites could be largely determined by various elements such as density, grain size, anisotropy, and A–B exchange interactions [1]. In this investigation, obtained ferrite products annealed at different temperatures were subjected to M–H hysteresis measurements carried out at room temperature. Various magnetic properties including saturation magnetization (M_s), coercivity (H_c), and remanent magnetization (M_r) are listed in Figure 7 and Table 2. It was observed that M_s value showed a positive correlation with particle size. This was in line with Kumar et al., suggesting that increased particle size could lead to improved magnetization [2].

Table 2. Magnetic parameter of the $CoFe_2O_4$ nanoparticles.

Samples	M_s (emu/g)	H_c (Oe)	M_r (emu/g)
CF500	44.41	1739.45	20.36
CF600	53.86	1234.10	22.88
CF700	59.40	1234.20	27.89
CF800	61.80	762.04	27.83

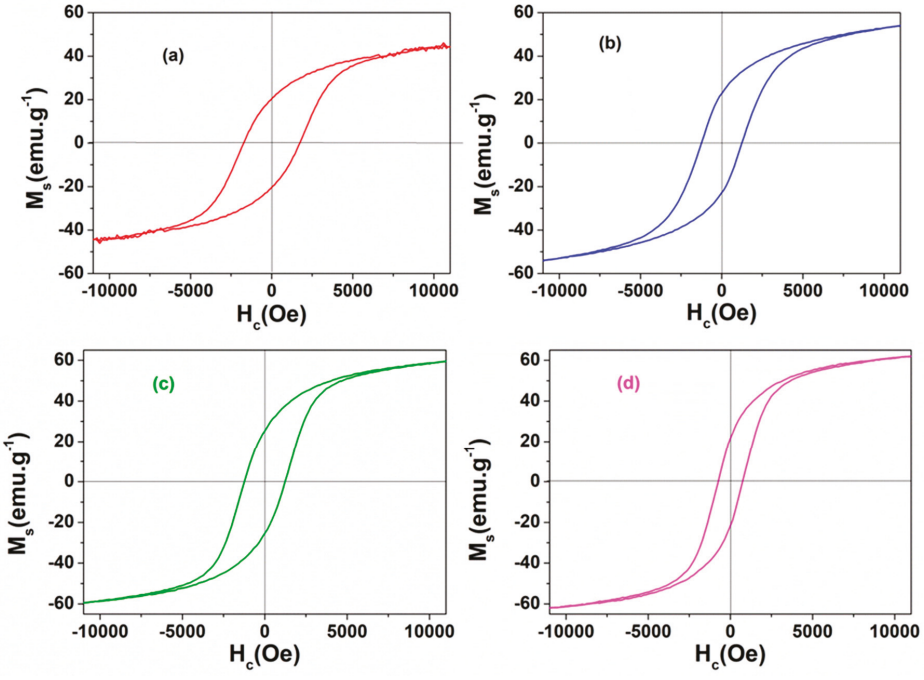

Figure 7. Hysteresis loop of $CoFe_2O_4$ nanoparticles: (**a** CF500, (**b**) CF600, (**c**) CF700, (**d**) CF800.

3.3. Photochemical Activities

Figure 8 represented the photocatalytic degradation of RhB versus irradiation time in different conditions. Generally, absorption peaks observed at 501 and 553 nm could be attributable to the absorption fully de-ethylated and tetraethylated rhodamine B molecules, respectively [41]. The role of oxidant and catalyst was further elaborated by performing reactions under typical conditions that were neither H_2O_2 nor $CoFe_2O_4$. Firstly, RhB degradation efficiency reached a marginal percentage, at just 10.2%, under visible light after 270 min in the sole presence of H_2O_2. This implied that RhB dye could be hardly photodegraded in the absence of $CoFe_2O_4$ catalyst. In the presence of $CoFe_2O_4$ sample without oxidation reagent H_2O_2, RhB degradation efficiency achieved 9.4% (in the dark) and 32.5% (under light irradiation) after 270 min. In the absence of light, 21.3% of RhB was degraded while using both $CoFe_2O_4$ and H_2O_2. Abul et al. also observed similar results by using $CoFe_2O_4$ as a catalyst for the degradation of methylene blue in liquid under air atmosphere [15].

Grasping this improvement, we speculated about an even better photodegradation efficiency when $CoFe_2O_4$ and H_2O_2 were combined for the next photoreaction. Photocatalyzed degradation efficiency (%) towards RhB under visible light irradiation and in the presence of $CoFe_2O_4$ and H_2O_2 against the interval irradiation time is indicated in the UV-visible spectra in Figure 9. Indeed, all the samples of $CoFe_2O_4$ (CF) nanoparticles offered an enhancement in catalytic performance, but the percentages of RhB decomposition varied according to the distinct annealing temperature (500, 600, 700, and 800 °C). The photocatalytic degradation efficiency of RhB was evaluated at about 90.6%, 67.6%, 51.6%, and 42.8% after 270 min of lighting in the presence of H_2O_2 and CF500, CF600, CF700, and CF800, respectively.

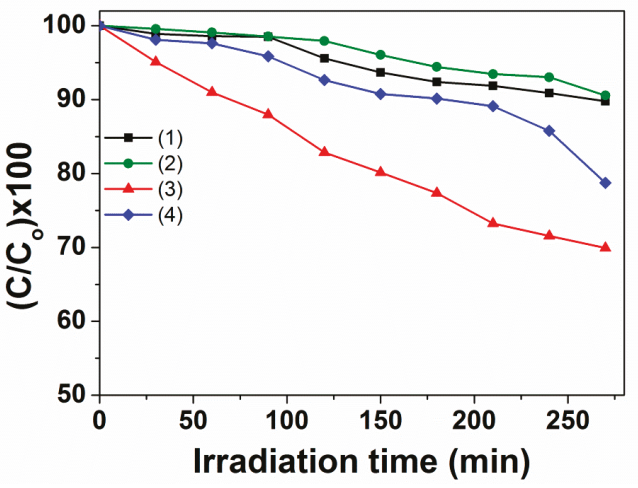

Figure 8. The plots of (C/C_o) ×100 versus irradiation time (t) in different conditions: (**1**) H_2O_2, (**2**) CF500 + dark, (**3**) CF500 + light, (**4**) CF500 + H_2O_2 + dark.

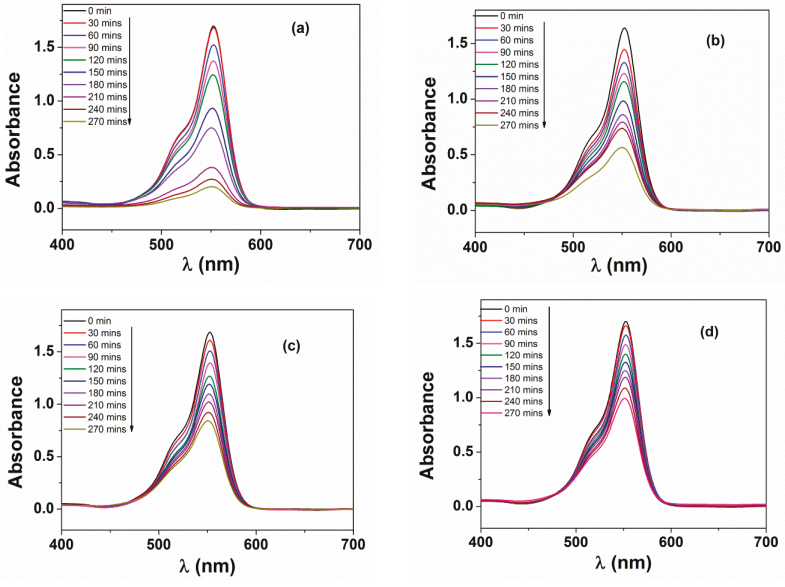

Figure 9. UV-visible spectra of RhB degraded by (**a**) H_2O_2 + CF500, (**b**) H_2O_2 + CF600, (**c**) H_2O_2 + CF700, (**d**) H_2O_2 + CF800 after 270 min of lighting.

The pollutant degradation rate could be substantially increased due to highly oxidative hydroxyl ($^{\bullet}OH$) radicals created by the heterogeneous photo-Fenton process, in the presence of spinel ferrite as a heterogeneous catalyst, using H_2O_2 as oxidant under light irradiation [15,42]. The mechanism of the heterogeneous photo-Fenton reaction was shown according to the following equations:

$$Fe^{3+} + H_2O_2 + h\nu \rightarrow Fe^{2+} + HOO^{\bullet} + H^+$$

$$Fe^{2+} + H_2O_2 + h\nu \rightarrow Fe^{3+} + {}^{\bullet}OH + OH^-$$

where Fe^{3+} and Fe^{2+} represent the iron species on the surface of a heterogeneous catalyst.

Due to Fe(II, III) cycling, the stability of the ferrite system is maintained during the degradation process and the active species are generated continuously [15].

The peak photocatalytic degradation efficiency for CF500 (90.6%) was due to the effective crystallite size (9 nm), separation, and prevention of electron-hole pair (e^-/h^+) recombination [43]. Photocatalytic performance of CF500 with the largest degradation rate could be interpreted via plausible hypotheses based on the following foundations:

(i) It was found that CF500 possessed the lowest pore sizes, which is indicative of a high surface area of nanoparticles. This could accelerate the adsorption of RhB molecules on the surface, leading to a higher likelihood of $^{\bullet}OH$ radical formation [43].

(ii) More importantly, CF500 nanoparticles with the lowest bandgap (1.57 eV) were more likely to form the electron–hole pair under visible light irradiation, dominating the charge carriers with oxidation of RhB [15].

(iii) Samples that were calcined at a higher temperature had greater band gap values, which possibly deferred the electron–hole pair recombination induced by visible light irradiation [44].

Figure 10 depicted the plots with different pseudo first order rates, which were obtained by fitting the following equation:

$$\ln\left(\frac{C_o}{C_t}\right) = kt$$

where C is the RhB concentration. The subscripts 0 and t denote initial state and time t after irradiation. k is the pseudo first order rate kinetics.

With the higher the coefficient of determination ($R^2 > 0.9$), the proposed model was highly compatible [45,46]. The estimated parameters, including pseudo first order rate constant k values and R^2 values, are shown in Table 3. The first order rate constant for CF500 was 0.839×10^{-2} min^{-1}, and it was 3.9 times faster than that of CF800. High R^2 values also confirmed the adherence of the photocatalytic degradation of RhB to the first order kinetics.

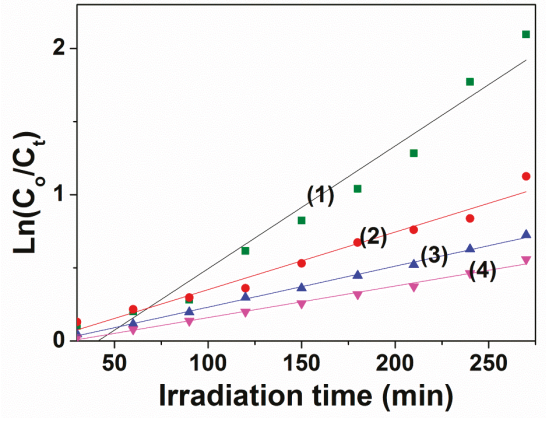

Figure 10. The plots of $\ln(C_o/C_t)$ versus irradiation time (t) in the presence of H_2O_2 and $CoFe_2O_4$ nanoparticles: (**1**) CF500, (**2**) CF600, (**3**) CF700, (**4**) CF800.

Table 3. Pseudo first order rate constant (k) for the photocatalytic degradation of RhB using $CoFe_2O_4$ nanoparticles.

Samples	Rate Constant, ($k \times 10^{-2}$ min^{-1})	R^2
CF500	0.839	0.960
CF600	0.394	0.967
CF700	0.280	0.997
CF800	0.216	0.990

4. Conclusions

$CoFe_2O_4$ spinel nanoparticles were successfully synthesized via solution combustion method using urea as a fuel. The effect of annealing temperature on phase composition, morphology, optical property, and magnetic properties of $CoFe_2O_4$ materials was studied. The crystallite size calculated by the Scherer formula increased from 9 to 29 nm with an increase in the annealing temperature. By elevating the annealing temperature, it was found that the band gap energy value and saturation magnetization of $CoFe_2O_4$ spinel were also accordingly increased. The photocatalytic degradation against RhB dye of $CoFe_2O_4$ spinel decreased with increasing annealed temperature. Among all the cobalt ferrite samples, CF500 exhibited an enhanced degradation efficiency of 90.6% at a visible light exposure time of 270 min. The first-order rate constant for CF500 was 0.839×10^{-2} min^{-1} and was 3.9 times faster than CF800. The photocatalytic degradation of RhB dye followed first order kinetics. The current results suggest a possible application of cobalt ferrites nanoparticles in treatment of dye-contaminated water.

Author Contributions: Investigation, N.T.H.L., N.T.T.H., N.Q.H., D.T.T.A., V.T.H., L.V.T. and T.V.T.; Writing—original draft, N.T.T.L.

Funding: This research received no external funding.

Conflicts of Interest: The authors declare no conflict of interest.

References

1. Phong, P.T.; Phuc, N.X.; Nam, P.H.; Chien, N.V.; Dung, D.D.; Linh, P.H. Size-controlled heating ability of $CoFe_2O_4$ nanoparticles foráhyperthermia applications. *Phys. B Condens. Matter* **2018**, *531*, 30–34. [CrossRef]
2. Kumar, E.R.; Jayaprakash, R.; Kumar, S. Effect of annealing temperature on structural and magnetic properties of manganese substituted $NiFe_2O_4$ nanoparticles. *Mater. Sci. Semicond. Process.* **2014**, *17*, 173–177. [CrossRef]
3. Tong, J.; Bo, L.; Li, Z.; Lei, Z.; Xia, C. Magnetic $CoFe_2O_4$ nanocrystal: A novel and efficient heterogeneous catalyst for aerobic oxidation of cyclohexane. *J. Mol. Catal. A Chem.* **2009**, *307*, 58–63. [CrossRef]
4. Rao, K.S.; Choudary, G.; Rao, K.H.; Sujatha, C. Structural and magnetic properties of ultrafine $CoFe_2O_4$ nanoparticles. *Procedia Mater. Sci.* **2015**, *10*, 19–27. [CrossRef]
5. Kumar, S.; Munjal, S.; Khare, N. Metal-semiconductor transition and Seebeck inversion in $CoFe_2O_4$ nanoparticles. *J. Phys. Chem. Solids* **2017**, *105*, 86–89. [CrossRef]
6. Salazar-Kuri, U.; Estevez, J.O.; Silva-González, N.R.; Pal, U. Large magnetostriction in chemically fabricated $CoFe_2O_4$ nanoparticles and its temperature dependence. *J. Magn. Magn. Mater.* **2018**, *460*, 141–145. [CrossRef]
7. Annie Vinosha, P.; Jerome Das, S. Investigation on the role of pH for the structural, optical and magnetic properties of cobalt ferrite nanoparticles and its effect on the photo-fenton activity. *Mater. Today Proc.* **2018**, *5*, 8662–8671. [CrossRef]
8. Dong, N.; He, F.; Xin, J.; Wang, Q.; Lei, Z.; Su, B. Preparation of $CoFe_2O_4$ magnetic fiber nanomaterial via a template-assisted solvothermal method. *Mater. Lett.* **2015**, *141*, 238–241. [CrossRef]
9. Varma, P.C.R.; Manna, R.S.; Banerjee, D.; Varma, M.R.; Suresh, K.G.; Nigam, A.K. Magnetic properties of $CoFe_2O_4$ synthesized by solid state, citrate precursor and polymerized complex methods: A comparative study. *J. Alloys Compd.* **2008**, *453*, 298–303. [CrossRef]
10. Maleki, A.; Hosseini, N.; Taherizadeh, A. Synthesis and characterization of cobalt ferrite nanoparticles prepared by the glycine-nitrate process. *Ceram. Int.* **2018**, *44*, 8576–8581. [CrossRef]

11. Gabal, M.A.; Al-Juaid, A.A.; El-Rashed, S.; Hussein, M.A. Synthesis and characterization of nano-sized CoFe2O4 via facile methods: A comparative study. *Mater. Res. Bull.* **2017**, *89*, 68–78. [CrossRef]
12. Pourgolmohammad, B.; Masoudpanah, S.M.; Aboutalebi, M.R. Synthesis of $CoFe_2O_4$ powders with high surface area by solution combustion method: Effect of fuel content and cobalt precursor. *Ceram. Int.* **2017**, *43*, 3797–3803. [CrossRef]
13. Rajan Babu, D.; Venkatesan, K. Synthesis of nanophasic $CoFe_2O_4$ powder by self-igniting solution combustion method using mix up fuels. *J. Cryst. Growth* **2017**, *468*, 179–184. [CrossRef]
14. Yadav, N.G.; Chaudhary, L.S.; Sakhare, P.A.; Dongale, T.D.; Patil, P.S.; Sheikh, A.D. Impact of collected sunlight on $ZnFe_2O_4$ nanoparticles for photocatalytic application. *J. Colloid Interface Sci.* **2018**, *527*, 289–297. [CrossRef]
15. Kalam, A.; Al-Sehemi, A.G.; Assiri, M.; Du, G.; Ahmad, T.; Ahmad, I.; Pannipara, M. Modified solvothermal synthesis of cobalt ferrite ($CoFe_2O_4$) magnetic nanoparticles photocatalysts for degradation of methylene blue with H2O2/visible light. *Results Phys.* **2018**, *8*, 1046–1053. [CrossRef]
16. Vinosha, P.A.; Xavier, B.; Anceila, D.; Das, S.J. Nanocrystalline ferrite (MFe_2O_4, M = Ni, Cu, Mn and Sr) photocatalysts synthesized by homogeneous Co-precipitation technique. *Optik* **2018**, *157*, 441–448. [CrossRef]
17. Guo, X.; Wang, K.; Li, D.; Qin, J. Heterogeneous photo-Fenton processes using graphite carbon coating hollow $CuFe_2O_4$ spheres for the degradation of methylene blue. *Appl. Surf. Sci.* **2017**, *420*, 792–801. [CrossRef]
18. Kurian, M.; Nair, D.S. Heterogeneous Fenton behavior of nano nickel zinc ferrite catalysts in the degradation of 4-chlorophenol from water under neutral conditions. *J. Water Process Eng.* **2015**, *8*, e37–e49. [CrossRef]
19. Annie Vinosha, P.; Xavier, B.; Ashwini, A.; Ansel Mely, L.; Jerome Das, S. Tailoring the photo-Fenton activity of nickel ferrite nanoparticles synthesized by low-temperature coprecipitation technique. *Optik* **2017**, *137*, 244–253. [CrossRef]
20. Nguyen, L.T.T.; Nguyen, L.T.H.; Manh, N.C.; Quoc, D.N.; Quang, H.N.; Nguyen, H.T.T.; Nguyen, D.C.; Bach, L.G. A Facile Synthesis, Characterization, and Photocatalytic Activity of Magnesium Ferrite Nanoparticles via the Solution Combustion Method. *J. Chem.* **2019**, *2019*, 3428681. [CrossRef]
21. Xie, H.; Gu, S.; Zhang, J.; Hu, Q.; Yu, X.; Kong, J. Novel PEI–AuNPs–MnIIIPPIX nanocomposite with enhanced peroxidase-like catalytic activity in aqueous media. *C. R. Chim.* **2018**, *21*, 104–111. [CrossRef]
22. Sahnoun, S.; Boutahala, M.; Tiar, C.; Kahoul, A. Adsorption of tartrazine from an aqueous solution by octadecyltrimethylammonium bromide-modified bentonite: Kinetics and isotherm modeling. *C. R. Chim.* **2018**, *21*, 391–398. [CrossRef]
23. Khelifi, S.; Ayari, F. Modified bentonite for anionic dye removal from aqueous solutions. Adsorbent regeneration by the photo-Fenton process. *C. R. Chim.* **2019**, *22*, 154–160. [CrossRef]
24. da Rosa, A.L.D.; Carissimi, E.; Dotto, G.L.; Sander, H.; Feris, L.A. Biosorption of rhodamine B dye from dyeing stones effluents using the green microalgae Chlorella pyrenoidosa. *J. Clean. Prod.* **2018**, *198*, 1302–1310. [CrossRef]
25. Van Tran, T.; Nguyen, D.T.C.; Le, H.T.N.; Duong, C.D.; Bach, L.G.; Nguyen, H.-T.T.; Nguyen, T.D. Facile synthesis of manganese oxide-embedded mesoporous carbons and their adsorbability towards methylene blue. *Chemosphere* **2019**, *227*, 455–461. [CrossRef]
26. Sanchez-Hachair, A.; Hofmann, A. Hexavalent chromium quantification in solution: Comparing direct UV–visible spectrometry with 1,5-diphenylcarbazide colorimetry. *C. R. Chim.* **2018**, *21*, 890–896. [CrossRef]
27. Ignat, M.; Rotaru, R.; Samoila, P.; Sacarescu, L.; Timpu, D.; Harabagiu, V. Relationship between the component synthesis order of zinc ferrite–titania nanocomposites and their performances as visible light-driven photocatalysts for relevant organic pollutant degradation. *C. R. Chim.* **2018**, *21*, 263–269. [CrossRef]
28. Dimić, D. The importance of specific solvent–solute interactions for studying UV–vis spectra of light-responsive molecular switches. *C. R. Chim.* **2018**, *21*, 1001–1010. [CrossRef]
29. Sharma, R.; Singhal, S. Structural, magnetic and electrical properties of zinc doped nickel ferrite and their application in photo catalytic degradation of methylene blue. *Phys. B Condens. Matter* **2013**, *414*, 83–90. [CrossRef]
30. Van Tran, T.; Nguyen, D.T.C.; Le, H.T.N.; Bach, L.G.; Vo, D.-V.N.; Lim, K.T.; Nong, L.X.; Nguyen, T.D. Combined Minimum-Run Resolution IV and Central Composite Design for Optimized Removal of Tetracycline Drug Over Metal–Organic Framework-Templated Porous Carbon. *Molecules* **2019**, *24*, 1887. [CrossRef]

31. Jinisha, R.; Gandhimathi, R.; Ramesh, S.T.; Nidheesh, P.V.; Velmathi, S. Removal of rhodamine B dye from aqueous solution by electro-Fenton process using iron-doped mesoporous silica as a heterogeneous catalyst. *Chemosphere* **2018**, *200*, 446–454. [CrossRef] [PubMed]
32. Shi, P.; Hu, X.; Wang, Y.; Duan, M.; Fang, S.; Chen, W. A PEG-tannic acid decorated microfiltration membrane for the fast removal of Rhodamine B from water. *Sep. Purif. Technol.* **2018**, *207*, 443–450. [CrossRef]
33. Saleh, T.A.; Ali, I. Synthesis of polyamide grafted carbon microspheres for removal of rhodamine B dye and heavy metals. *J. Environ. Chem. Eng.* **2018**, *6*, 5361–5368. [CrossRef]
34. Tuzen, M.; Sarı, A.; Saleh, T.A. Response surface optimization, kinetic and thermodynamic studies for effective removal of rhodamine B by magnetic AC/CeO_2 nanocomposite. *J. Environ. Manag.* **2018**, *206*, 170–177. [CrossRef] [PubMed]
35. Guégan, R. Organoclay applications and limits in the environment. *C. R. Chim.* **2019**, *22*, 132–141. [CrossRef]
36. Nabbou, N.; Belhachemi, M.; Boumelik, M.; Merzougui, T.; Lahcene, D.; Harek, Y.; Zorpas, A.A.; Jeguirim, M. Removal of fluoride from groundwater using natural clay (kaolinite): Optimization of adsorption conditions. *C. R. Chim.* **2019**, *22*, 105–112. [CrossRef]
37. Abidi, N.; Duplay, J.; Jada, A.; Errais, E.; Ghazi, M.; Semhi, K.; Trabelsi-Ayadi, M. Removal of anionic dye from textile industries' effluents by using Tunisian clays as adsorbents. Zeta potential and streaming-induced potential measurements. *C. R. Chim.* **2019**, *22*, 113–125. [CrossRef]
38. Van Tran, T.; Nguyen, D.T.C.; Nguyen, H.-T.T.; Nanda, S.; Vo, D.-V.N.; Do, S.T.; Van Nguyen, T.; Thi, T.A.D.; Bach, L.G.; Nguyen, T.D. Application of Fe-based metal-organic framework and its pyrolysis products for sulfonamide treatment. *Environ. Sci. Pollut. Res.* **2019**, *26*, 28106–28126. [CrossRef]
39. Sundararajan, M.; John Kennedy, L.; Nithya, P.; Judith Vijaya, J.; Bououdina, M. Visible light driven photocatalytic degradation of rhodamine B using Mg doped cobalt ferrite spinel nanoparticles synthesized by microwave combustion method. *J. Phys. Chem. Solids* **2017**, *108*, 61–75. [CrossRef]
40. Nadumane, A.; Shetty, K.; Anantharaju, K.S.; Nagaswarupa, H.P.; Rangappa, D.; Vidya, Y.S.; Nagabhushana, H.; Prashantha, S.C. Sunlight photocatalytic performance of Mg-doped nickel ferrite synthesized by a green sol-gel route. *J. Sci. Adv. Mater. Devices* **2019**, *4*, 89–100. [CrossRef]
41. Almessiere, M.A.; Slimani, Y.; Güner, S.; Nawaz, M.; Baykal, A.; Aldakheel, F.; Akhtar, S.; Ercan, I.; Belenli, İ.; Ozçelik, B. Magnetic and structural characterization of Nb^{3+}-substituted $CoFe_2O_4$ nanoparticles. *Ceram. Int.* **2019**, *45*, 8222–8232. [CrossRef]
42. Sharma, R.; Bansal, S.; Singhal, S. Augmenting the catalytic activity of $CoFe_2O_4$ by substituting rare earth cations into the spinel structure. *RSC Adv.* **2016**, *6*, 71676–71691. [CrossRef]
43. Han, L.; Zhou, X.; Wan, L.; Deng, Y.; Zhan, S. Synthesis of $ZnFe_2O_4$ nanoplates by succinic acid-assisted hydrothermal route and their photocatalytic degradation of rhodamine B under visible light. *J. Environ. Chem. Eng.* **2014**, *2*, 123–130. [CrossRef]
44. Wu, X.; Wang, W.; Li, F.; Khaimanov, S.; Tsidaeva, N.; Lahoubi, M. PEG-assisted hydrothermal synthesis of $CoFe_2O_4$ nanoparticles with enhanced selective adsorption properties for different dyes. *Appl. Surf. Sci.* **2016**, *389*, 1003–1011. [CrossRef]
45. Van Tran, T.; Nguyen, D.T.C.; Le, H.T.N.; Nguyen, O.T.K.; Nguyen, V.H.; Nguyen, T.T.; Bach, L.G.; Nguyen, T.D. A hollow mesoporous carbon from metal-organic framework for robust adsorbability of ibuprofen drug in water. *R. Soc. Open Sci.* **2019**, *6*, 190058. [CrossRef]
46. Van Tran, T.; Nguyen, D.T.C.; Le, H.T.N.; Bach, L.G.; Vo, D.-V.N.; Hong, S.S.; Phan, T.-Q.T.; Nguyen, T.D. Tunable Synthesis of Mesoporous Carbons from Fe_3O (BDC) 3 for Chloramphenicol Antibiotic Remediation. *Nanomaterials* **2019**, *9*, 237. [CrossRef]

processes

MDPI

Article

Degradation of 2,4-Dichlorophenol by Ethylenediamine-*N*,*N*′-disuccinic Acid-Modified Photo-Fenton System: Effects of Chemical Compounds Present in Natural Waters

Wenyu Huang [1,2,3], Ying Huang [1], Shuangfei Wang [2,3], Hongfei Lin [3] and Gilles Mailhot [4,*]

[1] School of the Resources, Environment and Materials, Guangxi University, Nanning 530004, China; huangwenyu@gxu.edu.cn (W.H.); huangying_ing@163.com (Y.H.)
[2] Guangxi Key Laboratory of Clean Pulp & Papermaking and Pollution Control, Guangxi University, Nanning 530004, China; wangsf@gxu.edu.cn
[3] Guangxi Bossco Environmental Protection Technology Co., Ltd., Nanning 530007, China; linhf@bossco.cc
[4] Institut de Chimie de Clermont-Ferrand, CNRS, SIGMA Clermont, Université Clermont Auvergne, F-63000 Clermont-Ferrand, France
* Correspondence: gilles.mailhot@uca.fr

Abstract: This paper describes a study of the treatment of 2,4-dichlorophenol (2,4-DCP) with an ethylenediamine-*N*,*N*′-disuccinic-acid (EDDS)-modified photo-Fenton system in ultrapure water and different natural waters. The results showed that the EDDS-modified photo-Fenton system is adequate for 2,4-DCP degradation. Compared with a medium containing a single organic pollutant, the removal of pollutants in a more complex medium consisting of two organic compounds is slower by around 25 to 50% as a function of the organic pollutant. Moreover, 2,4-DCP can be further effectively degraded in the presence of organic materials and various inorganic ions. However, the photodegradation of 2,4-DCP in different natural waters, including natural lake water, effluent from domestic sewage treatment plants, and secondary effluent from pulp and paper mill wastewaters, is inhibited. Chemical compounds present in natural waters have different influences on the degradation of 2,4-DCP by adopting the EDDS-modified photo-Fenton system. In any case, the results obtained in this work show that the EDDS-modified photo-Fenton system can effectively degrade pollutants in a natural water body, which makes it a promising technology for treating pollutants in natural water bodies.

Keywords: photo-Fenton; EDDS; 2,4-DCP; organic matter; inorganic ions; natural water bodies

Citation: Huang, W.; Huang, Y.; Wang, S.; Lin, H.; Mailhot, G. Degradation of 2,4-Dichlorophenol by Ethylenediamine-*N*,*N*′-disuccinic Acid-Modified Photo-Fenton System: Effects of Chemical Compounds Present in Natural Waters. *Processes* **2021**, *9*, 29. https://dx.doi.org/10.3390/pr9010029

Received: 24 November 2020
Accepted: 23 December 2020
Published: 25 December 2020

1. Introduction

Advanced oxidation processes (AOPs) can effectively oxidize organic pollutants in water using active free radicals [1], which have been adopted to degrade pollutants from many types of wastewaters, such as tannery wastewaters and pharmaceutical wastewaters [2,3]. Fenton technology is one of the most simple and effective AOPs to degrade pollutants [4]. However, the Fenton reaction consumes a large number of chemical reagents and produces toxic by-products, resulting in secondary contamination [5]. In order to overcome the shortcomings of Fenton processes, different attempts have been carried out. First of all, irradiation has been introduced in the Fenton reaction, and the Fe(III)/H_2O_2 mixture (Fenton-like reagent) can absorb photons of wavelengths up to 550 nm [6,7]. The efficiency of the photo-Fenton process has been proven by many previous studies, most of which were carried out at an acidic pH value [8–10]. Additionally, the introduction of chelating agents, especially organic carboxylic acid into the Fenton reaction, proved to be an effective method for broadening the applicable pH values. Several different organic carboxylic acids, such as citric acid, oxalic acid, NTA, and EDTA, were used to modify the Fenton process and proved to be efficient [11–14]. Ethylenediamine-*N*,*N*′-disuccinic-acid (EDDS), a biodegradable isomer of EDTA, was used as a chelating agent in homogeneous

and heterogeneous Fenton and photo-Fenton systems in our previous studies [15–18]. Therefore, the EDDS-modified photo-Fenton reaction is proven to be a promising approach to treat refractory pollutants.

However, most laboratory studies on pollutant removal using the EDDS-modified photo-Fenton system are currently conducted using deionized water, which is far from the complex chemical composition of natural water, in which the inorganic ions and dissolved organic compounds in water can significantly influence pollutant removal. In previous research, it was found that the water matrix could significantly influence the efficiency and mechanism of AOPs processes, especially the Fenton process. The presence of common inorganic ions had no substantial effect on herbicide removal when using the photo-Fenton system, but the H_2O_2 (oxidant) consumption of this reaction was higher than that of the same reaction where inorganic ions were absent [19]. In the process of the photodegradation of 2,4-D by the photo-Fenton reaction, carbonate has little adverse effects, fluoride has a positive effect, and phosphate has an inhibitory effect [20]. The effect of typical inorganic water constituents (carbonates and chloride ions) and organic matter was also investigated and found to be different in the UVA-UVB activation of hydrogen peroxide and persulfate for advanced oxidation processes [21]. Therefore, it is necessary to study the influence of the natural water matrix on pollutant degradation efficiency in the EDDS-modified photo-Fenton system, including not only single inorganic ions or organic compounds but also natural water where various chemical compounds are present.

Chlorophenols (CPs) in wastewater represent a type of pollutant that greatly harms human health and the environment because they are toxic, teratogenic, and carcinogenic [22,23]. Nowadays, CPs are widespread in the environment, even in the most remote natural environments, as well as in aquatic and terrestrial food chains [24]. Among them, 2,4-DCP is present in most wastewaters generated by the textile and the pulp and papermaking industries and has attracted considerable attention because it is highly toxic and difficult to degrade. Furthermore, it is a kind of absorbable organic halide (AOX), which is the main pollution product in the pulping and papermaking industry [25]. It is poisonous, carcinogenic, and teratogenic. Direct discharge into water bodies can cause serious damage to the water environment. As a result, 2,4-DCP is usually degraded by AOPs and used as a target pollutant for developing new AOP methods.

In our previous study, we confirmed that the EDDS-modified photo-Fenton system can effectively degrade 2,4-DCP in deionized water in the laboratory. The effect of pH, H_2O_2 concentration, and Fe(III)-EDDS dosage was investigated, and the optimal condition was determined [26]. On the other hand, it was found that 2,4-DCP could be effectively degraded in the EDDS-modified photo-Fenton system at pH 3–7. Furthermore, •OH radicals were found to be the main active species of degradation. In this study, our purpose is to reveal the effect of chemical compounds (organic and inorganic compounds) on 2,4-DCP degradation using the EDDS-modified photo-Fenton system and the effect of the complex water matrix on the system. First, the effects of organic matter such as humic acids (HAs) (representing common organic matter in natural water) and 2,4,6-trichlorophenol (2,4,6-TCP) (representing the same kind of organic compounds always accompanying wastewater) on the degradation of 2,4-DCP are discussed. Second, the effects of inorganic ions on 2,4-DCP degradation are evaluated. Finally, three types of natural waters, including natural lake water (NLW), effluent from domestic sewage treatment plants (DSTP), and secondary effluent from pulp and paper mill wastewater (PPMW), are selected as the natural water matrix for 2,4-DCP degradation in the EDDS-modified photo-Fenton reaction. A metal halide lamp is used to mimic sunlight during these laboratory experiments. The expected selectivity of the EDDS-modified photo-Fenton reaction for 2,4-DCP in natural water is demonstrated by comparing the decrease in 2,4-DCP content in pure water with that in different natural waters. The results of these experiments on the efficiency of the EDDS-modified photo-Fenton system in removing pollutants from natural waters have important practical implications for advancing water treatment technologies.

2. Materials and Methods

2.1. Chemicals

EDDS (35% in water) was purchased from Shanghai Anpu Experimental Technology Co., Ltd. (Shanghai, China). 2,4-DCP and 2,4,6-TCP were purchased from Shanghai Macklin Biochemical (Shanghai, China). Ferric chloride hexahydrate, sodium chloride, sodium sulfate, sodium carbonate, sodium nitrate, sodium phosphate dodecahydrate, potassium chloride, magnesium chloride, calcium chloride, and H_2O_2 (30% in water) were purchased from Guangdong Guanghua Sci-Tech Co., Ltd. (Guangzhou, China). Humic acids (HAs) were purchased from Alfa (Shanghai, China). Methyl alcohol (HPLC grade) and acetonitrile (HPLC grade) were purchased from MERCK (Shanghai, China). The pH of the solutions was adjusted with sodium hydroxide (NaOH) and hydrochloric acid (HCl). The ferric carboxylic acid complex solution was prepared by mixing iron and EDDS aqueous solutions in a ratio of 1:1 (and left to stand for more than 1 h to ensure excellent chelation efficiency).

2.2. Analytical Procedures

Total organic carbon (TOC) was measured using an Analytikjena TOC-VCSN analyzer (Jena, Gremany). An ICS-5000 ion chromatography (IC) unit (Dionex Corporation, Sunnyvale, CA, USA) was used to monitor the release of chloride ions; this unit was equipped with a conductivity detector, an anion self-regenerating suppressor (ASRS^{TM} 300 × 4 mm, Dionex Corporation, Sunnyvale, CA, USA), and the AutoSuppression^{TM} Recycle Mode. Ultrapure water and 250 mM NaOH were supplied as the eluent to IC at a flow rate of 1 mL min^{-1}. Degradation of 2,4-DCP, 2,4,6-TCP, and a mixture of 2,4-DCP and 2,4,6-TCP was determined using ultra-high-pressure liquid chromatography (Waters ACQUITY UPLC® H-Class, C-18 column, UV detector) (Waters, Milford, MA, USA). The UPLC operating conditions for the target compounds are listed in Table 1.

Table 1. UPLC methods for target compounds.

Compound	Mobile Phase	Flow Rate (mL min^{-1})	Column Temperature (°C)	Injection Volume (μL)	Detection Wavelength (nm)
2,4-DCP	Water/methanol (40:60. v/v)	0.35	35	5	280
2,4,6-TCP	Water/methanol (20:80. v/v)	0.35	35	5	210
Mixture of 2,4-DCP and 2,4,6-TCP	Water/methanol (20:80. v/v)	0.35	35	5	Dual channel: 210 and 280

2.3. Experimental System

All experiments were performed in a cylindrical Plexiglas container, which was covered with aluminum foil to protect against light and avoid side photochemical processes, placed on a homemade photoreactor (Figure 1). The photoreactor was designed with a cylindrical container, and the lamp with a glass-jacket was fixed through the central axes of the cell. For the experiment, the target pollutant solution and the Fe(III)-EDDS complex solution (0.1 mM) were added to a 1 L beaker. An adequate volume of the mixture was sampled and transferred into a 1 L volumetric flask, to which hydrogen peroxide solution (1.0 mM) was added. The 1 L flask containing the reaction solution was placed under agitation in a reactor equipped with a metal halide lamp (continuous spectrum of 290–800 nm), and samples were taken from the reactor at different time intervals. In order to simulate the natural pH, the initial pH value of all the single-effect experiments was set close to 7.0. Since the reaction may have continued after sampling, methanol was added to stop the reaction.

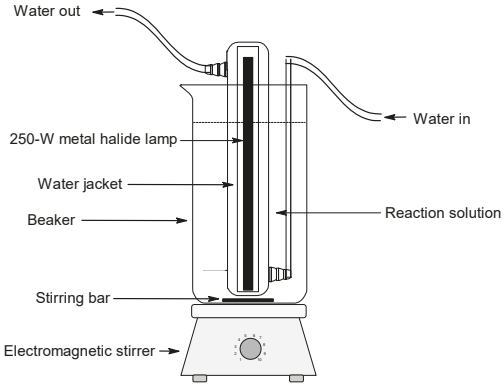

Figure 1. The scheme of the photoreactor used in this study.

3. Results

3.1. Effects of Organic Matter

3.1.1. Effect of Organic Compounds

Changes in pollutant concentration could significantly influence the degradation efficiency in the photo-Fenton system. Therefore, the influence of different initial concentrations of 2,4-DCP on the photochemical experiment was studied while keeping the other reaction parameters unchanged. The pollutant was almost completely degraded at concentrations of 5 to 20 mg L^{-1}. For 2,4-DCP concentrations equal to or exceeding 20 mg L^{-1}, the degradation rate and efficiency decreased as the 2,4-DCP concentration increased (Figure 2). This phenomenon can be interpreted because the number of hydroxyl radicals did not increase proportionally as the pollutant concentration increased [27]. 2,4-DCP exhibited a significant degradation efficiency of around 53% even at the maximum pollutant concentration of 100 mg L^{-1} considered in this study. The experimental results show that the EDDS-modified photo-Fenton process had an obvious degradation effect on 2,4-DCP, even at high initial concentrations.

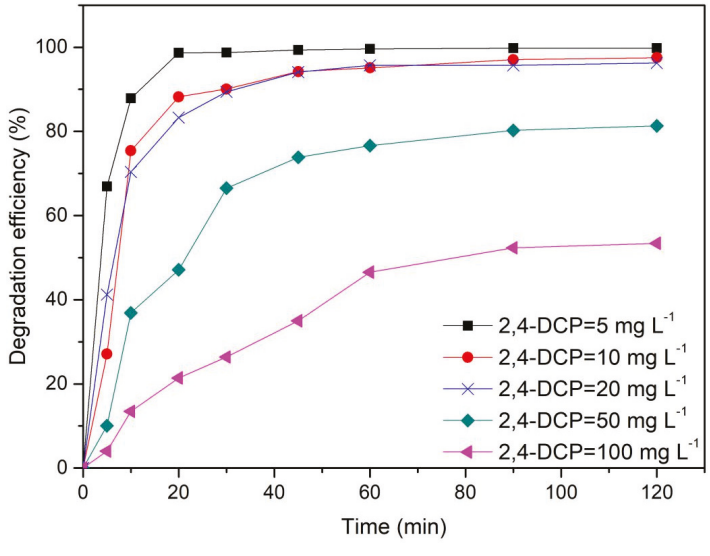

Figure 2. 2,4-DCP degradation efficiency for different 2,4-DCP initial concentrations. [Fe(III)-EDDS] = 0.1 mM, [H_2O_2] = 1.0 mM, and pH = 7.0 ± 0.1.

The toxicity of CPs can be ascribed to the number of Cl atoms on the benzene ring: the more Cl atoms in the chemical formula of CPs, the more toxic organic compounds there are [28]. Moreover, the quantity of Cl atoms on the benzene ring may affect the rate of degradation. Accordingly, we experimentally investigated the degradation of single 2,4,6-TCP and 2,4-DCP, as well as that of a mixture of these two pollutants.

In our photo-Fenton system and the single-substance experiments, the rate of 2,4-DCP pollutant removal was superior by around 65% to those of 2,4,6-TCP (Figure 3).

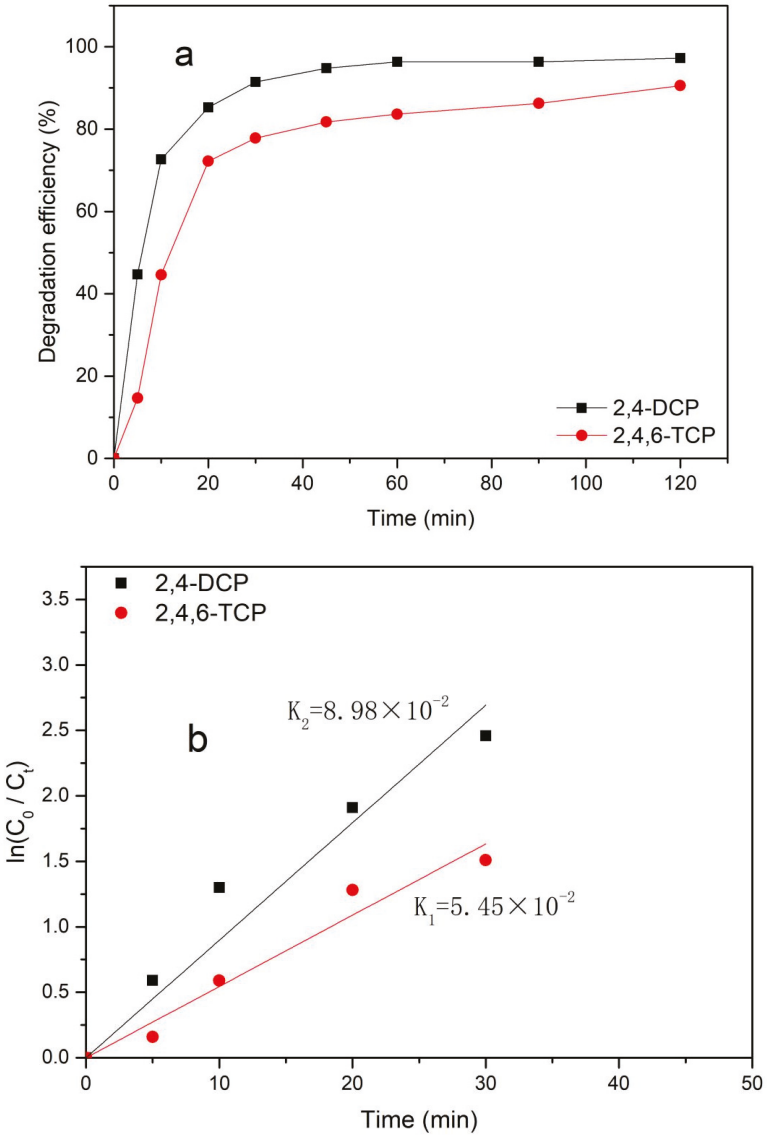

Figure 3. (**a**) EDDS-modified photo-Fenton degradation of 2,4-DCP and 2,4,6-TCP. (**b**) Variation of ln C/C_0 with time in 2,4-DCP and 2,4,6-TCP concentration using the EDDS-modified photo-Fenton system. [2,4-DCP] = [2,4,6-TCP] = 20 mg L^{-1}, [Fe(III)-EDDS] = 0.1 mM, [H_2O_2] = 1.0 mM, pH = 7.0 ± 0.1.

This difference in 2,4-DCP and 2,4,6-TCP degradation rates could be attributed to the number of chlorine atoms on these CPs, possibly because the OH and Cl groups of 2,4-DCP are aligned along the ortho and para directions, and the •OH radicals have the same preference for attack. By contrast, steric hindrance prevents the hydroxylation of 2,4,6-TCP [29]. It was reported that in the heterogeneous photo-Fenton system, the 4-CP removal rate was superior to that of 2,4,6-TCP, indicating that the quantity of Cl atoms significantly influenced the phenolic compounds' degradation rate [30]. However, our results showed the same effect but also that the EDDS-modified photo-Fenton process can be used to effectively treat 2,4-DCP and 2,4,6-TCP pollutants in deionized water.

Given that wastewaters contain multiple organic matters, we performed other experiments with a mixture of two soluble pollutant compounds (2,4-DCP and 2,4,6-TCP). The individual concentrations of 2,4-DCP and 2,4,6-TCP were set to 10 mg L^{-1} (total pollutant concentration is 20 mg L^{-1}) while keeping the other experimental conditions unchanged from those employed in the single-substance experiments.

The removal rate of residual pollutants after 20 min of irradiation was considerably slower than that before 20 min of irradiation (Figures 3 and 4). This was primarily ascribed to the low concentration of residual pollutants (around 20% in the single-pollutant experiment and 40% in the mixture of the two pollutants of the initial concentration) after the first 20 min of reaction, resulting in a higher competition reaction of •OH radicals with Fe^{2+} and H_2O_2 able to scavenge •OH radicals as well [31–33].

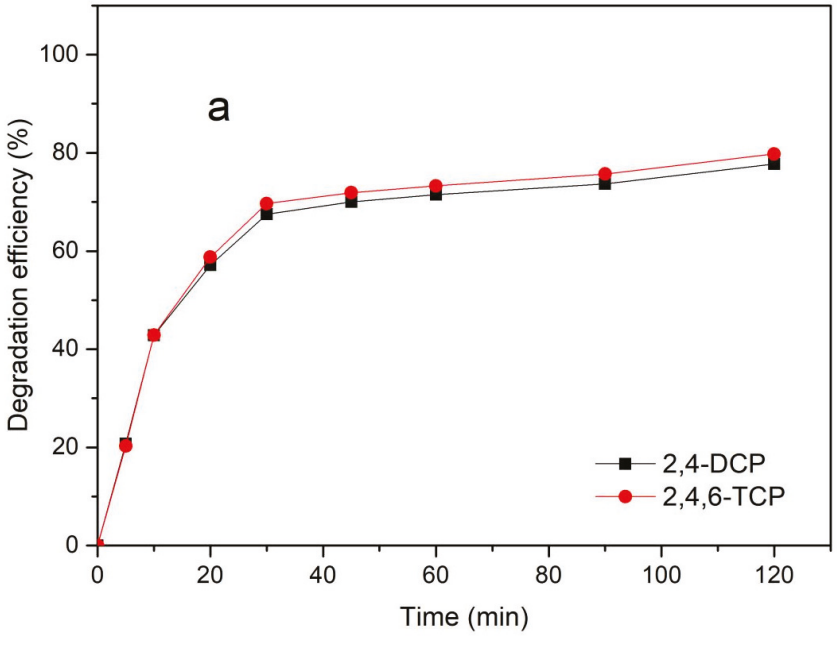

Figure 4. *Cont.*

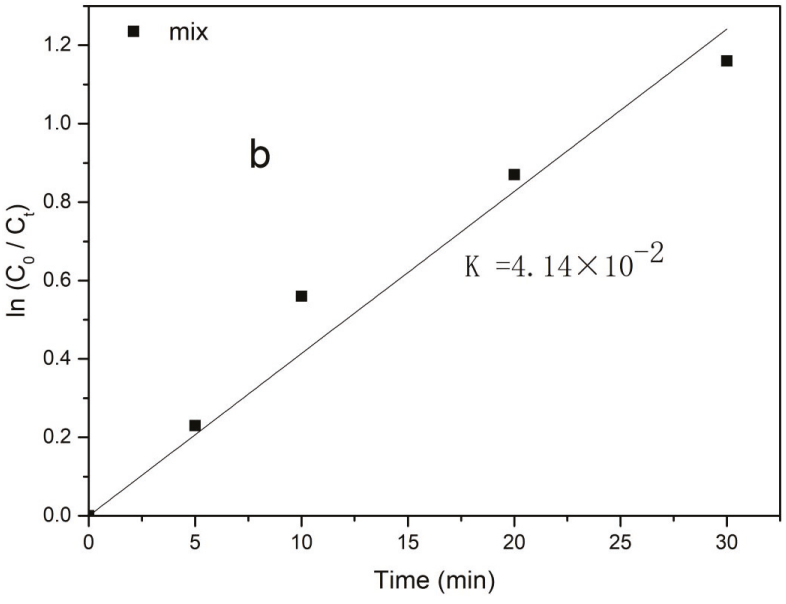

Figure 4. EDDS-modified photo-Fenton degradation of a mixture of 2,4-DCP and 2,4,6-TCP in the two-pollutants experiment ((**a**) 2,4-DCP and 2,4,6-TCP degradation efficiency; (**b**) apparent rate constant of degradation of mixed pollutants). [2,4-DCP] = 10 mg L^{-1}, [2,4,6-TCP] = 10 mg L^{-1}, [Fe(III)-EDDS] = 0.1 mM, [H_2O_2] = 1.0 mM, and pH = 7.0 ± 0.1.

In the two-pollutants experiment, approximately 80% of the two are degraded after 120 min. Compared with the single-pollutant experiment, the removal rate of the two pollutants was lower by around 54% for 2,4-DCP and 24% for 2,4,6-TCP. This result implies that the degradation of pollutants in complex media is slower. Therefore, our results demonstrate that the EDDS-modified photo-Fenton system is very effective for treating a single organic pollutant or a mixture of two organic pollutants.

The apparent rate constant of degradation of mixed pollutants is lower than that of a single pollutant (Figures 3b and 4b), which indicates that 2,4-DCP degradation will be significantly affected in more complex natural media (a detailed analysis of 2,4-DCP degradation in complex natural media is provided in Section 3.3). Compared with a medium containing a single pollutant, a medium containing two organic pollutants will decrease the removal rate and weaken the removal effect. Nevertheless, in this experiment, the main goal (of pollutant removal) was achieved within a reasonable timespan.

3.1.2. Effect of Humic Acids (HAs)

HAs are ubiquitous in aquatic environments [34]. To a large extent, the degradation of organic pollutants is affected by their interaction with dissolved organic matter (DOM, such as HA) in aquatic environments [35]. When DOM absorbs ultraviolet or solar radiation, it forms reactive oxygen intermediates and can also have a shielding effect and inhibits the AOPs [36,37]. DOM can enhance or inhibit the photodegradation rate [38,39]. DOM in water, such as HA, can trap •OH radicals and also produce •OH radicals under irradiation [40]. HA is a potential electron donor and can reduce Fe^{3+} in the system. For example, HA can significantly improve the degradation effect of pentachlorophenol by promoting the redox cycles of Fe(III) and Fe(II) in the photo-Fenton system [41,42]. Therefore, it is necessary to study the influence of HA on pollutant degradation in natural water. In our study, when HA was present in the solutions, the degradation rate of the EDDS-modified photo-Fenton system decreased marginally (around 10% less after 120 min of irradiation).

Moreover, when the HA concentration was increased from 2 to 5 mg L^{-1}, the 2,4-DCP degradation rate was almost unchanged (Figure 5).

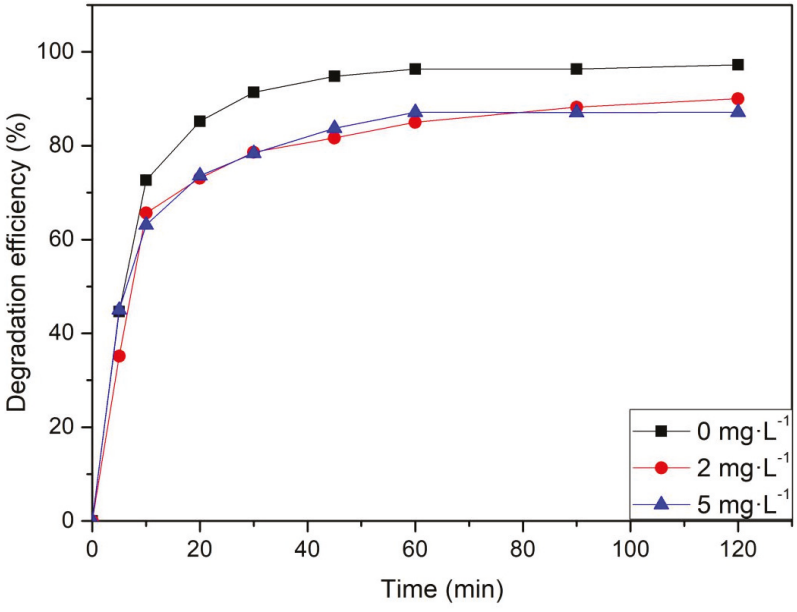

Figure 5. Effect of humic acid (HA) on 2,4-DCP degradation. [2,4-DCP] = 20 mg L^{-1}, [Fe(III)-EDDS] = 0.1 mM, [H_2O_2] = 1.0 mM, and pH = 7.0 ± 0.1.

The lower degradation rate could be ascribed to the fact that HA scavenged •OH radicals. Moreover, HA and the Fe(III)-EDDS complex compete for light absorption because HA is known to absorb sunlight, which reduces the photoredox process of the iron complex [35,43]. The photochemical properties of HA can be ascribed to complex phenomena and are influenced by multiple factors, including its origin and structural characteristics [35,44].

3.2. Effects of Inorganic Ions

The results above indicate that the EDDS-modified photo-Fenton process is a promising and novel technology that can completely degrade 2,4-DCP. However, industrial wastewaters contain various inorganic ions. These inorganic anions and cations can play complex roles in the EDDS-modified photo-Fenton process.

Cl^- and SO_4^{2-} ions could reduce the reaction efficiency by scavenging hydroxyl radicals and competing with the ligand for the complexation of iron ions [45]. The reaction of •OH radicals with SO_4^{2-} ions occurs only at very high concentrations of SO_4^{2-} ions [46]. Indeed, compared with the control experiment, the addition of SO_4^{2-} (at concentrations of 100 to 200 mM) can marginally improve the 2,4-DCP photodegradation rate of the EDDS-modified photo-Fenton system (Figure 6a).

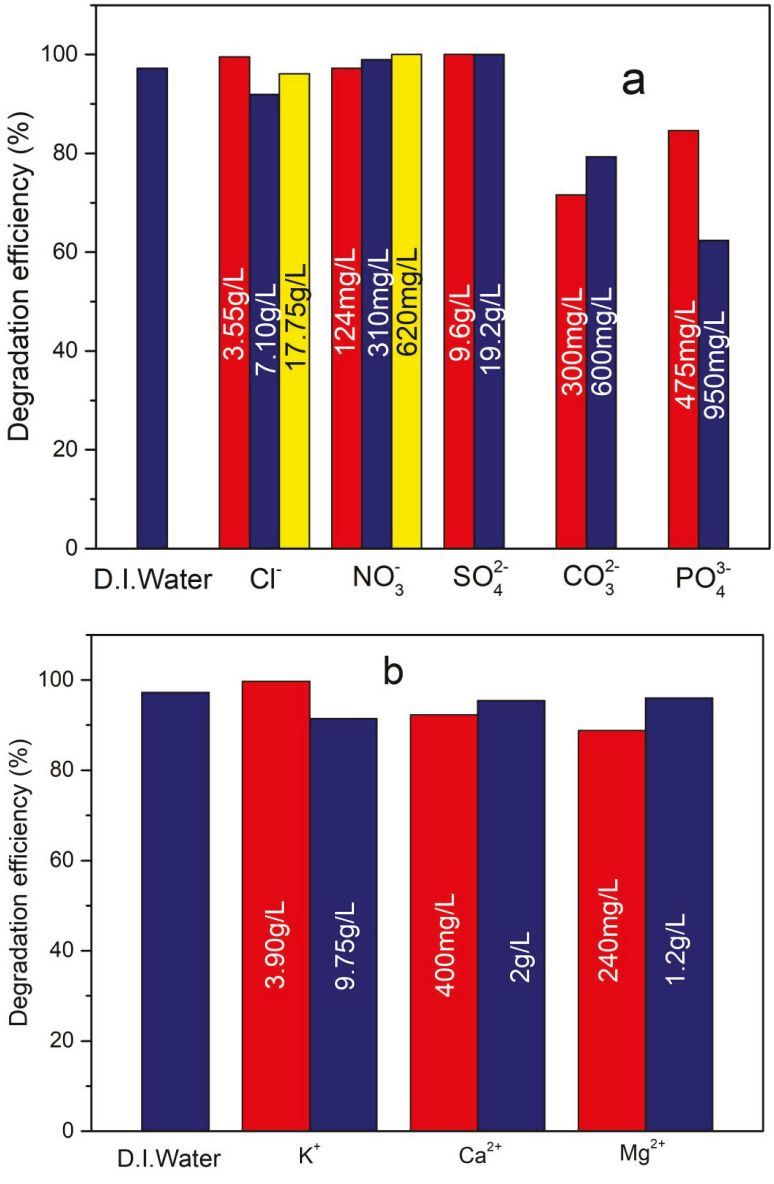

Figure 6. Effects of anions and cations on 2,4-DCP degradation. (**a**) Anions; (**b**) cations. [2,4-DCP] = 20 mg L^{-1}, [Fe(III)-EDDS] = 0.1 mM, [H_2O_2] = 1.0 mM, and pH = 7.0 ± 0.1.

From our results (Figure 6a), we show that the 2,4-DCP degradation efficiency decreased slightly at the chloride concentration up to 7.10 g/L, and the process continued to exhibit a significant degradation efficiency. The addition of chlorine ions to an aqueous solution of iron ions will result in the formation of the $Fe(Cl)^{2+}$ complex, which has a weaker (photo)reactivity than the Fe(III)-EDDS complex (R1) [47]. The effect of the concentration of chlorine ions is complicated in Fenton chemistry. When the Cl^- concentration is equal to 17.75 g/L, the 2,4-DCP degradation efficiency is higher than when a 7.10 g/L Cl^- concentration is added and lower than that in the deionized aqueous solution. This

may be because of the increased concentration of chloride ions and the formation of $Cl^{\bullet}$ radicals by the $Fe(Cl)^{2+}$ complex under irradiation (R2), which contribute toward 2,4-DCP degradation. The activity of $Cl^{\bullet}$ radicals is weaker than that of •OH radicals [48,49]. The inhibitory effect of chloride should also be attributed to the reactivity of •OH radical with Cl^- leading to the formation of $Cl^{\bullet}$ radical or $ClOH^{\bullet -}$ and after $Cl^{\bullet}$ radical reacts with Cl^- to form the radical $Cl_2^{\bullet -}$ [50,51]. These reactions are significant in the presence of •OH radicals and Cl^-.

$$Fe^{3+} + Cl^- \rightarrow Fe(Cl)^{2+} \quad (1)$$

$$Fe(Cl)^{2+} + hv \rightarrow Fe^{2+} + Cl^{\bullet} \quad (2)$$

We found that NO_3^- ions had a small effect on the system. When the NO_3^- ion concentration was increased, the degradation rate slightly increased (Figure 6a). NO_3^- ions can produce other •OH radicals (R3 and R4) under irradiation. However, NO_3^- ions have a strong ultraviolet (UV)-shielding effect, which is more significant than the formation of •OH radicals through NO_3^- photolysis [52]. The fact that the presence of NO_3^- ions did not significantly influence the degradation of 2,4-DCP can possibly be ascribed to the interaction of all the above mentioned factors.

$$NO_3^- + hv \rightarrow NO_2^- + O(3P) \quad (3)$$

$$NO_3^- + H^+ + hv \rightarrow NO_2^{\bullet} + HO^{\bullet} \quad (4)$$

On the contrary, the degradation of 2,4-DCP was severely affected by the presence of carbonates (Figure 6a). When the carbonate concentration was 300 mg/L, the 2,4-DCP degradation efficiency decreased by approximately 25%. It has been reported that carbonates play an essential role in AOPs by acting as scavengers of hydroxyl radicals through the reaction R5, increasing oxidant consumption [53]. Papautsakis et al. [54] reported that carbonate can scavenge •OH radicals and inhibit the degradation of imidacloprid in the Fe-EDDS photo-Fenton process. Moreover, carbonate has also been shown to have a destructive effect on the stability of soluble iron [53].

$$CO_3^{2-} + HO^{\bullet} \rightarrow CO_3^{\bullet -} + OH^- \quad (k = 3.9 \times 10^8 M^{-1} s^{-1}) \quad (5)$$

As the phosphate concentration increased, the 2,4-DCP degradation rate decreased, indicating that the PO_4^{3-} ion forms a complex with Fe^{3+} and reduces the efficiency of the EDDS-modified photo-Fenton system. It is reported in the literature that Fe^{3+} precipitation by PO_4^{3-} limited the Fenton and photo-Fenton reactions in aqueous solutions with high phosphate concentrations [55].

It is known that pH significantly influences the Fenton process. In the presence of carbonates and phosphates, the solution pH has a buffering capacity, owing to the hydrolysis of PO_4^{3-} and CO_3^{2-} ions. Under this condition, the solution pH is neutral at the end of the experiment, while in deionized water, the corresponding solution pH is approximately 4.8. This may be also an important reason for the effect of carbonate and phosphate ions on the removal of pollutants.

When K^+, Ca^{2+}, and Mg^{2+} ions were present in the solution, the degradation efficiency of the system decreased slightly (Figure 6b). Metal cations affect the degradation of the system by competing with Fe(III) ions for ligands. It has been shown that the higher the number of charges of metal ions, the greater their complexation ability [56]. The complexation ability of Fe^{3+} ions is the strongest, followed by Ca^{2+} and Mg^{2+} ions, and K^+ ions are the weakest. Therefore, even in the case of very high K^+ concentration, the effect on the system is very small.

The above results made clear that the EDDS-modified photo-Fenton process can efficiently degrade organic pollutants in the presence of inorganic ions. Even at high concentrations of inorganic ions, the EDDS-modified photo-Fenton system exhibited significant degradation efficiency. Furthermore, inorganic ions affect degradation mainly by

competing with trivalent iron for ligands and scavenging hydroxyl radicals. Therefore, an investigation of 2,4-DCP degradation using the EDDS-modified photo-Fenton system in the presence of the main constituents of water will help to improve our understanding of their effects on pollutant degradation in real aquatic systems.

3.3. Effect of Natural Water Bodies

TOC and ionic chromatography analyses of the three natural water bodies show significantly different matrix contents. In terms of ions, the amounts of Cl^-, $NO_3{}^-$, and $SO_4{}^{2-}$ detected in the DSTP, PPMW, and NLW water samples varied significantly. $NO_3{}^-$ was not detected in NLW (Table 2). The chromaticity of the three water bodies varied considerably, which is of great importance for the photo-Fenton system. In conclusion, the chemical compositions of the three water samples differed considerably, and the influences of ion concentration and chromaticity were non-negligible.

Table 2. Physicochemical parameters and chemical compositions of natural water bodies.

Water Bodies	Color	pH	TOC (mg L^{-1})	TC (mg L^{-1})	IC (mg L^{-1})	Anion	Concentration (mg L^{-1})
PPMW	Dark yellow	7.84	49.8	88.0	38.2	Cl^-	188.1
						$SO_4{}^{2-}$	67.7
						$NO_3{}^-$	20.1
DSTP	Light yellow	7.05	6.6	17.0	10.4	Cl^-	37.2
						$SO_4{}^{2-}$	21.9
						$NO_3{}^-$	16.4
NLW	Yellow	8.47	6.4	9.4	3.0	Cl^-	7.6
						$SO_4{}^{2-}$	21.8
						$NO_3{}^-$	Not detected

Pollutant degradation in natural water is a more complex process than degradation in the presence of single inorganic ions and organic matter. The EDDS-modified photo-Fenton system was used to evaluate the photocatalytic removal of 2,4-DCP dissolved in natural waters, including NLW, DSTP, and PPMW. The 2,4-DCP degradation rate in deionized water was considerably faster than that in natural waters. The degradation efficiencies after 120 min of irradiation were 52.5%, 64.4%, and 38.5% in DSTP, NLW, and PPWM, respectively (Figure 7) and around 100% in deionized water after 60 min of irradiation.

The lower 2,4-DCP degradation rate in NLW, DSTP, or PPMW than that in deionized water could be ascribed to the presence of inorganic ions and dissolved organic compounds. As given in Table 2, we determined some of the chemical constituents. The concentrations of chloride, sulfate, and nitrate ions in the studied natural waters were different. Among the three aforementioned water systems, 2,4-DCP degradation was most severely inhibited in PPMW, which may be ascribed to the relatively higher concentrations of inorganic ions in this compartment than those in the other two other water systems. Secondly, PPMW is dark yellow in color, which means it can cause a screen effect and thus decrease the Fe(III)-EDDS photoredox process. Thirdly, the presence of higher TC concentration can affect the degradation efficiency of 2,4-DCP. A more comprehensive understanding of the influence of TOC and total inorganic ion concentration in water on pollutant removal is therefore needed.

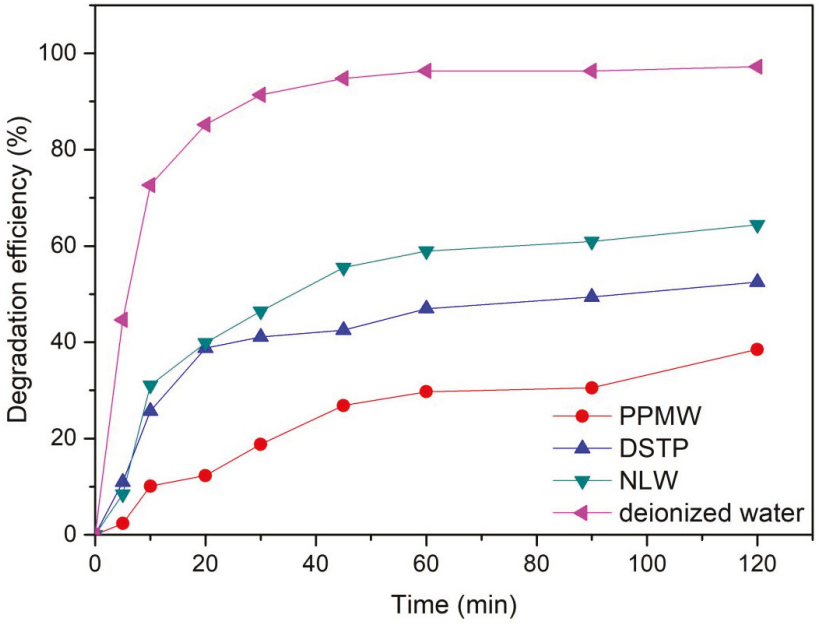

Figure 7. Degradation of 2,4-DCP in natural water bodies. [2,4-DCP] = 20 mg L^{-1}, [Fe(III)-EDDS] = 0.1 mM, [H_2O_2] = 1.0 mM, and pH = 7.0 ± 0.1.

The TOC concentration of NLW, DSTP, and PPMW increased successively, contrary to the decreased 2,4-DCP degradation efficiencies (Figure 8a). The high concentration of TOC in the natural water body was in competition with the target pollutant for the reactivity of •OH radicals, which is an essential reason for the resulting low degradation efficiency. Moreover, compared with that in deionized water, the decreased 2,4-DCP photodegradation efficiency in natural water may be ascribed to the optical filter effect of organic matter in natural water. Indeed, organic matter can be one of the critical absorbers of sunlight in aquatic environments [35]. We speculate that TOC concentration is not the only factor affecting 2,4-DCP degradation in the studied water bodies. The effect of total inorganic ion concentration in water on 2,4-DCP removal was explored. Overall, the 2,4-DCP degradation efficiency decreased as the total inorganic ion concentration increased (Figure 8b). The same effect was observed in the study by Sakkas et al. [25]. As the salinity of water increased, chlorothalonil combined with DOM through hydrophobic interaction or weak van der Waals forces, thus affecting the photodegradation of the pollutants. Obviously, the factors affecting the 2,4-DCP removal in natural water included inorganic ion concentration, TOC concentration, and chromaticity.

The UV–visible absorption spectrum of different water matrices containing 2,4-DCP is shown in Figure 9, and it was noted that most change in UV–visible absorption occurred in the UV zone (lower than 290 nm), which was out of the wavelength range of the lamp used in this study. As a result, it was preliminarily indicated that the influence had nothing to do with UV–visible absorption.

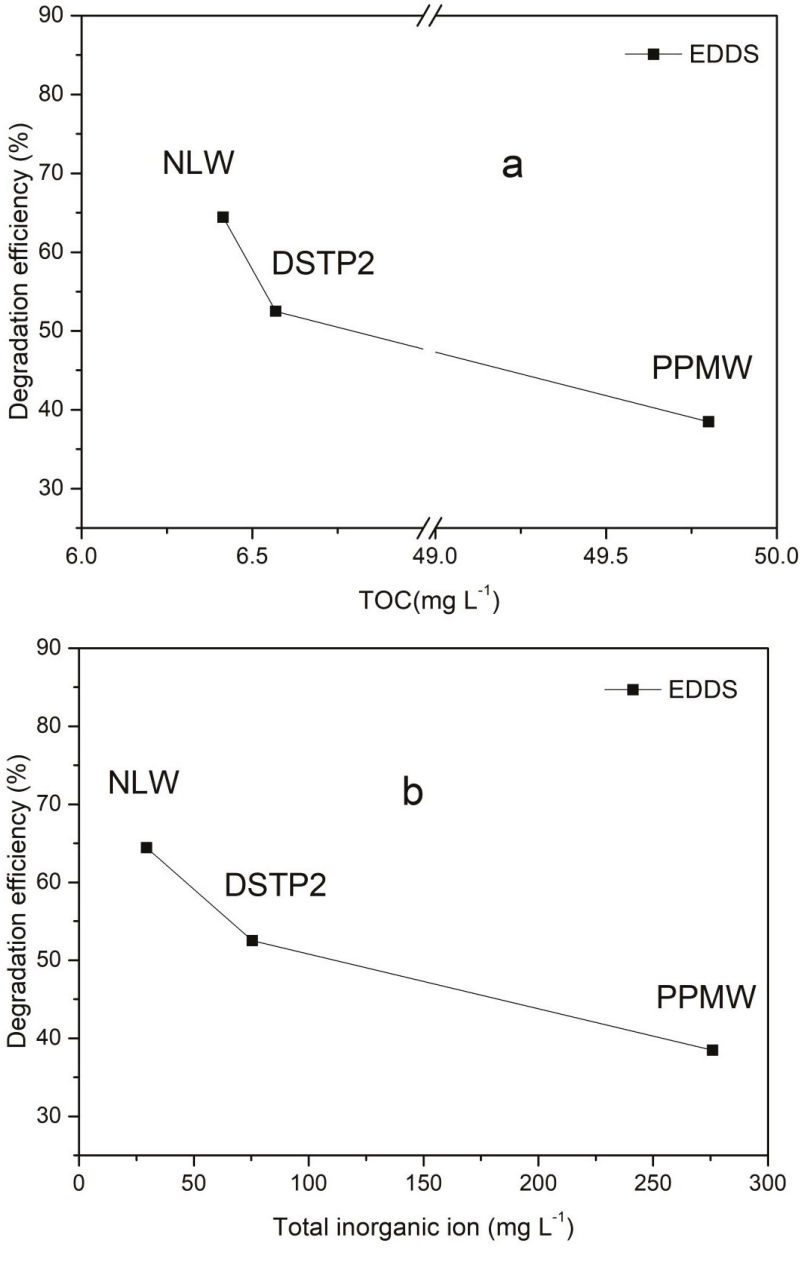

Figure 8. Effects of (**a**) TOC and (**b**) total inorganic ion concentration on 2,4-DCP degradation efficiency in different water bodies. [2,4-DCP] = 20 mg L^{-1}, [Fe(III)-EDDS] = 0.1 mM, [H_2O_2] = 1.0 mM, and pH = 7.0 ± 0.1.

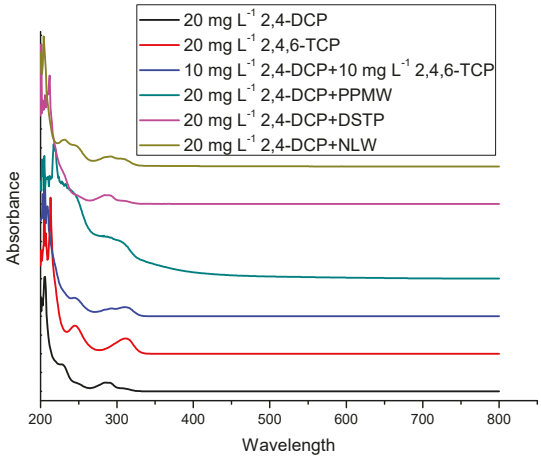

Figure 9. UV-visible absorption spectrum of different water bodies.

The degradation of 2,4-DCP was affected differently by different natural water compositions. However, the more the water is loaded with organic/inorganic compounds, the more significant the inhibition of 2,4-DCP degradation. Regardless, the EDDS-modified photo-Fenton system still removed more than 50% of 2,4-DCP in NLW and DSTP and more than 30% in PPMW. This finding indicates that the EDDS-modified photo-Fenton process can be used to effectively treat pollutants in natural waters and potentially simulate solar photocatalytic water treatment. Thus, 2,4-DCP degradation in natural water bodies justifies a more in-depth study to understand and evaluate the parameters that are essential for the efficiency of the process.

4. Conclusions

The results indicate that the EDDS-modified photo-Fenton system is suitable for 2,4-DCP removal. It is a promising route for treating 2,4-DCP by simulating natural sunlight, which is a low-cost alternative light source and significantly reduces the process cost. The system could effectively degrade single 2,4-DCP and 2,4,6-TCP pollutants and the mixture of 2,4-DCP and 2,4,6-TCP. Furthermore, it could effectively degrade pollutants in the presence of common inorganic ions. The effect of anions on 2,4-DCP degradation was found to be stronger than that of cations. Finally, the degradations of 2,4-DCP in different water bodies, including NLW, DSTP, and PPMW, were remarkably different. The 2,4-DCP degradation rate in PPMW was severely inhibited, which may be related to the high absorption of light, high TOC concentration, and high inorganic ion content in this water compartment. The use of several different natural waters to treat 2,4-DCP with the EDDS-modified photo-Fenton process shows the efficiency of this process for industrial applications. Nevertheless, the application will be particularly more efficient when this process is used in a ternary treatment when the water is not too loaded.

Author Contributions: Conceptualization, W.H. and G.M.; methodology, W.H. and Y.H.; software, Y.H.; validation, W.H. and S.W.; formal analysis, W.H. and G.M.; investigation, W.H. and Y.H.; resources, G.M.; data curation, G.M.; writing—original draft preparation, W.H.; writing—review and editing, G.M.; visualization, H.L.; supervision, G.M.; project administration, W.H. All authors have read and agreed to the published version of the manuscript.

Funding: This research received no external funding.

Institutional Review Board Statement: Not applicable.

Informed Consent Statement: Not applicable.

Acknowledgments: This work was partially supported by the National Natural Science Foundation of China (No. 21367003), Guangxi Science and Technology Research Program (No. AA17202032) and Open Fond of Guangxi Key Laboratory of Clean Pulp & Papermaking and Pollution Control (KF201724).

Conflicts of Interest: The authors declare no conflict of interest.

References

1. Glaze, W.H.; Lay, Y.; Kang, J.-W. Advanced Oxidation Processes. A Kinetic Model for the Oxidation of 1,2-Dibromo-3-chloropropane in Water by the Combination of Hydrogen Peroxide and UV Radiation. *Ind. Eng. Chem. Res.* **1995**, *34*, 2314–2323. [CrossRef]
2. Sivagami, K.; Sakthivel, K.P.; Nambi, I.M. Advanced oxidation processes for the treatment of tannery wastewater. *J. Environ. Chem. Eng.* **2018**, *6*, 3656–3663. [CrossRef]
3. Kanakaraju, D.; Glass, B.D.; Oelgemoller, M. Advanced oxidation process-mediated removal of pharmaceuticals from water: A review. *J. Environ. Manag.* **2018**, *219*, 189–207. [CrossRef] [PubMed]
4. Pignatello, J.J.; Oliveros, E.; MacKay, A. Advanced Oxidation Processes for Organic Contaminant Destruction Based on the Fenton Reaction and Related Chemistry. *Crit. Rev. Environ. Sci. Technol.* **2006**, *36*, 1–84. [CrossRef]
5. Fatta-Kassinos, D.; Vasquez, M.I.; Kümmerer, K. Transformation products of pharmaceuticals in surface waters and wastewater formed during photolysis and advanced oxidation processes—Degradation, elucidation of byproducts and assessment of their biological potency. *Chemosphere* **2011**, *85*, 693–709. [CrossRef]
6. Pignatello, J.J.; Liu, D.; Huston, P. Evidence for an Additional Oxidant in the Photoassisted Fenton Reaction. *Environ. Sci. Technol.* **1999**, *33*, 1832–1839. [CrossRef]
7. Pérez, M.; Torrades, F.; García-Hortal, J.A.; Domènech, X.; Peral, J. Removal of organic contaminants in paper pulp treatment effluents under Fenton and photo-Fenton conditions. *Appl. Catal. B Environ.* **2002**, *36*, 63–74. [CrossRef]
8. Cruz, A.; Couto, L.; Esplugas, S.; Sans, C. Study of the contribution of homogeneous catalysis on heterogeneous Fe(III)/alginate mediated photo-Fenton process. *Chem. Eng. J.* **2017**, *318*, 272–280. [CrossRef]
9. Du, D.; Shi, W.; Wang, L.; Zhang, J. Yolk-shell structured Fe_3O_4@void@TiO_2 as a photo-Fenton-like catalyst for the extremely efficient elimination of tetracycline. *Appl. Catal. B Environ.* **2017**, *200*, 484–492. [CrossRef]
10. Mico, M.M.; Zapata, A.; Maldonado, M.I.; Bacardit, J.; Malfeito, J.; Sans, C. Fosetyl-Al photo-Fenton degradation and its endogenous catalyst inhibition. *J. Hazard. Mater.* **2014**, *265*, 177–184. [CrossRef]
11. Borba, F.H.; Leichtweis, J.; Bueno, F.; Pellenz, L.; Inticher, J.J.; Seibert, D. Pollutant removal and acute toxicity assessment (Artemia salina) of landfill leachate treated by photo-Fenton process mediated by oxalic acid. *J. Water Process Eng.* **2019**, *28*, 159–168. [CrossRef]
12. Cuervo Lumbaque, E.; Salmoria Araújo, D.; Moreira Klein, T.; Lopes Tiburtius, E.R.; Argüello, J.; Sirtori, C. Solar photo-Fenton-like process at neutral pH: Fe(III)-EDDS complex formation and optimization of experimental conditions for degradation of pharmaceuticals. *Catal. Today* **2019**, *328*, 259–266. [CrossRef]
13. Liu, H.; Tong, M.; Zhu, K.; Liu, H.; Chen, R. Preparation and photo-fenton degradation activity of α-Fe2O3 nanorings obtained by adding H2PO4−, SO42−, and citric acid. *Chem. Eng. J.* **2020**, *382*, 123010. [CrossRef]
14. Mejri, A.; Soriano-Molina, P.; Miralles-Cuevas, S.; Sanchez Perez, J.A. Fe(3+)-NTA as iron source for solar photo-Fenton at neutral pH in raceway pond reactors. *Sci. Total. Environ.* **2020**, *736*, 139617. [CrossRef] [PubMed]
15. Huang, W.; Luo, M.; Wei, C.; Wang, Y.; Hanna, K.; Mailhot, G. Enhanced heterogeneous photo-Fenton process modified by magnetite and EDDS: BPA degradation. *Environ. Sci. Pollut. Res.* **2017**, *24*, 10421–10429. [CrossRef]
16. Huang, W.; Brigante, M.; Wu, F.; Hanna, K.; Mailhot, G. Development of a new homogenous photo-Fenton process using Fe(III)-EDDS complexes. *J. Photochem. Photobiol. A Chem.* **2012**, *239*, 17–23. [CrossRef]
17. Huang, W.; Brigante, M.; Wu, F.; Hanna, K.; Mailhot, G. Effect of ethylenediamine-N,N′-disuccinic acid on Fenton and photo-Fenton processes using goethite as an iron source: Optimization of parameters for bisphenol A degradation. *Environ. Sci. Pollut. Res. Int.* **2013**, *20*, 39–50. [CrossRef]
18. Huang, W.; Brigante, M.; Wu, F.; Mousty, C.; Hanna, K.; Mailhot, G. Assessment of the Fe(III)-EDDS complex in Fenton-like processes: From the radical formation to the degradation of bisphenol A. *Environ. Sci. Technol.* **2013**, *47*, 1952–1959. [CrossRef]
19. Conte, L.O.; Schenone, A.V.; Gimenez, B.N.; Alfano, O.M. Photo-Fenton degradation of a herbicide (2,4-D) in groundwater for conditions of natural pH and presence of inorganic anions. *J. Hazard. Mater.* **2019**, *372*, 113–120. [CrossRef]
20. Gutierrez-Zapata, H.M.; Rojas, K.L.; Sanabria, J.; Rengifo-Herrera, J.A. 2,4-D abatement from groundwater samples by photo-Fenton processes at circumneutral pH using naturally iron present. Effect of inorganic ions. *Environ. Sci. Pollut. Res. Int.* **2017**, *24*, 6213–6221. [CrossRef]
21. Huang, W.; Bianco, A.; Brigante, M.; Mailhot, G. UVA-UVB activation of hydrogen peroxide and persulfate for advanced oxidation processes: Efficiency, mechanism and effect of various water constituents. *J. Hazard. Mater.* **2018**, *347*, 279–287. [CrossRef] [PubMed]
22. Wu, P.; Yang, G.-P.; Zhao, X.-K. Sorption behavior of 2,4-dichlorophenol on marine sediment. *J. Colloid Interface Sci.* **2003**, *265*, 251–256. [CrossRef]

23. Karci, A.; Arslan-Alaton, I.; Olmez-Hanci, T.; Bekbölet, M. Transformation of 2,4-dichlorophenol by H_2O_2/UV-C, Fenton and photo-Fenton processes: Oxidation products and toxicity evolution. *J. Photochem. Photobiol. A Chem.* **2012**, *230*, 65–73. [CrossRef]
24. Wolfenden, A.; Mones, E. Handbook of Environmental Fate and Exposure Data for Organic Chemicals. *J. Test. Eval.* **1990**, *18*, 458. [CrossRef]
25. Zhang, H.; Nie, S.; Qin, C.; Zhang, K.; Wang, S. Effect of hot chlorine dioxide delignification on AOX in bagasse pulp wastewater. *Cellulose* **2018**, *25*, 2037–2049. [CrossRef]
26. Huang, Y.; Xv, Z.; Luo, W.; Huang, W.; Wang, S.; Yang, Q. Two amino polycarbonate modified light-Fenton systems: 2,4-dechlorophenol degradation (in Chinese). *Technol. Water Treat.* **2020**, in press.
27. Gomathi Devi, L.; Girish Kumar, S.; Mohan Reddy, K.; Munikrishnappa, C. Effect of various inorganic anions on the degradation of Congo Red, a di azo dye, by the photo-assisted Fenton process using zero-valent metallic iron as a catalyst. *Desalination Water Treat.* **2012**, *4*, 294–305. [CrossRef]
28. Liu, Y.; Chen, J.N.; Zhao, J.S.; Yu, H.X.; Wang, X.D.; Jiang, J.; Jin, H.J.; Zhang, J.F.; Wang, L.S. Three-dimensional quantitative structure activity relationship (3D-QSAR) analysis for in vitro toxicity of chlorophenols to HepG2 cells. *Chemosphere* **2005**, *60*, 791–795. [CrossRef] [PubMed]
29. Tang, W.Z.; Huang, C.P. The effect of chlorine position of chlorinated phenols on their dechlorination kinetics by Fenton's reagent. *Waste Manag.* **1995**, *15*, 615–622. [CrossRef]
30. Martin del Campo, E.; Romero, R.; Roa, G.; Peralta-Reyes, E.; Espino-Valencia, J.; Natividad, R. Photo-Fenton oxidation of phenolic compounds catalyzed by iron-PILC. *Fuel* **2014**, *138*, 149–155. [CrossRef]
31. Zhang, Y.; Klamerth, N.; Messele, S.A.; Chelme-Ayala, P.; Gamal El-Din, M. Kinetics study on the degradation of a model naphthenic acid by ethylenediamine-N,N′-disuccinic acid-modified Fenton process. *J. Hazard. Mater.* **2016**, *318*, 371–378. [CrossRef] [PubMed]
32. Catastini, C.; Sarakha, M.; Mailhot, G.; Bolte, M. Iron (III) aquacomplexes as effective photocatalysts for the degradation of pesticides in homogeneous aqueous solutions. *Sci. Total Environ.* **2002**, *298*, 219–228. [CrossRef]
33. El-Morsi, T.M.; Emara, M.M.; Abd El Bary, H.M.H.; Abd-El-Aziz, A.S.; Friesen, K.J. Homogeneous degradation of 1,2,9,10-tetrachlorodecane in aqueous solutions using hydrogen peroxide, iron and UV light. *Chemosphere* **2002**, *47*, 343–348. [CrossRef]
34. Fukushima, M.; Tatsumi, K.; Nagao, S. Degradation characteristics of humic acid during photo-Fenton processes. *Environ. Sci. Technol.* **2001**, *35*, 3683–3690. [CrossRef]
35. Sakkas, V.A.; Lambropoulou, D.A.; Albanis, T.A. Study of chlorothalonil photodegradation in natural waters and in the presence of humic substances. *Chemosphere* **2002**, *48*, 939–945. [CrossRef]
36. Mill, T. Predicting photoreaction rates in surface waters. *Chemosphere* **1999**, *38*, 1379–1390. [CrossRef]
37. Konstantinou, I.K.; Zarkadis, A.K.; Albanis, T.A. Photodegradation of Selected Herbicides in Various Natural Waters and Soils under Environmental Conditions. *J. Environ. Qual.* **2001**, *30*, 121–130. [CrossRef]
38. Kamiya, M.; Kameyama, K. Photochemical effects of humic substances on the degradation of organophosphorus pesticides. *Chemosphere* **1998**, *36*, 2337–2344. [CrossRef]
39. Bachman, J.; Patterson, H.H. Photodecomposition of the Carbamate Pesticide Carbofuran: Kinetics and the Influence of Dissolved Organic Matter. *Environ. Sci. Technol.* **1999**, *33*, 874–881. [CrossRef]
40. Derbalah, A.S.; Nakatani, N.; Sakugawa, H. Photocatalytic removal of fenitrothion in pure and natural waters by photo-Fenton reaction. *Chemosphere* **2004**, *57*, 635–644. [CrossRef]
41. Deng, Y.; Stumm, W. Kinetics of redox cycling of iron coupled with fulvic acid. *Aquat. Sci.* **1993**, *55*, 103–111. [CrossRef]
42. Fukushima, M.; Tatsumi, K. Degradation pathways of pentachlorophenol by photo-Fenton systems in the presence of iron(III), humic acid, and hydrogen peroxide. *Environ. Sci. Technol.* **2001**, *35*, 1771–1778. [CrossRef] [PubMed]
43. Epling, G.A.; Lin, C. Investigation of retardation effects on the titanium dioxide photodegradation system. *Chemosphere* **2002**, *46*, 937–944. [CrossRef]
44. Aguer, J.P.; Richard, C.; Andreux, F. Comparison of the photoinductive properties of commercial, synthetic and soil-extracted humic substances. *J. Photochem. Photobiol. A Chem.* **1997**, *103*, 163–168. [CrossRef]
45. Evgenidou, E.; Konstantinou, I.; Fytianos, K.; Poulios, I. Oxidation of two organophosphorous insecticides by the photo-assisted Fenton reaction. *Water Res.* **2007**, *41*, 2015–2027. [CrossRef] [PubMed]
46. Pignatello, J.J. Dark and photoassisted iron(3+)-catalyzed degradation of chlorophenoxy herbicides by hydrogen peroxide. *Environ. Sci. Technol.* **1992**, *26*, 944–951. [CrossRef]
47. Devi, L.G.; Munikrishnappa, C.; Nagaraj, B.; Rajashekhar, K.E. Effect of chloride and sulfate ions on the advanced photo Fenton and modified photo Fenton degradation process of Alizarin Red S. *J. Mol. Catal. A Chem.* **2013**, *374*, 125–131. [CrossRef]
48. Neta, P.; Huie, R.E.; Ross, A.B. Rate Constants for Reactions of Inorganic Radicals in Aqueous Solution. *J. Phys. Chem. Ref. Data* **1988**, *17*, 1027–1284. [CrossRef]
49. Dong, Y.; Chen, J.; Li, C.; Zhu, H. Decoloration of three azo dyes in water by photocatalysis of Fe (III)–oxalate complexes/H_2O_2 in the presence of inorganic salts. *Dye. Pigment.* **2007**, *73*, 261–268. [CrossRef]
50. Devi, L.G.; Raju, K.S.A.; Kumar, S.G.; Rajashekhar, K.E. Photo-degradation of di azo dye Bismarck Brown by advanced photo-Fenton process: Influence of inorganic anions and evaluation of recycling efficiency of iron powder. *J. Taiwan Inst. Chem. Eng.* **2011**, *42*, 341–349. [CrossRef]

51. Soler, J.; Garcia-Ripoll, A.; Hayek, N.; Miro, P.; Vicente, R.; Arques, A.; Amat, A.M. Effect of inorganic ions on the solar detoxification of water polluted with pesticides. *Water Res.* **2009**, *43*, 4441–4450. [CrossRef] [PubMed]
52. Sillanpaa, M.E.; Kurniawan, T.A.; Lo, W.H. Degradation of chelating agents in aqueous solution using advanced oxidation process (AOP). *Chemosphere* **2011**, *83*, 1443–1460. [CrossRef] [PubMed]
53. Miralles-Cuevas, S.; Audino, F.; Oller, I.; Sánchez-Moreno, R.; Sánchez Pérez, J.A.; Malato, S. Pharmaceuticals removal from natural water by nanofiltration combined with advanced tertiary treatments (solar photo-Fenton, photo-Fenton-like Fe(III)–EDDS complex and ozonation). *Sep. Purif. Technol.* **2014**, *122*, 515–522. [CrossRef]
54. Papoutsakis, S.; Brites-Nóbrega, F.F.; Pulgarin, C.; Malato, S. Benefits and limitations of using Fe(III)-EDDS for the treatment of highly contaminated water at near-neutral pH. *J. Photochem. Photobiol. A Chem.* **2015**, *303*, 1–7. [CrossRef]
55. Klamerth, N.; Gernjak, W.; Malato, S.; Agüera, A.; Lendl, B. Photo-Fenton decomposition of chlorfenvinphos: Determination of reaction pathway. *Water Res.* **2009**, *43*, 441–449. [CrossRef]
56. Chang, P.H.; Li, Z.; Jean, J.S.; Jiang, W.T.; Wu, Q.; Kuo, C.Y.; Kraus, J. Desorption of tetracycline from montmorillonite by aluminum, calcium, and sodium: An indication of intercalation stability. *Int. J. Environ. Sci. Technol.* **2013**, *11*, 633–644. [CrossRef]

processes

MDPI

Article

Computational Fluid Dynamics Modeling of Rotating Annular VUV/UV Photoreactor for Water Treatment

Minghan Luo [1,2,*], Wenjie Xu [1], Xiaorong Kang [1], Keqiang Ding [1] and Taeseop Jeong [3]

[1] School of Environmental Engineering, Nanjing Institute of Technology, Nanjing 211167, China; wenjiexu@njit.edu.cn (W.X.); feixiang2004@163.com (X.K.); dingkq@njit.edu.cn (K.D.)
[2] Energy Research Institute, Nanjing Institute of Technology, Nanjing 211167, China
[3] Department of Environmental Engineering, Chonbuk National University, Jeonju 561-756, Korea; jeongts@jbnu.ac.kr
* Correspondence: leon96201@njit.edu.cn; Tel.: +86-25-86118963

Abstract: The ultraviolet photochemical degradation process is widely recognized as a low-cost, environmentally friendly, and sustainable technology for water treatment. This study integrated computational fluid dynamics (CFD) and a photoreactive kinetic model to investigate the effects of flow characteristics on the contaminant degradation performance of a rotating annular photoreactor with a vacuum-UV (VUV)/UV process performed in continuous flow mode. The results demonstrated that the introduced fluid remained in intensive rotational movement inside the reactor for a wide range of inflow rates, and the rotational movement was enhanced with increasing influent speed within the studied velocity range. The CFD modeling results were consistent with the experimental abatement of methylene blue (MB), although the model slightly overestimated MB degradation because it did not fully account for the consumption of OH radicals from byproducts generated in the MB decomposition processes. The OH radical generation and contaminant degradation efficiency of the VUV/UV process showed strong correlation with the mixing level in a photoreactor, which confirmed the promising potential of the developed rotating annular VUV reactor in water treatment.

Keywords: VUV; photoreactor; CFD; MB; water treatment

Citation: Luo, M.; Xu, W.; Kang, X.; Ding, K.; Jeong, T. Computational Fluid Dynamics Modeling of Rotating Annular VUV/UV Photoreactor for Water Treatment. *Processes* **2021**, *9*, 79. https://doi.org/10.3390/pr9010079

Received: 1 December 2020
Accepted: 29 December 2020
Published: 31 December 2020

1. Introduction

Use of ultraviolet-based photoreactors in water-treatment processes is rapidly increasing, and ultraviolet-based advanced oxidation processes (UV AOPs) have been studied for over 30 years. The H_2O_2/UV process presents increased economic cost and technical complexity due to the treatment of residual peroxide, leading to its application only in small and medium-sized water treatment facilities. The VUV/UV process uses ozone-generating mercury lamps that emit 185 nm VUV and 254 nm UV radiation, in which the 185 nm radiation reacts with water to produce hydroxyl radicals (·OH). Therefore, VUV/UV photodegradation is considered to be a simple and environmentally friendly water-treatment technology with attractive economic potential, which has shown promising potential in wastewater treatment [1]. Although plenty of experiments have yielded promising results at lab-scale, the VUV/UV AOP has not yet been implemented at a full-scale plant in water treatment. There are still problems that impede large-scale application of VUV/UV photoreactors in the water-remediation field. For example, lack of a proper simulation model to predict and analyze the performance of VUV/UV photoreactors is one of the problems hindering their practical implementation. An effective modeling of the VUV/UV process involves the simultaneous solution of momentum equations, mass transfer equations, and radiation energy equations (UV and VUV radiations), along with a complex kinetic scheme of more than 40 reactions.

Computational fluid dynamics (CFD) is an established and effective tool for modeling complex fluid dynamic processes, and has been used extensively for the design, optimization, and scale-up of UV disinfection and oxidation photoreactors in recent years [2,3].

Previous studies have pointed out the importance of using a comprehensive kinetic scheme and a detailed radiation model, including the reflection, refraction, and absorption of photons in UV photoreactors, for CFD simulation. However, few studies about modeling of H_2O_2/UV using the CFD method have individually reported the role of 254 nm irradiation in direct photolysis of water, or of the ·OH radical oxidation pathways in the process of removing target pollutants [2,4,5]. Moreover, despite of the similarities between the H_2O_2/UV and VUV/UV processes, the associated hydroxyl radical generation mechanisms are different [4–6]. The production of ·OH radicals in VUV/UV systems relies on the photolysis of water at 185 nm irradiation, while hydrogen peroxide photolysis at 254 nm irradiation is the predominant mechanism for the generation of ·OH radicals in H_2O_2/UV systems [5]. The direct photolysis of water will generate species such as ·OH, ·H and H^+, whereas the UV photolysis of hydrogen peroxide produces only ·OH, therefore causing different radical reaction schemes during H_2O_2/UV and VUV/UV processes. In addition, the emissions at 185 nm and 254 nm synchronously contribute to the removal of contaminants in a VUV/UV process. In contrast, H_2O_2/UV approaches primarily rely on the degradation functions of 254 nm photons. UV light at a wavelength of 185 nm, which plays the key role in ·OH production in VUV/UV AOPs, is transmitted a relatively short distance in solutions. As a result, VUV/UV AOPs normally require better mixing within reactors than UV AOPs, and the effective identification of mixing characteristics of the area around UV lamps is therefore of particular significance for VUV/UV AOP studies.

In this context, this work aimed to develop a comprehensive CFD simulation tool able to make an in-depth analysis of the VUV/UV process applied to water treatment. The proposed computational model integrates a series of sub-models such as hydrodynamic simulations, a multispecies mass transport model, chemical reaction kinetics, and irradiance distribution within the reactor. The radiation field within the reactor was modeled using a nongray discrete ordinate (DO) sub model, which allowed for independent and simultaneous studies of the transportation paths of 185 nm VUV and 254 nm UV. The developed model was experimentally evaluated in a continuous-flow VUV/UV photoreactor for the treatment of a selected pollutant: methylene blue (MB). Finally, we establish and discuss a model for degradation pathways within VUV/UV photoreactors. The results from this study revealed crucial hydrodynamic characteristics in the VUV/UV photoreactor, and provide useful suggestions for the design and optimization of VUV/UV photoreactors, promoting the practical application of VUV/UV techniques in the water-treatment field.

2. Materials and Methods

2.1. Hydrodynamics

Based on the principles of conservation of mass and momentum, the continuity equations in a rotating annular VUV reactor (RAVR) were described. A three-dimensional computational fluid dynamic model was developed to calculate the local hydrodynamics in the photoreactor.

$$\sum_{i=1}^{n} \alpha_i = 1 \tag{1}$$

where n is the total number of phases; the subscript i represents the gas or liquid phase. The conservation equations are written by performing an ensemble average of the local instantaneous balance for each phase. The motion of each phase is governed by the corresponding mass and momentum conservation equations.

Continuity equation:

$$\frac{\partial(\alpha_i \cdot \rho_i)}{\partial t} + \nabla \cdot (\alpha_i \rho_i \vec{u}_i) = 0 \tag{2}$$

where α, ρ, and $\vec{u}$ stand for the volume fraction, density, and velocity vector, respectively.

Momentum equation:

$$\frac{\partial(\alpha_i \rho_i \vec{u}_i)}{\partial t} + \nabla\cdot(\alpha_i \rho_i \vec{u}_i \vec{u}_i) = -\alpha_i \nabla P_i + \nabla\cdot\left(\alpha_i \mu_i (\nabla \vec{u}_i - (\nabla \vec{u}_i)^T)\right) + \alpha_i \rho_i \vec{g} \pm \vec{F}_i \quad (3)$$

where P, μ, and $\vec{g}$ are the pressure, viscosity, and gravity acceleration, respectively. $\vec{F}_i$ is the interfacial force acting on phase i due to the presence of the other phase, j.

The turbulent dispersion force is the result of the turbulent fluctuations of liquid velocity. In this study, the standard $k-\varepsilon$ model for single-phase flows was extended for the two-phase flows to simulate the turbulence, which can be described as follows:

$$\frac{\partial}{\partial t}(\alpha_l \rho_l k_l) + \frac{\partial}{\partial x_i}(\alpha_l \rho_l \vec{u}_l k_l) = \frac{\partial}{\partial x_i}\left[\alpha_l \left(\mu_l + \frac{\mu_{tl}}{\sigma_k}\right)\frac{\partial}{\partial x_i} k_l\right] + \alpha_l \rho_l - \alpha_l \rho_l \varepsilon_l \quad (4)$$

$$\frac{\partial}{\partial t}(\alpha_l \rho_l \varepsilon_l) + \frac{\partial}{\partial x_i}(\alpha_l \rho_l \vec{u}_l \varepsilon_l) = \frac{\partial}{\partial x_i}\left[\alpha_l \left(\mu_l + \frac{\mu_{tl}}{\sigma_\varepsilon}\right)\frac{\partial}{\partial x_i} \varepsilon_l\right] + \alpha_l \frac{\varepsilon_l}{k_l}(C_{\varepsilon 1 p_l} - C_{\varepsilon 2 \rho_l \varepsilon_l}) \quad (5)$$

where $C_{\varepsilon 1}$, $C_{\varepsilon 2}$, σ_k, and σ_ε are parameters in the standard k $-$ ε model and the following values were selected: $C_{\varepsilon 1} = 1.44$, $C_{\varepsilon 2} = 1.92$, $\sigma_k = 1.0$, and $\sigma_\varepsilon = 1.3$. In addition, the turbulent viscosities μ_{tl} can be computed by other equations [7,8].

2.2. Radiative Transfer Model

The radiative transfer equation (RTE) for an absorbing, emitting, and scattering medium at position $\vec{r}$ in the direction $\vec{s}$ is as follows:

$$\frac{dI(\vec{r},\vec{s})}{ds} + (a+\sigma_s)\, I(\vec{r},\vec{s}) = an^2 \frac{\sigma T^4}{\pi} + \frac{\sigma_s}{4\pi}\int_0^{4\pi} I(\vec{r},\vec{s}\,')\, \varnothing(\vec{s},\vec{s}\,')\, d\Omega' \quad (6)$$

where $\vec{r}$ and $\vec{s}$ are position and direction vectors, respectively. I is the radiation intensity, which depends on position and direction; n is the refractive index; σ is the Stefan–Boltzmann constant (5.67×10^{-8} $Wm^{-2}K^{-4}$); α is the absorption coefficient; σ_s is the scattering coefficient; ∅ is the phase function; and Ω' is the solid angle. Additionally, $(a+\sigma_s)$s is the optical thickness or opacity of the fluid (water mixture). The refractive index n is important when considering radiation in semitransparent media [7].

2.3. Kinetic Reaction Model

In previous studies, detailed kinetic models for VUV systems have been studied to find the perfect batch-scale mixing conditions [4,5]. In this study, 26 types of reaction occurring in the VUV/UV photoreactor (i.e., equilibrium, photochemical, and radical reactions) were summarized, as shown in Table 1, with reference to the previous study. Thus, in the presence of VUV and UV radiation, the main degradation pathways of the species are initiated by the OH radicals produced by the decomposition of water by 185 nm radiation, leading to radical chain reactions induced by 185 and 254 nm radiation.

Table 1. Kinetic model of the VUV/UV photoreactor for degradation of MB.

No.	Reaction Equation	Rate Constant	Reference
1	$H_2O + h\nu_{185nm} \rightarrow HO\cdot + H\cdot$	$\varnothing_6 = 0.330$ mol/ein	Gonzalez et al., 2004 [9]
2	$H_2O + h\nu_{185nm} \rightarrow H^+ + e^-_{aq} + HO\cdot$	$\varnothing_7 = 0.045$ mol/ein	Gonzalez et al., 2004 [9]
3	$H_2O_2 + h\nu_{185nm} \rightarrow 2HO\cdot$	$\varnothing_8 = 0.500$ mol/ein	Gonzalez et al., 2004 [9]
4	$H_2O_2 + h\nu_{254nm} \rightarrow 2HO\cdot$	$\varnothing_9 = 0.500$ mol/ein	Gonzalez et al., 2004 [9]
5	$O_2 + H\cdot \rightarrow HO_2^{\cdot}$	$k_1 = 2.1 \times 10^{10}\ M^{-1}s^{-1}$	Gonzalez et al., 2004 [9]
6	$O_2 + e^-_{aq} \rightarrow O_2^{\cdot -}$	$k_2 = 2.0 \times 10^{10}\ M^{-1}s^{-1}$	Gonzalez et al., 2004 [9]
7	$H_2O_2 + OH\cdot \rightarrow HO_2^{\cdot} + H_2O$	$k_3 = 2.7 \times 10^{7}\ M^{-1}s^{-1}$	Gonzalez et al., 2004 [9]
8	$H_2O_2 + HO_2^{\cdot} \rightarrow OH\cdot + O_2 + H_2O$	$k_4 = 5.3 \times 10^{2}\ M^{-1}s^{-1}$	Gonzalez et al., 2004 [9]
9	$H_2O_2 + O_2^{\cdot -} \rightarrow OH\cdot + O_2 + OH^-$	$k_5 = 1.6 \times 10^{1}\ M^{-1}s^{-1}$	Gonzalez et al., 2004 [9]
10	$H_2 + OH^{\cdot} \rightarrow H_2O + H^{\cdot}$	$k_6 = 6.0 \times 10^{7}\ M^{-1}s^{-1}$	Gonzalez et al., 2004 [9]
11	$OH^{\cdot} + OH^{\cdot} \rightarrow H_2O_2$	$k_7 = 4.0 \times 10^{9}\ M^{-1}s^{-1}$	Gonzalez et al., 2004 [9]
12	$HO_2^{\cdot} + HO_2^{\cdot} \rightarrow H_2O_2 + O_2 + H_2O$	$k_8 = 2.6 \times 10^{6}\ M^{-1}s^{-1}$	Gonzalez et al., 2004 [9]
13	$H\cdot + H\cdot \rightarrow H_2$	$k_9 = 1.0 \times 10^{10}\ M^{-1}s^{-1}$	Gonzalez et al., 2004 [9]
14	$OH\cdot + H\cdot \rightarrow H_2O$	$k_{10} = 7.0 \times 10^{9}\ M^{-1}s^{-1}$	Gonzalez et al., 2004 [9]
15	$OH\cdot + O_2^{\cdot -} \rightarrow O_2 + HO^-$	$k_{11} = 7.0 \times 10^{9}\ M^{-1}s^{-1}$	Bielski et al., 1985 [10]
16	$OH\cdot + HO_2^{\cdot} \rightarrow H_2O + O_2$	$k_{12} = 6.6 \times 10^{9}\ M^{-1}s^{-1}$	Buxton et al., 1988 [11]
17	$HO_2^{\cdot} + O_2^{\cdot -} \rightarrow O_2 + HO_2^-$	$k_{13} = 9.7 \times 10^{7}\ M^{-1}s^{-1}$	Buxton et al., 1988 [11]
18	$e^-_{aq} + OH^{\cdot} \rightarrow OH^-$	$k_{14} = 3.0 \times 10^{10}\ M^{-1}s^{-1}$	Gonzalez et al., 2004 [9]
19	$2O_2^{\cdot -} + 2H_2O \rightarrow O_2 + H_2O_2 + 2OH^-$	$k_{15} = 3.0 \times 10^{-1}\ M^{-1}s^{-1}$	Gonzalez et al., 2004 [9]
20	$e^-_{aq} + H^{\cdot} + H_2O \rightarrow H_2 + OH^-$	$k_{16} = 2.5 \times 10^{10}\ M^{-1}s^{-1}$	Gonzalez et al., 2004 [9]
21	$OH\cdot + HO_2^- \rightarrow HO_2^{\cdot} + OH^-$	$k_{17} = 7.5 \times 10^{9}\ M^{-1}s^{-1}$	Crittenden et al., 1999 [12]
22	$OH\cdot + OH^- \rightarrow O^{\cdot -} + H_2O$	$k_{18} = 3.9 \times 10^{8}\ M^{-1}s^{-1}$	Buxton et al., 1988 [11]
23	$H\cdot + OH^- \rightarrow e^-_{aq} + H_2O$	$k_{19} = 3.6 \times 10^{8}\ M^{-1}s^{-1}$	Draganic and Draganic, 1973 [13]
24	$H_2O_2 + e^-_{aq} \rightarrow OH\cdot + OH^-$	$k_{20} = 1.1 \times 10^{10}\ M^{-1}s^{-1}$	Basfar et al., 2005 [14]
25	$e^-_{aq} + H^+ \rightarrow H\cdot$	$k_{21} = 2.3 \times 10^{10}\ M^{-1}s^{-1}$	Basfar et al., 2005 [14]
26	$e^-_{aq} + H_2O \rightarrow H\cdot + OH^-$	$k_{22} = 1.9 \times 10^{1}\ M^{-1}s^{-1}$	Basfar et al., 2005 [14]
27	$H\cdot + HO_2^{\cdot} \rightarrow H_2O_2$	$k_{23} = 1.1 \times 10^{10}\ M^{-1}s^{-1}$	Basfar et al., 2005 [14]
28	$H\cdot + H_2O_2 \rightarrow H_2O + OH^{\cdot}$	$k_{24} = 9.0 \times 10^{7}\ M^{-1}s^{-1}$	Basfar et al., 2005 [14]
29	$e^-_{aq} + HO_2^- + H_2O \rightarrow 2OH^- + OH\cdot$	$k_{25} = 3.5 \times 10^{9}\ M^{-1}s^{-1}$	Mak et al., 1997 [15]
30	$H\cdot + O_2^{\cdot -} \rightarrow HO_2^-$	$k_{26} = 2.0 \times 10^{10}\ M^{-1}s^{-1}$	Mak et al., 1997 [15]
31	$OH\cdot + MB \rightarrow$ Products	$k_{27} = 6.9 \times 10^{10}\ M^{-1}s^{-1}$	Buxton et al., 1988 [11]

2.4. Geometry of RAVR and System Setup

A simple three-dimensional geometry and a mesh structure developed for the RAVR are shown in Figure 1a. The geometry was created using ANSYS DesignModeler software. The RAVR consisted of a reactor with a total length of 500 mm, a 20 mm diameter lamp and a 20 mm diameter inlet, a 30 mm diameter exit tube, and a 5 mm wall thickness. The inlet exit tube was attached to the reactor in a tangential direction to increase the mixing and reactivity of the reactor. The inlet and outlet entered the reactor tangentially to induce rotational flow in the reactor. The RAVR volume was discretized into 132,529 structured and unstructured volume cells using ANSYS Meshing software.

A flow-through, continuously operating RAVR was used to experimentally evaluate the CFD results. The RAVR system is presented in Figure 1b. The reactor had a tangential inlet and an outlet, with annular and rotation flow configuration, operated with a 17 W low-pressure mercury lamp (G10T5VH, Light Sources Inc., Orange, CT, USA) longitudinally placed at the axial center of the reactor. The inlet flow rate was adjusted to within a 1.963–23.550 L/min range with a defined concentration of MB, and the hydraulic retention time varied from 10 s to 120 s. Flow rates of the MB solutions were controlled by peristaltic pumps.

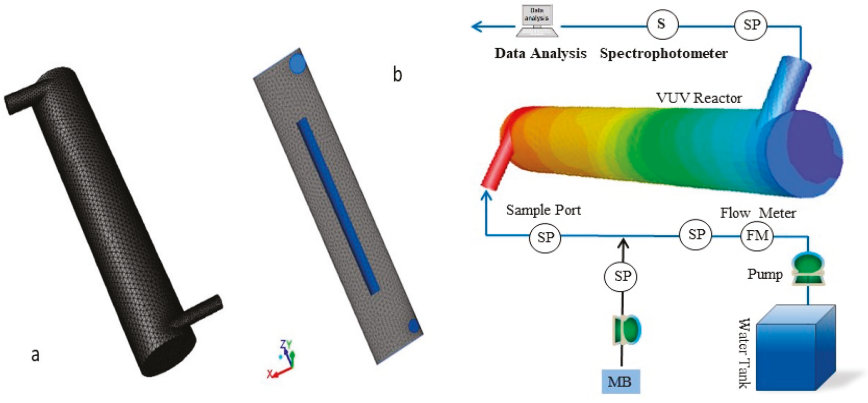

Figure 1. The rotating reactor geometry (**a**) and the VUV reactor system scheme (**b**).

2.5. Boundary Conditions and Numerical Solution

The inlet velocity had a range of 0.104–1.250 m/s, which corresponded to a flow rate of 1.963 to 23.550 L/min. The inlet concentration of the model contaminant MB was equal to 0.5 ppm. A no-slip boundary condition was imposed on the walls. In addition, zero diffusive flux of species was specified at the walls. As per radiation field boundary conditions, the radiation of lamp was defined as a zero-thickness, semitransparent, nonreflecting wall. The density and viscosity of water considered were 998.2 kg/m^3 and 1.003 × 10^{-3} Pa, respectively. The refractive indexes of 185 nm and 254 nm were assigned as 1.458 and 1.376, respectively, and the absorption coefficients 35.67 (m^{-1}, UVT = 70%) and 12.78 (m^{-1}, UVT = 88%), respectively.

ANSYS 16.2 Fluent was employed to read the mesh and perform the CFD computations. The segregated steady-state solver was used to solve the governing equations. Second-order upwind discretization schemes were applied except for pressure, for which the standard scheme was selected. The semi-implicit method for pressure linked equations (SIMPLE) algorithm was chosen for the pressure–velocity coupling. The variation of velocity magnitude, model contaminant concentration, and irradiation flux at several points of the computational domain were used as indicators of convergence (at least 20 iterations). Additionally, convergence of the numerical solution was assured by monitoring the scaled residuals to a criterion of at least 10^{-4} for the concentration of MB. While the simulation was always tracked with time, the solution algorithm was run with both steady and transient flow simulations.

2.6. Chemicals and Analytical Methods

For the VUV reactor experiments, the chemicals used for experiments were reagent-grade or higher, supplied by Sigma-Aldrich. MB powder was used as purchased without further purification. The MB was diluted separately with ultrapure laboratory water. Distilled water was used in all experiments and analytical determinations. The concentration of MB in the VUV reactor effluent was determined spectrophotometrically following the peak at 664 nm using a UV spectrophotometric probe (UV1800, Shimadzu Co., Marlborough, MA, USA, Kyoto, Japan spectrophotometer). The concentration of hydrogen peroxide was determined via UV spectrophotometry utilizing the I_3^- method [16].

3. Results and Discussion

3.1. Hydrodynamics

The fluid velocity magnitudes are shown in Figure 2 for selected cross-sections in the designed RAVR. The results showed that the fluid entered the inlet at a high velocity and

initiated a rotational motion along the wall of the RAVR. For the radial velocity distribution of the reactor, the velocity on the wall of the reactor was higher than that on the surface of central light source of the reactor. Because the rotational flow flowed tangentially onto the reactor wall, part of the kinetic energy was consumed when it reached the light source.

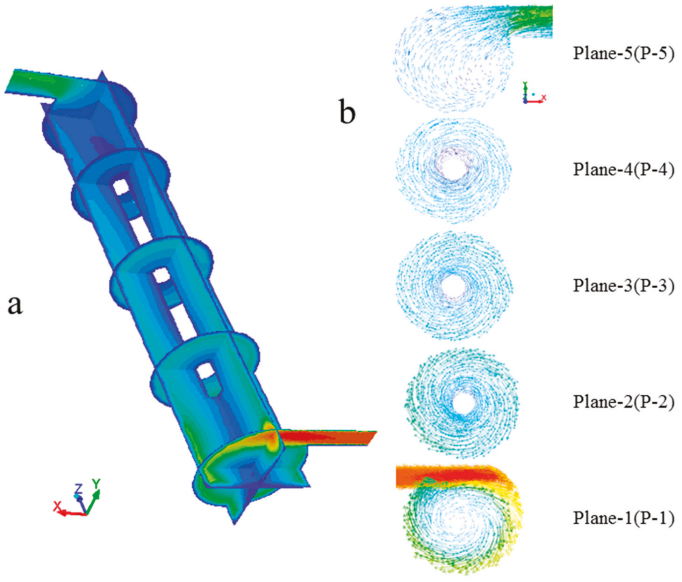

Figure 2. Velocity vectors (**a**) and contours of velocity magnitude (**b**) along the axial plane at different section planes located at 2 (P-1), 12.5 (P-2), 25 (P-3), 36.5 (P-4), and 48 (P-5) cm positions from the inlet.

As shown by the streamline in Figure 3, the fluid maintained rotational motion from the inlet to the outlet of the reactor, and thus the outflow also presented a rotating flow. Obviously, the rotational flow in the vicinity of outer wall of the reactor showed an upward motion; the rotation force was generated from the flowing force of fluid entering the inlet without additional energy supply. The fluid from the inlet raised along the reactor wall with a high movement velocity. The RAVR integrated the flow characteristics of a continuous-flow stirred-tank reactor (CSTR) and a plug flow reactor (PFR). As mentioned in Section 1, the RAVR is an economical reactor with good mixing function compared with long tubular reactors [17–19] or reactors with internal baffles [3,20,21]. The rotating flow along the VUV lamp in a RAVR reactor plays the role of mixing and extending the fluid-retention time, and there is thus no dead zone in a RAVR reactor.

3.2. Pressure Field

Pressure contour analyses of the longitudinal section of the reactor and of Plane-1 to Plane-5 were conducted for the 3.925 L/min inflow rate, and the results are plotted in Figure 4. Pressure increased from the inlet area to outlet area, and decreased along the radial direction from the reactor wall to the central lamp. For Plane-1 (P-1), where the rotation force of the fluid was induced, the entrance position and out-wall area presented high pressure, indicating a whirl flow along the wall surface. The pressure distribution on the cross-section (*X*–*Y* plane) of the reactor showed a low-pressure zone in the forced vortex region at the central position due to a high fluid rotating velocity. Since fluid flows from a high-pressure area to a low-pressure area, the longitudinal and radial distribution of pressure in reactor revealed that two circulation flows formed in the reactor: (i) an upward rotating flow along the out-wall surface and (ii) a downward stream adhering to the UV

lamp from the outlet position to the inlet position. Moreover, the pressure distribution shown in Figure 4 is consistent with the streamline shown in Figure 3. When the fluid entered the reactor, it climbed up along the reactor out-wall surface in a rotating flow (outer circulation ring) and flowed into the central part of reactor due to the pressure difference, then went down along the UV lamp at a slow flow rate (inner circulation ring). In this way, the retention time of introduced solutions in the RAVR reactor was extended through two circulation flows, thus enhancing the treatment effect. Additionally, the pressure difference of the RAVR system, which was identified by the ratio of maximum pressure to minimum pressure, was found to change with inflow rates.

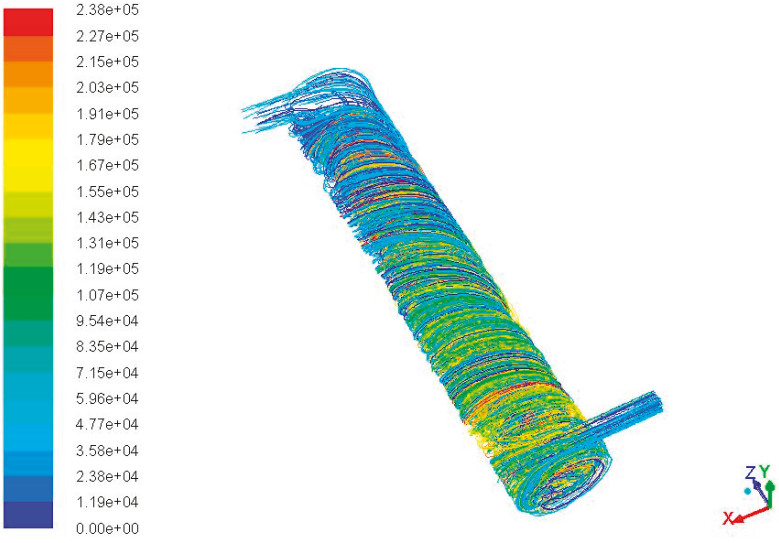

Figure 3. Streamline along the axial plane for inflows at 3.952 L/min velocity.

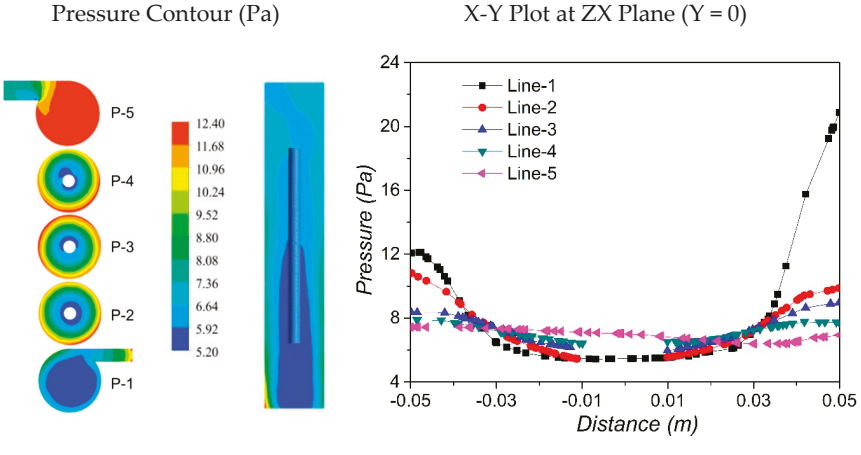

Figure 4. The contour and profiles of pressure in the axial direction of the reactor (including Plane-1 to Plane-5) at 3.925 L/min inflow rate.

3.3. UV Radiation

Figure 5 shows the contour distribution of ultraviolet radiation intensity on the *X*–*Z* and *X*–*Y* cross-sections of the reactor. The ultraviolet radiation at 185 nm, which reacts with and causes the formation of ·OH radicals, was decreased to almost zero in the wall area around 4 cm away from the lamp due to the limited transmission ability of ultraviolet radiation at 185 nm in water.

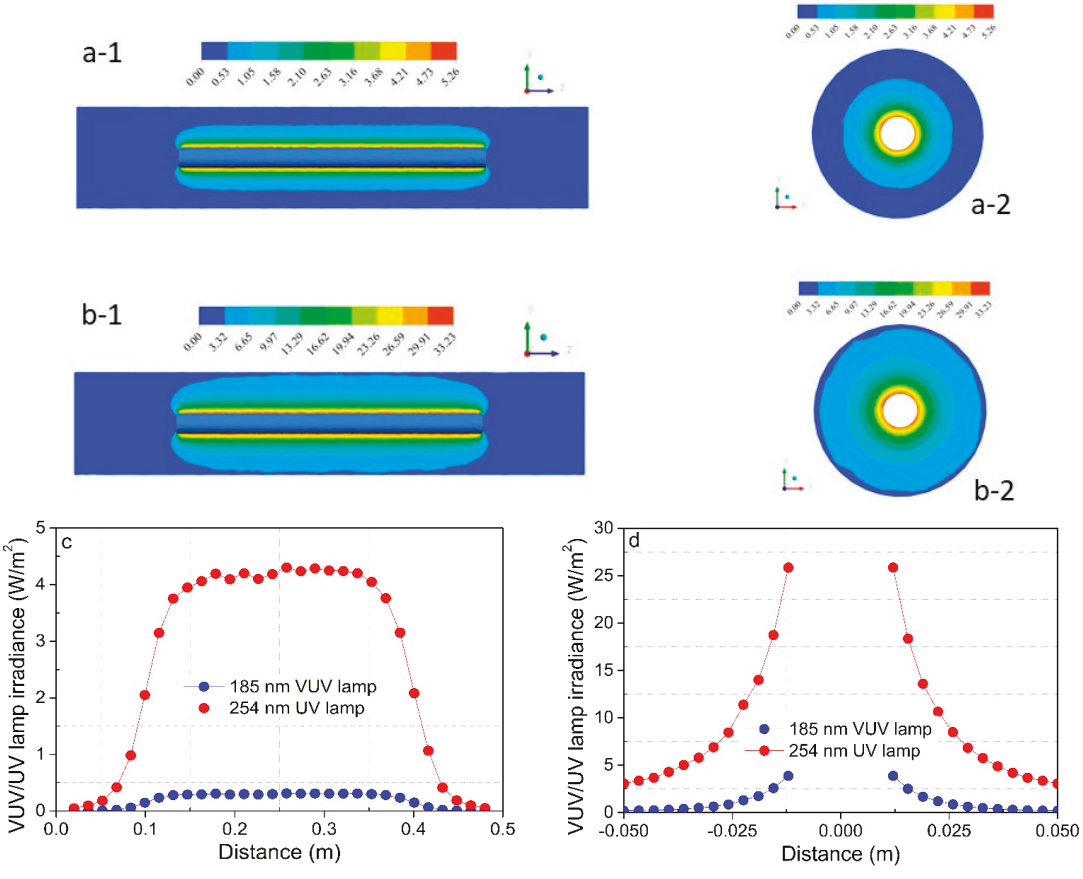

Figure 5. Local values of ultraviolet irradiance calculated in the whole reaction zone in the *X*–*Z* (**c**) and *X*–*Y* (**d**) planes of the reactor. The longitudinal (**a-1**, **b-1**) and radial (**a-2**, **b-2**) contours of lamp irradiance. a, 185 nm; b, 254 nm.

3.4. Degradation Reaction

The prediction of the RAVR performance was based on CFD modeling simulations, including the specific chemical kinetics of the reactions in the mass balance of involved species. On the basis of the hydrodynamic distribution characteristics of the RAVR, the kinetic responses of the VUV–H_2O–MB reactions in Table 1 at 3.925 L/min inflow rate are represented in Figure 6, with chemical reaction rates calculated by user defined function (UDF).

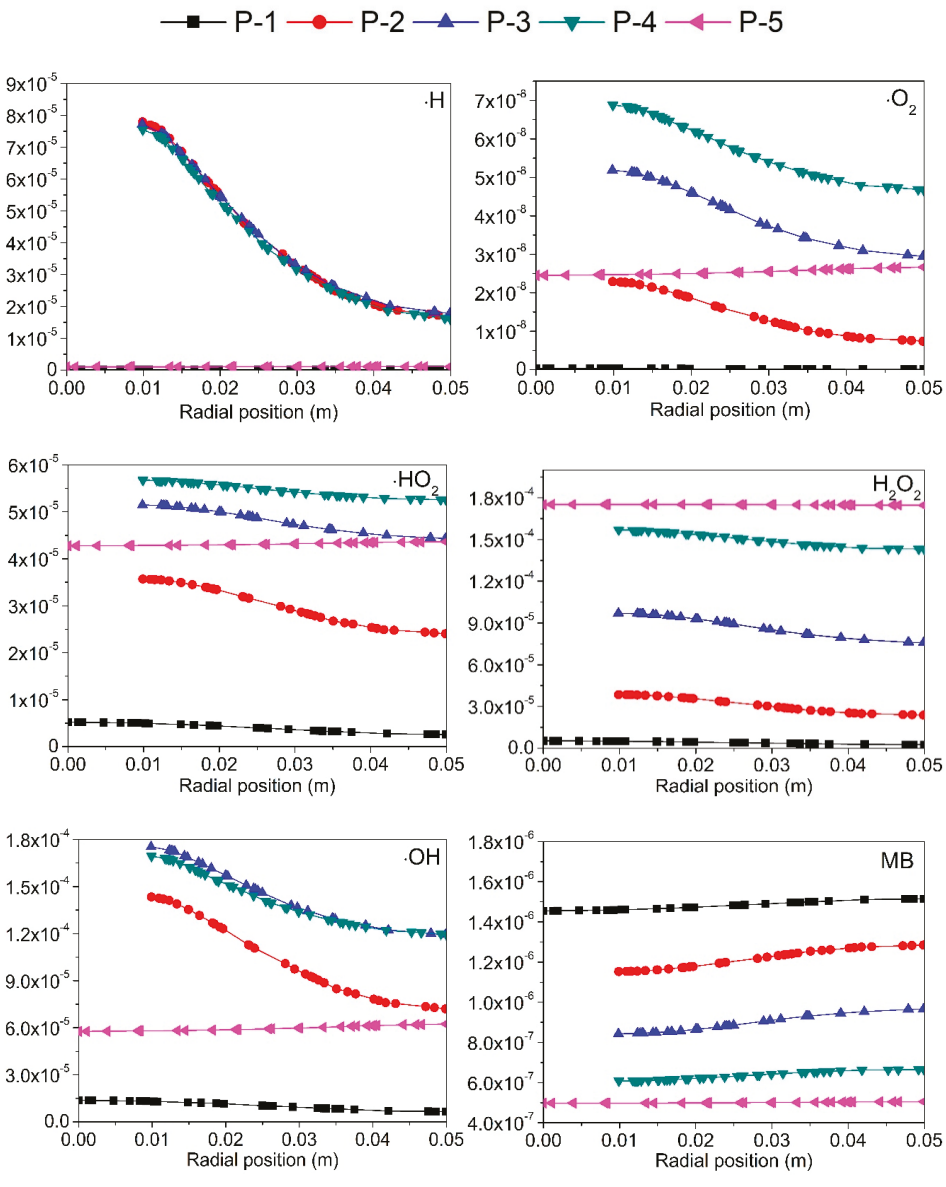

Figure 6. Concentration profile (mol/L) of the species in the center line of the plane as a function of the radial position in the reactor (flow rate = 3.925 L/min).

The profiles of molar concentrations of ·OH radicals (Figure 6) showed a gradual increase from the inlet position to the outlet position (Plane-1 to Plane-4), and then a decrease to a low level on Plane-5. As the Plane-1 was located at the inlet with a small dose of ultraviolet radiation, the concentration of ·OH radicals were accordingly low. More ·OH radicals were generated from P-2 to P-4 with increased ultraviolet radiation. Similarly, the amount of radicals was decreased from the center to wall area in the reactor due to the diminished UV radiation. Moreover, comparing the change of ·OH radicals on different cross-sections, the radical decrease rate from the UV lamp (center position) to the wall

surface was slowed down for Plane-2 to Plane-4. In other words, the concentration gradient of ·OH radicals on the same cross-section was decreased along the axial direction from inlet to outlet in the RAVR, albeit not as much as in P-1 and P-5. This is mostly because the upward flow accumulated ·OH radicals and weakened the concentration gradient. It should be noted here that the presented concentration changes of ·OH radicals in Figure 6 do not reflect the quantitative amounts of ·OH radicals directly generated from water by UV radiation: in fact, the radiation at 185 nm has a very low ultraviolet transmittance (UVT) and reaches almost zero at a distance of about 3–4 cm from the lamp source. Thus, the concentration profile of hydroxyl radicals reported in Figure 6 is rather a quantitative result based on the advection and diffusion of fluid in the reactor. In addition, the same distribution feature of ·OH radicals was observed for species like H_2O_2, ·H, $\cdot HO_2$, and $\cdot O_2^-$, except that the concentrations of ·H on Plane-2 to Plane-4 were very similar. As shown in Table 1, the reaction characteristics of the H radical are quite different from those of other species with higher kinetic parameters. Therefore, a gradient concentration along the radial direction was observed for the H radical at the central position of the reactor (P-2, P-3, and P-4), with higher concentrations near the light source. Furthermore, taking into account that the P-2, P-3, and P-4 profiles fully overlapped, it is possible to state that no appreciable gradient concentration occurred along the longitudinal direction in the central part of the reactor. On the other hand, the MB concentration showed an opposite trend to that of ·OH radicals as MB was decomposed and removed by the ·OH radicals. The ·OH-radical-rich zone coincided with active decomposition reactions of MB. Generally, the low concentration of MB in outflow confirmed the good mixing properties of the designed RAVR, which also implies that developing a process with excellent blending function to enhance the contact between ultraviolet light and each reactant is one important route to increase the efficiency of photolysis reactions.

3.5. Comparison of Experimental and Simulation Results

There are two major concerns to be faced in improving the photochemical reactions of VUV/UV AOP. First, the water must be sufficiently irradiated with 185 nm ultraviolet light for the production of ·OH radicals. In this study, the ·OH radicals were efficiently generated near the UV lamp (which has a high intensity of ultraviolet radiation at 185 nm) and then quickly diffused across the whole reaction tank. Second, the efficiency of VUV/UV AOP can be significantly enhanced by increasing contact opportunities between the species (like MB) to be treated and the ·OH radicals generated in the chain reactions. Various methods have been developed based on the two mentioned routes. For example, a pipe-type reactor with a small diameter has been explored for maximization of ultraviolet light intensity [17–19,22]. However, this method has the disadvantage that the long contact time (residence time) required for the reaction can be only obtained by designing a long reaction pipe, which is normally limited by actual situations. Another commonly studied method is the installation of baffles to increase vortexes inside the reactor [5,21]. However, this is suitable only for small-scale reactors (like the lab scale) and requires further considerations for application at the industry scale. The adsorption method using an adsorption medium (catalyst) has also been widely studied [21]. Its problem is that the catalysts utilized may hinder the irradiation transmission of ultraviolet light. In conclusion, the design optimization of photoreactors plays a key role in promoting the application of photochemical processes based on ·OH radical generation in water-treatment or wastewater-treatment fields. The study followed this idea and investigated the possibility of maximizing the utilization of rotational force of the fluid in the designed photoreactor by adjusting the inflow velocity of treated solutions.

The predicted and experimental degradation efficiencies of MB and CFD showed good consistency for the 3.925 L/min inflow rate, as shown in Figure 7. In addition, the pollutant abatement calculated by CFD modeling was slightly lower than the experimental value for all tested inflow velocities.

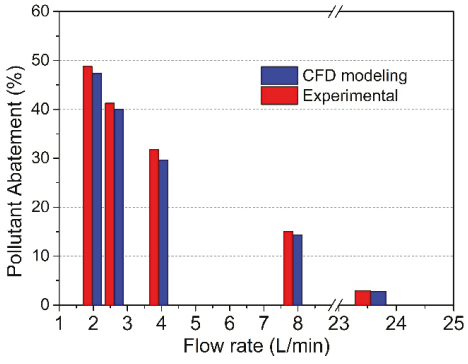

Figure 7. Comparison of removal rates of MB of experimental data and CFD-predicted results.

4. Conclusions

This study aimed to develop a novel rotating annular photoreactor with a tangential inlet and outlet to improve the performance of a VUV AOP for increased degradation efficiency of the photoreactor. The flow characteristics as well as the fluid dynamics were investigated and the kinetic model of involved species was simulated to evaluate the reaction characteristics in the designed reactor. Meanwhile, the concentration profiles of ·OH radicals, target pollutant (MB), and other important reacting species were also determined to assess the reactor properties. The results showed that the introduced fluid was in strong rotational movement inside the reactor across the wide range of influent velocities in this study. Moreover, the rotational movement was enhanced with the increasing of inflow rates in the studied velocity range. The CFD modeling results corresponded well to the experimental degradation of MB. They slightly underestimated degradation due to the limited kinetic analysis about radical annihilation effect from by-products of MB degradation. The results from this study confirmed that the ·OH radical generation and contaminant degradation efficiency of a VUV/UV process showed strong correlation with the mixing degree in a photoreactor. Therefore, the developed RAVR has high potential to promote the scale-up of VUV/UV AOP systems.

Author Contributions: Conceptualization, M.L. and T.J. Data curation, W.X. and X.K. Formal analysis, M.L. Funding acquisition, M.L. Methodology, M.L., W.X., X.K., T.J. and K.D. Validation, M.L. Visualization, M.L. Writing-original draft, M.L. Writing-review & editing, M.L, K.D. and T.J. Project administration, M.L. and T.J. Software, X.K. and W.X Experiments. All authors have read and agreed to the published version of the manuscript.

Funding: This work was funded by Natural Science Research of Jiangsu Higher Education Institutions of China (No.18KJB610006), and Introduction Talent Scientific Research Foundation Project of NanJing Institute of Technology (No. YKJ201847) and Supported by the Cooperation Fund of Energy Research Institute, Nanjing Institute of Technology (No. CXY201925).

Conflicts of Interest: The authors declare no conflict of interest.

References

1. Bagheri, M.; Mohseni, M. Computational fluid dynamics (CFD) modeling of VUV/UV photoreactors for water treatment. *Chem. Eng. J.* **2014**, *256*, 51–60. [CrossRef]
2. Alpert, S.M.; Knappe, D.R.U.; Ducoste, J.J. Modeling the UV/hydrogen peroxide advanced oxidation process using computational fluid dynamics. *Water Res.* **2010**, *44*, 1797–1808. [CrossRef] [PubMed]
3. Santoro, D.; Raisee, M.; Moghaddami, M.; Ducoste, J.; Sasges, M.; Liberti, L.; Notarnicola, M. Modeling Hydroxyl Radical Distribution and Trialkyl Phosphates Oxidation in UV−H_2O_2 Photoreactors Using Computational Fluid Dynamics. *Environ. Sci. Technol.* **2010**, *44*, 6233–6241. [CrossRef] [PubMed]
4. Imoberdorf, G.; Mohseni, M. Modeling and experimental evaluation of vacuum-UV photoreactors for water treatment. *Chem. Eng. Sci.* **2011**, *66*, 1159–1167. [CrossRef]

5. Imoberdorf, G.; Mohseni, M. Kinetic study and modeling of the vacuum-UV photoinduced degradation of 2,4-D. *Chem. Eng. J.* **2012**, *187*, 114–122. [CrossRef]
6. Li, W.; Li, M.; Wen, D.; Qiang, Z. Development of economical-running strategy for multi-lamp UV disinfection reactor in secondary water supply systems with computational fluid dynamics simulations. *Chem. Eng. J.* **2018**, *343*, 317–323. [CrossRef]
7. Luo, M.; Chen, Q.; Jeong, T.; Chen, J. Numerical modelling of a three-phase internal air-lift circulating photocatalytic reactor. *Water Sci. Technol.* **2017**, *76*, 3044–3053. [CrossRef]
8. Wiemann, D.; Mewes, D. Calculation of flow fields in two and three-phase bubble columns considering mass transfer. *Chem. Eng. Sci.* **2005**, *60*, 6085–6093. [CrossRef]
9. Gonzalez, M.; Oliveros, E.; Worner, M.; Braun, A. Vacuum-ultraviolet photolysis of aqueous reaction systems. *J. Photochem. Photobiol. C* **2004**, *5*, 225–246. [CrossRef]
10. Bielski, B.H.J.; Cabelli, D.E.; Arudi, R.L.; Ross, A.B. Reactivity of hydroperoxyl/superoxide radicals in aqueous solution. *J. Phys. Chem. Ref. Data* **1985**, *14*, 1041–1100. [CrossRef]
11. Buxton, G.V.; Greenstock, C.L.; Helman, W.P.; Ross, A.B. Critical Review of rate constants for reactions of hydrated electrons, hydrogen atoms and hydroxyl radicals in Aqueous Solution. *J. Phys. Chem. Ref. Data* **1988**, *17*, 513–886. [CrossRef]
12. Crittenden, J.C.; Hu, S.; Hand, D.W.; Green, S.A. A kinetic model for H_2O_2/UV process inacompletely mixed batch reactor. *Water Res.* **1999**, *33*, 2315–2328. [CrossRef]
13. Draganic, Z.D.; Draganic, I.G. Studies on the formation of primary yields of hydroxyl radical and hydrated electron in the g-radiolysis of water. *J. Phys. Chem.* **1973**, *77*, 765–772. [CrossRef]
14. Basfar, A.A.; Khan, H.M.; Al-Shahrani, A.A.; Cooper, W.J. Radiation induced decomposition of methyl tert-butyl ether in water in presence of chloroform: Kinetic modelling. *Water Res.* **2005**, *39*, 2085–2095. [CrossRef] [PubMed]
15. Mak, F.T.; Zele, S.R.; Cooper, W.J.; Kurucz, C.N.; Waite, T.D.; Nickelsen, M.G. Kinetic modeling of carbon tetrachloride, chloroform and methylene chloride removal from aqueous solution using the electron beam process. *Water Res.* **1997**, *31*, 219–228. [CrossRef]
16. Klassen, N.V.; Marchington, D.; McGowan, H.C. H_2O_2 determination by the I3- method and by $KMnO_4$ titration. *Anal. Chem.* **1994**, *66*, 2921–2925. [CrossRef]
17. Wols, B.; Harmsen, D.; Wanders-Dijk, J.; Beerendonk, E.; Hofman-Caris, C. Degradation of pharmaceuticals in UV (LP)/H_2O_2 reactors simulated by means of kinetic modeling and computational fluid dynamics (CFD). *Water Res.* **2015**, *75*, 11–24. [CrossRef]
18. Li, W.; Li, M.; Bolton, J.R.; Qiang, Z. Configuration optimization of UV reactors for water disinfection with computational fluid dynamics: Feasibility of using particle minimum UV dose as a performance indicator. *Chem. Eng. J.* **2016**, *306*, 1–8. [CrossRef]
19. Hofman-Caris, R.C.; Harmsen, D.J.; Beerendonk, E.F.; Knol, T.H.; Houtman, C.J.; Metz, D.H.; Wols, B. Prediction of advanced oxidation performance in various pilot UV/H_2O_2 reactor systems with MP- and LP- and DBD-UV lamps. *Chem. Eng. J.* **2012**, *210*, 520–528. [CrossRef]
20. Bagheri, M.; Mohseni, M. A study of enhanced performance of VUV/UV process for the degradation of micropollutants from contaminated water. *J. Hazard. Mater.* **2015**, *294*, 1–8. [CrossRef]
21. Casado, C.; Marugán, J.; Timmers, R.; Muñoz, M.; Vangrieken, R. Comprehensive multiphysics modeling of photocatalytic processes by computational fluid dynamics based on intrinsic kinetic parameters determined in a differential photoreactor. *Chem. Eng. J.* **2017**, *310*, 368–380. [CrossRef]
22. Yu, H.; Song, L.; Hao, Y.; Lu, N.; Quan, X.; Chen, S.; Zhang, Y.; Feng, Y. Fabrication of pilot-scale photocatalytic disinfection device by installing TiO_2 coated helical support into UV annular reactor for strengthening sterilization. *Chem. Eng. J.* **2016**, *283*, 1506–1513. [CrossRef]

MDPI
St. Alban-Anlage 66
4052 Basel
Switzerland
Tel. +41 61 683 77 34
Fax +41 61 302 89 18
www.mdpi.com

Processes Editorial Office
E-mail: processes@mdpi.com
www.mdpi.com/journal/processes

MDPI
St. Alban-Anlage 66
4052 Basel
Switzerland

Tel: +41 61 683 77 34
Fax: +41 61 302 89 18

www.mdpi.com

ISBN 978-3-0365-3436-7